NASA CR-72629

ANTENNA PATTERN SHAPING, SENSING AND STEERING STUDY

By

J. Savides

Prepared For The

NATIONAL AERONAUTICS AND SPACE ADMINISTRATION

NASA Lewis Research Center

Contract Number NAS3-11525

R. H. Myhre, Project Manager

FACILITY FORM 602

N70-32524 (ACCESSION NUMBER)

(THRU)

389 (PAGES)

1 (CODE)

CR-72629 (NASA CR OR TMX OR AD NUMBER)

07 (CATEGORY)

RECEIVED NASA STI FACILITY INPUT BRANCH JUL 1970

PHILCO-FORD CORPORATION

Western Development Laboratories Division

Palo Alto, California

Reproduced by the CLEARINGHOUSE for Federal Scientific & Technical Information Springfield Va. 22151

This report was prepared as an account of Government-sponsored work. Neither the United States, nor the National Aeronautics and Space Administration (NASA), nor any person acting on behalf of NASA:

A.) Makes any warranty or representation, expressed or implied, with respect to the accuracy, completeness, or usefulness of the information contained in this report, or that the use of any information, apparatus, method, or process disclosed in this report may not infringe privately-owned rights; or

B.) Assumes any liabilities with respect to the use of, or for damages resulting from the use of, any information, apparatus, method or process disclosed in this report.

As used above, "person acting on behalf of NASA" includes any employee or contractor of NASA, or employee of such contractor, to the extent that such employee or contractor of NASA or employee of such contractor prepares, disseminates, or provides access to any information pursuant to his employment or contract with NASA, or his employment with such contractor.

Requests for copies of this report should be referred to

National Aeronautics and Space Administration
Scientific and Technical Information Facility
P. O. Box 33
College Park, Md. 20740

NASA CR-72629

ANTENNA PATTERN SHAPING, SENSING AND STEERING STUDY

By

J. Savides

Prepared For The

NATIONAL AERONAUTICS AND SPACE ADMINISTRATION

NASA Lewis Research Center

Contract Number NAS3-11525

R. H. Myhre, Project Manager

FACILITY FORM 602

N70-32524 (ACCESSION NUMBER)

(THRU)

389 (PAGES)

1 (CODE)

CR-72629 (NASA CR OR TMX OR AD NUMBER)

07 (CATEGORY)

JUL 1970 RECEIVED NASA STI FACILITY INPUT BRANCH

PHILCO-FORD CORPORATION
Western Development Laboratories Division
Palo Alto, California

Reproduced by the CLEARINGHOUSE for Federal Scientific & Technical Information Springfield Va 22151

NASA CR-72629

FINAL REPORT

ANTENNA PATTERN SHAPING, SENSING AND STEERING STUDY

Prepared For The

NATIONAL AERONAUTICS AND SPACE ADMINISTRATION

Contract Number NAS3-11525

July 9, 1970

Under The Technical Management Of

R. H. Myhre, Project Manager

NASA Lewis Research Center
Cleveland, Ohio

Prepared By

John Savides

PHILCO-FORD CORPORATION
Western Development Laboratories Division
Palo Alto, California

PHILCO

PRECEDING PAGE BLANK NOT FILMED.

TABLE OF CONTENTS

Section		Page
	FOREWORD	xv
	ABSTRACT	xvii
	SUMMARY	xix
I	INTRODUCTION	1-1
II	SUMMARY OF RESULTS	2-1
III	RF ANALYSIS AND DESIGN	3-1
	3.1 Preliminary System Analysis	3-1
	3.1.1 Introduction	3-1
	3.1.2 Selection of Most Promising Antenna Configuration	3-1
	3.2 Reflector Feed Configuration Analysis and Trade-Off	3-2
	3.2.1 Analysis of Prime Focus Reflector with On-Axis Feed	3-8
	3.2.2 Analysis of On-Axis Cassegrain Feed	3-18
	3.2.3 Analysis of Prime Focus Reflector with Offset Feed	3-21
	3.2.4 Analysis of Horn Reflector	3-29
	3.2.5 Selection of Optimum Reflector Feed Configuration	3-36
	3.3 Design Analysis of Candidate Antenna Configuration	3-40
	3.3.1 Derivation of Optimum Aperture Taper for 28-Inch Diameter Reflector	3-40
	3.3.2 Estimation of Aperture Blockage Parameters	3-42
	3.3.3 Computed Radiation Pattern of 28-Inch Diameter Reflector with Optimized Aperture Distribution	3-42
	3.3.4 Active Element Sidelobe Suppression Techniques	3-48
	3.3.5 Estimation of Performance that May Be Achieved by Utilizing Active-Element Sidelobe Suppression Techniques	3-51
	3.3.6 Comments on Accuracy of Predicted Sidelobe Level	3-54
	3.3.7 Ellipticity of Polarization	3-55
	3.3.8 RF Losses and Power Handling	3-58
	3.3.9 Antenna Efficiency	3-60
	3.3.10 Beam Isolation	3-60
	3.3.11 Review of Proposed Antenna System	3-64
	3.3.12 Effect of Environmental Conditions on Antenna Performance	3-64
	3.4 Design Analysis of RF Subsystem	3-70
	3.4.1 Description of Proposed System	3-70

TABLE OF CONTENTS (Continued)

Section			Page
	3.4.2	Analysis of RF Components	3-72
	3.4.3	Analysis of Integrated RF Subsystem	3-85
3.5		Recommended Development Test Program	3-105
	3.5.1	Antenna Test Program	3-107
	3.5.2	Rotary Joint Feasibility Test Program	3-112
	3.5.3	Environmental Test Program	3-114
3.6		Effect of Variations in Design	3-120
	3.6.1	Beam Separation of Up to 2 HPBW on All Patterns	3-120
	3.6.2	Three Channels on Beam 3 and One on Beam 2	3-121
	3.6.3	Power Transfer from Solar Panels to Transmitters by Means of D.C. Sliprings	3-124
	3.6.4	Variation of Channel Separation to 1.2 Channel Widths with a Relaxation in Channel Isolation to 20 dB	3-124
	3.6.5	Variations in Power Level to as High as 2.5 KW per Channel	3-129
IV		DIRECTION SENSING SUBSYSTEM	4-1
4.1		Purpose	4-1
4.2		Study Summary and Conclusions	4-1
	4.2.1	Preferred Spacecraft DSS Approach	4-1
	4.2.2	Preferred Ground DSS Function	4-4
	4.2.3	DSS Integration into an On-Board Attitude Sensing and Control System	4-9
4.3		Spacecraft DSS	4-13
	4.3.1	Spacecraft Direction Sensing: Summary	4-13
	4.3.2	Interferometer Direction Sensing Subsystem Functional Description	4-22
	4.3.3	Interferometer Attitude Measurement Error	4-37
	4.3.4	Preliminary Interferometer Physical Configuration	4-63
	4.3.5	Reliability Analysis of Interferometer Receiver	4-66
4.4		Sensing the Direction of Satellite Narrow Antenna-Beam Axes by Pattern Measurement at Ground Receivers	4-71
	4.4.1	Direction Sensing by Beam Pattern Measurements on the Ground: Summary	4-72
	4.4.2	Direct Beam Pattern Measurement Techniques	4-74

TABLE OF CONTENTS (Continued)

Section			Page
	4.4.3	Sequential Power Measurement Technique	4-75
	4.4.4	Error Analysis of Beam Axis Location by Pattern and Partial Pattern Measurement	4-81
	4.4.5	Derivation of Antenna Pattern Geometric Center Location in Earth Coordinates	4-88
	4.4.6	Use of the Ground Beam Position Measurement to Resolve Ambiguities in the Spacecraft Interferometer Measurement	4-95
	4.4.7	Use of the Ground Direction Sensing Function as a Redundant DSS	4-97
V	MECHANICAL DESIGN ANALYSIS AND INTEGRATION		5-1
	5.1	Configuration	5-1
	5.1.1	Configuration Trade Offs	5-2
	5.1.2	Description of Proposal Design	5-2
	5.2	Thermal Design Studies	5-15
	5.2.1	Reflector Thermal Analysis	5-15
	5.2.2	Isolated Reflector Model	5-17
	5.2.3	Dual Reflector Model	5-17
	5.2.4	Reflector Transient Analysis	5-23
	5.2.5	Truss Structure Thermal Analysis	5-26
	5.2.6	RF Losses and Component Temperatures	5-28
	5.3	Structural Design Study	5-33
	5.3.1	Truss Structure	5-33
	5.3.2	Truss Distortion	5-36
	5.3.3	Reflector Distortions	5-36
	5.3.4	Structural Design Study Requirements	5-37
	5.3.5	Structural Design Analysis	5-44
	5.3.6	Truss Stress Analysis	5-59
	5.3.7	Truss Thermal Distortion Analysis	5-68
	5.3.8	Reflector Thermal Distortion Analysis	5-73
VI	ANTENNA CONTROL SUBSYSTEM		6-1
	6.1	Requirements	6-1

TABLE OF CONTENTS (Continued)

Section		Page
6.2	Control Techniques	6-6
6.2.1	Ground Commanded Antenna Control	6-6
6.2.2	On-Board Antenna Control	6-8
6.3	Computation Requirements	6-10
6.3.1	Ground Computations	6-10
6.3.2	Spacecraft Computations	6-19
6.4	Hardware Implementation	6-20
6.4.1	Open Loop System	6-21
6.4.2	Closed Loop System	6-21
6.4.3	Stepper Motor/DC Motor Trade-Off Analysis	6-30
6.4.4	Stepper Motor Control Simulation	6-33
6.5	Error Analyses	6-37
6.5.1	Summary of System Errors	6-37
6.5.2	Gear Ratio Selection/Step Resolution	6-37
6.5.3	Yaw Measurement Accuracy	6-40
6.5.4	Effects of Yaw Gimbal Error in Pitch and Roll	6-45
6.5.5	Computer Quantization	6-46
6.5.6	Inclination and Station Drift Errors	6-46
6.6	Alternate Requirements	6-48

LIST OF ILLUSTRATIONS

Figure		Page
3-1	Review of Antenna Configurations	3-3
3-2	Aperture Blockage for Prime Focus Reflector with On-Axis Feed	3-9
3-3	Prime Focus Reflector, On-Axis Feed, F/D = 0.4 Performance as Function of Aperture Taper	3-11
3-4	Prime Focus Reflector, On-Axis Feed, F/D = 0.35 Performance as Function of Aperture Taper	3-12
3-5	Prime Focus Reflector, On-Axis Feed, F/D = 0.30 Performance as Function of Aperture Taper	3-13
3-6	Prime Focus Reflector, On-Axis Feed, F/D = 0.25 Performance as Function of Aperture Taper	3-14
3-7	Prime Focus Reflector, On-Axis Feed: Optimum Sidelobe Performance as a Function of F/D Ratio	3-15
3-8	Prime Focus, On-Axis Feed F/D = 0.35 14 dB Edge-Directed Taper, Blockage Effects $\phi = 0^{o}$ (Best Plane)	3-16
3-9	Prime Focus, On-Axis Feed F/D = 0.35 14 dB Edge-Directed Taper, Blockage Effects $\phi = 90^{o}$ (Worst Plane)	3-17
3-10	Geometry of Cassegrain Feed Structure	3-19
3-11	On Axis Cassegrain Feed Optimum Performance as a Function of F/D Ratio	3-22
3-12	Cassegrain Feed F/D = 0.25 10 dB Edge-Directed Taper Blockage Effect	3-23
3-13	Geometry of Offset Feed Configuration	3-24
3-14	Aperture Taper Generated in the Plane PP by Offset Feed	3-27
3-15	Co-ordinate System Used for Computation of Radiation Pattern of Offset Feed Configuration	3-28
3-16	Form of Aperture Distribution Generated by Offset Feed	3-28
3-17	Prime Focus Reflector with Offset Feed Radiation Pattern for $\phi = 0^{o}$	3-31
3-18	Prime Focus Reflector with Offset Feed Radiation Pattern for $\phi = 45^{o}$	3-32
3-19	Prime Focus Reflector with Offset Feed Radiation Pattern for $\phi = 90^{o}$	3-33
3-20	Horn Reflector Configurations	3-34
3-21	Antenna Configuration Based on Prime Focus Reflector with Offset Feeds	3-38
3-22	Feed-Horn Configuration for Suppression of Back-Lobes	3-44
3-23	Blockage Parameters for 28-inch Diameter Reflector	3-45
3-24	Optimized 28-inch Diameter Reflector No Distortion $\phi = 0$	3-46
3-25	Optimized 28-inch Diameter Reflector No Distortion $\phi = 90$	3-47
3-26	Optimized 28-inch Diameter Reflector Near-in Sidelobe as a Function of Rotational Angle	3-49

LIST OF ILLUSTRATIONS (Continued)

Figure		Page
3-27	Antenna Configuration for Aperture Blockage Compensation	3-50
3-28	Suppression of Near-in Sidelobes by Aperture Blockage Compensation	3-50
3-29	Antenna Configuration for Active Zone Sidelobe Cancellation	3-52
3-30	Suppression of Near-in Sidelobes by Active Zone Cancellation	3-52
3-31	Septum Polarizer	3-56
3-32	Operation of Septum Polarizer	3-56
3-33	Integrated Circular Polarizer/Feed-Horn Structure	3-57
3-34	Geometry Used for Calculating Beam Isolation	3-61
3-35	Review of Proposed Antenna Configuration	3-65
3-36	Configuration for Evaluating Effect of Thermal Distortion on Antenna Radiation Pattern	3-67
3-37	28-inch Diameter Reflector Max Thermal Distortion Ø = 60	3-68
3-38	28-inch Diameter Reflector Max Thermal Distortion Ø = 90	3-69
3-39	Proposed RF Subsystem	3-71
3-40	4-Channel Rotary Joint for Use at 7-8 GHz	3-73
3-41	Rectangular Waveguide Corporate Feed Section for 12 GHz Rotary Joint	3-75
3-42	Proposed 4-Channel, High Power, Rotary Joint, Schematic	3-76
3-43	Detail of Waveguide Sections, 4-Channel Rotary Joint	3-77
3-44	Channel-Select Switch	3-78
3-45	Power Divider	3-80
3-46	Band-Stop Filter Design	3-81
3-47	Reflection and Transmission Coefficients for 7-Element Band Stop Filter	3-83
3-48	Phase Angle of Reflection Coefficient of Band Stop Filters	3-84
3-49	Multipactor Regions	3-87
3-50	The Coordinate System of the Coaxial Waveguide Choke Section	3-96
3-51	Transformed Outgassing Volume	3-99
3-52	Worst-Case Insertion Loss for System Based on Aluminum WR75	3-104
3-53	Worst-Case Insertion Loss for System Based on OFHC Copper WR90	3-106
3-54	Antenna Configuration and Test Equipment for Investigation of Aperture Blockage Compensation	3-108
3-55	Configuration for Investigating RF Coupling Between High-Power Antennas and Interferometer Elements	3-111
3-56	RF Test Set-up	3-115

LIST OF ILLUSTRATIONS (Continued)

Figure		Page
3-57	Patterns Considered in Estimating Effect of Increased Beam Separation	3-122
3-58	Configuration for Transmitting Three Channels on Beam 3 and One on Beam 2	3-123
3-59	Satellite Configurations for System Based on DC Power Transfer from Solar Panels	3-125
3-60	Combination of 2 Channels in a Single Beam	3-127
3-61	Filter Transmission Loss as a Function of Channel Separation	3-128
4-1	Basic Pilot-Tone Interferometer Receiver	4-5
4-2	Antenna Platform Attidude Sensing Error for Sensing Two Right Angle, .05°	4-10
4-3	Functional Block Diagram of Antenna Direction Sensing and Control System	4-11
4-4	Model of Direction Sensing Subsystem Measurement Coordinates	4-14
4-5	Pilot-Tone Receiver for Interferometer	4-25
4-5a	Phase Measurement and Output Averaging Circuit	4-26
4-6	Envelope Detector Noise Spectra	4-28
4-7	High Level Transmission Spectrum Centered at 12.2 or 8.2 GHz.	4-31
4-8	First-Order Cross-Product Spectral Density Reduction to a Level Equal to Receiver Noise Density	4-31
4-9	Coupling Between Feed-Horn and Adjacent Interferometer Element.	4-36
4-10	Beacon/Aiming-Point Geometry for Worst Case DSS Error Due to Baseline Length Variation	4-43
4-11	Description of Direction Angles to LOS Vector to Ground Beacon Transmitted #2 When the Aiming Point is Aligned with Beacon #1.	4-48
4-12	Yaws/Pitch Random Error Ratio vs. Angle Between LOS Vectors	4-50
4-13	Direction Angle from Interferometer Arm j to LOS Vector to Transmitter i	4-52
4-14	Nonorthogonality of the Interferometer Arms	4-59
4-15	Crossed-Arm Interferometer Configuration (Sketch)	4-64
4-16	Interferometer Horn Antenna Element Mounting Location, Plan View.	4-65
4-17	Horn Mounting, Isometric View	4-65
4-18	Multiple Frequency, Single Receiver Approach	4-68
4-19	Reliability Block Diagram - Receiver Only	4-70

LIST OF ILLUSTRATIONS (Continued)

Figure		Page
4-20	Antenna Pattern Slope	4-73
4-21	Measurement of the Total Power of an Angle-Modulated Signal . . .	4-77
4-22	Measurement of Power of a Fixed Spectral.	4-78
4-23	Error in Determining Off-Axis Angle vs. Off-Axis Angle.	4-86
4-24	Beam Boresight and Ground Receiver Vector in Antenna Platform Coordinates	4-89
4-25	Two Ground Receivers Sensing One Beam	4-93
4-26	Pattern Center Vector Geometry	4-94
4-27	Increment Angles $\Delta\ \theta$, Off-Axis Angle and Azimuth	4-98
4-28	Antenna Platform Attitude Sensing Error vs. Off-Axis Beam Angle of Ground Receiver	4-100
5-1	**Influence of Solar Array on Antenna Configuration**	5-3
5-2	**Antenna Configuration Trade-Off**	5-4
5-3	**View 1: Antenna Layout Design, Profile of Reflectors and Structures**	5-5
5-3	**View 2: Antenna Layout Design, Back of Reflectors and Structures. .**	5-6
5-3	**View 3: Antenna Layout Design, Motor Drive and Gimbal Assemblies. .**	5-7
5-3	**View 4: Antenna Layout Design Interferometer and Reflector Assemblies**	5-8
5-4	**Roll/Yaw Actuator**	5-11
5-5	**Solar Angle as a Function of Position in Orbit**	5-16
5-6	**Nodal Breakdown for Isolated Reflector Model**	5-18

LIST OF ILLUSTRATIONS (Continued)

Figure		Page
5-7	Maximum Temperature Difference and Maximum Temperature Gradient Versus Solar Angle	5-19
5-8	Reflector Temperature Distribution for $\theta = 0^{\circ}$	5-20
5-9	Reflector Temperature Distrubution for $\theta = 10^{\circ}$	5-21
5-10	Nodal Breakdown for Dual Reflector Model	5-22
5-11	Dual Reflector Temperature Distribution	5-24
5-12	Temperature Response of an Idealized Isothermal Reflector	5-25
5-13	Temperature Versus Solar Angle for Isothermal Rod Model	5-27
5-14	Solar Vector Orientation for Most Severe Temperature Distribution	5-29
5-15	Analytical Model Nodal Breakdown	5-30
5-16	Cylinder Temperature as a Function of Solar Illumination and Power Density	5-34
5-17	RF Loss Distribution and Component Temperatures	5-35
5-18	Upper Truss Support Structure	5-38
5-19	Lower Truss Support Structure	5-40
5-20	Alternate Tower Support Structure	5-41
5-21	Truss Computer Model	5-42
5-22	Truss Structural Analysis	5-46
5-23	Proposed Structural Design	5-48
5-24	Facesheet Thickness as a Function of Lateral Frequency	5-63
5-25	Combined Loads and Equivalent Point Load for Flight Load Factors	5-64
5-26	Equivalent Point Loads and Moment for 1g Sinusoidal Base Input	5-65
5-27	Compressive Stresses for the Conical Shell	5-67
5-28	Weight of Conical Honeycomb Shell as a Function of Facesheet Thickness	5-69
5-29	Reflector and Interferometer Deflection Studies	5-72
5-30	Finite Elements Model, NASA Lewis Antenna	5-76
5-31	Reflector Thermal Distortion-Zero Degree Sun Angle, 0.25 Inch Invar Honeycomb Core, 0.003 Inch Invar Face Sheets, 3-Point Support	5-77
6-1	Sketch of Antenna Patterns	6-4
6-2	Antenna Coverage Effects of a Five Degree Yaw Error	6-5
6-3	Ground Commanded Control Technique	6-7
6-4	On-Board Control Technique	6-9
6-5	Symbol Definition	6-11
6-6	Ground Computation Requirements	6-15

LIST OF ILLUSTRATIONS (Continued)

Figure		Page
6-7	Open Loop Stepper Motor Drive System	6-22
6-8	Closed Loop Stepper Motor Drive	6-24
6-9	Stepper Motor Control Loop	6-25
6-10	Brushless DC Motor Control Loop	6-26
6-11	Resolver Diagram	6-28
6-12	Motor-Resolver Block Diagram	6-29
6-13	Analog Computer Antenna Control Response	6-34
6-14	Analog Computer Antenna Control Response	6-35
6-15	Analog Computer Antenna Control Response	6-36
6-16	Excluded Area for Location of Second Ground Station (Shaded Area)	6-44
6-17	Geometry and Notation	6-48
6-18	Automatic Update System for Use with Ground Based Computer Concept	6-31

LIST OF TABLES

Table		Page
3-1	Preliminary Selection of Antenna Configuration	3-4
3-2	Relative Advantages and Disadvantages of Alternative Reflector Configurations	3-6
3-3	Maximum Edge-Directed Aperture Taper Compatible with 2.7° Beamwidth for 26" Diameter Reflector	3-20
3-4	Required Subreflector Dimensions as a Function of F/D Ratio	3-20
3-5	Derivation of Equal-Intensity Contours for Offset Feed Configuration	3-26
3-6	Aperture Distribution (in Volts/m) for Prime Focus, Offset Feed Configuration	3-30
3-7	Comparison of Candidate Reflector Antenna Configuration	3-41
3-8	Optimum Edge-Directed Taper as a Function of F/D Ratio for 28-inch Diameter Reflector	3-43
3-9	Rotary Joint Power to Initiate Multipacting	3-92
4-1	Direction Sensing Subsystem (DSS) Requirements	4-2
4-2	Interferometer Error Budget	4-6
4-3	Axis Location Uncertainty (Full Pattern Measurement)	4-8
4-4	Required Development Tests	4-12
4-5	Comparison of Interferometer and Monopulse Attitude Sensing	4-18
4-6	Evaluation of Interferometer Receiver Input Filter Rejection at 12.2 (or 8.2) GHz	4-32
4-7	Comparison of Isolation Filters	4-34
4-8	Interferometer Receiver Measurement Errors	4-38
4-9	Propagation of Errors into Pitch, Roll and Yaw	4-39
4-10	Interferometer Beacon Power & Receiver SNR Summary	4-41
4-11	Beacon #2 Location vs. Yaw/Pitch Random Error Ratio	4-51
4-12	Consolidated Reliability Analysis - Interferometer Receiver	4-69
4-13	Downlink Power Budget for Beam Axis Direction Sensing	4-80
4-14	Axis Location Uncertainty (Full Pattern Measurement)	4-82
5-1	System Weights	5-14
5-2	Reflector Truss Structure Temperature (°F) Distribution for Worst Case Orientation	5-31 5-31
5-3	Truss Temperature Summary	5-32

LIST OF TABLES (Continued)

Table		Page
5-4	Structural Design Criteria	5-43
5-5	Weight Distribution	5-45
5-6	Truss Member Sizes and Weights, Material-Aluminum	5-49
5-7	Truss Member Sizes and Weights, Material-Graphite/Epoxy (HY-E 1101)	5-50
5-8	Truss Member Sizes and Weights, Material-Boron Epoxy	5-31
5-9	Modal Participation Factors	5-56
5-10	Node Response to 1g RMS Sine Input	5-58
5-11	Truss Member Changes Based on Stress Analysis	5-60
5-12	Pointing Errors	5-74
6-1	Devised Requirements	6-3
6-2	Motor Trade Study	6-32
6-3	System Errors Sources	6-38
6-4	Effect of Alternate Requirements	6-53
6-5	Effect of Alternate Requirements	6-54

FOREWORD

The Antenna Pattern Shaping, Sensing, and Steering Study was performed under contract NAS 3-11525, from December 1968 through November 1969 by the Philco-Ford Corporation. The study results are presented in this volume. The study was performed under the management of the NASA/LeRC Project Managers.

Mr. Royce H. Myhre	NASA/LeRC
Mr. Perry W. Kuhns	NASA/LeRC

The study effort was conducted at Philco-Ford Space and Re-entry Systems Division under the management of John Savides. The following Philco-Ford engineering personnel comprised the permanent Study Team and performed the technical work reported in this volume:

John H. Cowan	-	RF Analysis and Design
Kenneth C. Ward	-	Direction Sensing Subsystem
Carl A. Zierman	-	Thermal Analysis and Overall Mechanical Design Integration
Oscar O. Steinbronn	-	Structural Analysis
William L. Nelms	-	Mechanical Configuration
Roger L. Rollins	-	Antenna Control Subsystem

ABSTRACT

This report presents the results of a study for determining the feasibility of multibeam antenna systems for the transmission of high RF power (in the order of 1 KW CW) from geostationary satellites. Conceptual designs are analyzed with respect to generation of multibeam patterns, low sidelobe levels, low RF insertion losses, high power handling capability of microwave components, antenna pointing capability and structural thermal distortions affecting antenna patterns and pointing errors.

A conceptual design is described that satisfies the desired requirements and constraints, concluding that such antenna systems are feasible for satellites to be launched in 1975. The hardware technology development efforts required to verify the analytical results are identified.

combining providing low loss characteristics and good power-handling capabilities. High-power breakdown in RF components was one of the most critical issues addressed. Multipactor and ionization breakdown were examined for all components, concluding that ionization breakdown was more critical than multipactor and that success depends on ease of outgassing and surface cleanliness. The problem of power dissipation in RF components and its effect on dimensional stability is solved by introducing external thermal radiators. The results of the structural thermal distortion analysis indicated that using Invar honeycomb reflectors, the effect of thermal gradients on the antenna patterns was negligible. Through iterative thermal distortion analysis, the pointing error due to deflections between the interferometer and antenna structure was reduced to an acceptable level. The phase measurement errors in the interferometer receiver were greatly reduced by using "pilot tone receiver", thus minimizing one of the key pointing errors. The necessary hardware development programs for verifying the analytical results have been identified.

SUMMARY

This report describes a study, performed under NASA/LeRC contract NAS 3-11525, which investigated the feasibility of a multibeam antenna system for the transmission of RF energies in the order of 1 KW CW per beam from a geostationary satellite. The system includes the antenna direction sensing and steering but does not include the high power RF devices such as TWT's or klystrons.

The study encompasses a program that involves conceptual design and analysis of an antenna system transmitting four partially overlapping beams of 2.7 degrees half power beam width at a frequency of 12.2 GHz; evaluation of the state of the art and its growth as applicable to the proposed antenna systems, recommendations for hardware development tests to confirm the antenna concept performance, and evaluation of the effect of alternate design requirements on the conceptual design and system performance.

The study resulted in a conceptual design that indicates it is feasible to achieve the desired objectives within the constraint of 1975 launch.

The basic concept arrived involves four separate prime focus reflectors with aperture blockage compensation for sidelobe suppression. The four reflectors are mounted on a platform having 360 degree (continuous) freedom of rotation with respect to the spacecraft, and two axes of limited motion. A receiving interferometer system is used for direction sensing and control of the antenna platform. The antenna reflectors and the interferometer horns are supported by truss structure. A four-channel RF rotary joint is used for transferring the RF power from the four transmitters located in the main spacecraft to the antenna platform.

This concept was arrived as a result of iterative analysis of the performance relating to the critical design features. The antenna concept selected results in sidelobe levels of -35 dB with aperture blockage compensation or -28 dB without the compensation feature. A four-channel rotary joint is prescribed based on a previous rotary joint developed by Philco-Ford. Using OFHC copper waveguide, the overall RF insertion losses were estimated as 1.19 dB. A band-stop filter and hybrid power divider is used for power

SECTION I

INTRODUCTION

The overall purpose of this study is to examine the technologies involved in multi-beam antenna systems for high power transmission applications from geostationary satellites. Continuous transmission of RF power in the order of 1 KW with emphasis on extremely low sidelobes and low RF losses presents new technological problems that do not hold the same prominence in present-day communication satellite antenna systems. The need for high power transmission systems is becoming more and more pronounced as the communication satellite requirements are increasing from communications to large terminals to communications to smaller and smaller terminals, to the point of broadcasting to home receivers. While this study is dealing with the antenna system for transmitting efficiently high RF energy in a given direction, NASA has been expanding considerable efforts towards the design and development of the associated high power transmitters with emphasis on high efficiency and long life.

High power transmission from satellites presents the problem of interference with non-participating receivers and must be restricted to well defined regions and thus the generation of sidelobes adjacent to the main antenna beam need to be greatly suppressed. Low sidelobe level antennas therefore have become a technological design challenge.

The specific objectives of this study were as follows:

1. Arrive at a multi-beam antenna system with fairly closely spaced beams, exhibiting very low sidelobe levels, and low RF losses with components capable of handling high power.

2. Define a system to point the antenna to any desired direction within a prescribed region with a fairly high accuracy.

3. Define through analysis a mechanical design that results in minimum thermal distortions, both from the point of view of beam distortion (increased side lobe level) and the point of view of pointing errors.

The study also examined the effect of variations in the basic requirements with the objective of defining trends and limits in performance and implementation feasibility. The study also defined the hardware developments required to verify the study results.

The basic philosophy used in meeting the objectives of this study was to emphasize the analyses, trade-offs, and solution of the key technological problems rather than detail system synthesis and detail definition of routine implementation functions.

The nature of the study was such that it required detailed analysis in several technical disciplines in order to arrive at the proper conclusions. To meet those requirements a four phase program was defined.

The first phase consisted of investigations of the state of the art, parametric analyses, and generation of interface requirements and constraints between the antenna subsystems.

The second phase involved the generation of alternate system configurations and the selection of a baseline configuration.

The third phase involved the performance of detailed analysis of the baseline design in all technical disciplines. It was during this phase that the final concept evolved. The results of the detail analysis were used to modify the initial baseline configuration, thus arriving at a design concept that met the design objectives.

The fourth phase consisted of the final performance analysis, detail definition of suggested hardware development program as the next step in the system development, and examination of the sensitivity of the design to variations in design parameters.

SECTION II

SUMMARY OF RESULTS

2.1 SCOPE

The scope of the contracted effort reported herein involved the analysis and design of an antenna system for a geostationary satellite.

The system was defined to include the transmitting antennas and the necessary antenna steering devices. As such, it included an interferometer system for direction sensing, the antenna drive mechanisms, all RF, electrical and mechanical connections to the antenna system from the rest of the spacecraft, and all those parts which are articulated with respect to the rest of the spacecraft to properly direct the transmitting antenna beams toward earth. The study scope did not include the high power RF devices such as the TWT's or klystrons.

The general requirements called for an antenna system which could transmit to earth four beams of 2.7 degree beamwidth at a frequency of 12.2 GHz, with a pointing accuracy of 0.1 degree. The power rating was to be 1 KW CW per channel, with one or two channels per beam.

The detailed requirements and system constraints are listed in Sections 2.2 and 2.3 below.

2.2 CONSTRAINTS

- Geostationary orbit
- 1975 launch date
- Five-year minimum expected life
- Atlas/Centaur class launch vehicle
- Main spacecraft and solar panels sun oriented
- Continuous rotation (360°/day) of the antenna system with respect to spacecraft accomplished by antenna system

2.3 DESIGN REQUIREMENTS

a) RF Characteristics

Operating Frequency	:	12.2 GHz
Number of Beams	:	4
Number of Channels	:	Four Transmission Channels Operating Simultaneously with Minimum One Channel Per Beam
Power	:	1 KW CW Per Channel
Polarization	:	Circular
Beamwidth	:	2.7 Degrees Half Power Beamwidth
Beam Separation	:	0.55 and/or 0.72 HPBW
Near-in Sidelobe Level	:	-30 to -35 dB
Channel Bandwidth	:	50 MHz
Channel Separation	:	100 MHz
Channel Isolation	:	40 dB
RF Losses	:	1.5 dB

b) Control Requirements

- o Capability for switching two RF channels to one beam on command.
- o Capability for changing the direction of one beam to a second position
- o Capability to point the antenna system to any direction within ± 20 degrees longitude and 45 degrees north, 10 degrees south latitude.

c) Direction Sensing

- o Use of signal transmitted from ground station, either beacon, command or uplink.
- o Use of the transmitting signal or beacon signal from the spacecraft.

d) Pointing Accuracy

- o Pointing accuracy ± 0.1 degrees RMS.
- o Accuracy maintained with spacecraft attitude error in three axes of ± 5.0 degrees and rates of 1.0 degree per minute.
- o Accuracy maintained with spacecraft drifting from station by 0.5 degrees RMS latitude or longitude at a rate of 0.1 degree per day.

2.4 STUDY RESULTS

The study has resulted in a feasible conceptual design that meets all the requirements and constraints stated above.

The basic concept involves four separate prime focus reflectors with aperture blockage compensation for sidelobe suppression. The four reflectors are mounted on a platform having 360 degree (continuous) freedom of rotation with respect to the spacecraft, and two axes of limited motion. A receiving interferometer system is used for direction sensing and control of the antenna platform. The antenna reflectors and the interferometer horns are supported by truss structure. A four-channel RF rotary joint is used for transferring the RF power from the four transmitters located in the main spacecraft to the antenna platform.

The antenna concept was arrived at after several trade-offs and design analyses. A broad state-of-the-art review was first of all carried out to determine which techniques were applicable. From this, it was concluded that the design requirements could best be met by utilizing a mechanically despun reflector system.

Various reflector/feed combinations were investigated in some detail before a decision was made to adopt a configuration based on multiple prime focus reflectors. This approach is seen to be advantageous in that it immediately simplifies the RF design and at the same time provides a convenient means of steering individual beams since the appropriate reflector can be independently pivoted about a gimbal axis.

The only shortcoming with respect to the system being considered was that aperture blockage effects would limit the suppression of the near-in sidelobes in the secondary radiation pattern. Extensive computational analyses were therefore performed in order to identify the antenna geometry which could provide maximum suppression. From these analyses, it was concluded that a near-in sidelobe level of approximately -28 dB can be achieved by using a 28-inch diameter reflector with an F/D ratio of 0.35.

Further calculation then showed that the system design goal of -30 to -35 dB can be realized by employing relatively simple aperture blockage compensation techniques in conjunction with the optimized prime focus geometry. A compensating element in the form of a hollow thin-walled dielectric tube antenna can be conveniently located behind the prime focus feed horn since it will not add to the blockage area and will have only a minimal effect on the phase front of the plane wave emanating from the reflector. A small fraction of the total power (approximately 2%) can then be radiated from this element with its phase adjusted so as to achieve the required sidelobe cancellation.

To minimize the detrimental effects of solar heating, the reflector contours must be fabricated from low coefficient of expansion materials. Mechanical and thermal design considerations indicated that a 0.003-inch Invar face sheet backed by a 0.25-inch Invar honeycomb core would be a suitable structure. A computational analysis was therefore carried out to evaluate the performance which could be obtained by utilizing this technique. It was found that the worst-case thermal distortions will occur when the solar vector is at right angles to the reflector axes. The maximum calculated distortion corresponds to a 0.002-inch deflection of the sunlit edge of the reflector and, to a first-order approximation, the overall distortion can be compared to a small (0.009°) rigid body rotation of the reflector. The maximum deflection of the aluminum feed horn support was calculated as being 0.018 inch, which gives rise to a beam-pointing error of 0.06° RMS in longitude and latitude. The worst-case distortions were converted into equivalent phase errors and the secondary radiation pattern of the reflector antenna recalculated. This yielded the result that the highest near-in sidelobes remain at essentially the same level. Thus, it is concluded that, with the proposed fabrication technique, there will be no significant deterioration of the antenna radiation pattern due to the effects of solar heating.

One of the most critical issues involved in high-power spaceborne transmission systems is the RF losses in various components and waveguide runs. The losses not only translate into large solar array raw power,

but they result in significant thermal problems due to the power dissipation in the RF components. A great deal of effort was expanded in arriving at a system that results in minimum losses. The proposed configuration is outlined schematically in Figure 2-1. As shown in the diagram, the required channel-combining functions are achieved by a network of band-stop filters, hybrid power dividers and two-way switches. A key design feature is the utilization of OFHC copper waveguide in conjunction with band-stop (rather than band-pass) filters, the latter being selected because of their low loss characteristics and good power-handling capabilities. Figure 2-2 is a flow diagram of all losses in the RF system. The circuit shown represents the combined channel into one beam mode, and therefore it is the worst-case insertion loss mode.

As seen in the diagram, the initial waveguide run from the transmitter to the rotary joint is 6 feet long. This is due to the fact that the antenna reflectors had to be mounted as high as the shroud would allow above the spacecraft, so that the radiation beams can clear the solar panels.

Another critical issue is, of course, the problem of high-power breakdown in the space entironment. In this respect, there are three potential failure mechanisms: (1) Multipactor breakdown, (2) Ionization breakdown in regions of localized gas entrapment, (3) Dimensional variations brought about by RF power dissipation within the structure.

The critical area for multipactor breakdown was found to be the choke section of the innermost coaxial channel. Calculation showed, however, that this section has a probable breakdown power of 18 KW CW and it was therefore concluded that multipactor effects would in no way compromise the performance of the RF system.

The critical area for ionization breakdown was also identified as being the coaxial waveguide choke sections which have a relatively high surface area-to-volume ratio and which serve as a conductance path for particles outgassing from inside the rotary joint structure. The maximum pressure due to outgassing, however, was estimated to be of the order of 10^{-5} torr,

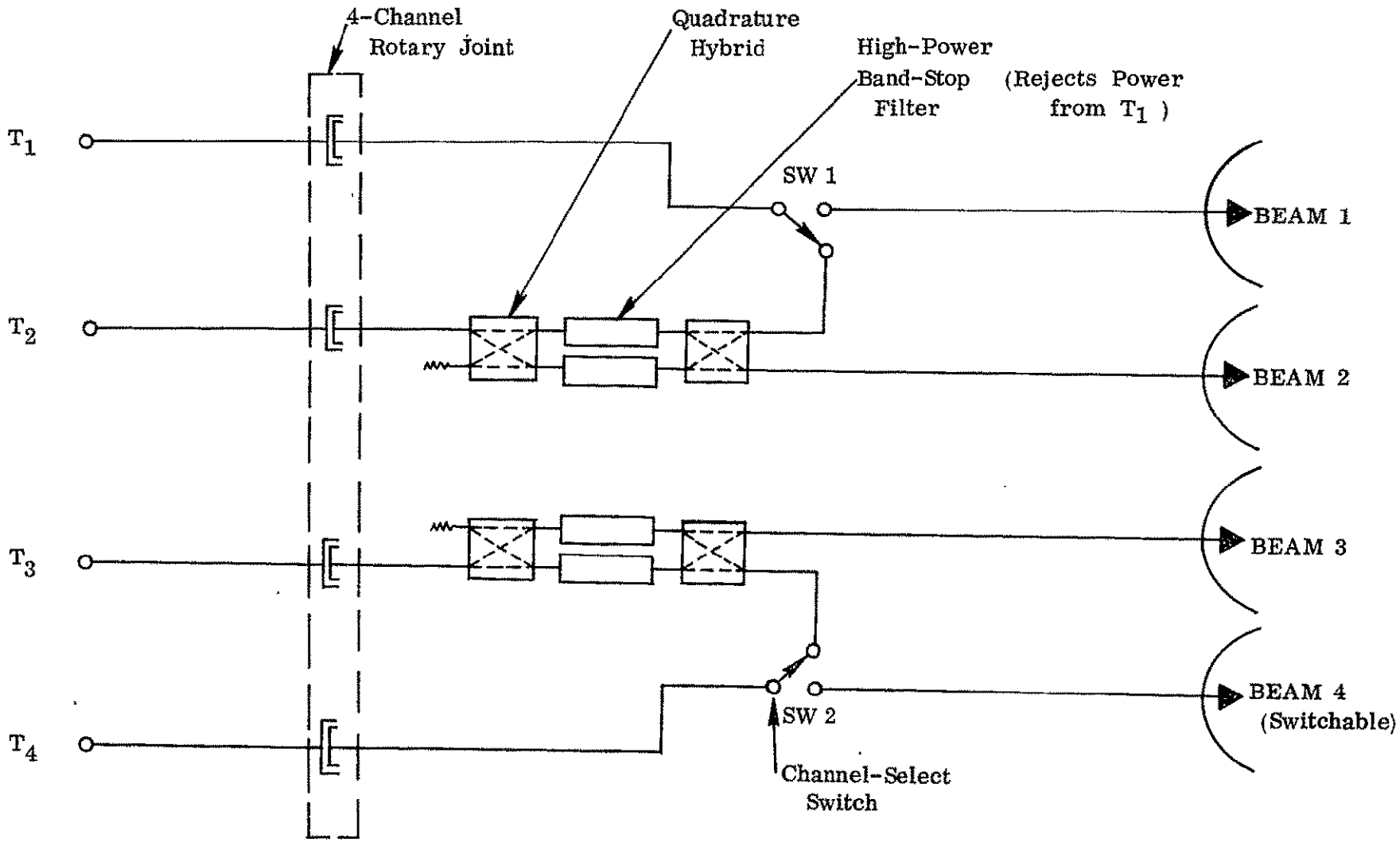

FIGURE 2-1 RF SUBSYSTEM

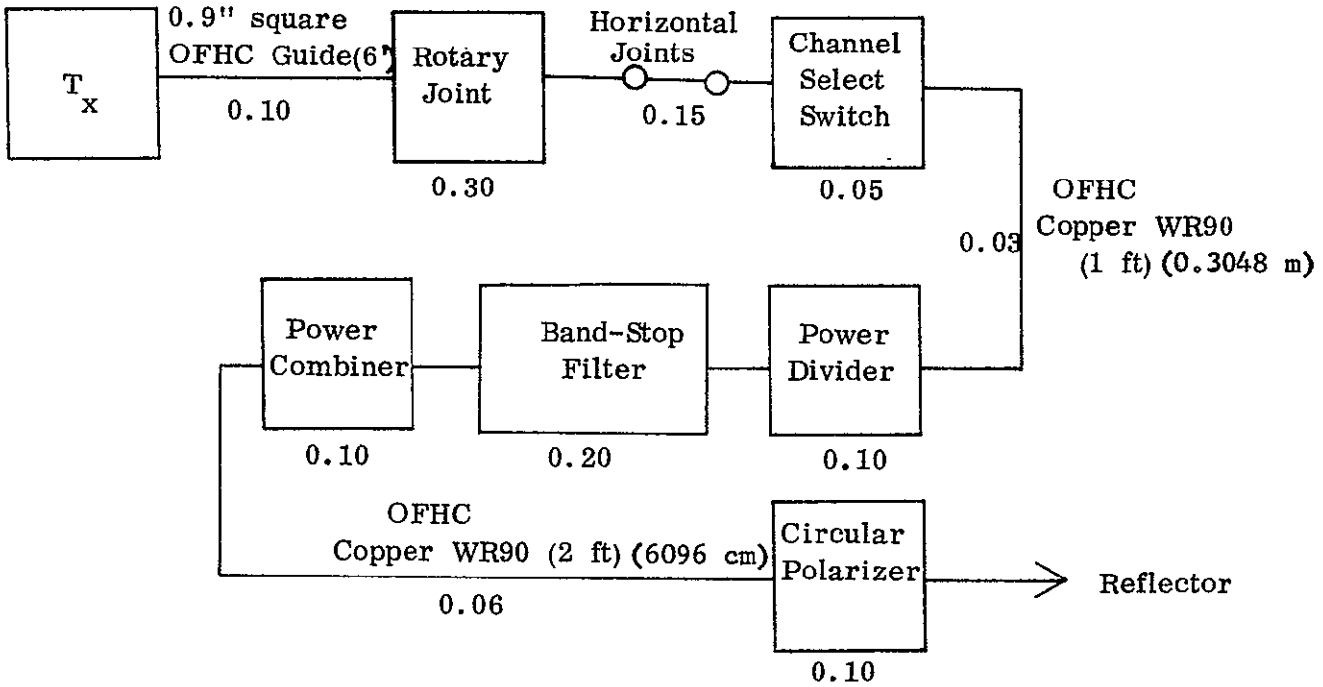

TOTAL LOSS = 1.19 dB

Figure 2-2 Worst-Case Insertion Loss for System Based on OFHC Copper WR90

which is well within the ionization breakdown limit of approximately 10^{-2} torr. Further calculation revealed that the time constant associated with the initial venting process is extremely small (0.5 milliseconds); thus, for a clean structure the pressure within the choke sections will drop below the critical level within a few seconds.

Analysis of the effect of RF power dissipation revealed that external thermal radiators will be needed to achieve the dimensional stability required by the band-stop filter cavities and the coaxial choke sections of the rotary joint. For example, calculation showed that 6 ft^2 of radiator surface will be required for the rotary joint.

The direction sensing system consists of two orthogonal axes interferometers of 32-inch baseline with the receiving horns mounted directly on the truss members connecting the four antenna reflectors. The frequency used is 8 GHz. A second, shorter baseline for ambiguity resolution is not used, on the basis that the ambiguity can be easily resolved on the ground.

One receiver is used for both axes and it is being switched between interferometer arms by means of PIN diode RF switches at a 20 Hz rate. The receiver is a "pilot-tone" type to achieve negligible phase bias error in the receiver channel. This is achieved by measuring the phase of all incoming signals relative to a reference RF sinusoid. Two ground beacons are required to derive three axes information. The second beacon is required for measuring an angle about the line of sight.

The interferometer information is in the form of direction cosines of the angle between the beacon station line of sight and the interferometer arm. The interferometer output is fed to an onboard or ground computer which compares the measured angles with a set of desired interferometer angles and computes the required three axes gimbal drive signals. Both onboard self-contained and ground controlled antenna pointing systems were studied. The choice depends primarily on spacecraft body rates and operational constraints.

An extensive thermal and structural computer analysis was conducted to determine the structural distortions due thermal gradients and to establish component temperatures. Some of the results on the antenna patterns and pointing were discussed earlier. One of the key considerations recognized early in the study was the pointing error that would result due to thermal deflections between the interferometer reference system and the four antenna reflectors. An iterative process of thermal distortion analysis was conducted until an optimum location for mounting the interferometer horns with respect to the reflectors was established that provided an acceptable pointing error. A system analysis was conducted to establish the overall pointing error considering all possible error sources. Table 2-1 summarizes the error sources and the net pointing error per axis.

In general, the design concept presented indicates that it is feasible to achieve the antenna performance, the power handling and pointing errors required. High power breakdown in microwave components in the critical issue, and a detail development test program to verify the analytical result and provide information on manufacturing techniques, has been generated.

TABLE 2-1

SYSTEM ERROR SOURCES

Pitch Axis (Brushless DC Motor Drive)

Alignment of Interferometer to Antenna Structure	$\pm.018$
Thermal Deflection in Horn	$\pm0.06^{\circ}$
Interferometer Measuring Accuracy (20 Hz)	$\pm.02$
Computer Quantizing Errors (10 bit)	±0.02
Station Drift	±0.02
D/A Conversion	±0.01
Yaw Gimbal Error	±0.05
RSS Total	$\pm.088$

Roll Axis (Stepper Motor)

Alignment of Interferometer to Antenna Structure	$\pm0.05^{\circ}$
Thermal Deflection in Horn	$\pm0.06^{\circ}$
Step Resolution	±0.03
Interferometer Measuring Accuracy	$\pm.02$
Linear Actuator Backlash	±0.01
Computer Quantizing Errors	±0.02
Inclination (0.5°)	±0.03
Yaw Gimbal Error ($\pm1^{\circ}$)	±0.05
RSS Total	±0.095

Yaw Axis (Stepper Motor)

Interferometer Measuring Accuracy	±0.95
Step Resolution	±0.03
Linear Actuator Backlash	±0.01
Computer Quantizing Errors	±0.02
RSS Total	$\pm0.95^{\circ}$

SECTION III

RF ANALYSIS AND DESIGN

3.1 PRELIMINARY SYSTEM ANALYSIS

3.1.1 Introduction

This section of the study encompasses the conceptual design and analysis of the 12 GHz multiple-beam antenna system, the development test program required to verify its performance and the evaluation of the effects of alternate design requirements on the system concept and performance characteristics.

The proposed antenna configuration takes the form of four separate prime focus reflectors, each with aperture blockage compensation incorporated in its design. A network of band-stop filters, hybrid power dividers and two-way switches performs the required channel-combining functions. This network and the reflector antennas form an integrated structure which is despun from the main body of the satellite by means of four-channel RF rotary joint.

The initial effort in the study is directed towards establishing which antenna concept represents the best means of achieving the system design goals. The most promising configuration is seen to be a mechanically despun reflector system, and extensive computational analyses are therefore carried out to optimize its theoretical performance in terms of beamwidth and sidelobe suppression.

The conceptual design and analysis of the key RF subcomponents then yields performance figures which are used to evaluate the capabilities of the integrated system. In carrying out this evaluation, particular emphasis is placed on demonstrating that theoretically the system can transmit 1 KW CW power levels while operating in a space environment.

Test programs are then devised to verify:

a. The proposed aperture blockage compensation techniques
b. The power rating of the system under hard vacuum conditions

Finally, the effect of alternate design requirements on the system performance are evaluated. For the purpose of the analysis, the design goals are specified to be as follows:

Operating Frequency	:	12.2 GHz
Number of Beams	:	4
Half-Power Beamwidth (HPBW)	:	2.7°
Beam Separation	:	0.55 and/or 0.72 HPBW
Near-in Sidelobe Level	:	-30 to -35 dB
Polarization	:	Circular (ellipticity less than 1.1)
Number of Channels	:	Four transmission channels operating simultaneously with a minimum of one channel per beam.
Channel Width	:	50 MHz
Channel Separation	:	100 MHz
Channel Isolation	:	40 dB
Attenuation	:	Transmitted signal of each channel from the final output stage shall not be attenuated by more than 1.5 dB and flat within ± 0.5 dB over 0.9 of the channel width.
Phase Delay	:	Phase delay of each channel shall be linear within $\pm 1^{\circ}$ over 0.9 of the channel width.
Power-Handling Capability of System	:	1 KW CW per channel

3.1.2 Selection of Most Promising Antenna Configurations

The antenna concepts which cane under review are listed diagramatically in Figure 3-1 and the principal reasons for their being rejected or selected for further consideration are given in Table 3-1.

From this table it is seen that the preferred approach is to utilize a mechanically despun reflector system and that there are three potentially useful configurations of this type:

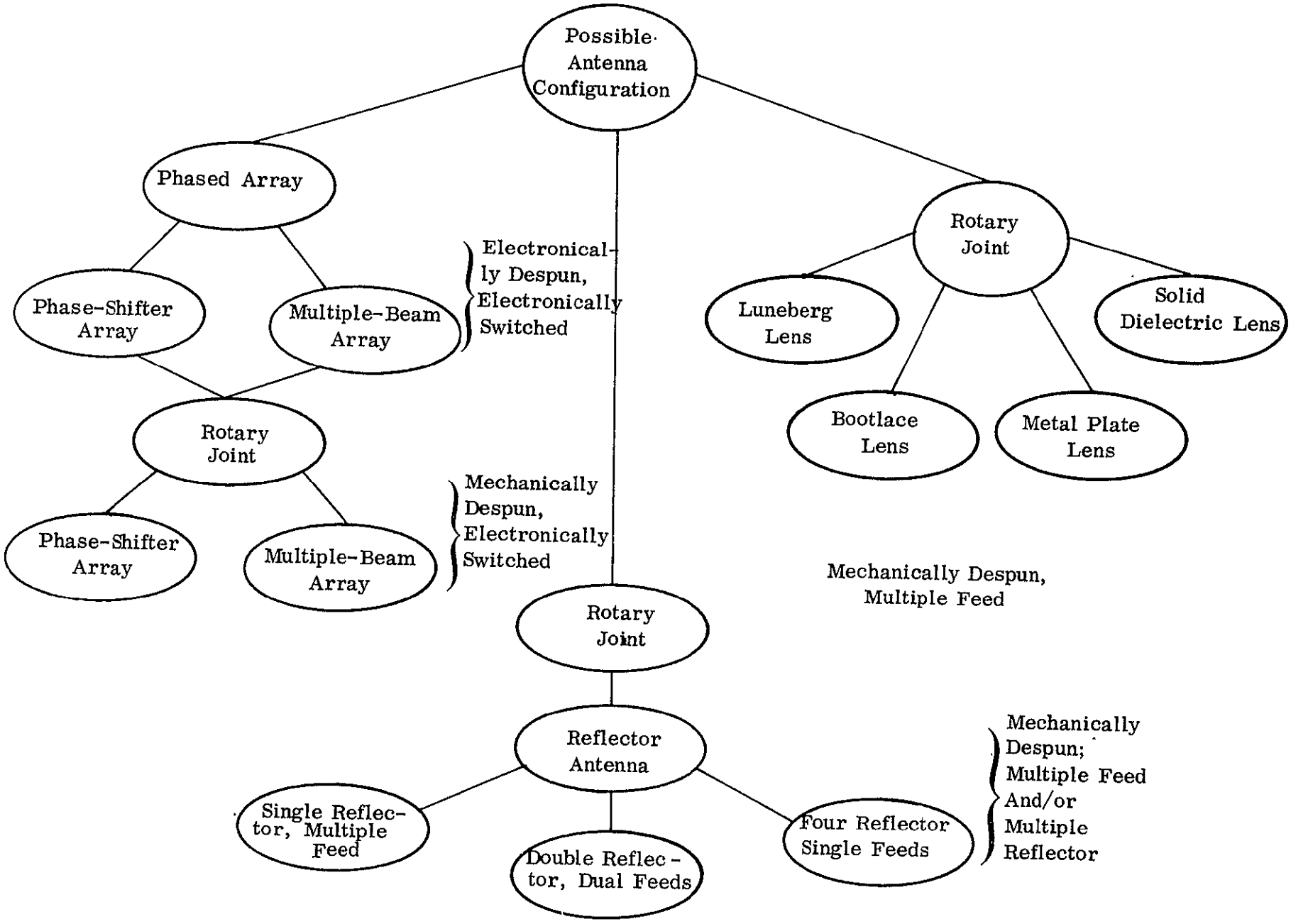

Figure 3-1 Review of Antenna Configurations

TABLE 3-1

Preliminary Selection of Antenna Configuration

CONFIGURATION	REASONS FOR REJECTION	REASONS FOR SELECTION
Phased Array	Highly Complex, Heavy, High Insertion Loss	
Mechanically Despun Phase-Shifter Array	Despun antenna is only required to produce a limited number of beams, therefore complexity of phased array system is not justified.	
Mechanically Despun Multiple-beam Array	Cannot simultaneously achieve the required beam spacing and isolation.	
Mechanically Despun Luneberg Lens	Complex Mechanical Assembly; Heavy; Poor Structural Integrity; High Insertion Loss	
Mechanically Despun Bootlace Lens	Complex Mechanical Structure; Heavy; High Insertion Loss	
Mechanically Despun Metal Plate Lens	Complex Mechanical Structure; Susceptible to Thermal Distortion	
Mechanically Despun Solid Dielectric Lens	Heavy; High Insertion Loss	
Mechanically Despun Single Reflector		Light Weight; Compact Feed Structure
Mechanically Despun Double Reflector		Light Weight; Fairly Compact Mechanical Structure
Mechanically Despun Four-reflector		Fairly Light Weight; Simple RF Design

1. Single reflector with a multiple feed.
2. Two reflectors, each with a dual feed.
3. Four separate reflectors, each with a single feed.

The relative advantages and disadvantages of these configurations, for both the axial and offset feed conditions, are directly compared in Table 3-2.

As shown in the Table, the dual and multiple-feed techniques are the most attractive from the standpoint of weight and mechanical complexity. Unfortunately, they are susceptible to mutual coupling and off-axis defocusing effects which could lead to unacceptable performance degradation.

These effects were recently the subject of an experimental investigation by Philco-Ford. Measurements were made at 7.5 GHz using a 40-inch parobolic reflector with an F/D ratio of 0.38. Two waveguide horns, each designed to give a 20 dB aperture taper, were used as feed elements.

Feeding the reflector with a single on-axis horn gave a half-power beamwidth (HPBW) of 3° and a sidelobe level of -26 dB. The two horns were then mounted symmetrically on either side of the reflector axis. Due to their physical dimensions, the minimum spacing which could be achieved was 1.15 λ_o, corresponding to a main beam separation of 1.7 HPBW. With this spacing and with one horn terminated, the secondary radiation pattern had a -17.3 dB sidelobe on the side of the main beam adjacent to the reflector axis and a -24 dB lobe on the opposite side. Also, it was observed that the HPBW had increased to 3.3°.

Since the isolation between the feed elements had a measured value of greater than 27 dB, the pattern degradation could not be attributed to mutual coupling effects. It was, therefore, a consequence of the phase error brought about by the off-axis displacement of the feed horns.

TABLE 3-2

Relative Advantages and Disadvantages of Alternative Reflector Configurations

CONFIGURATION		ADVANTAGES	DISADVANTAGES
(1) Single Reflector	On-axis Feed	Minimizes number of reflector surfaces required to produce multibeam pattern; very compact mechanical structure; minimizes antenna weight.	Severe aperture blockage due to multiple feed structure; mutual coupling between feed elements; pattern degradation due to off-axis defocusing.
	Offset Feed	Minimizes number of reflector surfaces required to produce multibeam pattern; compact mechanical structure; minimizes antenna weight; no aperture blockage.	Mutual coupling between feed elements; complex RF design; pattern degradation due to off-axis defocusing.
(2) Double Reflector	On-axis Feeds	Reduces number of reflector surfaces required to produce multibeam pattern; fairly compact mechanical structure; reduces antenna weight.	Aperture blockage; mutual coupling between dual feed elements; pattern degradation due to off-axis defocusing.
	Offset Feeds	Reduces number of reflector surfaces required to produce multibeam pattern; fairly compact mechanical structure; reduces antenna weight; no aperture blockage.	Mutual coupling between dual feed elements; complex RF design; pattern degradation due to off-axis defocusing.
(3) Four-Reflectors	On-axis Feeds	Simple RF design; good beam isolation.	Aperture blockage; requires four separate reflector surfaces
	Offset Feeds	No aperture blockage; fairly good beam isolation.	Requires four separate reflector surfaces; fairly complex RF design.

These results indicate that multiple feeds based upon waveguide horn elements can only be usefully applied to systems in which beam separations of approximately 1·5 to 2·0 HPBW are required. Hence, to achieve smaller separations, as will be required for this project (0·55 and 0·72 HPBW) it would be necessary to resort to the use of end-fire antennas, such as dielectric rods, for feed elements.

A configuration of this type has already been investigated by Koenig and Dalley.* Their principal finding was that, while off-axis defocusing effects were relatively small, considerable performance degradation resulted from mutual coupling when beam separations of less than 1·0 HPBW were employed.

The experiments described were carried out at 6 GHz, using dielectric rods to illuminate a six-foot parabolic section (F/D = 0·5). It was found that a single rod, placed on-axis could produce a secondary radiation pattern with a -25 dB sidelobe level. However, when two such rods were positioned so as to obtain beams separated by 1·0 HPBW, the resultant mutual coupling caused this level to rise to approximately 14 dB.

From these results, it is evident that dual, or multiple-feed structures cannot be used to generate closely spaced pencil beams which have low sidelobes. Therefore, since this project requires very stringent control of near-in sidelobes (design goal -30 to -35 dB), it is necessary to forego the use of such techniques and employ an antenna system based on four separate reflectors, each with a single feed.

This type of system is more complex mechanically. However, it does have certain advantages in that:

a. Good beam isolation is readily obtained.

b. A convenient means of steering beam number 4 is provided, since the appropriate reflector can be independently pivoted about a gimbal axis.

---

* "Multiple Beam Antennas for Regional Coverage Communications Satellites" by W. A. Koenig and D. G. Dalley -- AIAA 2nd Communications Satellite Systems Conference, San Francisco, April 1968.

In addition, since each reflector is only required to generate a single beam, there is a considerable reduction in the antenna design problems.

Before the antenna system can be completely specified, it is necessary to determine which reflector feed configuration is best suited to this particular application. In this respect, there are four promising configurations:

(1) Prime focus, on-axis feed,
(2) Cassegrain, on-axis feed
(3) Prime focus, offset feed
(4) Horn reflector (cornucopia)

Hence, the main effort in the antenna analysis is directed towards establishing which of these represents the best means of achieving the required system performance.

3.2 REFLECTOR FEED CONFIGURATION ANALYSIS AND TRADE-OFF

Detailed analyses were carried out to evaluate the performances of the various reflector feed configurations with respect to the requirements of this system. These are presented in the following sections, after which the trade-off leading to the final definition of the antenna system is described.

3.2.1 Analysis of Prime Focus Reflector with On-Axis Feed

The primary objective of this analysis was to optimize the antenna geometry by adjusting the aperture taper, F/D ratio and blockage parameters so as to produce the required 2.7° HPBW with maximum suppression of the near-in sidelobe level.

For the purpose of the calculations, the following assumptions were made:

1. The feed element is a circular waveguide horn which provides an essentially symmetrical primary pattern with zero phase error.
2. The feed-horn radiation pattern, when expressed in dB's, may be very closely approximated by a simple quadratic function, i.e., the edge-directed aperture taper may be defined as:

   $T(\theta) = -k\,\theta^2$ dB, where θ = angle from horn axis and k = a constant.
3. There is zero mechanical error in the contour of the main reflector.
4. The aperture blockage is of the form shown in Figure 3-2. (The waveguide run to the feed is taken to the edge of the reflector, as shown, in order to eliminate shadowing of the primary feed pattern.)

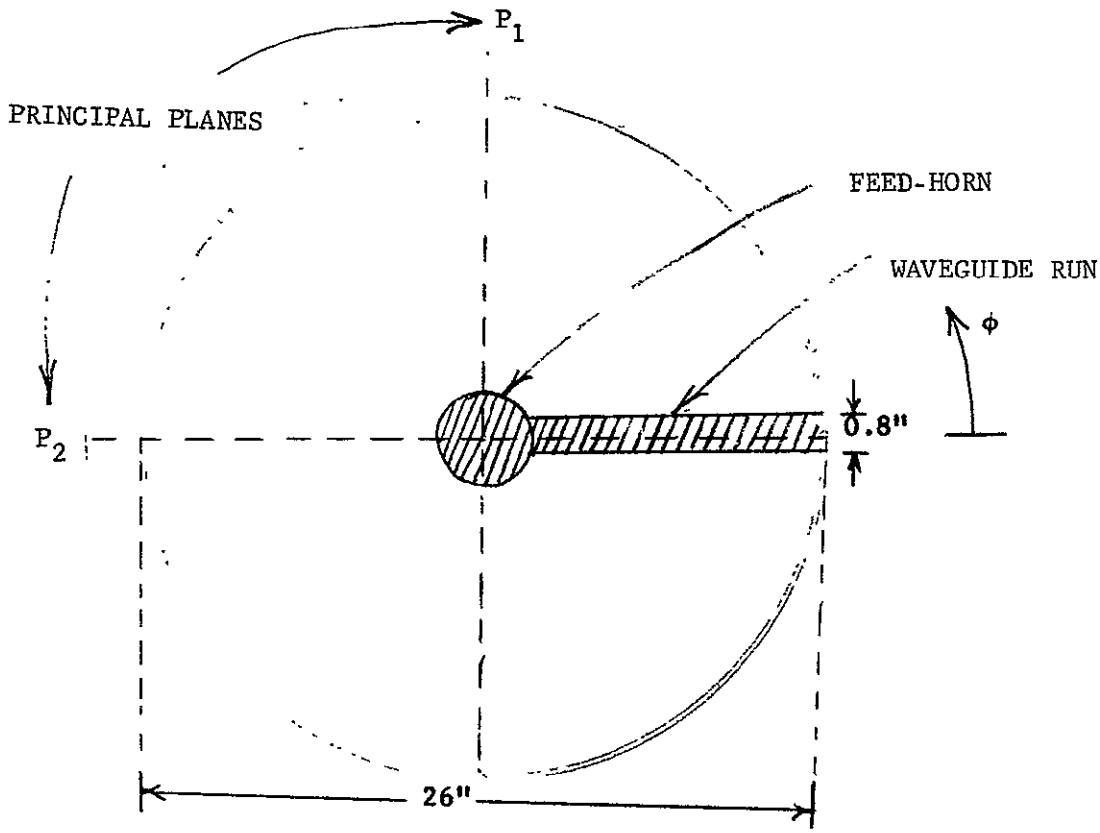

FIGURE 3-2 APERTURE BLOCKAGE FOR PRIME FOCUS REFLECTOR WITH ON-AXIS FEED

These assumptions were used in conjunction with the following basic design parameters:

1. Diameter of main reflector = 26.0 inches (66.04 centimeters): determined by overall mechanical design considerations.
2. Operating frequency = 12·2 GHz.

In calculating the performance obtainable for a given F/D ratio, the following procedure was adopted:

1. Calculate the angle subtended by the radiating aperture at the focal point of the parabolic reflector.
2. Calculate the primary patterns associated with 10 ,12 ,14 ,16 , 18 and 20 dB edge-directed aperture tapers.
3. Estimate the diameters of the feed-horns required to produce these tapers.
4. Compute the secondary radiation 3-2 patterns in the orthogonal planes P1 and P2 (see Figure 2-1), with and without aperture blockage.
5. From these patterns, derive plots of near-in sidelobe level, beamwidth and gain as a function of aperture taper.
6. Hence, obtain sidelobe level corresponding to a $2{\cdot}7^{\circ}$ beamwidth and thereby define the maximum suppression obtainable for the F/D ratio being considered.

This analysis was carried out using the WDL SECPAT Antenna Computer Program for a range of F/D ratios and the performance curves obtained are shown in Figures 3-3 through 3-6. These were used to obtain a plot of the minimum sidelobe level as a function of F/D ratio and this is given in Figure 3-7, together with the corresponding gain values.

From this, it is seen that a maximum sidelobe suppression of approximately 27·5 dB may be obtained by utilizing an F/D ratio in the region of 0·34.

(Because of the "shallow" optimization curve, the computed patterns for the optimized F/D = 0·35 configuration are representative of the best achievable performance. These are shown in Figures 3-8 and 3-9.)

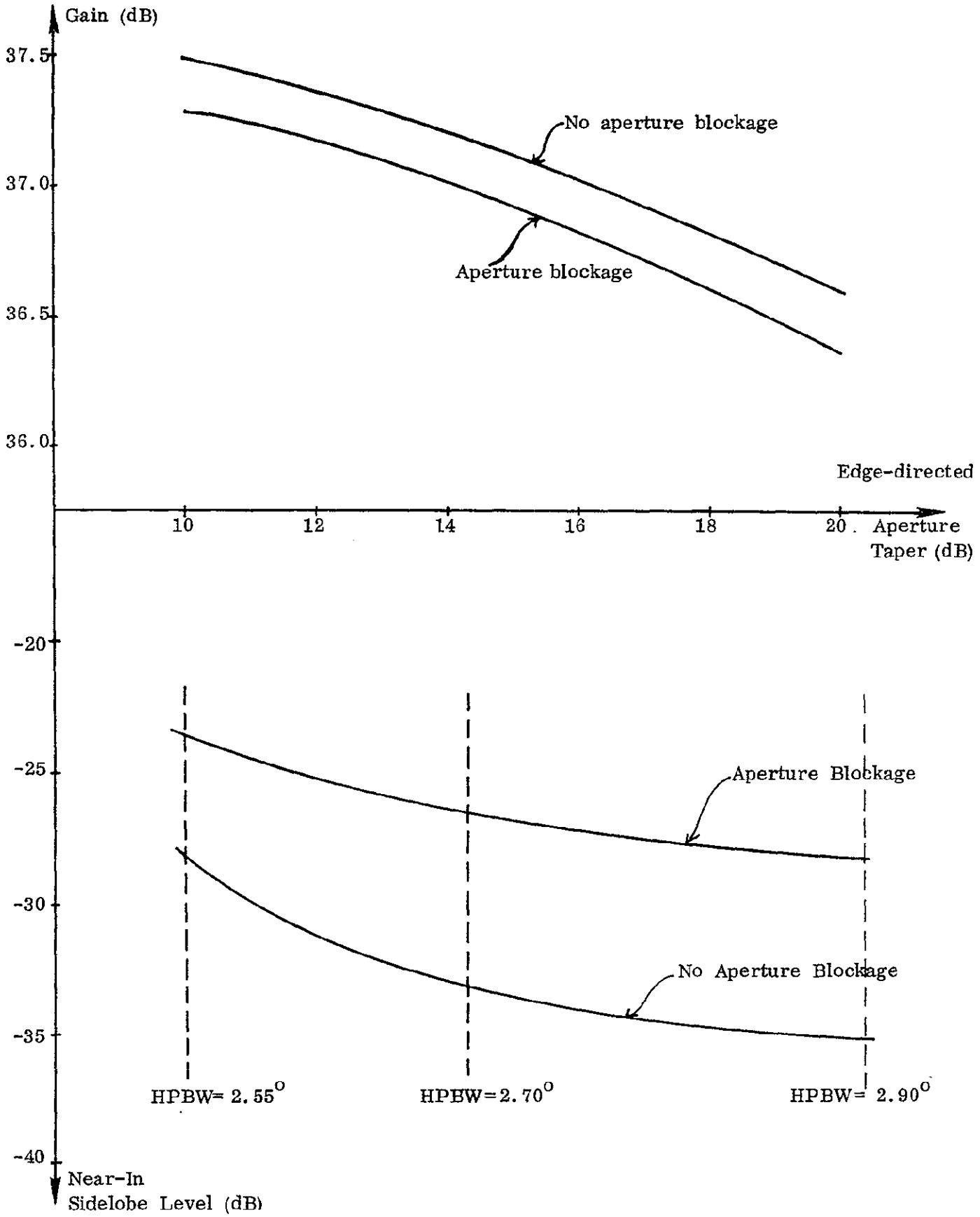

Figure 3-3 Prime Focus Reflector, On Axis Feed, F/D = 0.4 Performance as Function Of Aperture Taper

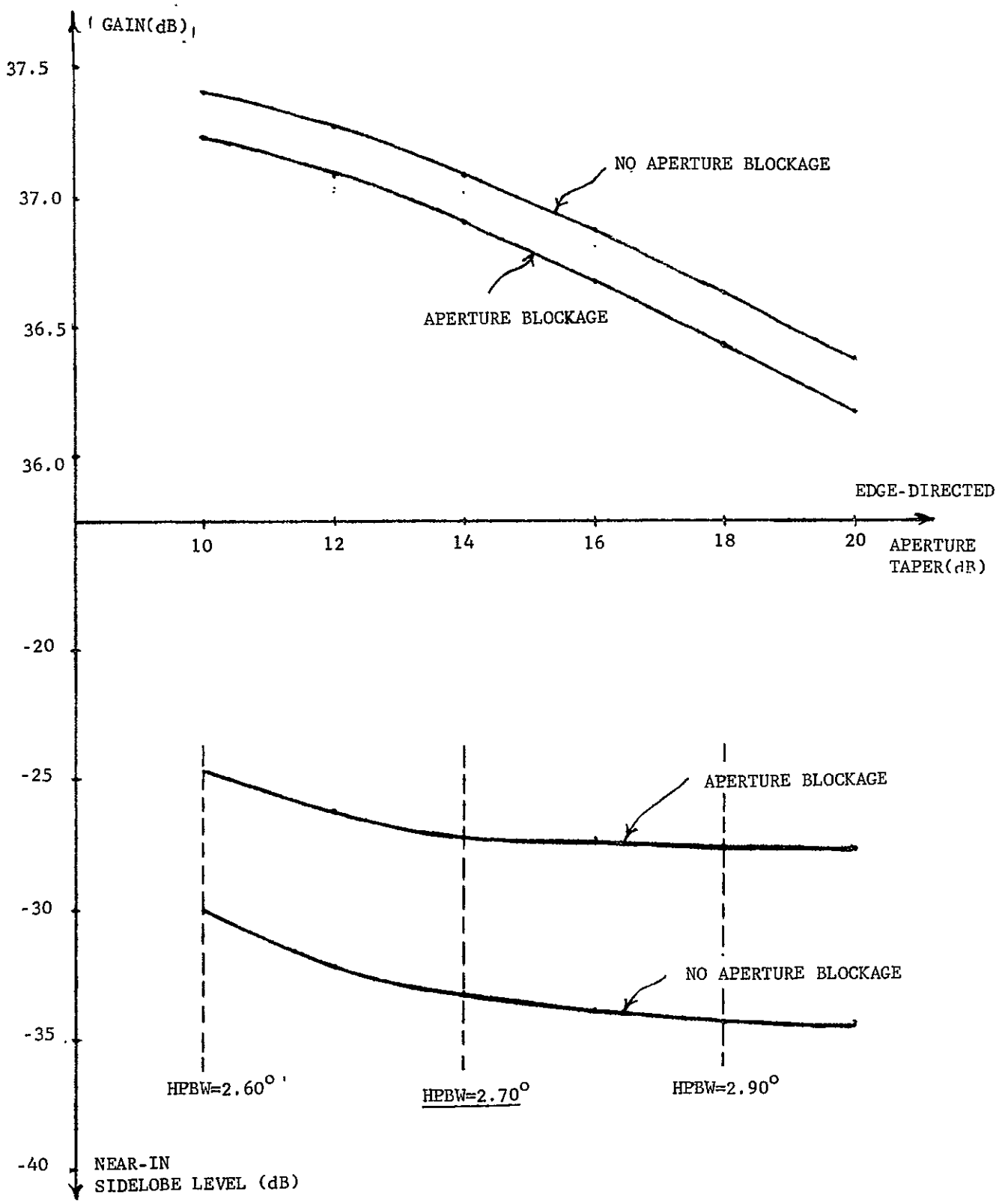

FIGURE 3-4 PRIME FOCUS REFLECTOR, ON-AXIS FEED, F/D=0.35 PERFORMANCE AS FUNCTION OF APERTURE TAPER

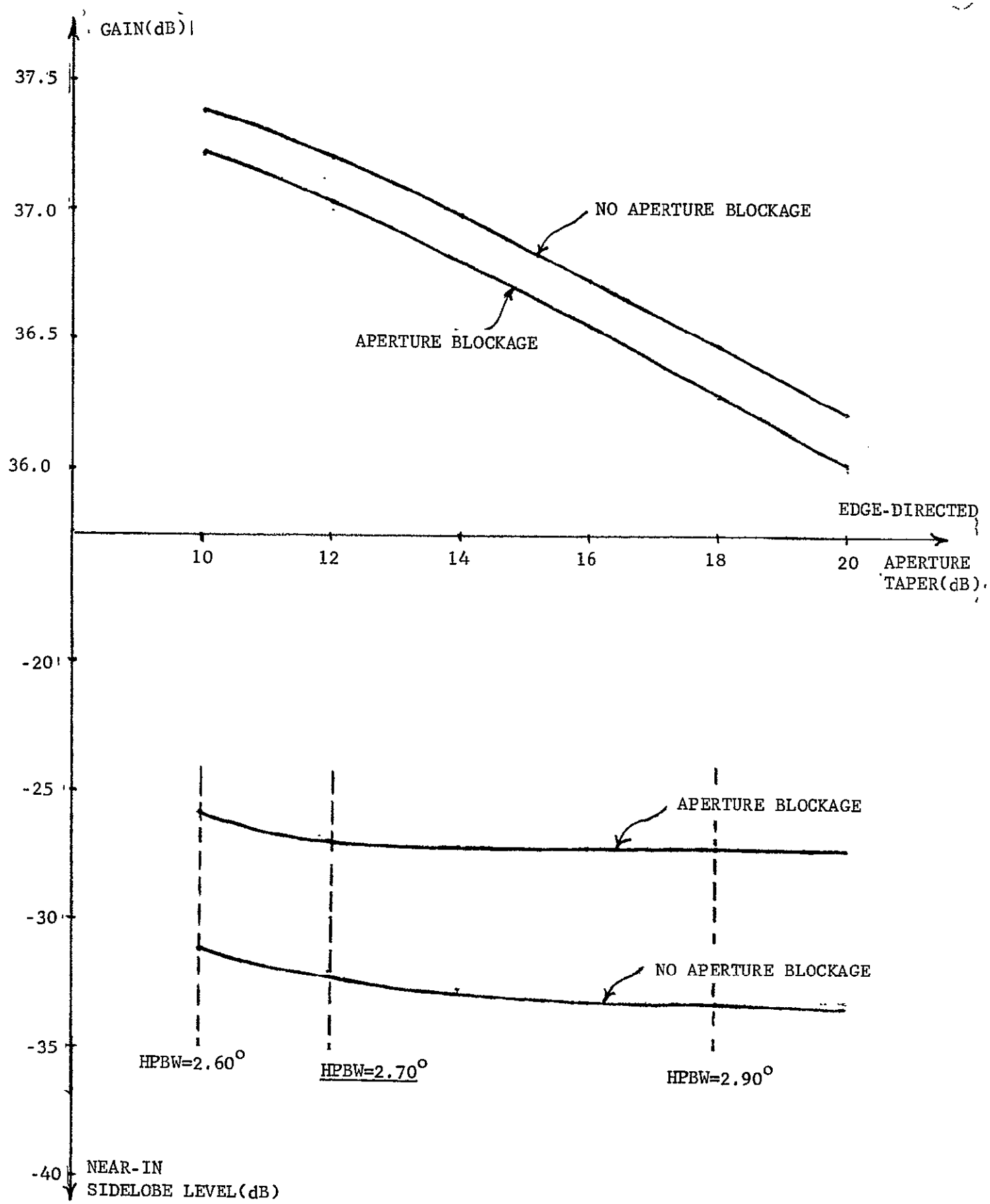

FIGURE 3-5 PRIME FOCUS REFLECTOR, ON-AXIS FEED, F/D=0.30 PERFORMANCE AS FUNCTION OF APERTURE TAPER

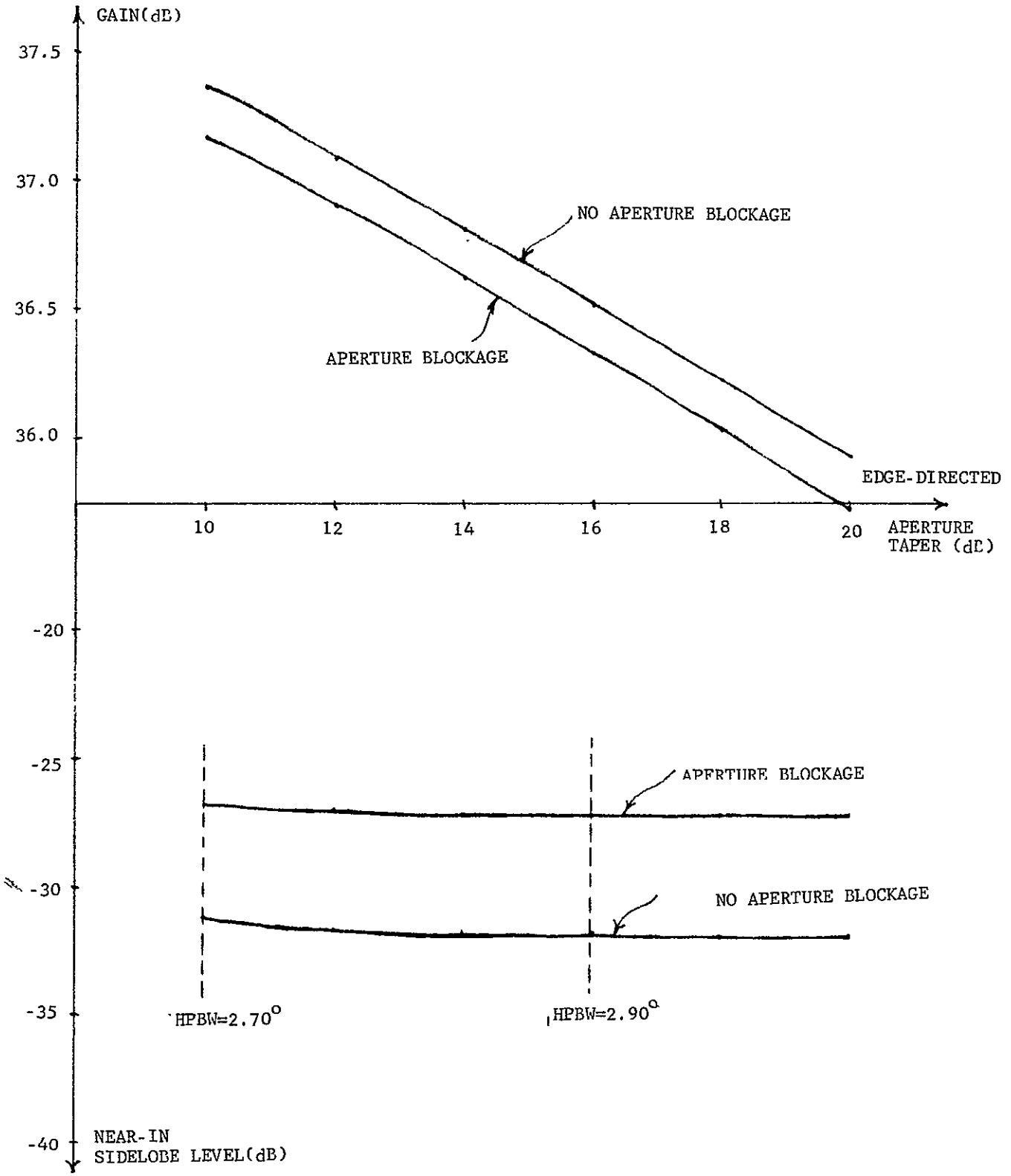

FIGURE 3-6 PRIME FOCUS REFLECTOR, ON-AXIS FEED, F/D=0.25 PERFORMANCE AS FUNCTION OF APERTURE TAPER

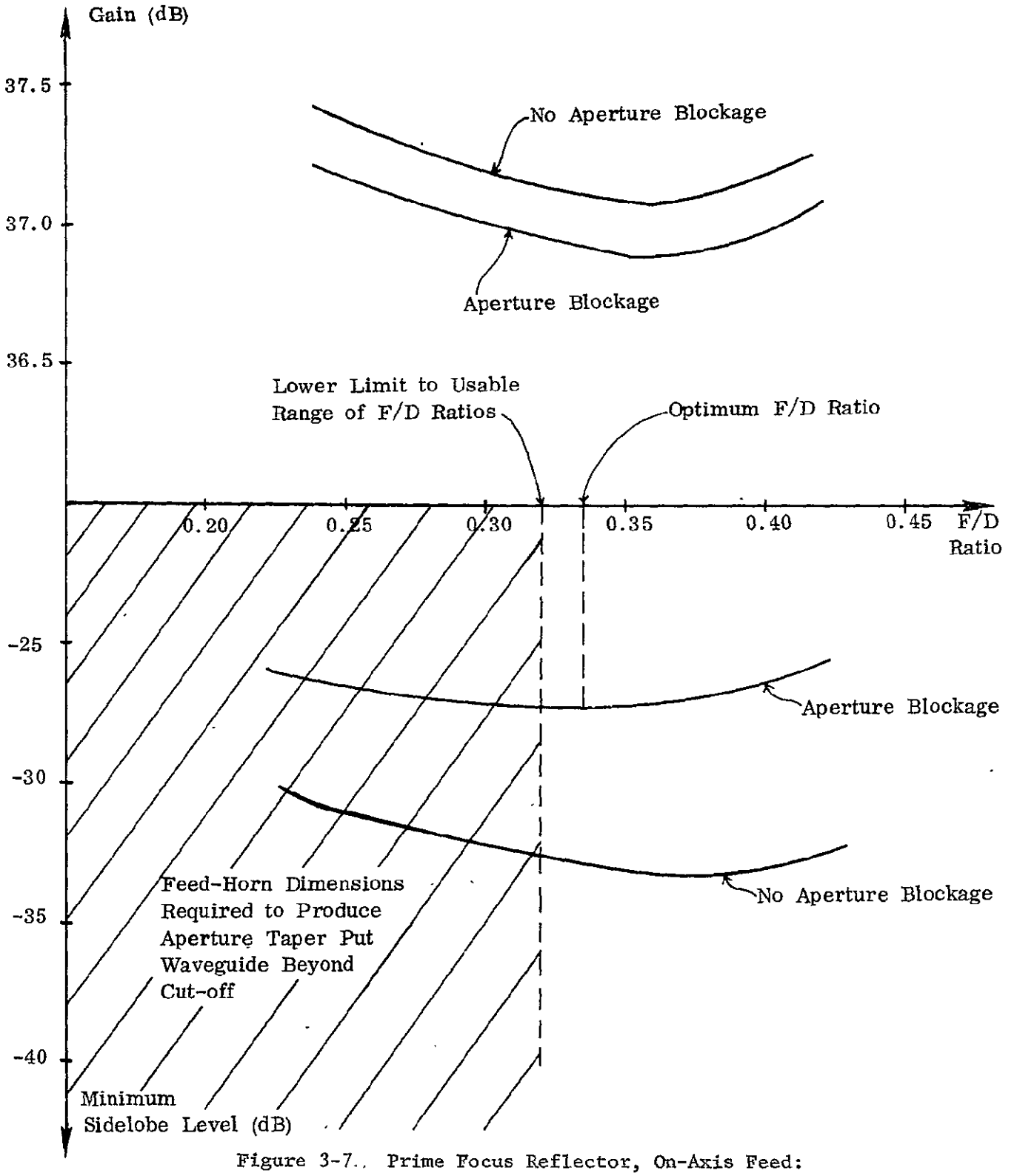

Figure 3-7. Prime Focus Reflector, On-Axis Feed:
Optimum Sidelobe Performance as a Function
of F/D Ratio

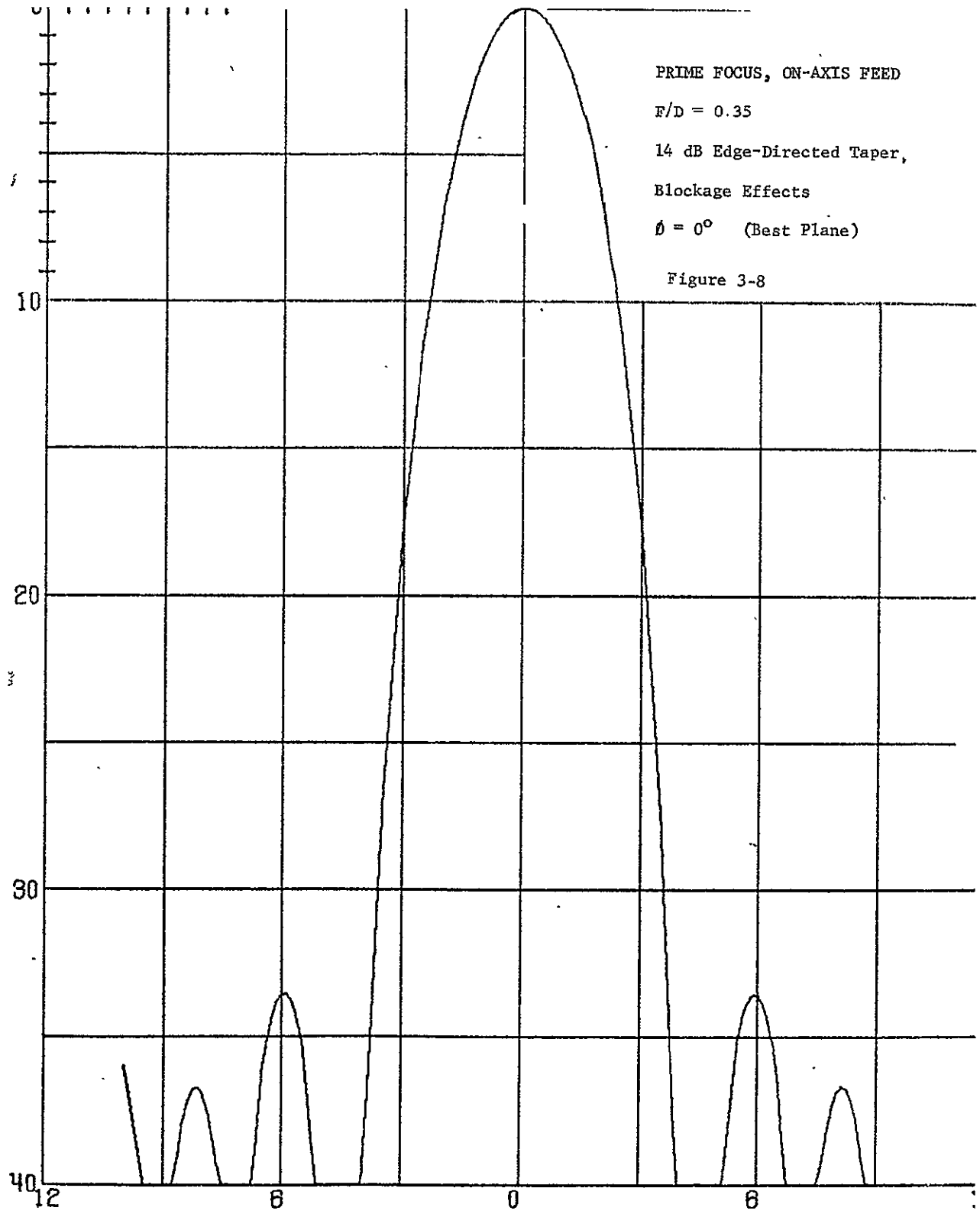
PRIME FOCUS, ON-AXIS FEED
F/D = 0.35
14 dB Edge-Directed Taper,
Blockage Effects
Ø = 0° (Best Plane)
Figure 3-8
10
20
30
40
12
6
0
6

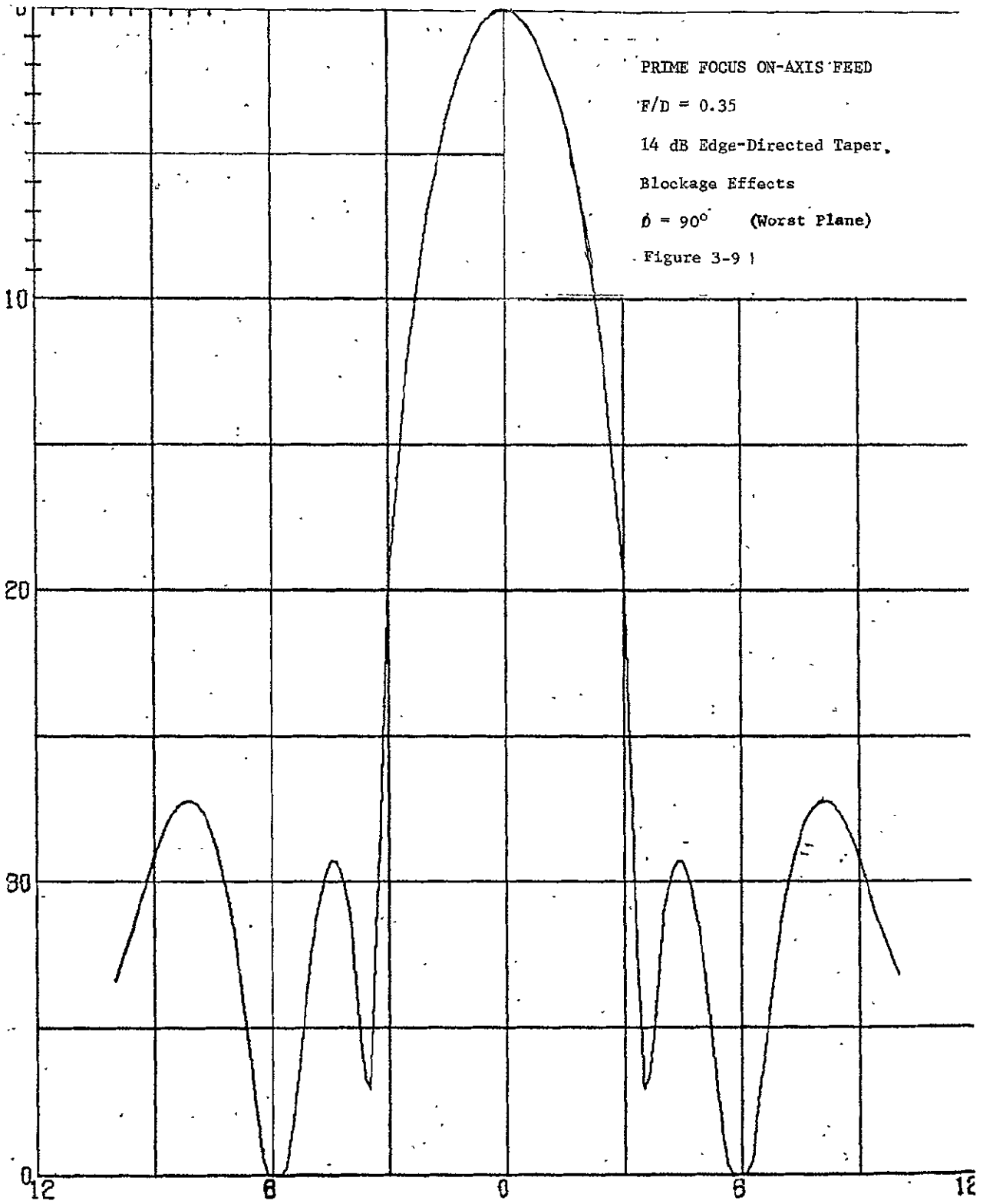
PRIME FOCUS ON-AXIS FEED
F/D = 0.35
14 dB Edge-Directed Taper,
Blockage Effects
ϕ = 90° (Worst Plane)
Figure 3-9
10
20
30
0
12
8
0
8
12

3.2.2 Analysis Of On-Axis Cassegrain Feed

The geometry of this configuration (see Figure 3-10) is such that the main reflector "sees" a virtual image of the feed-horn aperture in its focal plane. Hence, a realistic estimate of the antenna performance can be made by assuming an edge-directed aperture taper of the form generated by a prime focus feed-horn and using it in conjunction with the blockage parameters associated with a subreflector and its supporting struts.

This approach was adopted for the analysis since it permitted direct use of the results already obtained for the on-axis prime focus case. These results for a 26" (66.04 cm) diameter dish, provided the maximum edge-directed aperture taper compatible with a 2.7° HPBW and this is listed in Table 3-3 as a function of F/D ratio.

The aperture blockage associated with a given taper was obtained by estimating the subreflector diameter required to optimize the antenna geometry.

This is given * by:

$$\frac{\text{Aperture blockage area}}{\text{Total aperture area}} = 2 \times (\text{HPBW in radians}) \times F/D$$

Hence, for a 26-inch (66.04 cm) diameter reflector and a 2.7° HPBW

$$r^2 = 15{\cdot}92\ F/D, \text{ where } r \text{ is the radius of the subreflector}$$

The values of $\underline{r}$ yielded by this relationship for the required range of F/D ratios are listed in Table 2-2.

Now, the dimensions of this antenna are such that it would be feasible to support the subreflector by means of hollow, thin-walled dielectric

---

* "Antenna Engineering Handbook" -- H. Jasik.

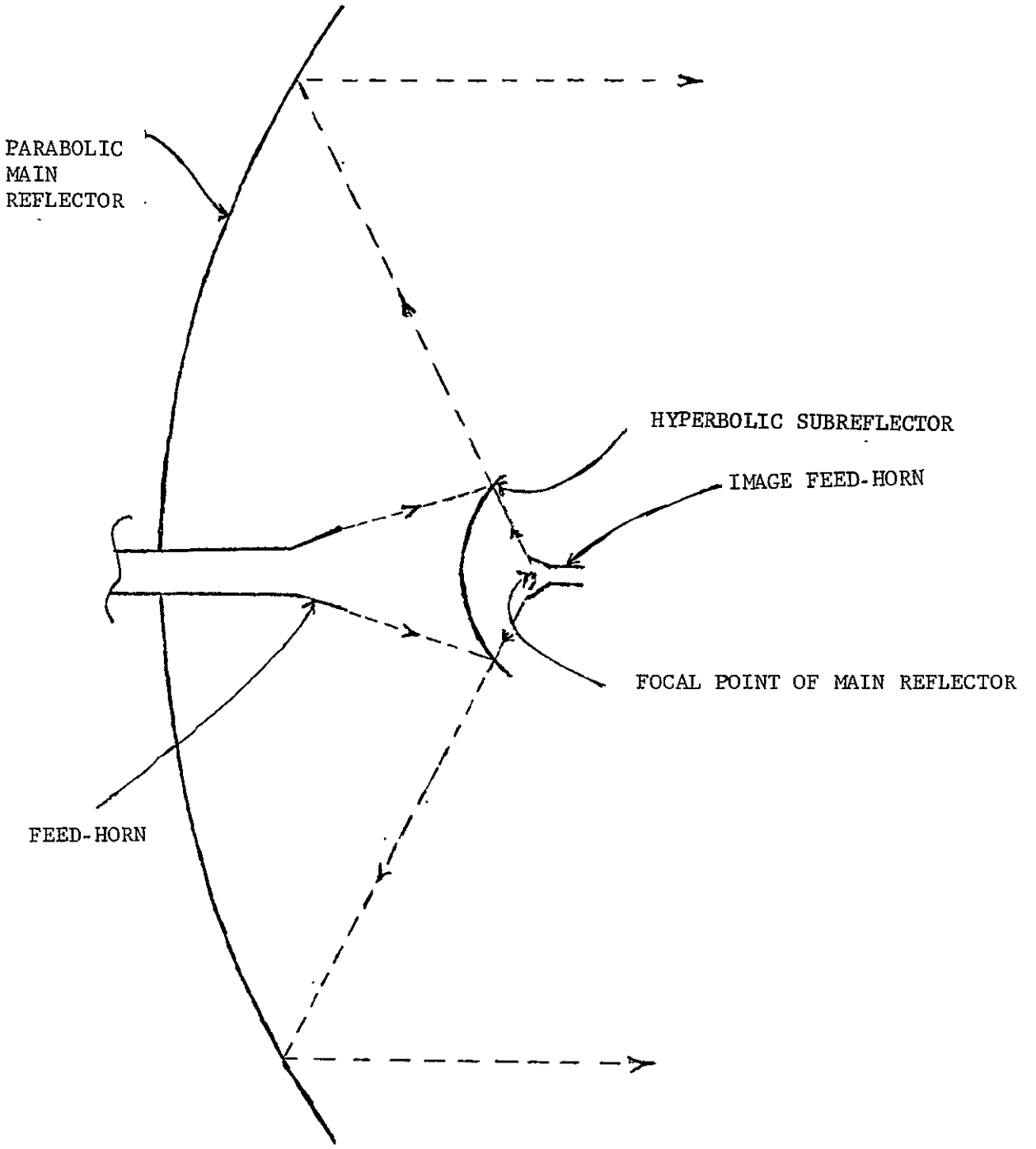

FIGURE 3-10 GEOMETRY OF CASSEGRAIN FEED STRUCTURE

TABLE 3-3

MAXIMUM EDGE-DIRECTED APERTURE TAPER

COMPATIBLE WITH 2.7° BEAMWIDTH

FOR 26" DIAMETER REFLECTOR

F/D RATIO	MAXIMUM TAPER (dB)
0.40	14
0.35	14
0.30	12
0.25	10

TABLE 3-4

REQUIRED SUBREFLECTOR DIMENSIONS

AS A FUNCTION OF F/D RATIO

F/D RATIO	RADIUS OF SUBREFLECTOR (IN)
0.40	2.52
0.35	2.36
0.30	2.18
0.25	1.99

tubing which has negligible effect on the aperture distribution. Therefore, for the purpose of computing the radiation patterns, it was further assumed that the only aperture blockage present was that due to the subreflector dish.

The radiation patterns obtained were used to derive plots of sidelobe level and gain of the optimum configurations as a function of the F/D ratio. These plots are shown in Figure 3-11, from which it can be seen that, if a Cassegrainian feed structure is employed, the sidelobe suppression which can be achieved is limited to approximately -25 dB. The computed pattern for F/D = 0·25 (see Figure 3-12) serves to illustrate the best performance which may be realized.

3.2.3 Analysis of Prime Focus Reflector with Offset Feed

3.2.3.1 Definition of Reflector/Feed Geometry. The configuration which was analyzed for this case is depicted in Figure 3-13. As shown, the reflector is a section of a 52-inch diameter paraboloid surface, its contour being such that its projected area in the direction of the main beam is a circle of 26 inches (66.04 cm) diameter. The F/D ratio of the paraboloid was taken to be 0·4, giving a focal length of 20.8 inches (22.832 cm). Hence, the total angle subtended by the reflector at the focal point is 64° in the plane pp (see Figure 3-13).

3.2.3.2 Derivation of Aperture Distribution. With a symmetrical unblocked 26-inch diameter reflector, the required beam shape (2.7° beamwidth, 30-35 dB side lobes) may be generated by imposing a 17 dB aperture taper. The parameters of the offset feed were, therefore, chosen so as to produce an aperture distribution which closely approximated this taper. A feed-horn pattern which provided a 16 dB taper across a 64° sector was utilized. It was then possible to adequately compensate for the asymmetry in the space attenuation by judiciously choosing the angle at which the feed-horn was tilted relative to the paraboloid axis of symmetry.

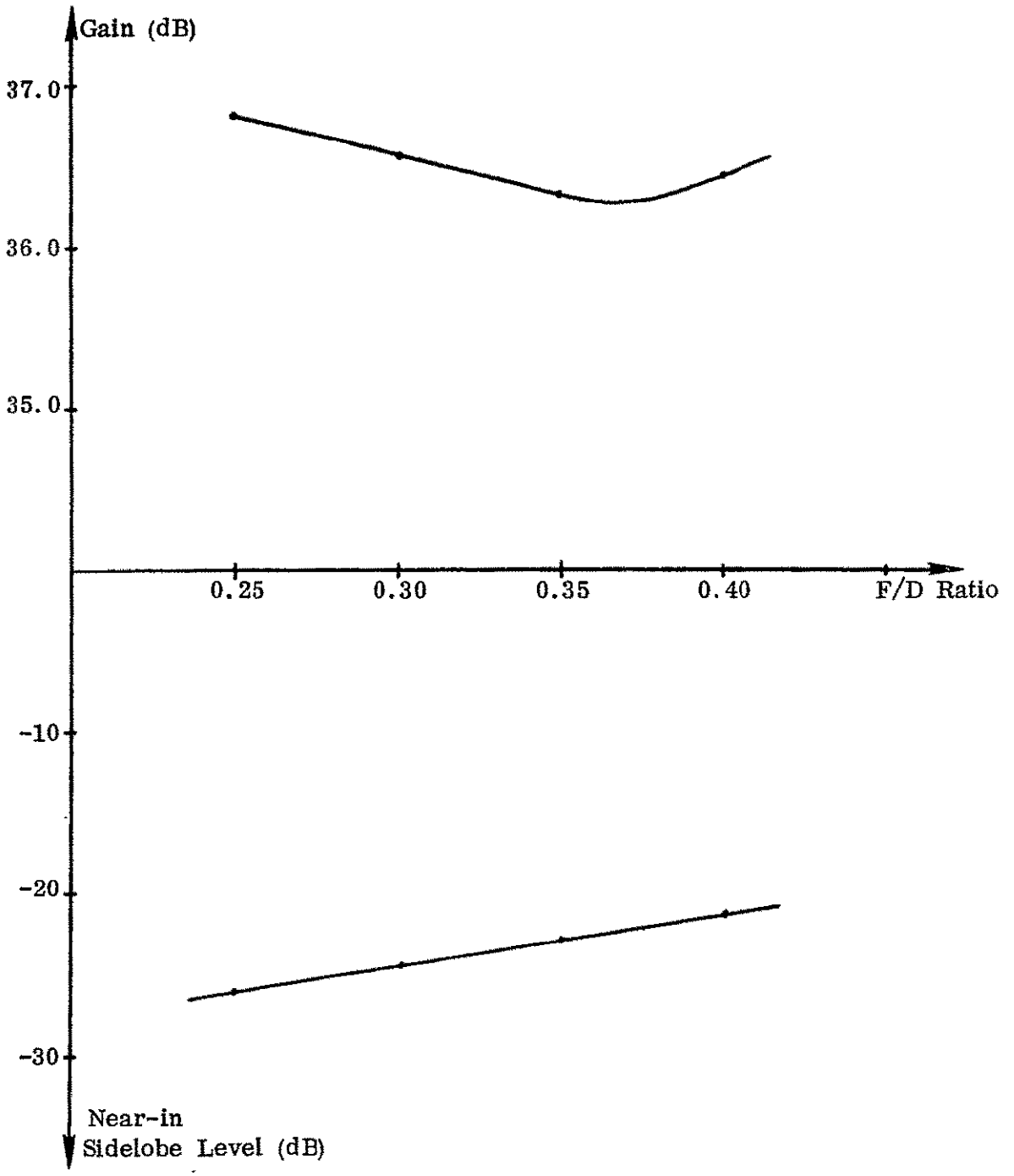

Figure 3-11 On-Axis Cassegrain Feed Optimum Performance As A Function of F/D Ratio

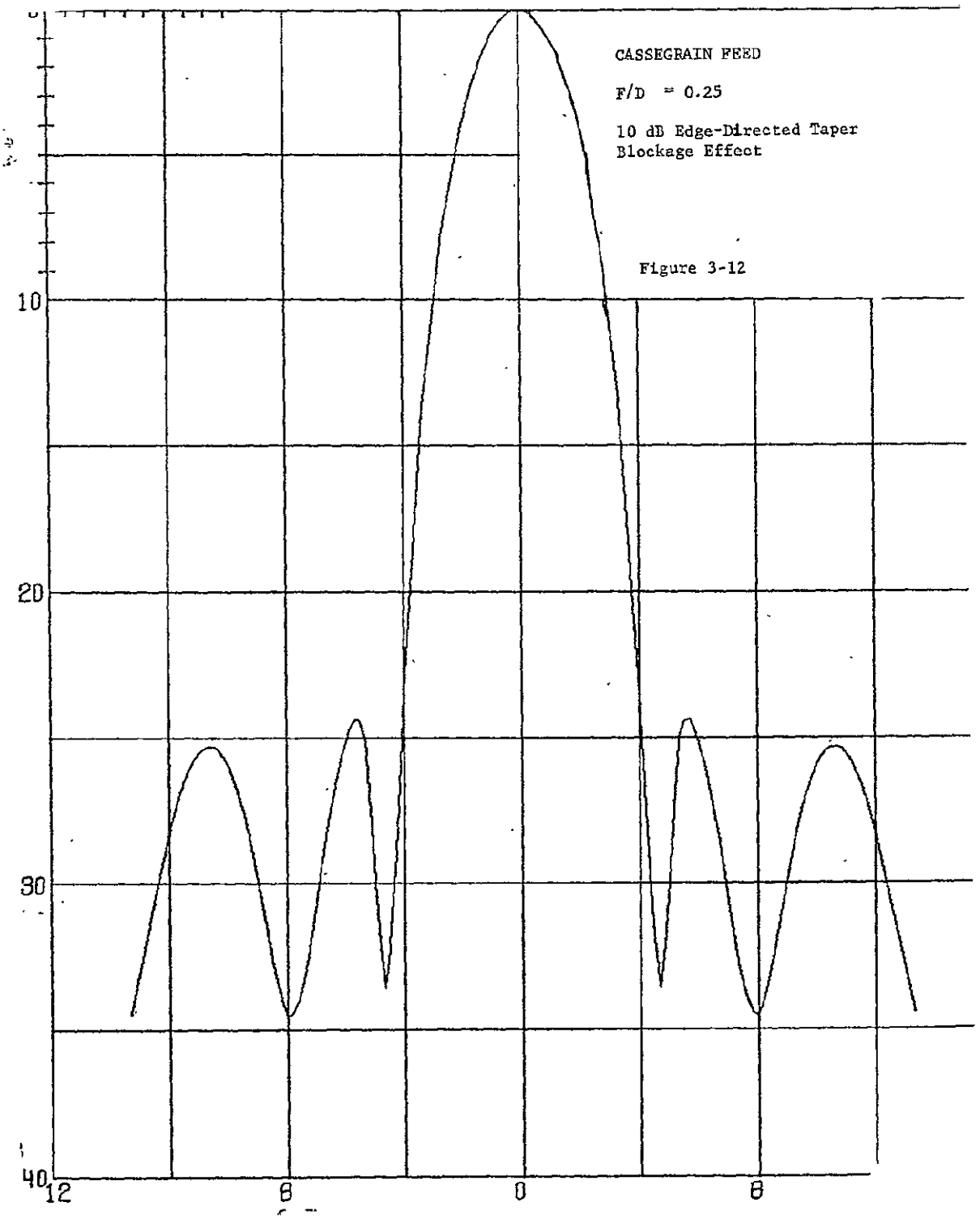
CASSEGRAIN FEED
F/D = 0.25
10 dB Edge-Directed Taper
Blockage Effect
10
20
30
40
12
8
0
8

Figure 3-12

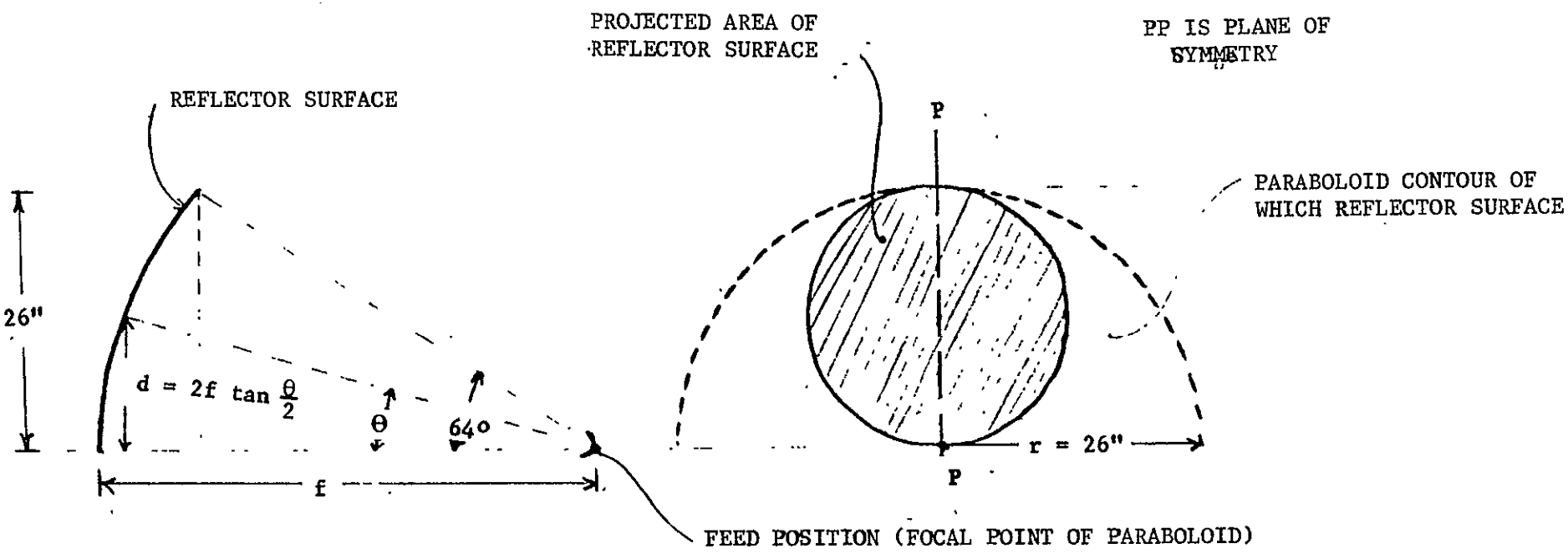

FIGURE 3-13 GEOMETRY OF OFFSET FEED CONFIGURATION

It was assumed that the feed-horn pattern, expressed in dB's, was a simple quadratic function of the form:

$T(\theta) = R\theta^2$, where θ degress is the angle from the peak of the horn pattern and R is a constant.

The requirement that $T(\pm 32) = -16$, then gave the pattern as:

$$T(\theta) = \frac{-\theta^2}{64}$$

By tilting this pattern at an angle of 33° relative to the paraboloid axis, a good approximation to the required 17 dB aperture taper was obtained in the plane PP, as is demonstrated by Table 3-5. (The angles θ_p and θ_H referred to in this table are defined in Figure 3-14, which also gives a graph of the normalized aperture distribution in the plane PP).

To compute the secondary radiation pattern for this configuration it was necessary to have the complete aperture distribution in terms of the polar coordinates defined in Figure 3-15. The following procedure was adopted as a means of achieving this:

1) The two angular positions θ_1, θ_2 corresponding to each of the -1, -2, ---, -16, -17 dB levels were read from the graph of Figure 2-8.

2) The angles θ_1, θ_2 were converted into displacements d_1, d_2 above the paraboloid axis by making use of the relationship:

$$d = 2f \tan \frac{\theta}{2} \qquad \text{(see Figure 3-13)}$$

Each pair of values d_1, d_2, therefore, defined the position of two points on an equal intensity contour of the aperture distribution.

TABLE 3-5

Derivation of Equal-Intensity Contours
for Offset feed Configuration

Contour (db)	θ_1 degrees	θ_2 degrees	d_1'' $(2f \tan \frac{\theta_1}{2})$	d_2'' $(2f \tan \frac{\theta_2}{2})$	$\frac{d_2+d_1}{2}$	$\frac{d_2-d_1}{2}$
0	33.0	33.0	12.31	12.31	12.31	0.0
-0.5	25.0	37.0	9.24	13.92	11.58	4.68
-1	23.0	39.4	8.46	14.89	11.68	3.22
-2	20.2	42.8	7.41	16.29	11.85	4.44
-3	18.2	45.1	6.67	17.30	11.99	5.32
-4	16.3	47.1	5.96	18.19	12.08	6.12
-5	14.4	49.0	5.26	18.98	12.12	6.86
-6	12.7	50.8	4.63	19.78	12.21	7.58
-7	11.0	52.3	4.01	20.47	12.24	8.23
-8	9.6	53.9	3.48	21.2	12.34	8.86
-9	8.1	55.1	2.94	21.77	12.36	9.42
-10	7.0	56.4	2.54	22.3	12.40	9.88
-11	5.7	57.5	2.07	22.9	12.49	10.42
-12	4.6	58.8	1.67	23.45	12.56	10.89
-13	3.5	59.8	1.27	23.95	12.61	11.34
-14	2.4	60.9	0.80	24.50	12.65	11.85
-15	1.4	61.9	0.51	25.0	12.76	12.25
-16	0.5	62.9	0.17	25.5	12.84	12.67
-17	-0.5	63.8	-0.17	25.9	12.87	13.04

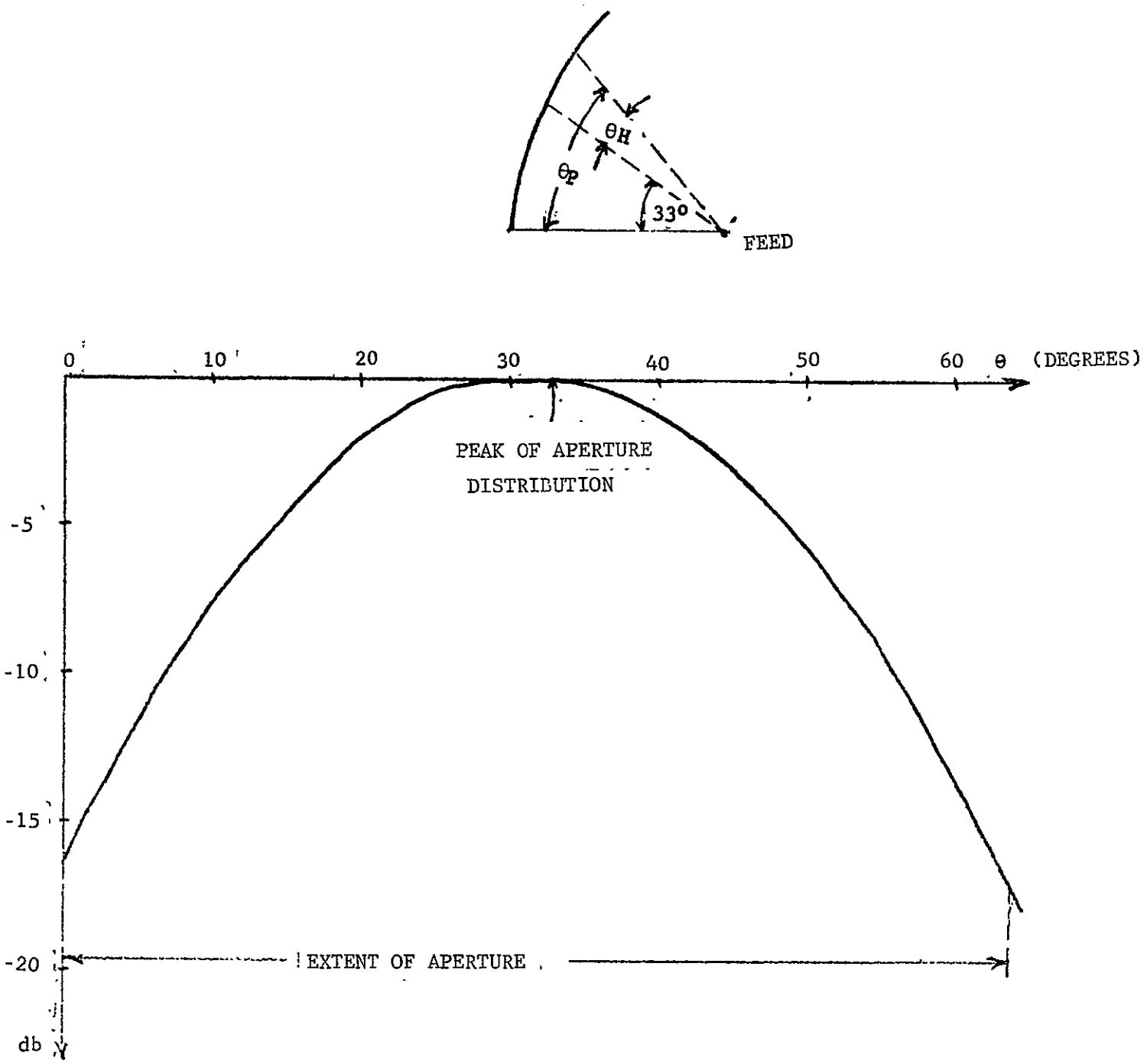

FIGURE 3-14 APERTURE TAPER GENERATED IN THE PLANE PP BY OFFSET FEED

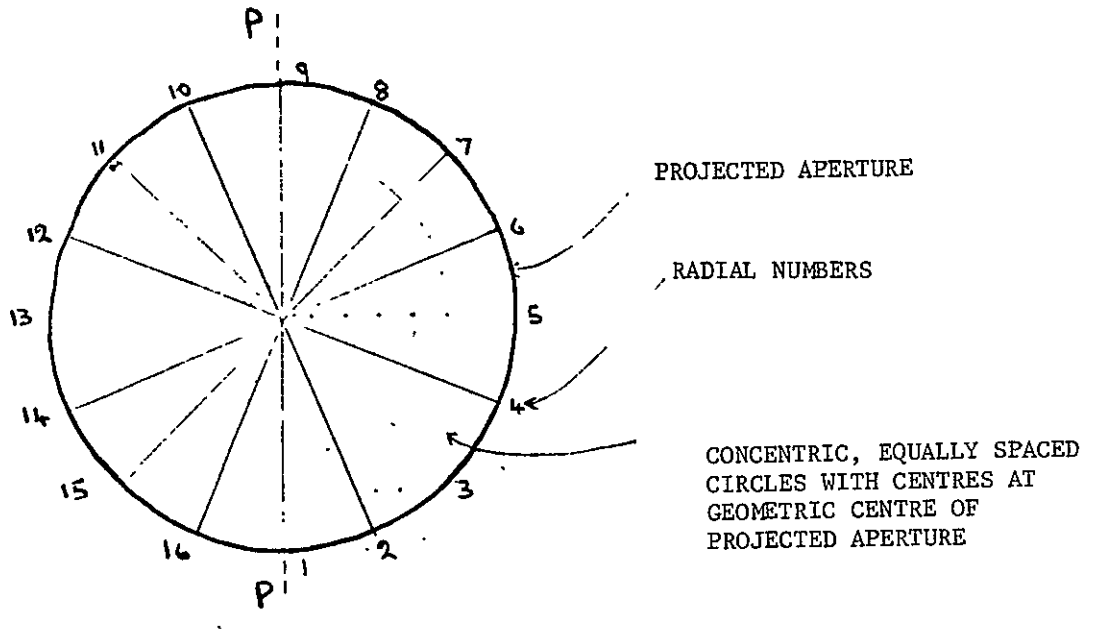

FIGURE #3-15 CO-ORDINATE SYSTEM USED FOR COMPUTATION OF RADIATION PATTERN OF OFFSET FEED CONFIGURATION

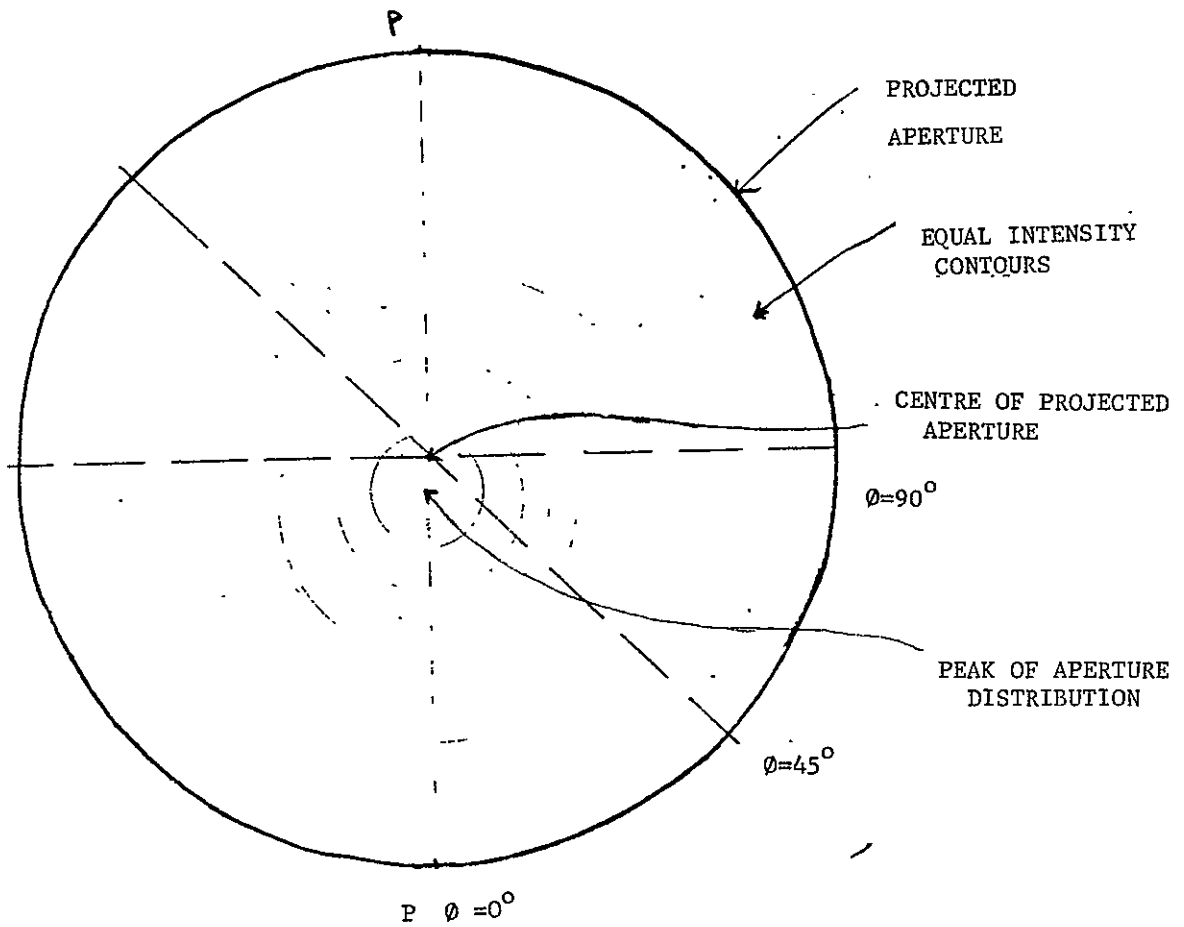

FIGURE 3-16 FORM OF APERTURE DISTRIBUTION GENERATED BY OFFSET FEED

3) The assumption was made that the contour joining these two points could be represented to a good first approximation by a circle, radius $\frac{d_2-d_1}{2}$ with its center at a distance $\frac{d_1 + d_2}{2}$ above the paraboloid axis, (i.e., the aperture distribution was assumed to be of the form shown in Figure 3-16). This assumption is justified by the fact that the reflector is symmetrical about the plane PP, with an aperture which has a circular projection in the direction of the main beam.

4) The required values $\frac{d_2 - d_1}{2}$, $\frac{d_2 + d_1}{2}$ were calculated and a scale drawing of the equal intensity contours thus obtained.

5) The radial coordinates (see Figure 3-15) were superimposed on this diagram and, hence, the aperture distribution as a function of the required parameters was obtained. The results which this procedure yielded are listed in Table 3-6. These were used to compute the radiation patterns in the planes $\phi = 0^o, 45^o, 90^o$ shown in Figure 3-16. The patterns thus obtained are given in Figures 3-17 thru 3-19. These indicate that, although there is some asymmetry in the beam shape, the required 30-35 dB side lobe level can be realized by the offset feed configuration.

3.2.4 Analysis of Horn Reflector

The horn reflector (or cornucopia) was considered as a possible alternative to the prime-focus, offset-feed configuration. As can be seen from the diagram of Figure 3-20, it operates on essentially the same principle, except

TABLE 3-6

APERTURE DISTRIBUTION (IN VOLTS/m) FOR PRIME FOCUS, OFFSET FEED CONFIGURATION

RADIUS (IN)	RADIAL NUMBER															
	1	2	3	4	5	6	7	8	9	10	11	12	13	14	15	16
0	0.977	0.977	0.977	0.977	0.977	0.977	0.977	0.977	0.977	0.977	0.977	0.977	0.977	0.977	0.977	0.977
1	0.989	0.989	0.983	0.971	0.966	0.955	0.944	0.940	0.933	0.940	0.944	0.955	0.966	0.971	0.983	0.989
2	0.977	0.971	0.966	0.955	0.933	0.912	0.896	0.881	0.876	0.881	0.896	0.912	0.933	0.955	0.966	0.971
3	0.955	0.950	0.944	0.912	0.881	0.856	0.832	0.813	0.809	0.813	0.832	0.856	0.881	0.912	0.944	0.950
4	0.933	0.912	0.891	0.851	0.813	0.785	0.759	0.737	0.728	0.737	0.759	0.785	0.813	0.851	0.891	0.912
5	0.841	0.822	0.804	0.770	0.724	0.692	0.668	0.653	0.649	0.653	0.668	0.692	0.724	0.770	0.804	0.822
6	0.741	0.724	0.708	0.668	0.638	0.606	0.582	0.565	0.562	0.565	0.582	0.606	0.638	0.668	0.708	0.724
7	0.631	0.617	0.603	0.569	0.543	0.519	0.507	0.490	0.484	0.490	0.507	0.519	0.543	0.569	0.603	0.617
8	0.537	0.525	0.513	0.490	0.462	0.442	0.427	0.417	0.409	0.417	0.427	0.442	0.462	0.490	0.513	0.525
9	0.447	0.437	0.427	0.407	0.382	0.367	0.355	0.344	0.339	0.344	0.355	0.367	0.382	0.407	0.427	0.437
10	0.359	0.351	0.345	0.327	0.311	0.302	0.292	0.285	0.282	0.285	0.292	0.302	0.311	0.327	0.345	0.351
11	0.282	0.275	0.270	0.257	0.244	0.237	0.229	0.224	0.221	0.224	0.229	0.237	0.244	0.257	0.270	0.275
12	0.211	0.207	0.204	0.200	0.194	0.191	0.184	0.182	0.180	0.182	0.184	0.191	0.194	0.200	0.204	0.207
13	0.153	0.153	0.151	0.148	0.145	0.141	0.141	0.140	0.138	0.140	0.141	0.141	0.145	0.148	0.151	0.153
	NORMALIZED FIELD STRENGTH (VOLTS/m)															

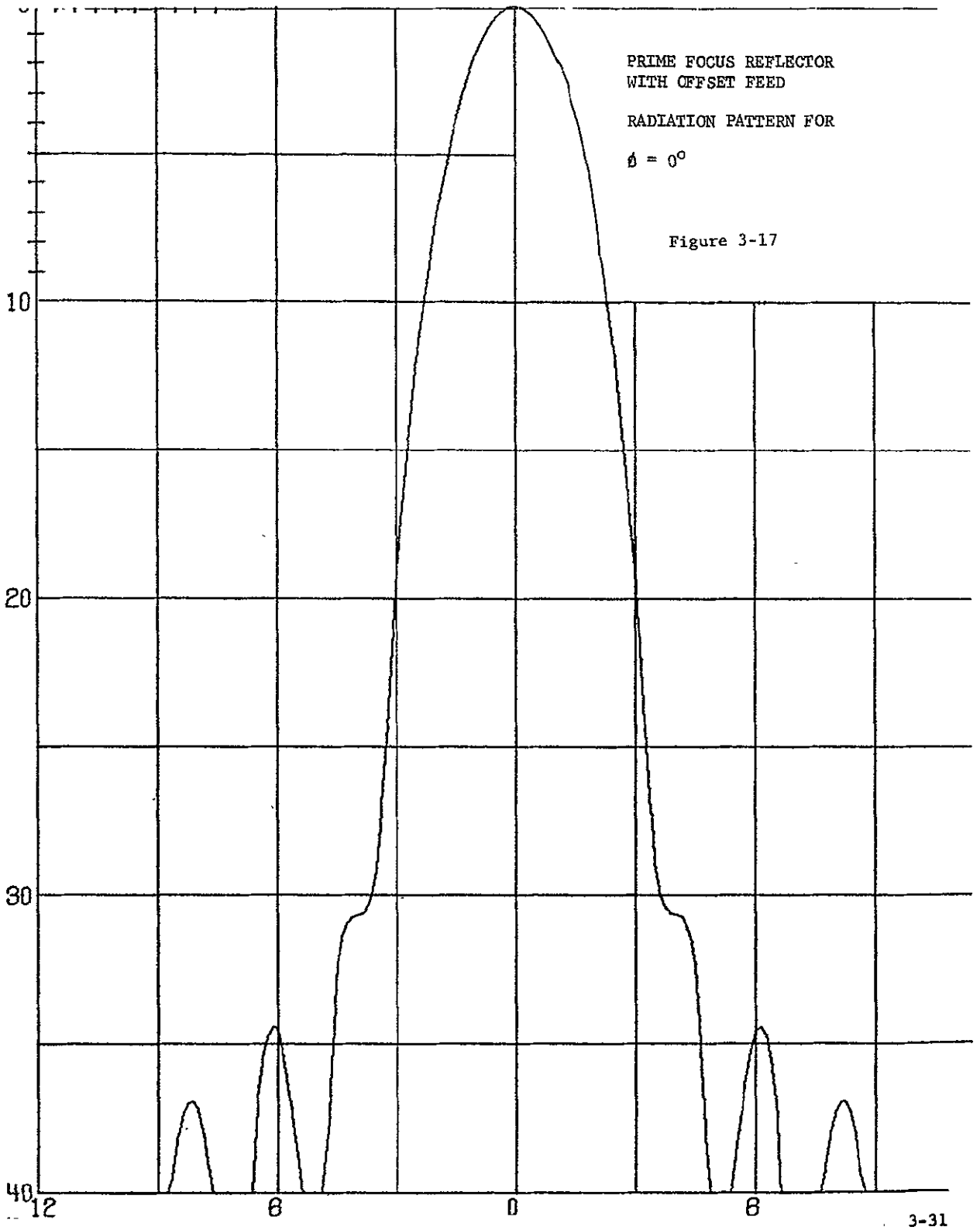
PRIME FOCUS REFLECTOR
WITH OFFSET FEED
RADIATION PATTERN FOR
ø = 0°
10
20
30
40
12
8
0
8

Figure 3-17

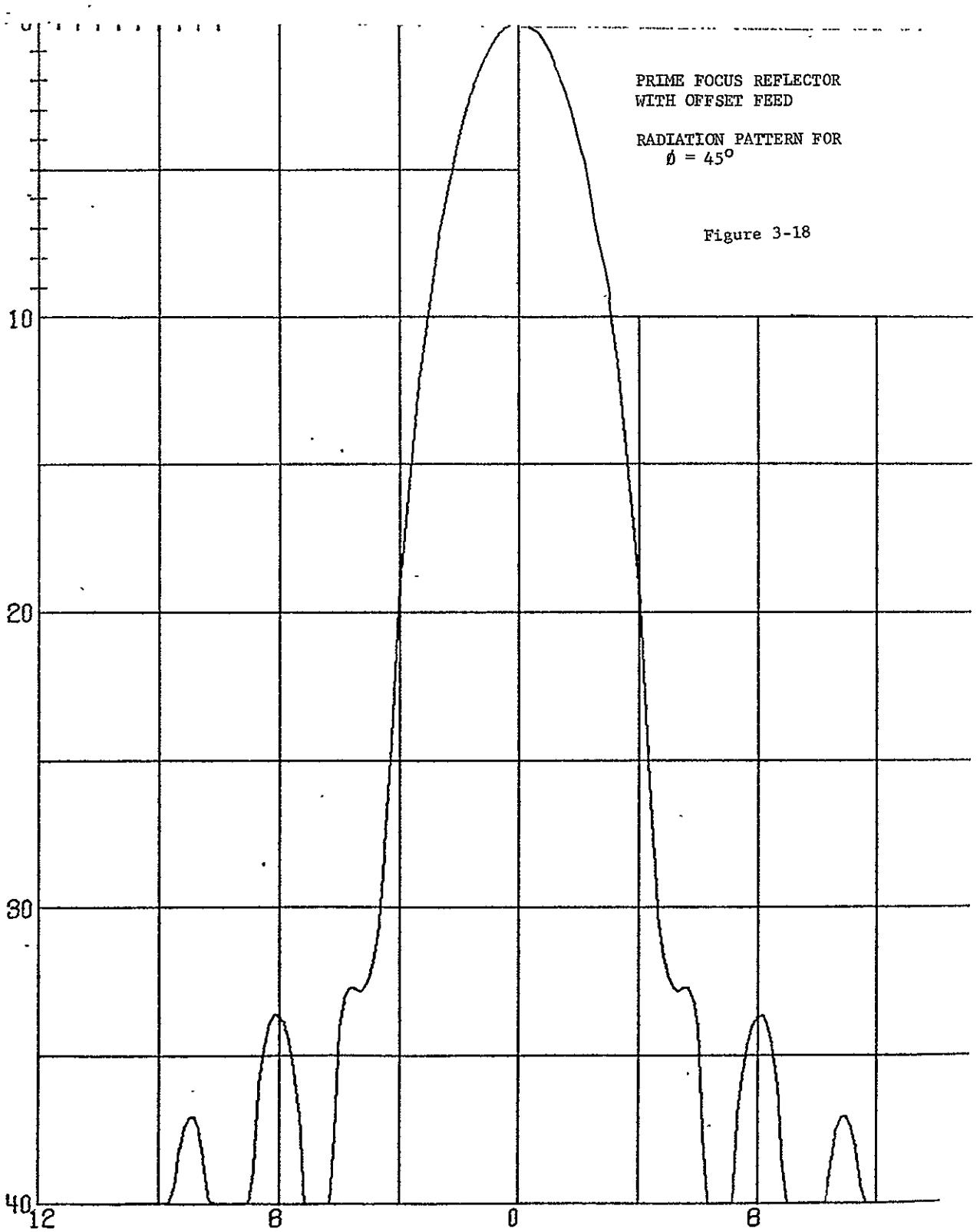
PRIME FOCUS REFLECTOR
WITH OFFSET FEED
RADIATION PATTERN FOR
Ø = 45°
10
20
30
40
12
8
0
8

Figure 3-18

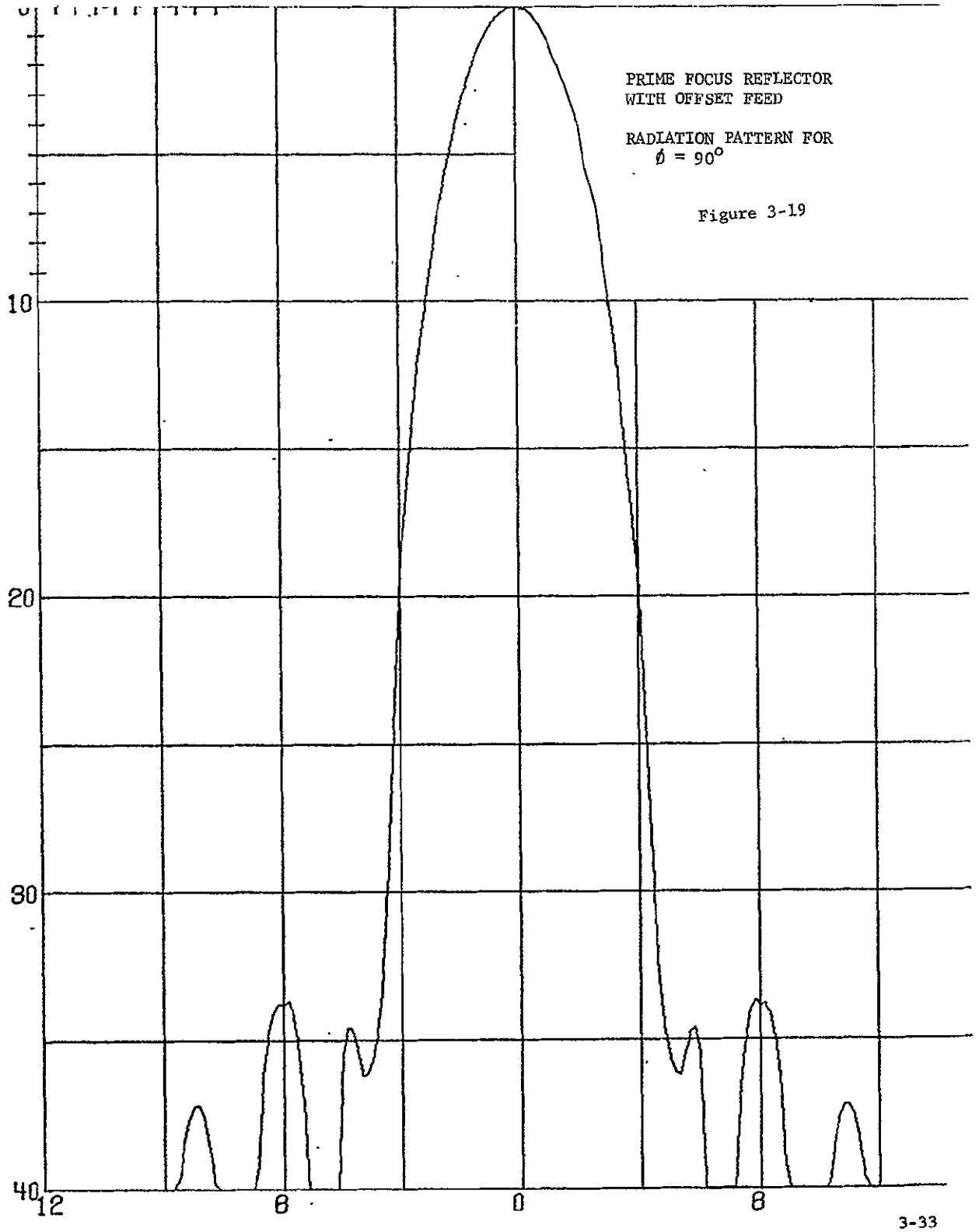
PRIME FOCUS REFLECTOR
WITH OFFSET FEED
RADIATION PATTERN FOR
Ø = 90°
10
20
30
40
12
8
0
8

Figure 3-19

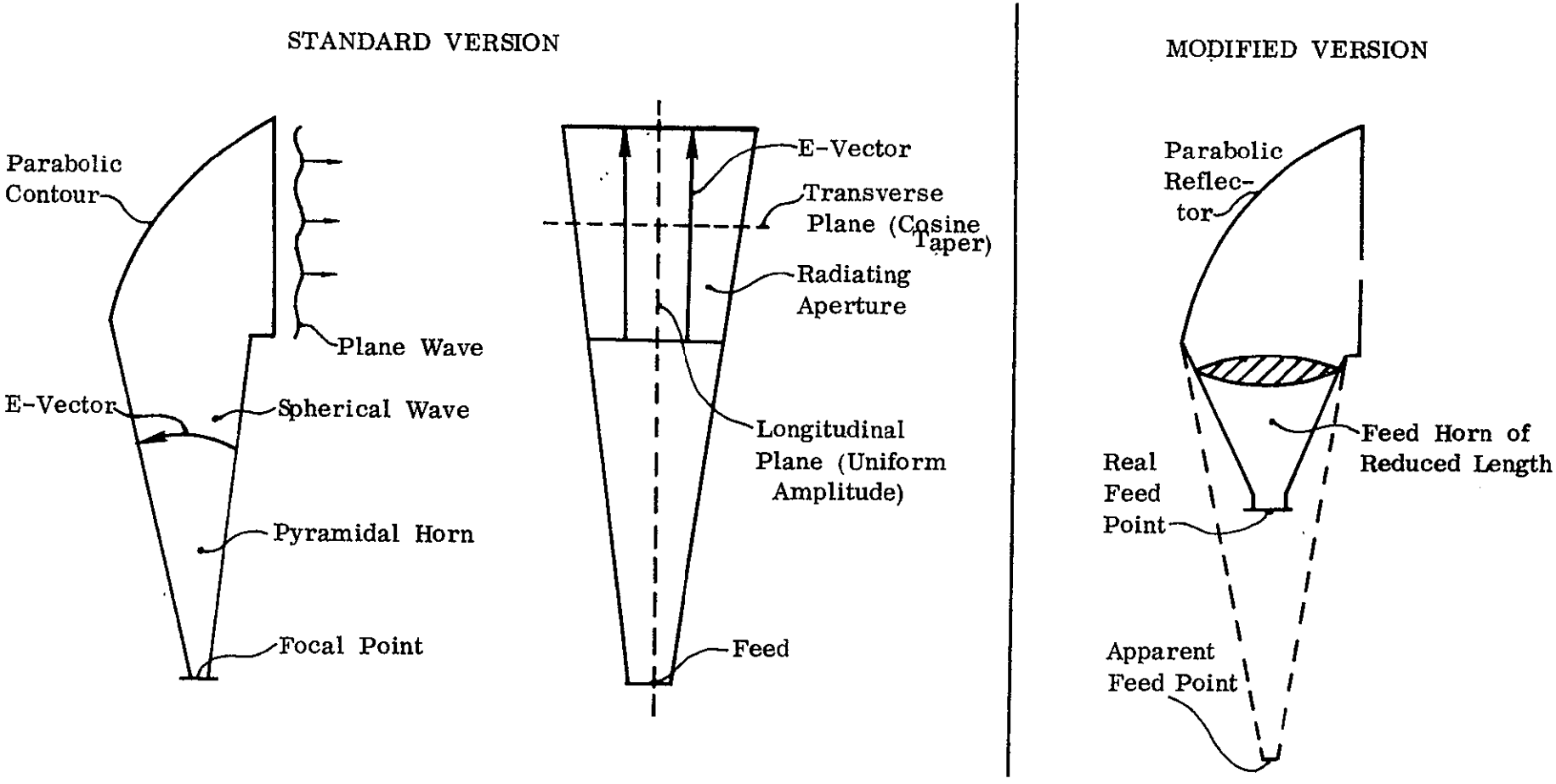

Figure 3-20 Horn Reflector Configurations

that the transmitted power is concentrated onto the reflector by means of an extended feed-horn. This offers certain advantages in that the far-out sidelobes are reduced and a good back-to-front ratio is obtained. However, since the feed horn normally propagates only the dominant TE_{01} mode, control of the aperture taper and hence of the near-in sidelobe level is somewhat limited. This is illustrated in Figure 3-20 (a) for the case of linear polarization in the longitudinal plane of the antenna. As shown, the aperture distribution in this plane is uniform; hence the resulting sidelobe level is approximately -13 dB. In the orthogonal (i.e., transverse) plane, however, the cosinusoidal aperture taper associated with the TE_{01} mode gives rise to a -23 dB sidelobe level.

From this, it is apparent that a conventional horn reflector cannot provide a near-in sidelobe level of better than -23 dB in all planes. Measurements by other investigators have shown, in fact*, that when a circularly polarized beam is being generated, a sidelobe level of -15 to -20 dB is to be expected.

A further disadvantage is that, for the proposed application, the horn feed is a rather cumbersome structure. Because of this, it may not be mechanically feasible to switch the position of beam 4 by pivoting the appropriate reflector about a gimbal axis. Should this be the case, it would be necessary to resort to a system based on five separate reflectors.

Both the problem of near-in sidelobe suppression and that of mechanical incompatibility can be alleviated to some extent by utilizing a horn/lens

* Bell System Technical Journal, July 1961.

combination as shown in Figure 3-20(b). With this modification, the length of the horn can be substantially reduced and, because of the additional illumination taper associated with the lens itself, the near-in sidelobes may be suppressed to approximately -25 dB. in any plane.*

Unfortunately, these advantages are offset by the fact that introducing the lens will give rise to impedance matching problems. Also, for a 1 KW CW input at 12.2 GHz, the power dissipation within the lens structure could prove to be unacceptably high.

3.2.5 Selection of Optimum Reflector Feed Configuration

The results of the analyses performed for the four candidate reflector systems formed a basis for selecting the optimum antenna configuration. In conducting the final trade-off, these results were reviewed in conjunction with the other characteristics of the antennas which have a bearing on their compatibility with the overall system requirements. The principal factors involved in the trade-off are discussed for each configuration in the following paragraphs.

3.2.5.1 Prime Focus, On-Axis Feed

The analysis of this case indicates that for a 26-inch diameter reflector, aperture blockage effects will limit the side lobe suppression to approximately -27.5 dB. However, a four-dish antenna system based on this configuration would have a symmetrical geometry which would facilitate realization of the design goals in terms of ellipticity of polarization and beam isolation.

---

* "Theoretical and Experimental Investigations on Methods of Reducing Antenna Sidelobes" - AFCRC-TR-58-139, June 26, 1956 to June 15, 1958.

In addition, it would offer the advantages of a lightweight, reasonably compact antenna structure with a straightforward RF design.

3.2.5.2 On-Axis Cassegrain Feed

This system would provide a more compact feed structure at the expense of a slight increase in the complexity of the RF design. Unfortunately, the severe aperture blockage associated with the subreflector imposes a limit of approximately -25 dB on the level to which the side lobes can be suppressed.

3.2.5.3 Prime Focus, Offset Feed

As has been demonstrated in the analysis, this configuration is capable (due to the absence of aperture blockage effects) of realizing the design target of 30-35 dB sidelobe suppression. Furthermore, it creates the possibility of mounting the four reflector feed elements on a single, central mast. (See Figure 3-21.) These advantageous features are largely negated, however, by undesirable effects which arise as a consequence of the offset geometry.

The most significant drawback is that the inherent asymmetry of the resultant aperture distribution will give rise to a substantial cross-polarized component (assuming for the moment a linearly polarized primary pattern). A precise theoretical evaluation of the magnitude of this effect is complex. However, it may be stated that it is unlikely that the cross-polarized lobes will be more than -25 dB below the level set by the peak of the main beam in the principal plane of polarization.

In terms of the proposed system, this means that although the radiation pattern, as measured in the main sense of circular polarization has its near-in side lobes in the opposite sense of polarization will lie well above that level. The asymmetry of the antenna geometry and, hence, the

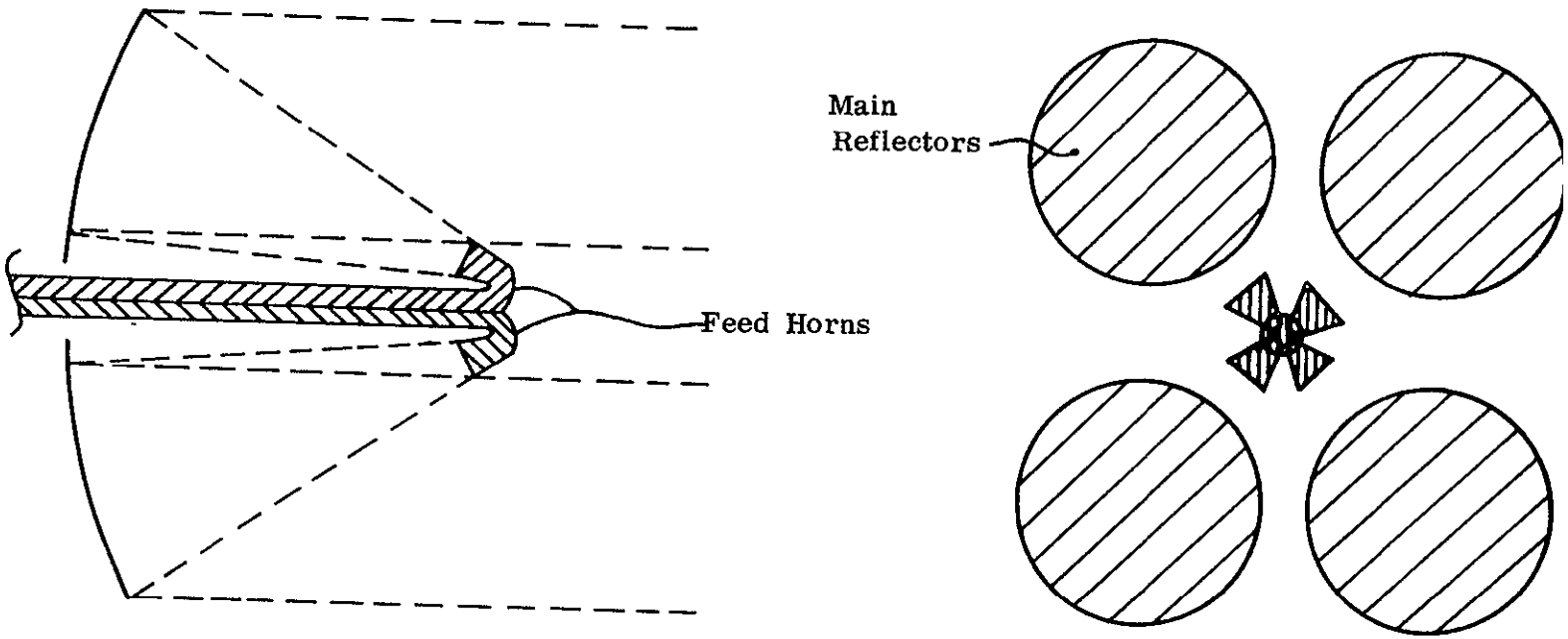

Figure 3-21 Antenna Configuration Based On Prime Focus Reflectors With Offset Feeds

cross-polarized effect can, of course, be reduced by increasing the focal length of the paraboloid. Unfortunately, this step introduces new problems in that it decreased the angle subtended by the reflector at the focal point and, therefore, increases the size of the feed horn necessary to achieve the required aperture taper. Thus, a significant reduction in the asymmetry effects can only be achieved at the expense of rather cumbersome feed structure.

Further disadvantages of this system are that:

1) It requires a fairly complex RF design.
2) For the preferred case, in which a central mast structure is employed, the proximity of the feed elements will tend to lower the beam isolation.
3) For the preferred case, again, it will be difficult to avoid pattern degradation in beam 4 when it is in the switched position i.e., it will be necessary to move both the main dish and the feed element if off-axis defocusing effects are to be avoided.

3.2.5.4 Horn Reflector

The principal advantage of the horn reflector is that it provides very low far-out sidelobes. This has an added advantage for the system being considered since it means that very good beam isolation is readily obtained.

There are, however, two major disadvantages associated with this configuration:

(1) Suppression of near-in sidelobes is limited to approximately -25 dB.
(2) The extended feed-horn is a mechanically awkward structure.

An additional drawback is that it will be prone to the same type of cross-polarization effects as have been described for the prime-focus, offset-feed case.

From a consideration of the relative advantages and disadvantages of the four candidate systems (summarized for convenience in Table 2-5), it was concluded that the prime-focus, on-axis feed configuration represents the best means of achieving the antenna design goals. This configuration has one shortcoming, namely that, in its basic form, it cannot realize the design goal of -30 to -35 dB near-in sidelobes. (Although it does adequately meet the minimum requirement of -25 dB). Techniques are available, however, by means of which this difficulty can be overcome. These techniques, and their application to the project, are discussed in the design analysis of the candidate antenna system.

3.3 DESIGN ANALYSIS OF CANDIDATE ANTENNA CONFIGURATION

A cluster of four separate prime-focus reflectors with on-axis feeds was chosen as the best means of meeting the overall antenna system requirements. In the design analysis of this configuration, particular emphasis was placed on investigating the extent to which the near-in sidelobes can be suppressed. Now, the amount of suppression that can be achieved is primarily limited by aperture blockage effects. A first step towards minimizing these effects was therefore taken by re-organizing the mechanical integration of the system so as to maximize the area available for the reflector surfaces. In this way, the diameter of the reflectors was increased from 26-inches to 28-inches (66.04 cm to 71.12 cm).

3.3.1 Derivation of Optimum Aperture Taper for 28-Inch Diameter Reflector

The analysis performed for the 26-inch diameter reflector was extended to accommodate this case by making use of the fact that, at a fixed frequency, beamwidth is inversely proportional to diameter for a given aperture distribution. Thus, for a given aperture taper, the beamwidths Θ_{26} and

TABLE 3-7

COMPARISON OF CANDIDATE REFLECTOR ANTENNA CONFIGURATIONS

CONFIGURATION	ADVANTAGES	DISADVANTAGES
Prime Focus, On-Axis Feed	Simple RF design; good beam isolation; good circular polarization characteristics; lightweight, reasonably compact structure	Side lobe suppression limited by aperture blockage to approximately -27.5 dB (26-inch diameter aperture)
On-Axis Cassegrain Feed	Compact feed structure	Severe aperture blockage effects; more complex RF design
Prime Focus, Offset Feed	Can achieve 30-35 dB side lobe level; feed elements can be mounted on a single mast	Substantial cross-polarized component in radiation pattern; cumbersome feed structure required for reduction of asymmetry effects; reduced beam isolation; complex RF design; difficulty of avoiding pattern degradation when beam 4 is in switched position.
Horn reflector (Cornucopia)	Very low far-out sidelobes; Very good beam isolation.	Mechanically awkward structure; suppression of near-in sidelobes limited to approximately - 25 dB; Substantial cross-polarized component in radiation pattern

θ_{28}, corresponding to 26-inch and 28-inch diameter reflectors respectively, are related by:

$$\theta_{26} = \frac{28}{26} \quad \theta_{28}$$

For this application, it is required that $\theta_{28} = 2.7°$ and therefore

$$\theta_{26} = \frac{28}{26} \times 2.7° = 2.9°$$

Hence, the maximum edge-directed aperture taper compatible with a 2.7° beamwidth for the 28-inch reflector is that which corresponds to a 2.9° beamwidth for the 26-inch reflector. This taper is listed in Table 3-8 as a function of F/D ratio, together with the inner diameters of the corresponding circular feed horns. A final choice was made in favor of the configuration based on an F/D ratio of 0.35.

3.3.2 Estimation of Aperture Blockage Parameters

Back radiation from the feed-horn could make a substantial contribution towards raising the sidelobe level of the secondary radiation pattern. To reduce this effect to an acceptable level, the horn design was modified by the addition of a double choke section, giving the configuration illustrated in Figure 3-22. The aperture blockage parameters associated with this configuration are defined in Figure 3-23 and these were used for the purpose of computing the antenna radiation pattern.

3.3.3 Computed Radiation Pattern of 28-Inch Diameter Reflector With Optimized Aperture Distribution

The radiation patterns in the planes $\phi = 0°$ and $\phi = 90°$ were the first of all computed. From these (see Figures 3-24 and 3-25) it is seen that, for $\phi = 0°$, the first minor lobe is highest at -33.4 dB below the peak of the main beam, whereas, for $\phi = 90°$, the second lobe predominates at -28.4 dB. To investigate the behavior of these lobes over the complete

TABLE 3-8

OPTIMUM EDGE-DIRECTED TAPER AS A FUNCTION

OF F/D RATIO FOR 28 IN. DIAMETER REFLECTOR

F/D Ratio	Taper Required for 2.7° HPBW (dB)	Appropriate Inner Diameter of Feed-Horn (ins.)
0.40	20	0.88
0.35	18	0.77
0.30	18	0.68
- - - - -	- - - - -	- - - - - -
0.25	16	0.59

* Waveguide cuts off at approximate 0.6 in.

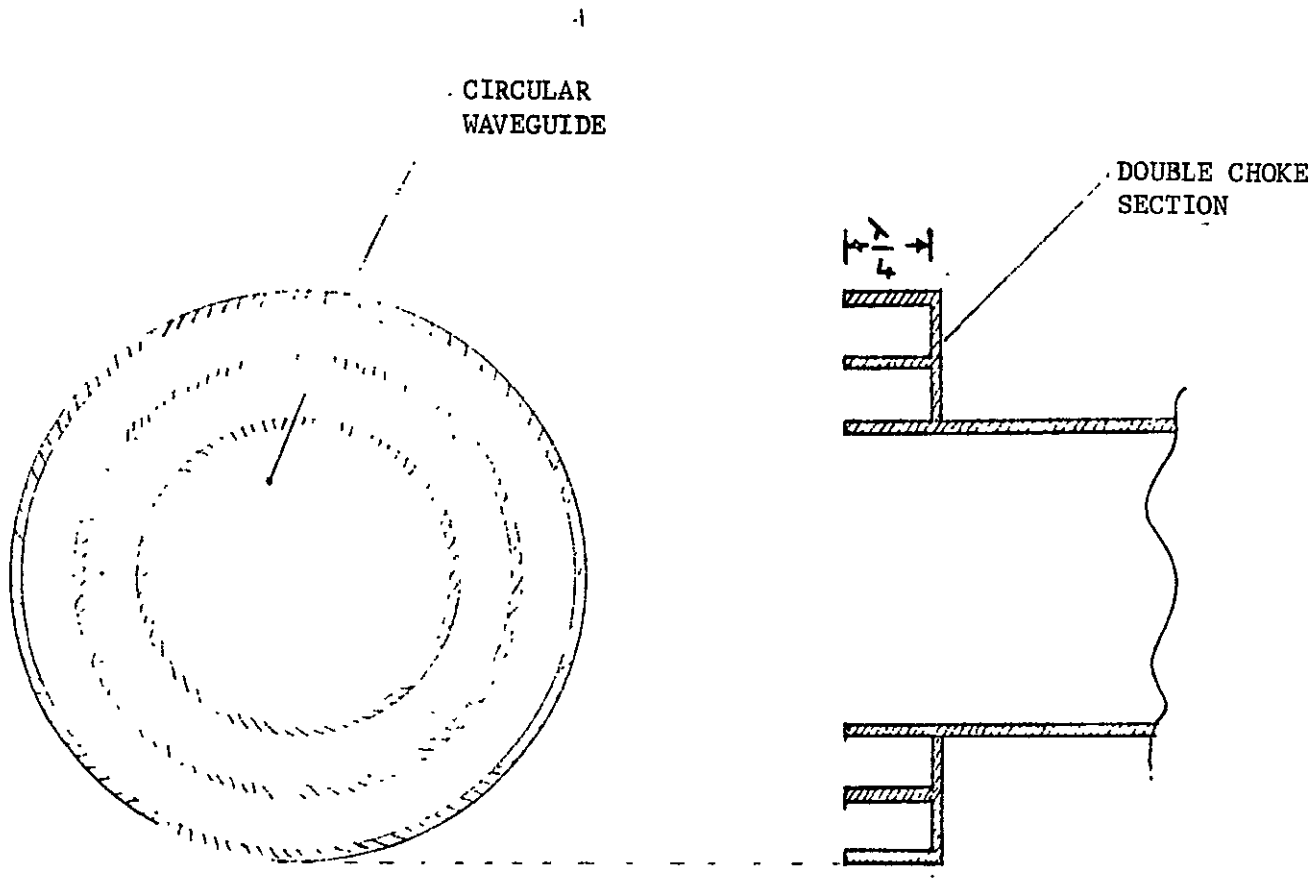

FIGURE 3-22 FEED-HORN CONFIGURATION FOR SUPPRESSION OF BACK-LOBES

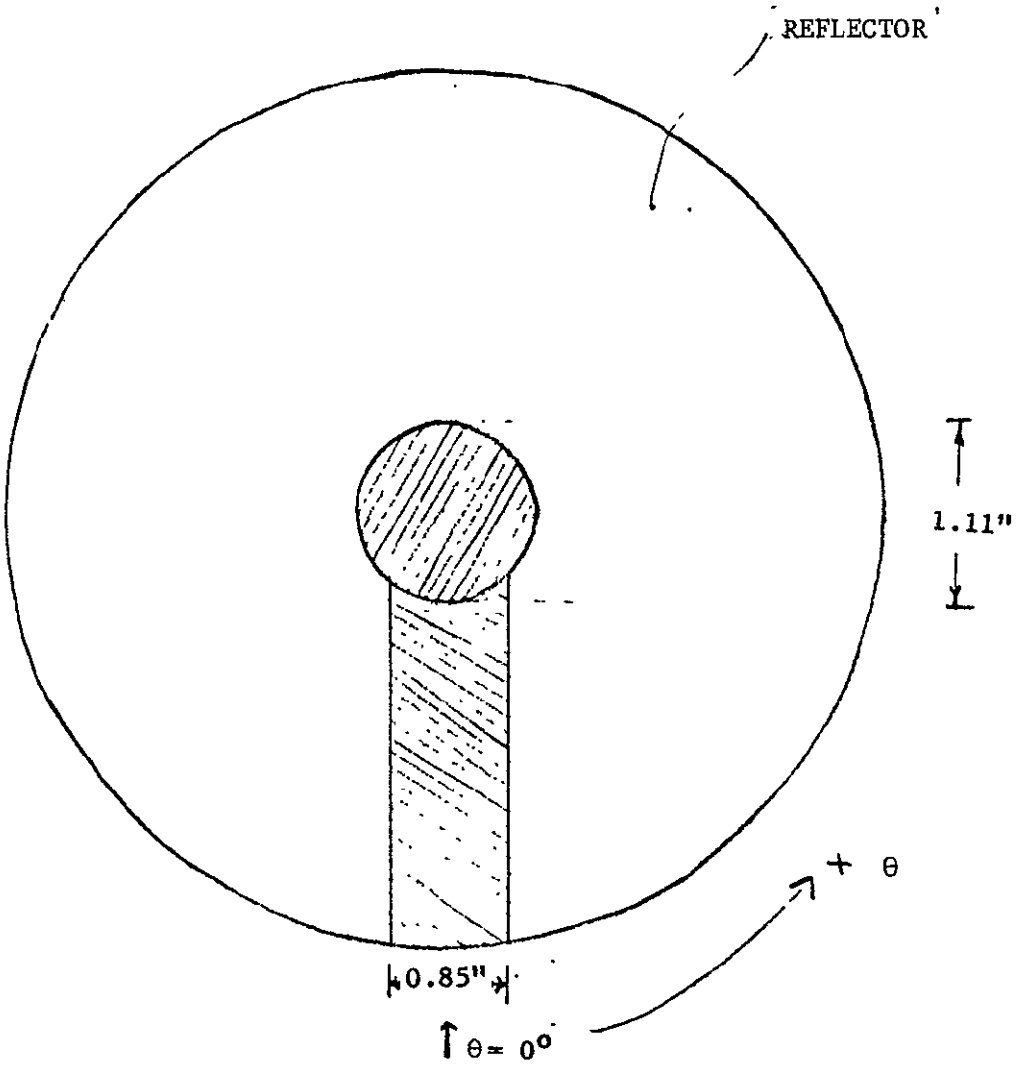

FIGURE 3-23 BLOCKAGE PARAMETERS FOR 28 INCH DIAMETER REFLECTOR

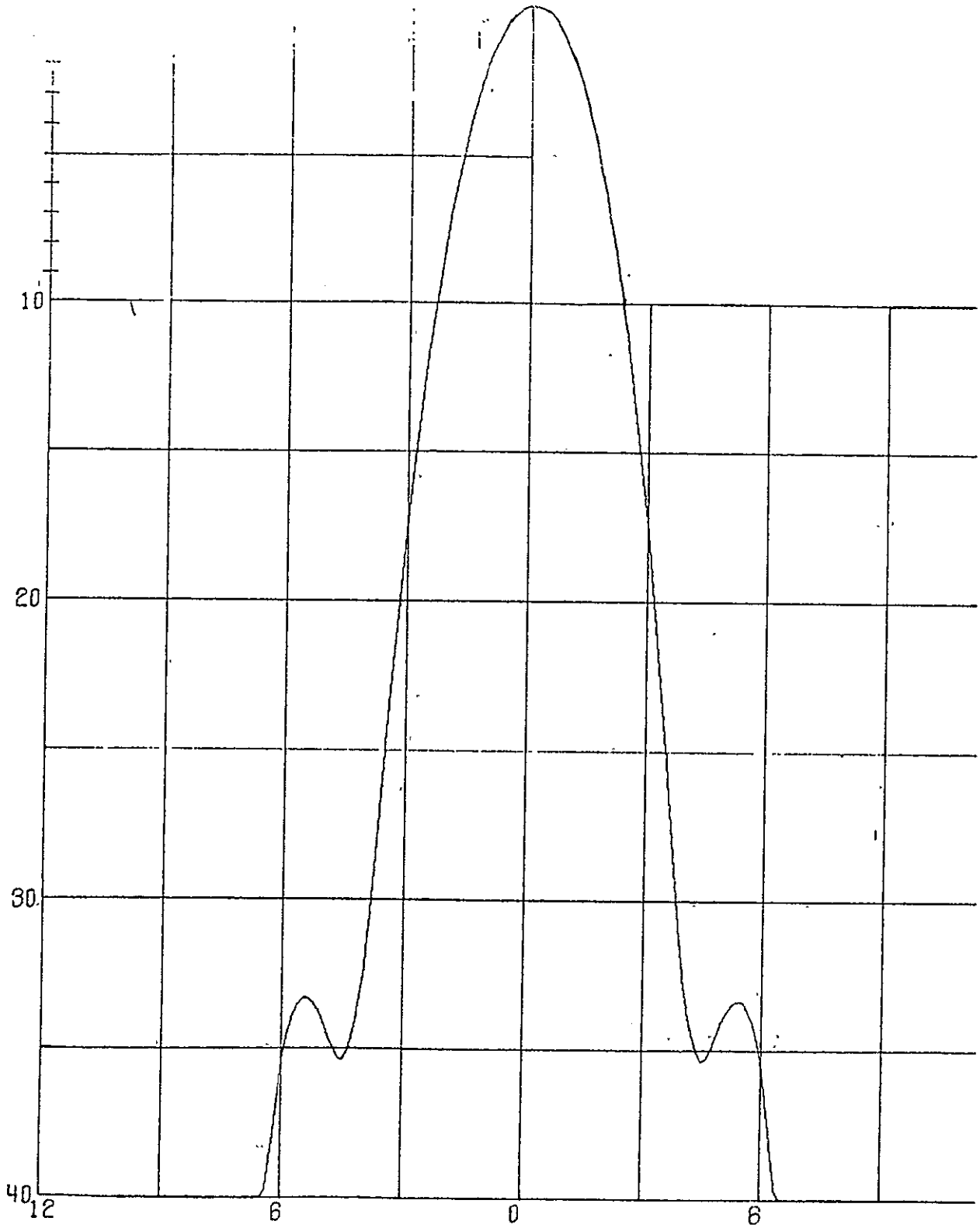

FIGURE 3-24 OPTIMIZED 28IN. DIAMETER REFLECTOR NO DISTORTION O = Ø

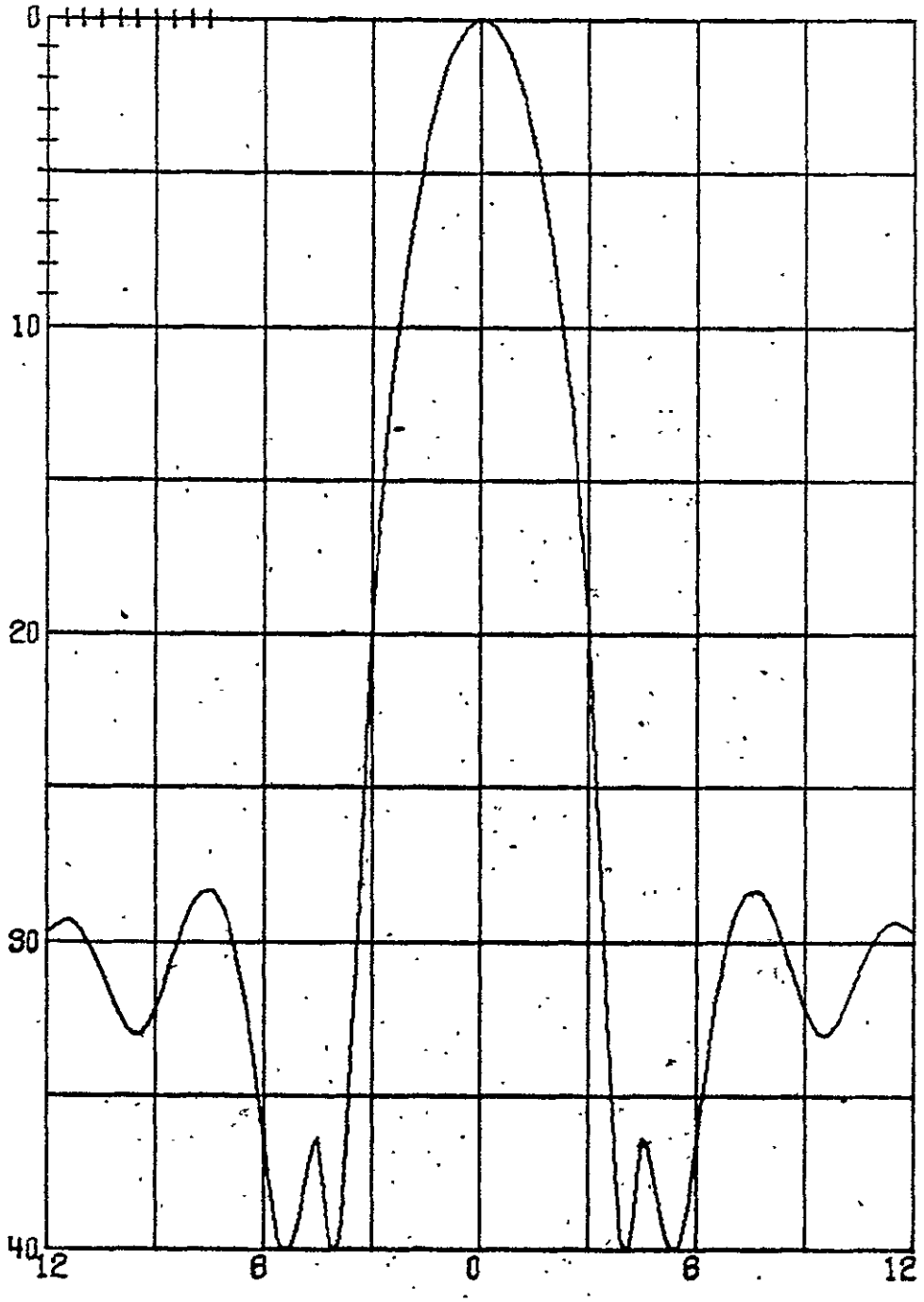

FIGURE 3-25, OPTIMIZED 28IN. DIAMETER REFLECTOR NO DISTORTION $\phi = 90°$

range of ϕ values, a series of patterns were computed for ϕ = 10°, 20° . . . . . 170°, 180°.

From these, the variation in near-in sidelobe level as a function of ϕ was obtained and this is plotted in the graph of Figure 3-26. This graph defines the upper limit on the amount of sidelobe suppression that can be obtained by means of a conventional prime focus reflector with an optimized aperture distribution. It therefore formed the basis for estimating the performance that could be achieved by utilizing active-element sidelobe suppression techniques.

3.3.4 Active-Element Sidelobe Suppression Techniques

To improve the near-in sidelobe performance of the antenna beyond that specified by Figure 3-26 it is necessary to resort to active-element suppression techniques. These fall into two categories:*

1. Aperture blockage compensation
2. Active zone suppression

In the former technique, a single radiating element (see Figure 3-27) is used as a means of partially compensating for the aperture blockage associated with the antenna feed structure. The relative phase and amplitude of this element are adjusted so as to suppress the highest near-in sidelobe in the manner depicted in Figure 3-28.

If further suppression is required, then it may be obtained by simultaneously employing the active zone technique. In this, the reflector is surrounded by a ring of elements as shown in Figure 3-29. The diameter of the ring is chosen so that the lobes of its radiation pattern coincide

---

* "Analytical and Experimental Investigation of Sidelobe Suppression Techniques for Reflector Type Spacecraft Antenna"
- Goebels, Meier and Thomas, NASA Report NASA CR-72462

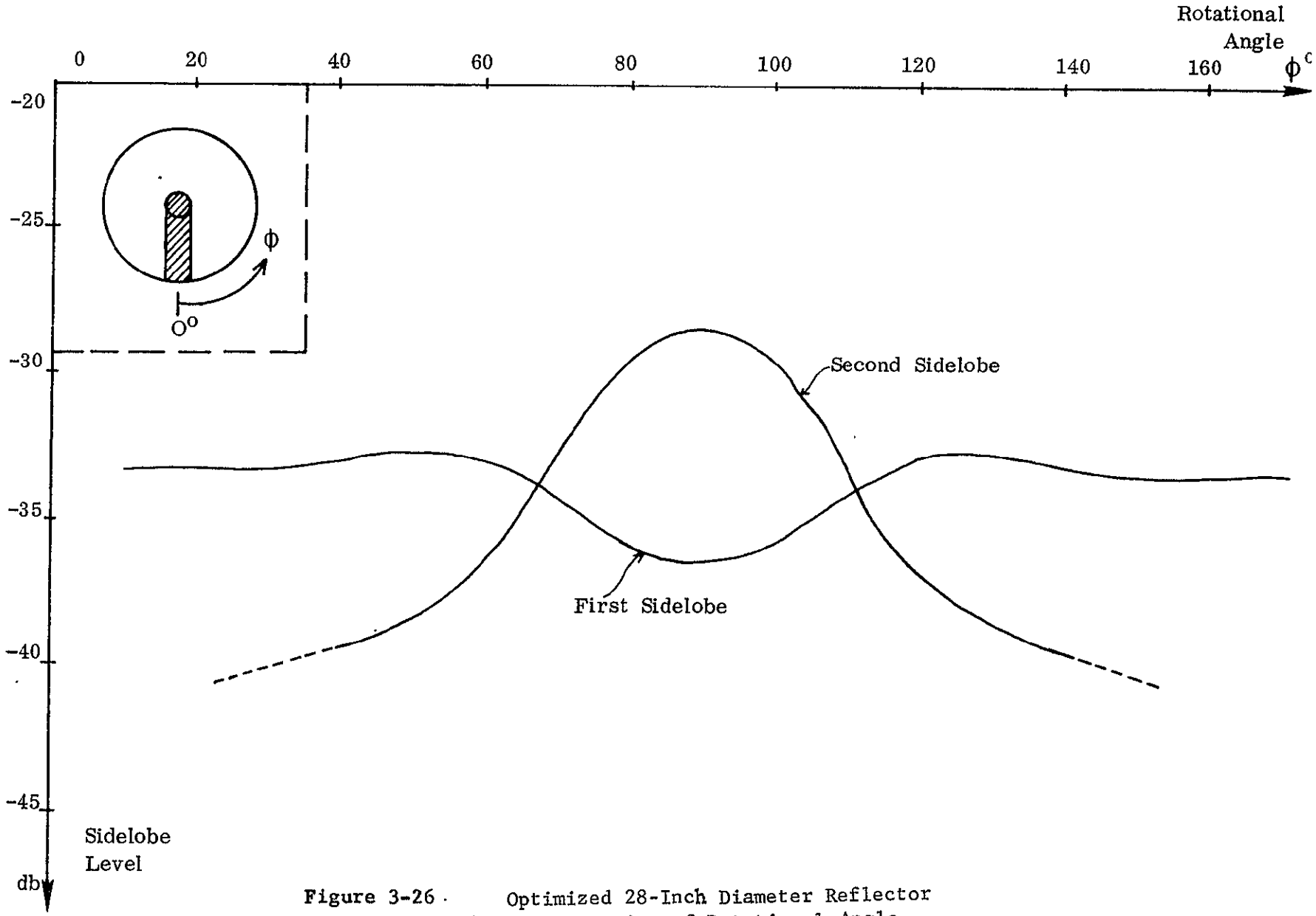

Figure 3-26 · Optimized 28-Inch Diameter Reflector Near-in Sidelobe as a Function of Rotational Angle

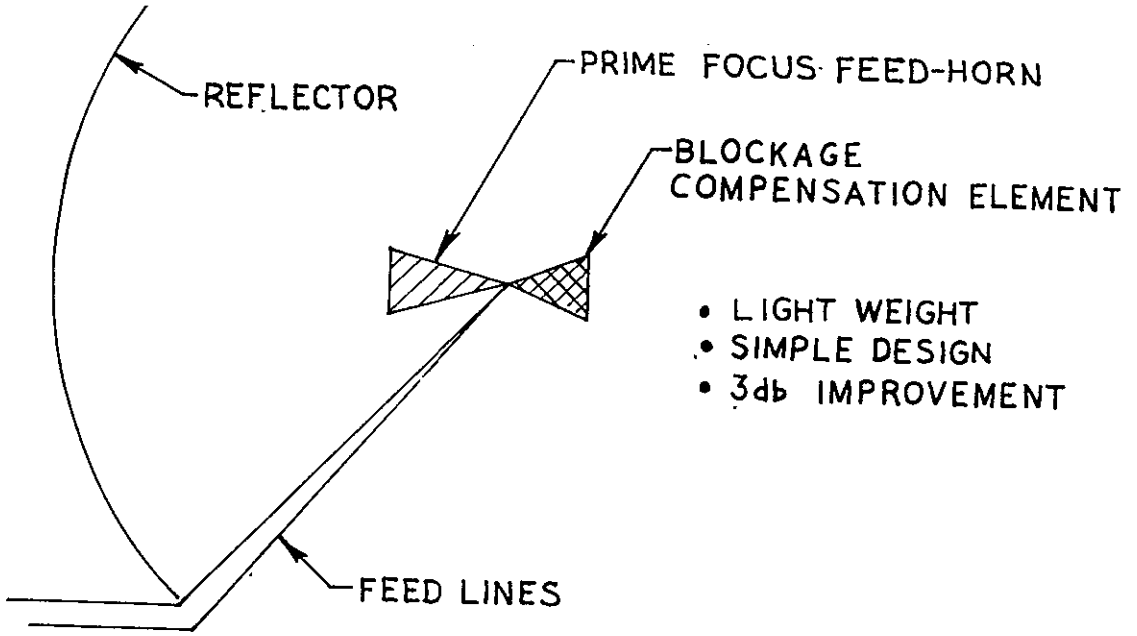

Figure 3-27 Antenna Configuration for Aperture Blockage Compensation

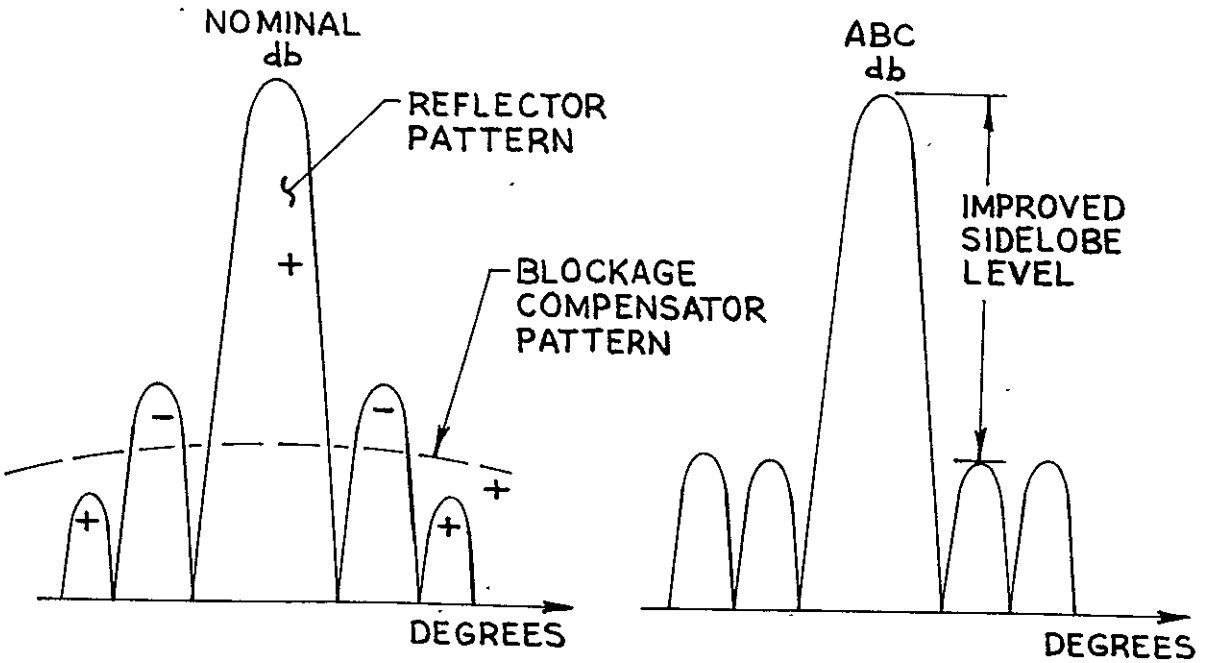

Figure 3-28 Suppression of Near-in Sidelobes by Aperture Blockage Compensation.

with the near-in sidelobes of the reflector pattern. Suppression is again achieved by adjusting the phase and amplitude of the elements to obtain cancellation. This is illustrated in Figure 3-30 for a given plane.

3.3.5 Estimation of Performance That May Be Achieved By Utilizing Active-Element Sidelobe Suppression Techniques

The graph of Figure 3-26 suggests that is should be possible to achieve an all-round near-in sidelobe level of approximately -32 dB by employing only aperture blockage compensation. (This would be accomplished by suppressing the high sidelobe in the $\phi = 90°$ plane until the point was reached at which the near-in sidelobes in all planes were at a common level).

The power required for this operation may be estimated in the following way:

Let P_T = Total power delivered to antenna system

P_R = Power delivered to prime focus reflector

P_C = Power delivered to blockage compensator

Then, assuming a loss-free system,

$$P_T = P_R + P_C \qquad (3.1)$$

If G_R = gain of reflector, then the power per unit solid angle at peak of main beam is:

$$P_R' = \frac{G_R}{4\pi} \cdot P_R \qquad (3.2)$$

Similarly, for the blockage compensator:

$$P_C' = \frac{G_C}{4\pi} \cdot P_C \qquad (3.3)$$

Combining equations (3.2) and (3.3) gives:

$$\frac{P_C}{P_R} = \frac{G_R}{G_C} \cdot \frac{P_C'}{P_R'}$$

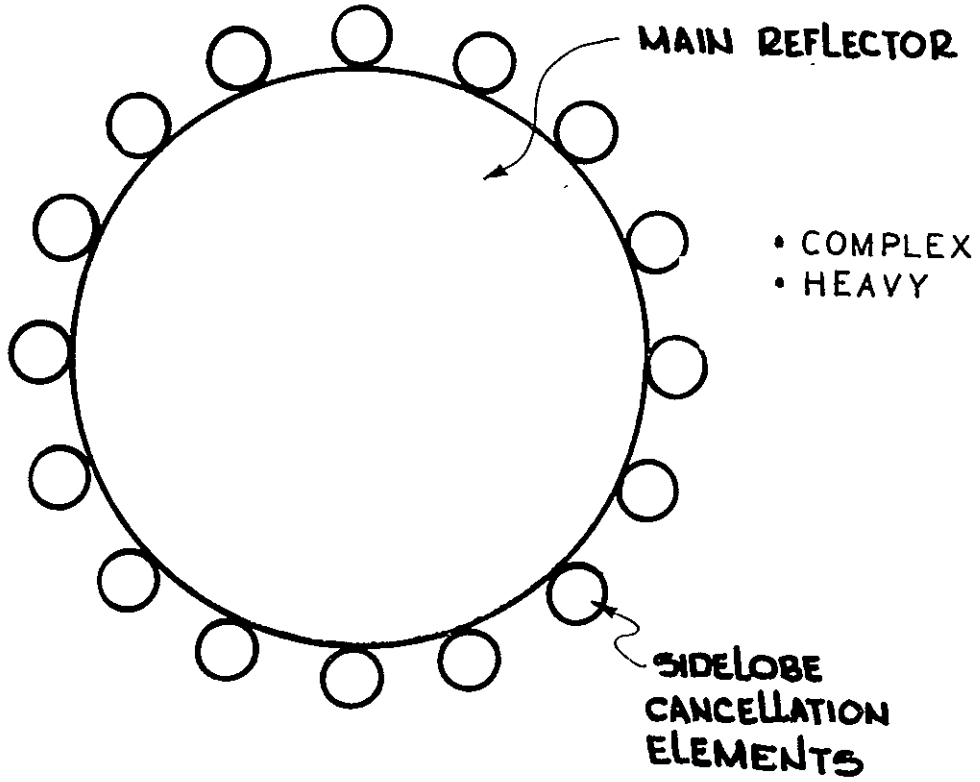

Figure 3-29 Antenna Configuration for Active Zone Sidelobe Cancellation

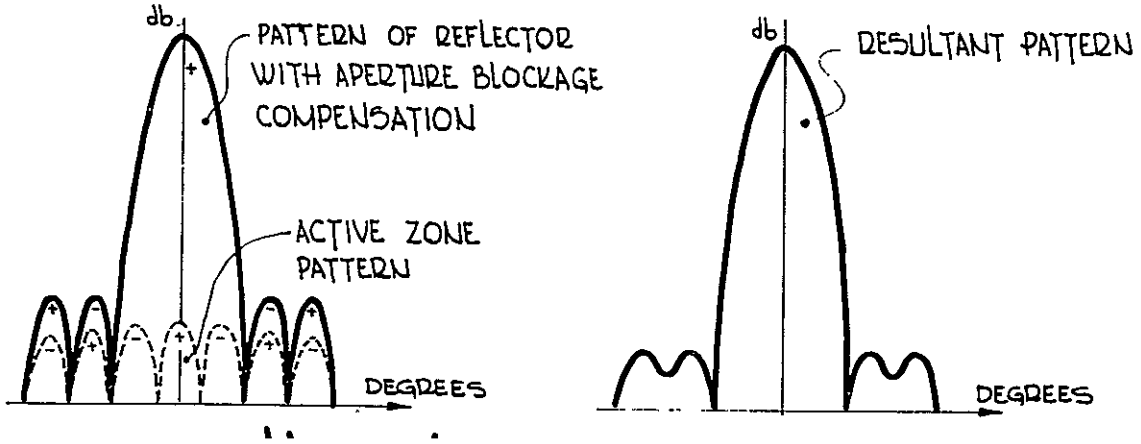

Figure 3-30 Suppression of Near-in Sidelobes by Active Zone Cancellation

and, from equation (3.1), $P_R = P_T - P_C$, so that

$$\frac{P_C}{P_T - P_C} = \frac{G_R}{G_C} \cdot \frac{P_{C'}}{P_{R'}} ,$$

which may be re-written as:

$$\frac{P_C}{P_T} = \frac{1}{1 + \frac{G_C}{G_R} \cdot \frac{P_{R'}}{P_{C'}}} \qquad (3.4)$$

If P_R' is normalized to unity, then the power density at the peak of the highest sidelobe is 14.05×10^{-4}, which corresponds to a normalized amplitude of 3.75×10^{-2}. Now, for a sidelobe level of -32 dB, the equivalent amplitude is 2.45×10^{-2}, so that to obtain the required suppression the compensating element must provide an out-of-phase field with a normalized amplitude of $(3.75 - 2.45 \times 10^{-2} = 1.30 \times 10^{-2}$.

Hence, for this application, $\frac{P_{R'}}{P_{C'}} = 0.592 \times 10^4$ and, since the computed value of G_R is 37 dB, equation (3.4) becomes:

$$\frac{P_C}{P_T} = \frac{1}{1 + 1.18\, G_C} \qquad (3.5)$$

It is envisaged that the compensating element will take the form of a hollow, thin-walled dielectric tube antenna. (Such a device, with a length of 7λ to 8λ , has a gain of approximately 16 dB. It may be conveniently located behind the prime focus feed since it will not add to the blockage area and will have only a minimal effect on the phase front of the plane wave emanating from the reflector).

Therefore: $G_C = 40$ which gives:

$$\frac{P_C}{P_T} = \frac{1}{48.3} = 0.0208 \qquad (3.6)$$

i.e., approximately 2% of the total power delivered to the antenna will be required for aperture blockage compensation. (It is anticipated that this power would be extracted from the main waveguide run to the feed-horn by means of a broad-watt directional coupler). The near-in sidelobes could be suppressed below the -32 dB level by utilizing the active zone technique in addition to aperture blockage compensation. However, the use of the second technique is not advocated for this project, since it is felt that its implementation would lead to an unacceptable increase in antenna weight and complexity.

3.3.6 Comments on Accuracy of Predicted Sidelobe Level

In computing the radiation patterns of the prime focus antenna, it was assumed that the following conditions prevailed:

1. Zero phase error in the feed-horn aperture
2. Zero mechanical error in the contour of the parabolic reflector.

These ideal conditions cannot be realized in practice and consequently the predicted -32dB near-in sidelobe level is somewhat optimistic. Past experience indicates, however, that by employing a precision reflector and optimizing the feed position, it should be possible to obtain a sidelobe level which is within 2 dB of the theoretically predicted value. It is therefore concluded that a near-in sidelobe level of approximately -30 dB may be achieved by means of the proposed antenna configuration.

(The extent to which this performance will be affected by the conditions which exist in a space environment is analyzed later in the report).

3.3.7 Ellipticity of Polarization

The power-handling requirements of this system make it desirable to avoid the use of any circular polarizer which entails loading the waveguide runs with posts or dielectric slabs. It was, therefore, decided to employ the septum polarizer*, which is illustrated in Figure 3-31. The mode of operation of this device can best be understood by considering its action on an incident circularly polarized wave.

This wave may be considered as being composed of two orthogonal linearly polarized waves of equal amplitude which are in phase quadrature. The manner in which the septum operates on each of these components is illustrated in Figure 3-32. As shown, the component normal to the septum is simply divided so as to generate two in-phase H_{10}-modes in the rectangular waveguides. The other component, however, is transformed into two out-of-phase H_{10}-modes. Phase cancellation is therefore achieved in one of the rectangular waveguides and, hence, the net result of the incident circularly polarized wave is to produce a linearly polarized signal at one of the output ports. It then follows, by reciprocity, that an H_{10}-mode propogating in one of the rectangular waveguides will cause a circularly polarized wave to be radiated with no power being coupled into the remaining port.

This device can therefore be neatly incorporated in the prime focus feed structure in the manner shown in Figure 3-33. The inner dimensions of the rectangular waveguide (0.75 inch x 0.375 inch) are such that a smooth transition can very easily be made into the circular aperture of 0.77 inch diameter required to feed a reflector with F/D = 0.35. (Making this transition

* "A New Type of Circularly Polarized Antenna Element", by Davis, Digiondomenico and Kempic, Univ. of Michigan, 1967, International Antenna and Propagation Symposium.

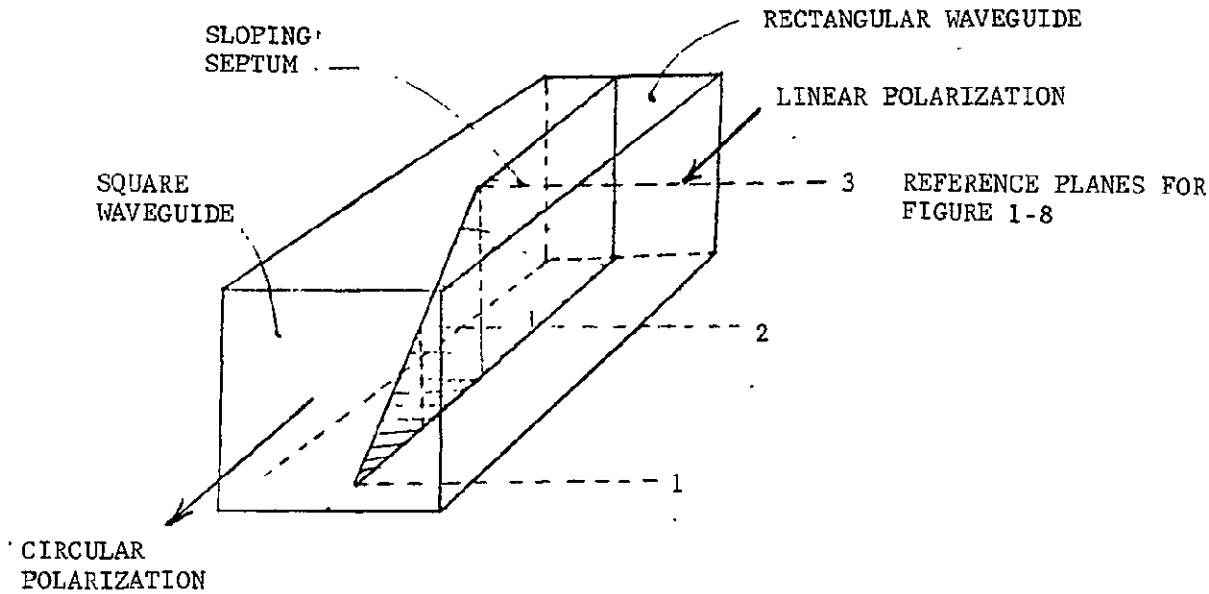

FIGURE 3-31 SEPTUM POLARIZER

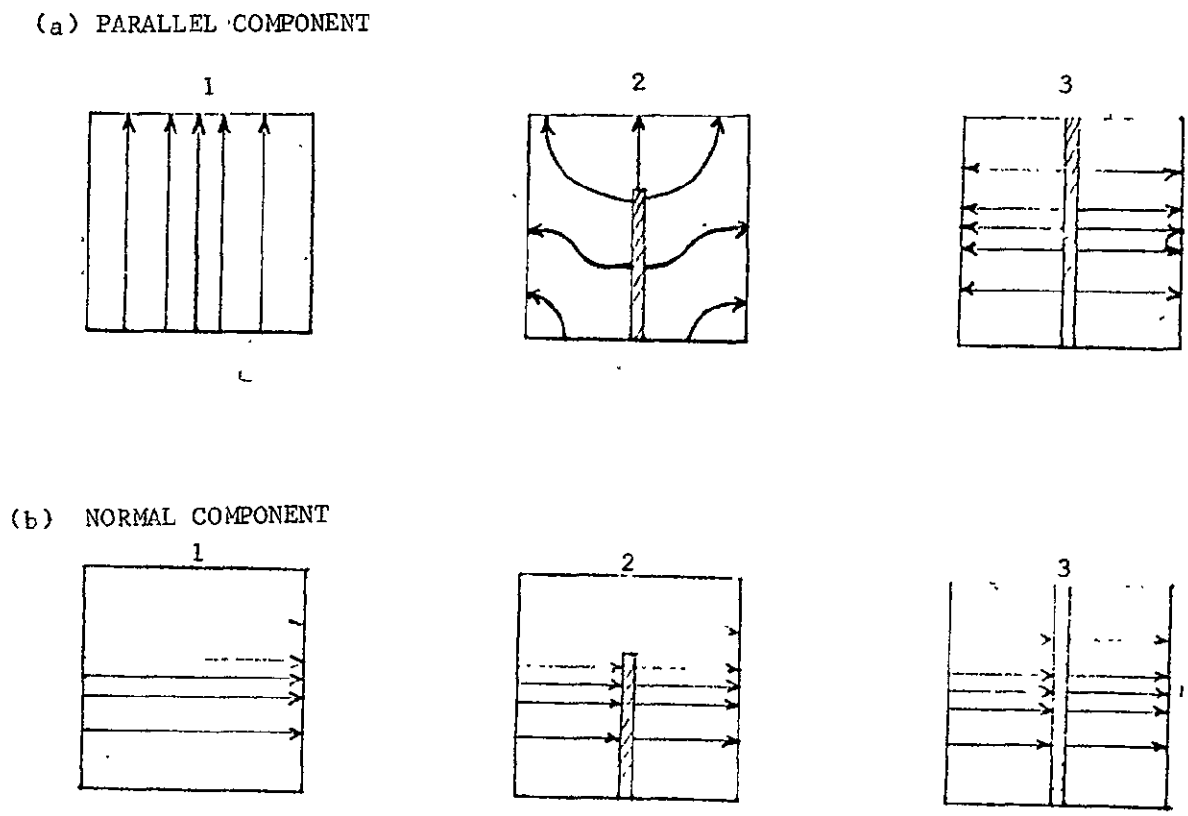

FIGURE 3-32 OPERATION OF SEPTUM POLARIZER

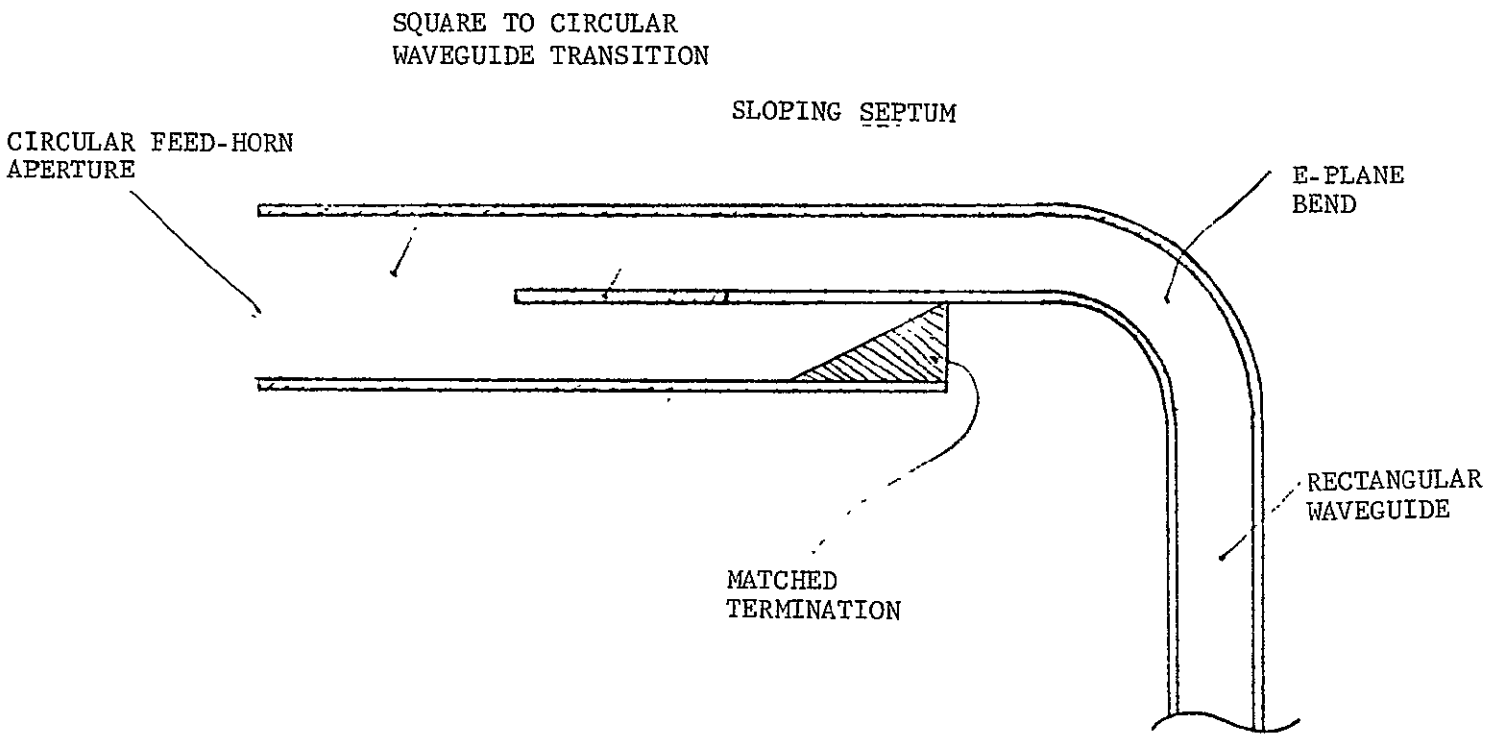

FIGURE 3-33 INTEGRATED CIRCULAR POLARIZER/FEED-HORN STRUCTURE

in a short distance will tend to enhance the performance of the polarizer and this consideration was a factor in choosing an F/D ratio of 0.35 for the reflector.)

Therefore, it is anticipated that, over the 4% bandwidth required for this system, an axial ratio of 0.5 dB and an isolation of 30 dB can be maintained. (The second of these performance figures is of particular significance since it means that the power which must be dissipated in the matched termination is limited to approximately 1 Watt CW.)

3.3.8 R.F. Losses and Power-Handling

For a rectangular waveguide with copper walls and inside dimensions a, b (cms), the attenuation constant is: *

$$\alpha c = \frac{0{\cdot}104\sqrt{\epsilon r}}{\sqrt{\lambda o}} \; \frac{\left[\frac{1}{b} + \frac{1}{2a}\left(\frac{\lambda o}{a\sqrt{\epsilon r}}\right)^2\right]}{1 - 0{\cdot}25\left(\frac{\lambda o}{a\sqrt{\epsilon r}}\right)} \quad \text{dB / Meter}$$

For the system being considered:

$$\lambda o = 2{\cdot}46 \text{ cm}, \; a = 1{\cdot}91 \text{ cm}, \; b = 0{\cdot}952 \text{ cm}, \; \epsilon r = 1{\cdot}0$$

Hence,

$$\alpha c = 0{\cdot}129 \text{ dB/meter}$$

$$\text{i.e., } \alpha c = 3{\cdot}94 \text{ dB per 100 ft.}$$

The corresponding figure for aluminum waveguide may be obtained from the above result as follows:

---

* "Principles and Applications of Waveguide Transmission", Southworth.

For the H_{10}-mode in rectangular waveguide, the attenuation coefficient associated with conductor losses at a fixed frequency is:

$$= \frac{K}{\sqrt{\sigma}}$$

Where k is a constant and σ is the conductivity of the metal from which the waveguide is fabricated.

From this, it is seen that:

$$\frac{\alpha A}{\alpha C} = \frac{\sigma C}{\sigma A}$$

where αA = attenuation constant for aluminum waveguide

αC = attenuation constant for copper waveguide

σC = conductivity of copper

σA = conductivity of aluminum

Therefore:

$$\alpha A = \alpha C \quad \frac{5 \cdot 8 \times 10^7}{3 \cdot 475 \times 10^7} = 1.29 \alpha C$$

i.e., αA = <u>5·08 dB per 100 ft</u>.

Current estimates indicate that the waveguide run from the last power combiner to the prime focus feed-horn will be approximately 2 feet long. Hence, the R.F. losses associated with the antenna will be in the region of 0.1 dB.

Since there are no abrupt discontinuities in the waveguide run to the feed-horn aperture, multipactor breakdown in the rectangular waveguide will be the limiting factor in the power-handling ability of the antenna feed. An adequate discussion of this effect is given in the analysis of the power handling ability of the 4-channel rotary joint (see paragraph 3.4.1). From this analysis, it is concluded that the antenna feed will have a <u>minimum</u> CW power-handling ability of 18·6 KW.

3.3.9 Antenna Efficiency

The computational process used in calculating the radiation pattern of the prime focus reflector also provided the following results:

Gain of uniformly illuminated 28-inch diameter aperture	= 39.15 dB
Reduction in gain due to aperture blockage	= -0.24 dB
Reduction in gain due to spillover	= -0.05 dB
Reduction in gain due to aperture taper	= -1.83 dB
Total gain reduction	= -2.12 dB

Thus, Net Gain = 37.03 dB

To obtain the gain of the proposed antenna system, this figure must be modified to include the effects of:

a. RF power dissipated in waveguide run to feed-horn

b. Power required for aperture blockage compensation

In the previous section, power dissipation was estimated to be 0.1 dB. Also, it was shown in paragraph 3.3.5 that approximately 2% of the input power will be required for blockage compensation. These two effects constitute an additional loss in gain of approximately -0.2 dB. Therefore, the resultant gain of the antenna system is approximately 36.8 dB, which corresponds to a net efficiency of 59%.

3.3.10 Beam Isolation

A good estimate of the beam isolation provided by the antenna system may be obtained by calculating the power coupled between two adjacent prime focus reflectors. The relative positions of two such reflectors and their respective feed-horns are defined in Figure 3-34. For the purpose of the calculations, the antenna designated Tx transmits while the antenna Rx is a matched receiver.

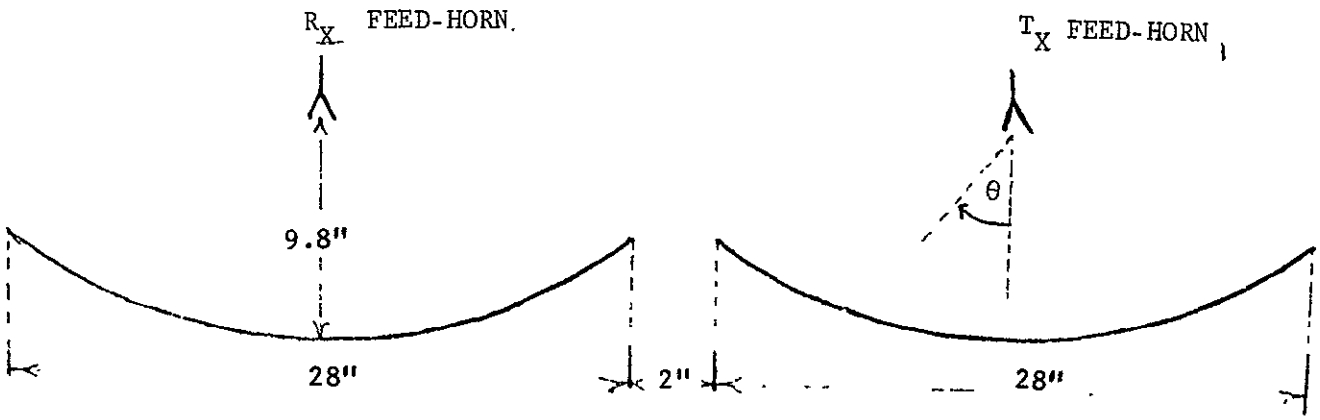

FIGURE 3-34. GEOMETRY USED FOR CALCULATING BEAM ISOLATION

Two principal coupling mechanisms exist:

1. Direct coupling between feed-horns
2. Coupling of power by the Tx feed-horn from the near-field of the Tx reflector.

Each of these effects were evaluated separately inthe manner shown below:

3.3.10.1 Coupling Between Feed-Horns

The dimensions of the feed elements are such that the Rx horn is in the far-field of the Tx horn. Hence, the coupling between them may be extimated as follows:

Let $G_T(\theta)$ = Gain of Tx feed-horn angle where θ is the angle from the peak of the horn's radiation pattern

Similarly, $G_R(\theta)$ = Gain of Rx feed-horn

The power per unit area at a distance r from the Tx horn is therefore defined by:

$$P(\theta) = \frac{P_T}{4\pi r^2} \cdot G_T(\theta)$$

Where P_T is the total power transmitted by the horn.

Hence, the power coupled into the Rx horn is:

$$P_R = \frac{P_T}{4\pi r^2} \cdot G_T(90°) \cdot A_R(90°)$$

Where $A_R(\theta)$ represents the effective area of the Rx feed-horn.

Now, $G_R(\theta) \cong \frac{4\pi}{\lambda^2} A_R(\theta)$, where λ = free-space wavelength

Therefore, $A_R(\theta) = \frac{\lambda^2}{4\pi} \cdot G_R(\theta)$, which gives

$$P_R = \frac{P_T}{4\pi r^2} \cdot G_T(90°) \cdot \frac{\lambda^2}{4\pi} \cdot G_R(90°)$$

Since the two feed-horns are identical, this reduces to:

$$\frac{P_R}{P_T} = \left[\frac{\lambda}{4\pi r} \cdot G(90°) \right]^2 \qquad \text{where } G(\theta) = G_T(\theta) = G_R(\theta).$$

The computed on-axis gain of the feed-horns is 10·6 dB; using this figure in conjunction with the theoretical horn pattern gives:

$$G(90°) = G(o°) - 29.8 \text{ dB} = (10{\cdot}6 - 29.8) \text{ dB} = -19{\cdot}2 \text{ dB}$$

$$\text{i.e., } G(90°) = 0.012$$

Also, the geometry of the antenna configuration is such that r = 30 inches.

Thus, $$\frac{P_R}{P_T} = \left(\frac{0.97 \times 0.012}{4 \times 3.142 \times 30} \right)^2 = 9.54 \times 10^{-10}$$

$$\text{i.e., } \frac{P_R}{P_T} = -90\text{dB}$$

3.3.10.2 Near-Field Coupling

In a rigorous theoretical treatment of this effect, the total power coupled from the near-field would be obtained by integrating the contributions from all points on the radiating aperture. This would entail a lengthy computational process, it was therefore decided to resort to a much simpler analysis by means of which a good first approximation to the solution could readily be obtained. This analysis follows:

Main reflector subtends a semi-angle of 71° at feed-horn, and thus

Space attenuation = 3 dB

Feed-horn gives an 18 dB edge-directed taper, and thus

Aperture taper = (18 + 3) dB = 21 dB

Now, since the Rx feed-horn is in the immediate near-field of the Tx reflector, the power density at that point is approximately 21 dB below

the power density at the peak of the main beam (i.e., the Tx radiation pattern in this region is still essentially the reflector aperture distribution).

Peak gain of Tx horn is G = 10.6 dB = 11·5 times, and thus the power density at the center of the reflector surface, and hence at the peak of the near-field main beam is:

$$P_P = \frac{P_T}{4\pi x(9\cdot 8)^2} \quad X\ 11\cdot 5$$

The power density at the Rx feed-horn is of the order of 21 dB below this level; therefore, the power coupled into the horn is

$$P_H = \frac{P_{Tx}11\cdot 5}{4\pi x(9\cdot 8)^2} \quad X\ 0.008\ X\ A,$$

Where A is effective area of horn

Hence, $$P_H = \frac{P_{Tx}11\cdot 5}{4\pi x(9\cdot 8)^2} \quad x\ 0.008\ x\ \frac{\lambda^2}{4\pi} \quad x\ 11\cdot 5 = \left(\frac{11\cdot 5x0\cdot 97^2}{4\pi x9\cdot 8}\right) x\ 0.008$$

$$= 0.656 \times 10^{-4}$$

i.e., $\frac{P_H}{P_T} = -42$ dB

3.3.11 Review of Proposed Antenna System

The proposed antenna configuration is illustrated in Figure 3-35. A comparison between the theoretically derived performance figures and the antenna system design goals is also provided.

3.3.12 Effect of Environmental Conditions on Antenna Performance

When the system is operating in the space environment, it will be subjected to solar heating effects which will tend to cause distortion of the antenna

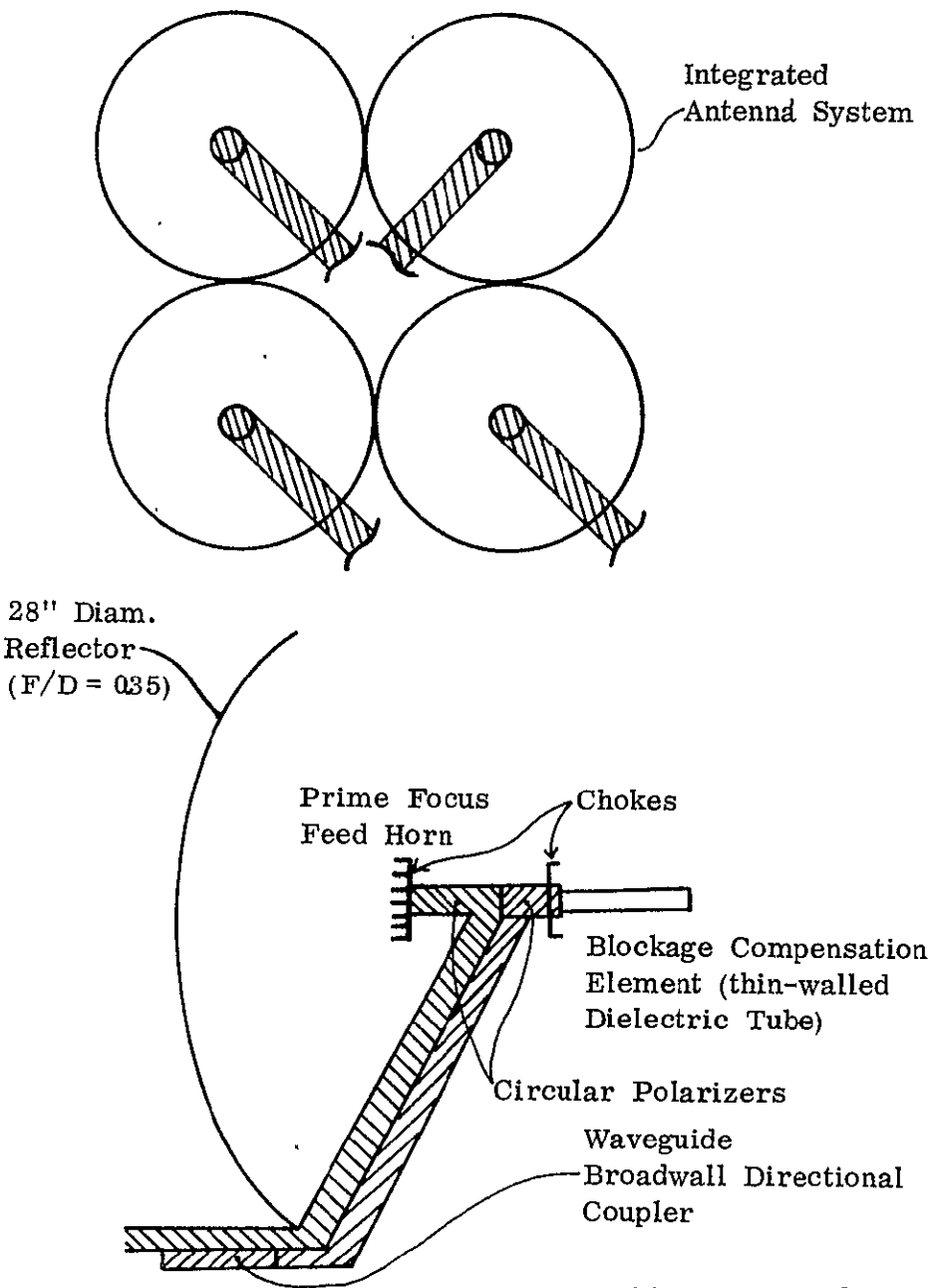

Parameter	System Design Goal	Theoretical Estimate
Antenna Configuration	Cluster of Four Prime Focus Reflectors (28" Diam, F/D-0.35), each with aperture blockage compensation	
HPBW	2.7^{o}	2.7^{o}
Near-in Sidelobe Level	30-35 dB	-30 dB
Net Gain		37 dB
Net Antenna Efficiency		59%
Ellipticity of Polarization	<1 dB	<1 dB
Power Handling Per Channel	1 KW CW	18 KW CW
Beam Isolation	40 dB	>40 dB

Figure 3-35 Review of Proposed Antenna Configuration

structure, particularly the parabolic reflectors. It will therefore be necessary to employ special fabrication techniques in the manufacture of the antenna components if the performance degradation associated with these effects is to be minimized.

The recommended approach is to use invar metal as a basis for forming the reflector surfaces. (Analyses already performed by Philco Ford for similar antenna configurations have shown that, for an all-aluminum structure, there would be an unacceptable deterioration of the radiation pattern.) Mechanical design considerations indicate that a 0.003-inch (7.62 mm) invar face sheet backed by a 0.25-inch (6.35 mm) thick invar honeycomb core would be a suitable structure. A computational analysis was therefore carried out to verify the performance of an antenna constructed in this manner.

The case of "edge-on" solar illumination (see Figure 3-36) was studied since the distortions associated with this configuration are representative of the worst-case values. The computed distortions were converted into equivalent phase errors and the secondary radiation pattern was calculated at 10° intervals in the rotational angle, Φ. (Φ is defined in Figure 3-36). These patterns revealed that the effect of the distortion was most pronounced in the $\Phi = 60°$ plane. This is shown in Figure 3-37. However, the pattern for $\Phi = 90°$ is essentially the same as the corresponding one for the undistorted case, as can be seen by comparing Figures 3-38 and 3-25. Thus, the highest near-in sidelobes are still at the level originally set by aperture blockage effects.

From this, it is concluded that with the proposed fabrication techniques there will be no significant increase of the sidelobe level due to the effects of solar heating.

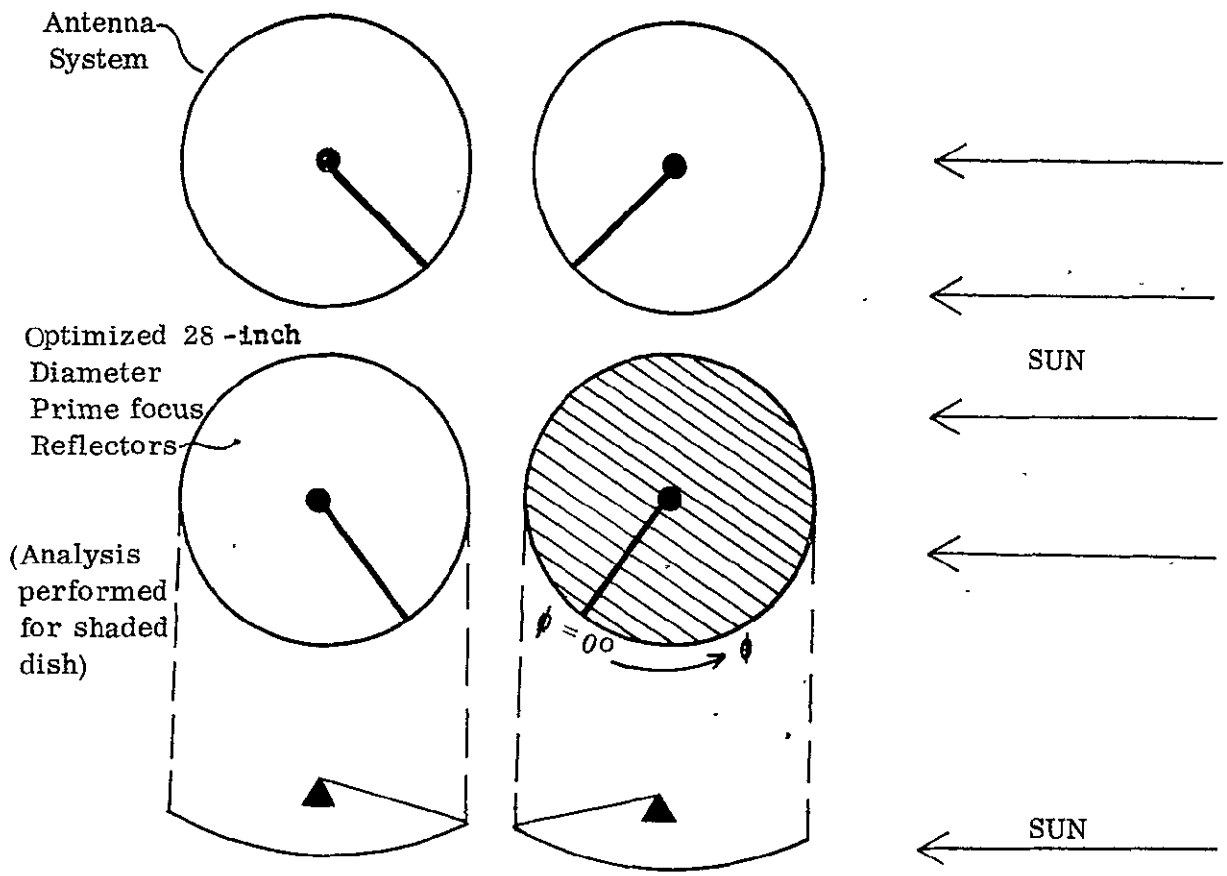

Figure 3-36 Configuration for Evaluating Effect of Thermal Distortion on Antenna Radiation Pattern

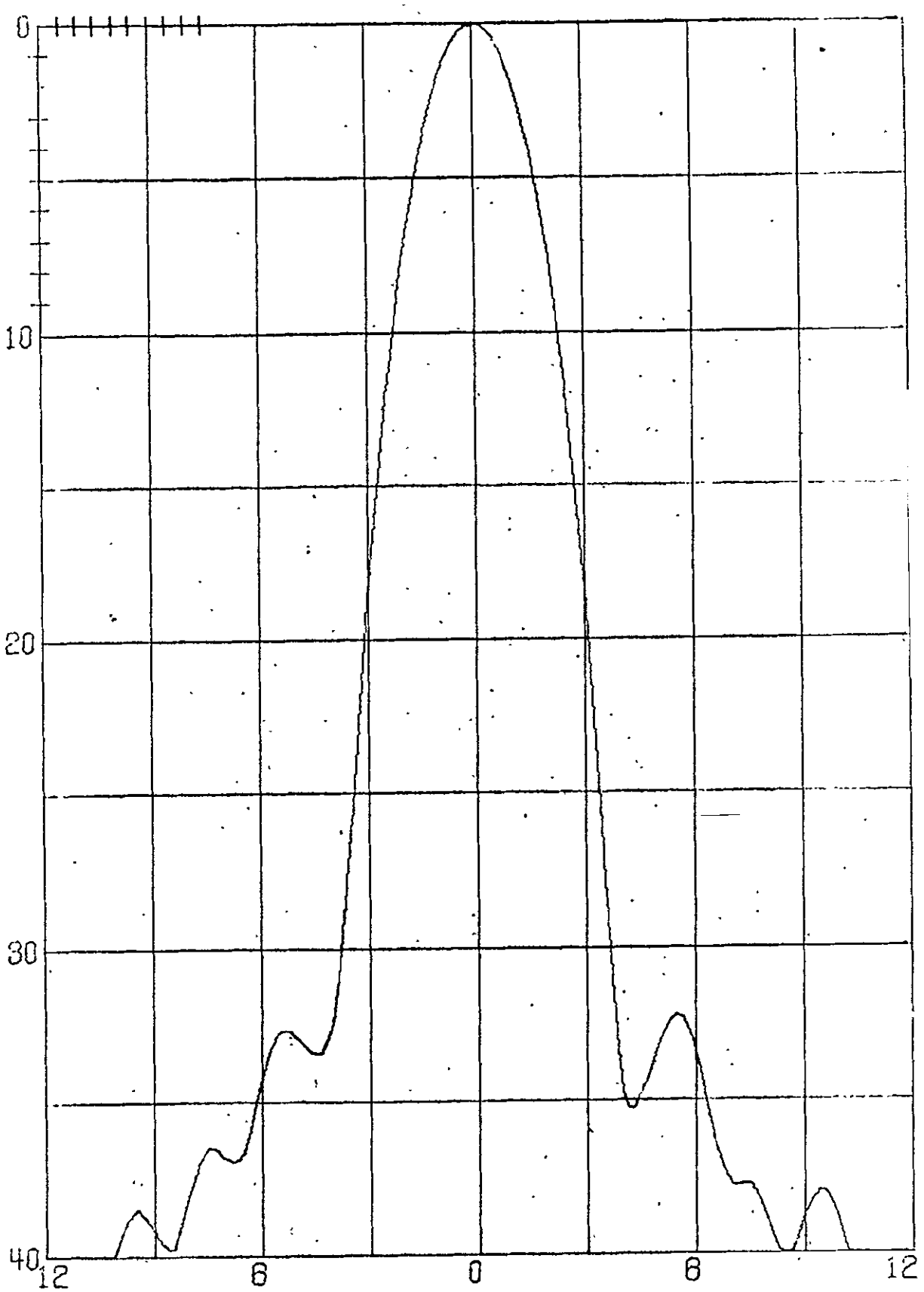

FIGURE 3-37 28 IN. DIAM. REFLECTOR MAX THERMAL DISTORTION Ø = 60

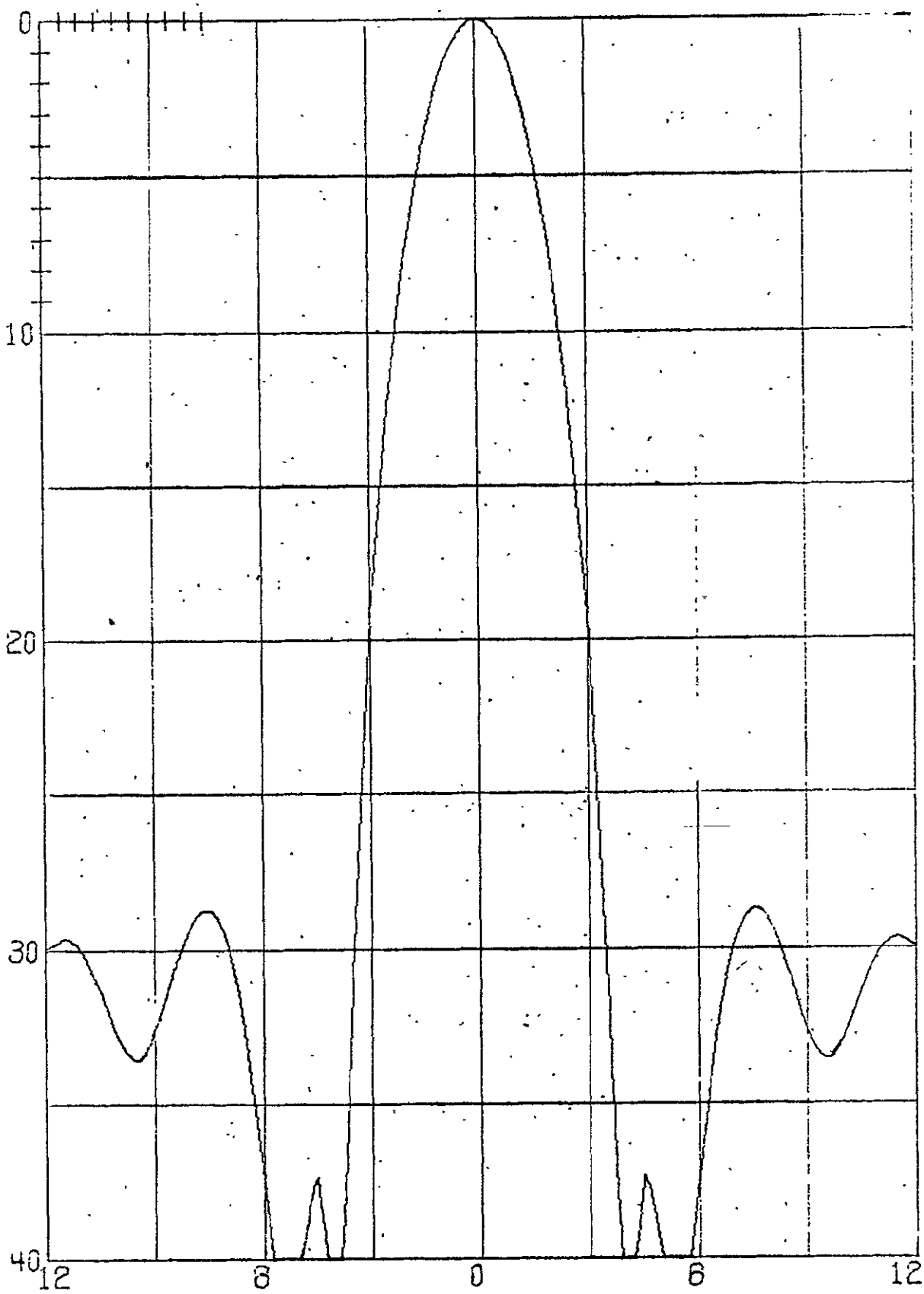

FIGURE 3-38 28IN. DIAM. REFLECTOR MAX THERMAL DISTORTION Ø = 90

The analysis did show, however, that thermal expansion of the aluminum waveguide feed arm causes the feed horn to be displaced by 0.025 inch from the reflector axis.

For the reflector geometry being employed, this corresponds to a beam displacement of 0.08°. This displacement occurs in the $\phi = 0^{\circ}$ plane, which lies at 45° to the spacecraft spin axis (see Figure 3-36). It can therefore be resolved into two equal, orthogonal components of magnitude 0.06°, which represent displacements about the pitch and roll axes, respectively.

Thus, the antenna system will have a worst-case beam-pointing error of 0.06° in both pitch and roll due to the effect of environmental conditions.

3.4 DESIGN ANALYSIS OF RF SUBSYSTEM

3.4.1 Candidate System Design

The RF subsystem which has been selected for use in conjunction with the four-reflector antenna is outlined diagrammatically in Figure 3-39. It has a principle of operation which may be described as follows:

RF power from the separate transmitters $T1_1$, $T2_1$, T3 and T4 is transferred across the spin interface between the satellite and the antenna platform by means of a four-channel rotary joint. The two-way switches SW1 and SW2 can then be activated so as to permit either transmission of one channel on each of the four beams or transmission of two channels on Beams 2 and 3 with no power being delivered to Beams 1 and 4.

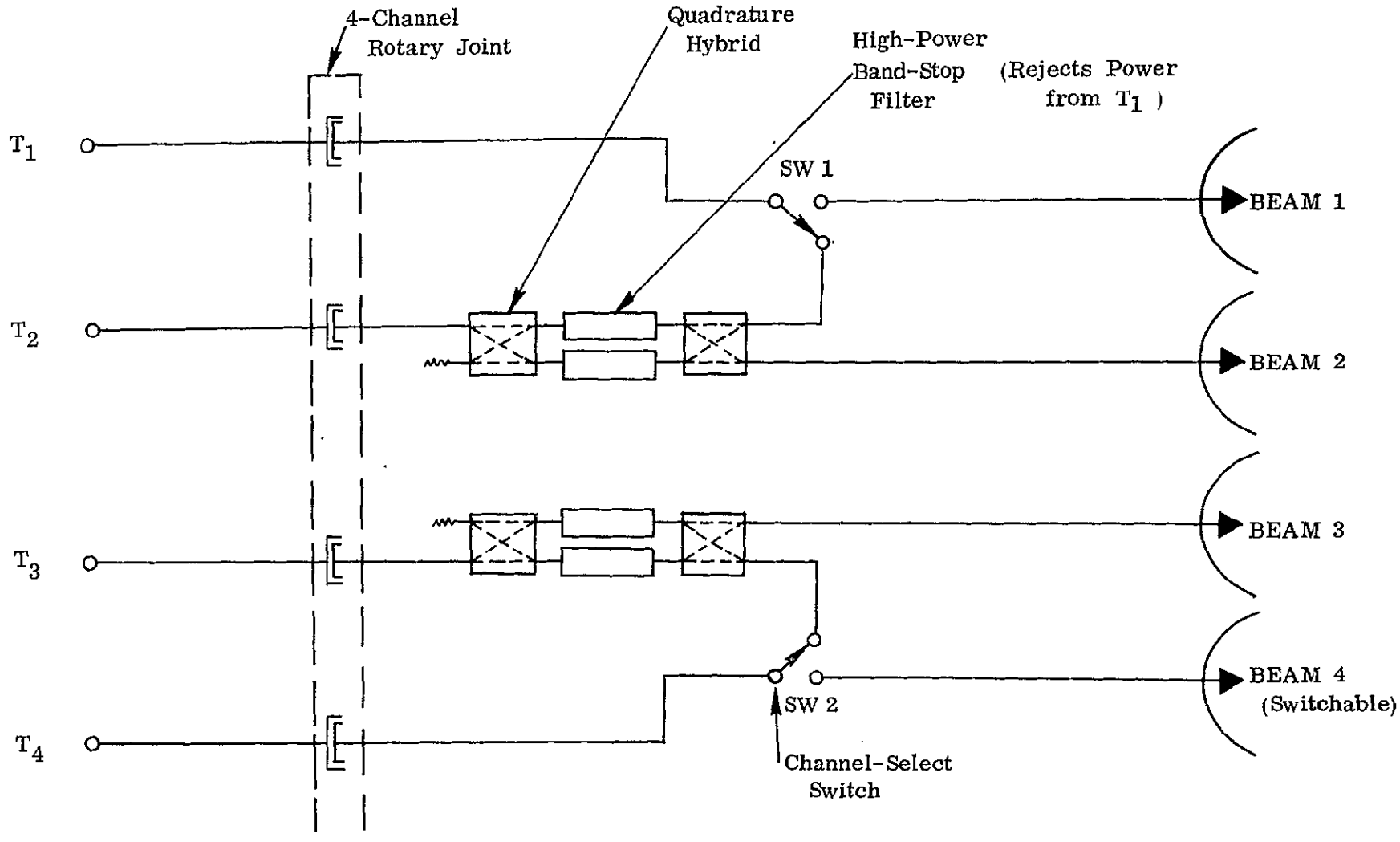

Figure 3-39 Candidate RF Subsystem

In the second mode of operation, power from transmitter T2 enters a quadrature hybrid where it is divided into two equal parts. These pass through the band-stop filters, which are tuned to reject the power from Transmitter T1, and then recombine in a second hybrid. Power from transmitter T1 enters this hybrid and divides into two equal parts. These are rejected by the band-stop filters and hence recombine at the antenna port of the hybrid. In this way, the powers from transmitters T1 and T2 are radiated in beam 2. Similarly, the powers from transmitters T3 and T4 may be simultaneously radiated in beam 3.

The analysis of this system fell naturally into two parts. In the first, the components which go to make up the system were considered separately to establish their nominal RF performance and specify their overall dimensions. The information thus gained was then used in the second part of the analysis as a basis for evaluating the performance of the integrated unit.

Since a compact, light-weight system is required, the design of each component was based upon aluminum WR75 waveguide.

3.4.2 Analysis of RF Components

3.4.2.1 Four-Channel Rotary Joint

Figure 3-40 illustrates the design of a rotary joint that can provide 4-channel operation in the 7-8 GHz frequency range. As can be seen from the diagram, the device consists of four concentric coaxial waveguide sections, the innermost being a "straight-through" channel, while the remaining three are excited by air-dielectric stripline corporate feed networks. Since this configuration has a power rating of only 200-300 Watts CW per channel (the upper

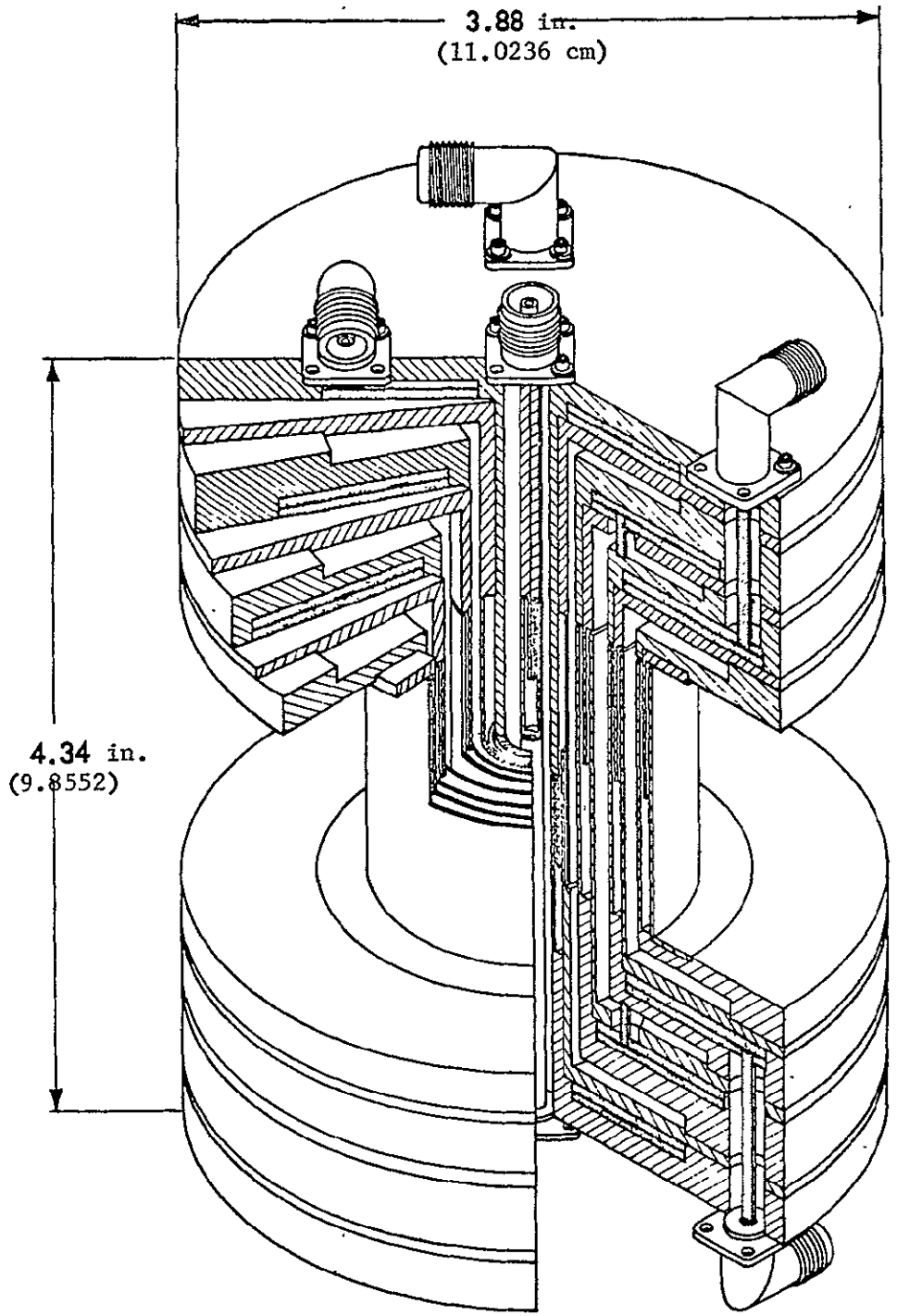

Figure 3-40 4-Channel Rotary Joint for Use at 7-8 GHz

limit being imposed by the stripline networks), it cannot be directly applied to the current project. However, the basic design may be extended to cope with the increased power-handling requirements by replacing the stripline networks by waveguide structures of the type shown in Figure 3-41.

A candidate design based on this technique was derived and is illustrated in the composite drawing of Figure 3-42. Details of the proposed coaxial waveguide sections, the non-contacting chokes and the rectangular-to-coaxial waveguide transitions are given in Figure 3-43.

With this configuration, the design performance figures for the rotary joint are as listed below:

Channel	Frequency (GHz)	Loss (dB)	CW Power Rating (KW)	VSWR	Isolation (dB)
1	12.025 - 12.075	< 0.4	>1.0	< 1.2	↑↓ >40
2	12.125 - 12.175	< 0.4	>1.0	< 1.2	↑↓ >40
3	12.225 - 12.275	< 0.4	>1.0	< 1.2	↑↓ >40
4	12.325 - 12.375	< 0.3	>1.0	< 1.2	

3.4.2.2 Channel-select Switches

The high CW power levels required for this system preclude the use of any currently-available solid-state switching device. Also, the requirement for low insertion losses rules out any switching circuit based on gas discharge tubes. It is therefore necessary to utilize an electro-mechanical switch of the type illustrated in Figure 3-44.

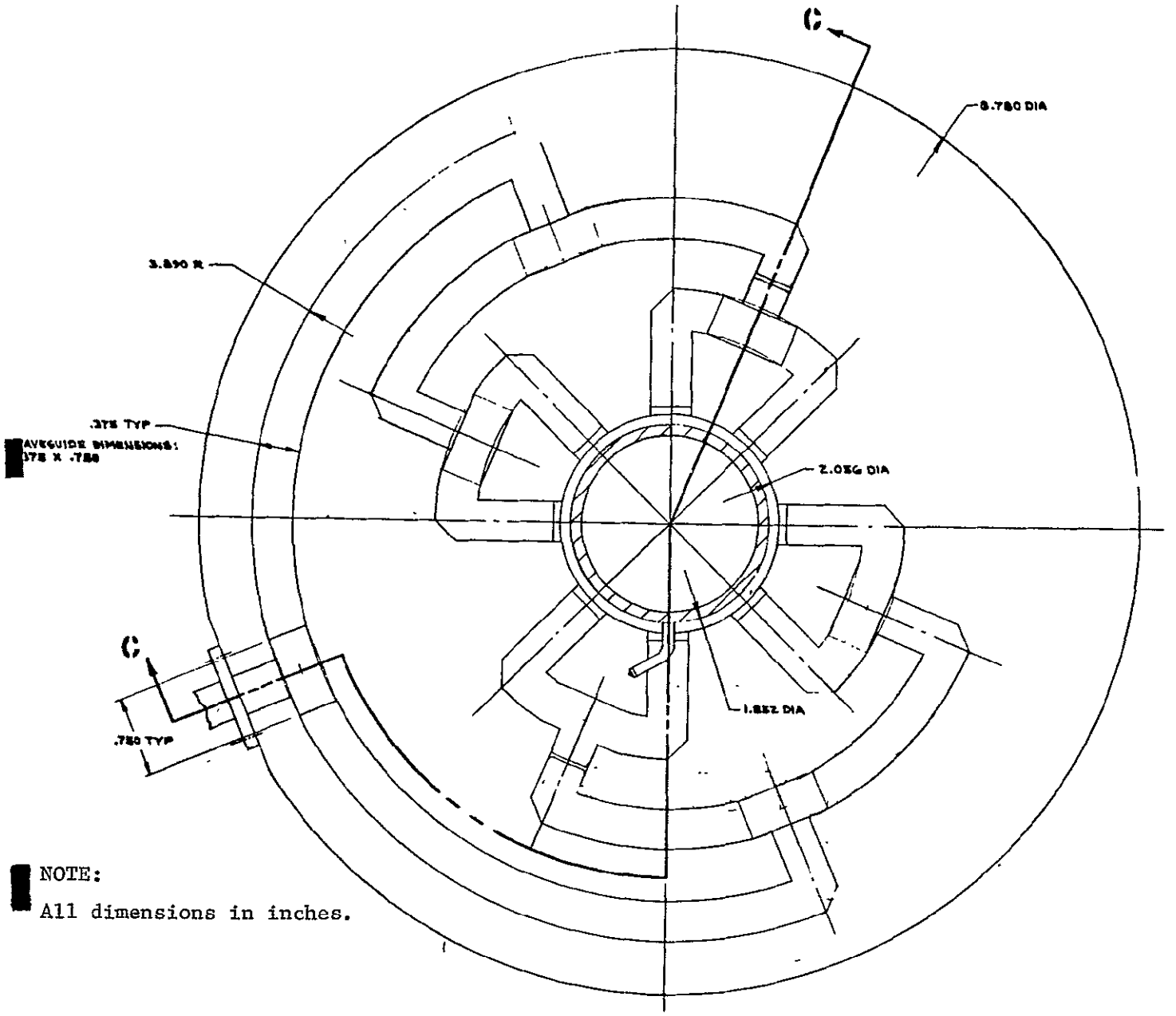

NOTE:
All dimensions in inches.

Figure 3-41 Rectangular Waveguide
Corporate Feed Section for 12 GHz Rotary Joint

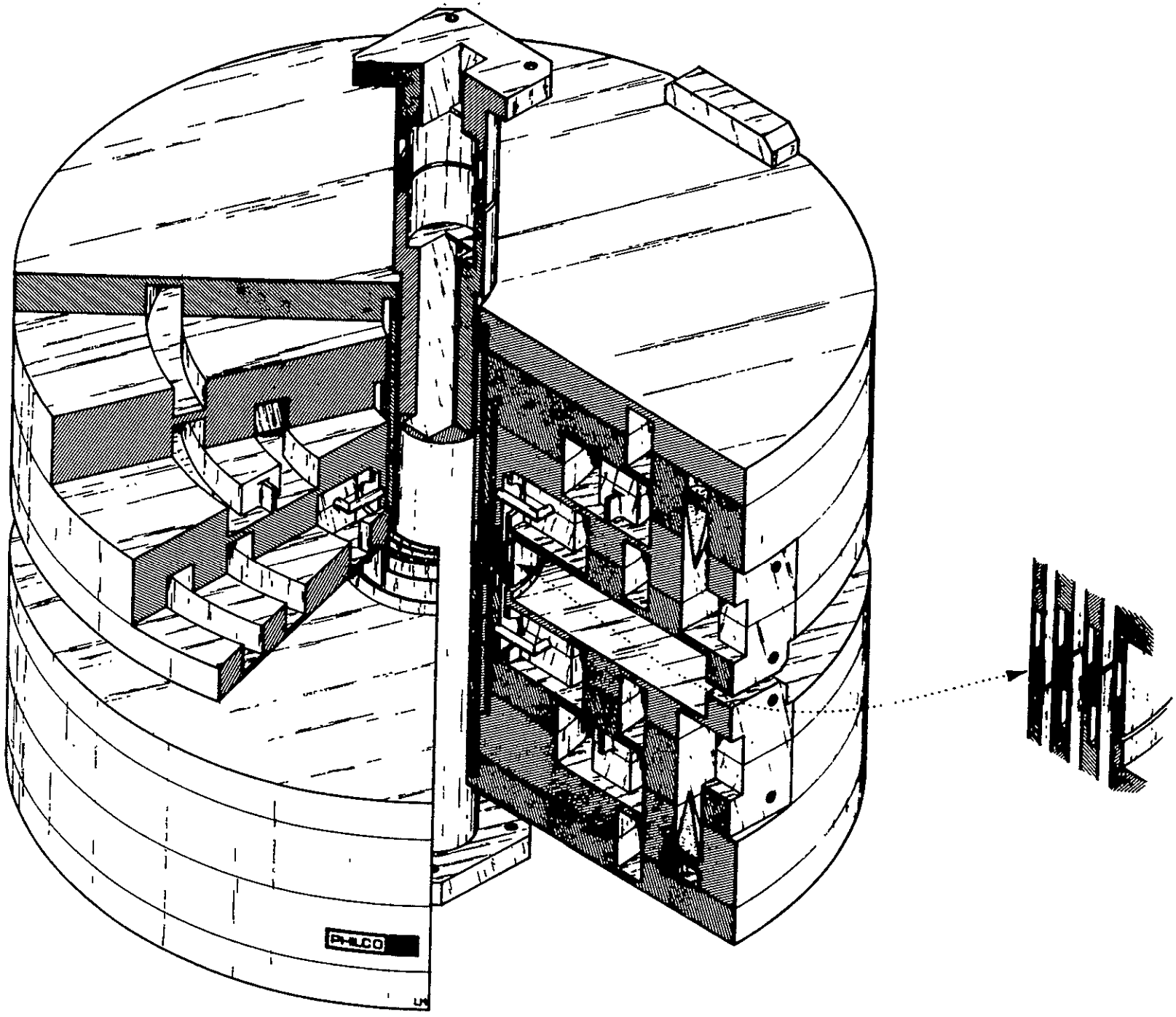

Figure 3-42 Candidate 4-Channel, High-Power, Rotary Joint, Schematic

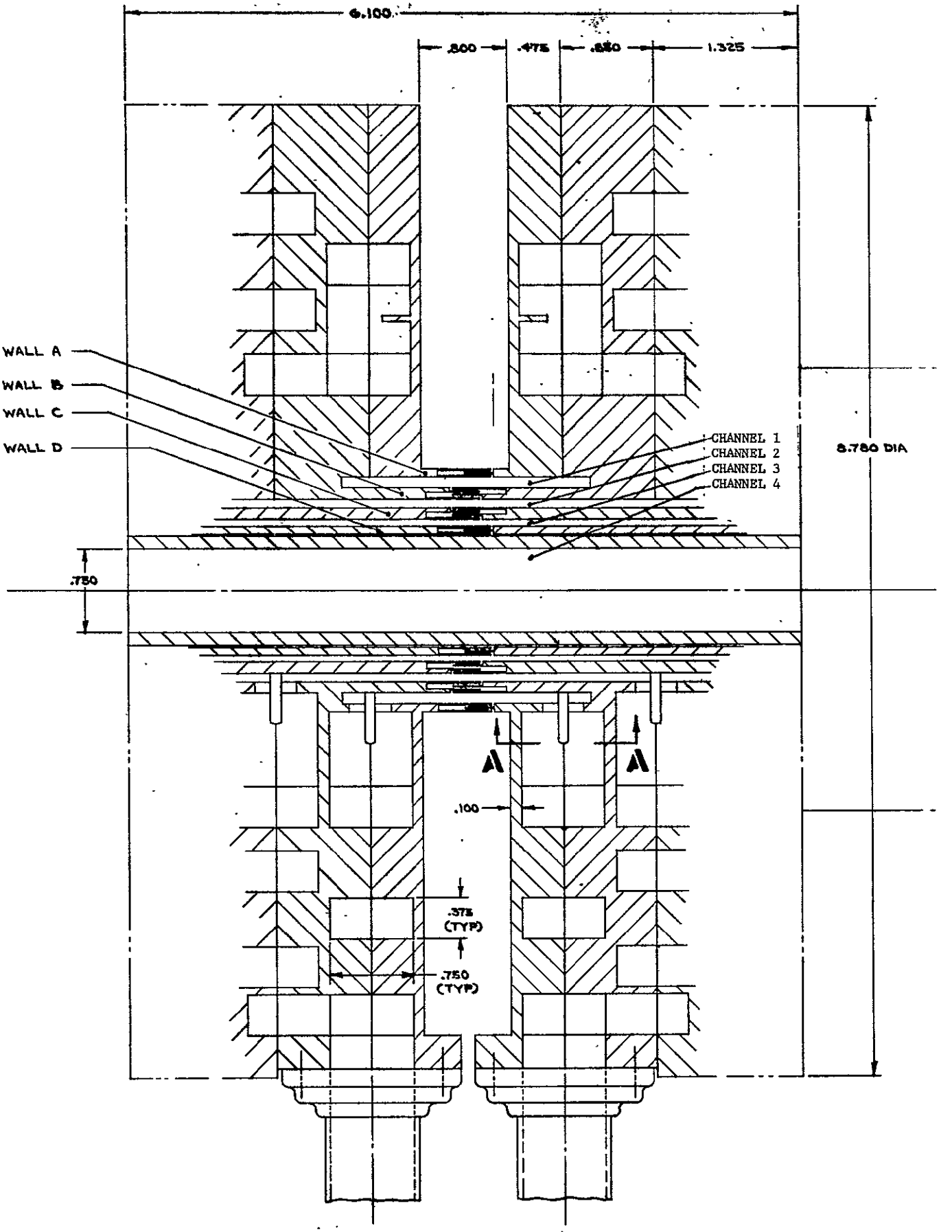

FIGURE 3-43. DETAIL OF WAVEGUIDE SECTIONS, 4-CHANNEL ROTARY JOINT

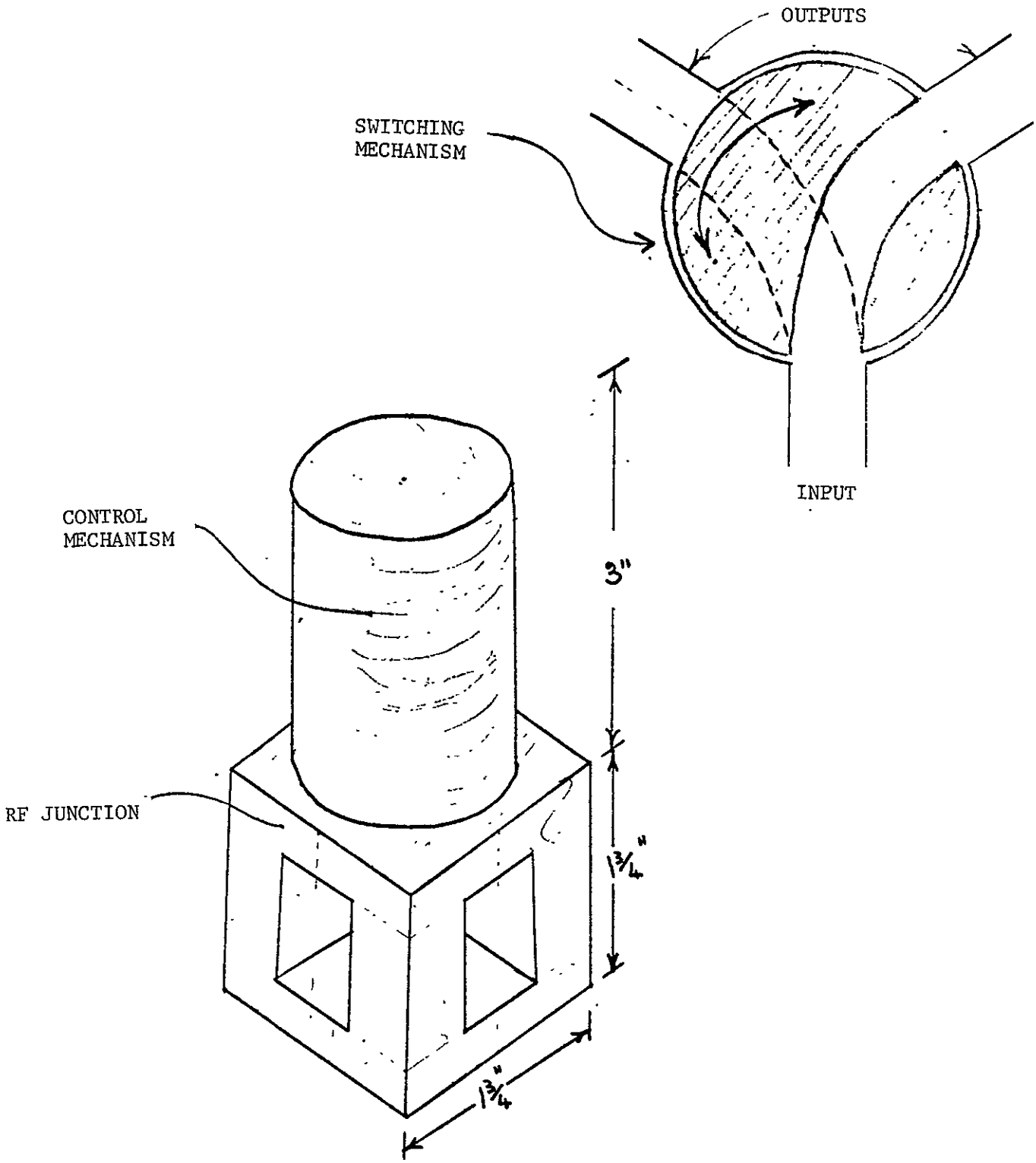

FIGURE 3-44 CHANNEL-SELECT SWITCH

A state-of-the-art review indicated that such devices are capable of handling 1 KW CW power levels at frequencies in the region of 12 GHz, while introducing an insertion loss of only 0.05 dB into the system. In addition, channel isolations of greater than 40 dB may be achieved. From this, it is evident that an electromechanical switch may be obtained whose RF performance is compatible with system requirements.

3.4.2.3 Power Dividers/Combiners

The power splitting/combining operations are performed by short-slot hybrid junctions (Riblet 3 dB couplers). The design procedure for these components is well established and it is anticipated that, by using both inductive and capacitive tuning, equal power division to within $\pm$ 0.2 dB with an isolation of approximately 30 dB can be maintained across the required frequency band. An insertion loss of less than 0.2 dB should also be achieved.

Due to the high power requirements of the system, it may be necessary to employ "rounded" tuning elements. The proposed configuration is therefore as shown in Figure 3-45.

3.4.2.4 Filters

The use of diplexers (i.e. band-pass filters) involves placing inductive posts or irises within the main waveguide transmission lines. This leads to high field concentrations within those areas and thereby limits the power-handling ability of the system.

For this reason, it was decided to base the RF subsystem on band-stop filters of the type shown in Figure 3-46. A preliminary design analysis was performed from which it was concluded that the system requirements could be adequately met by employing a 7-element Tchebyscheff device.

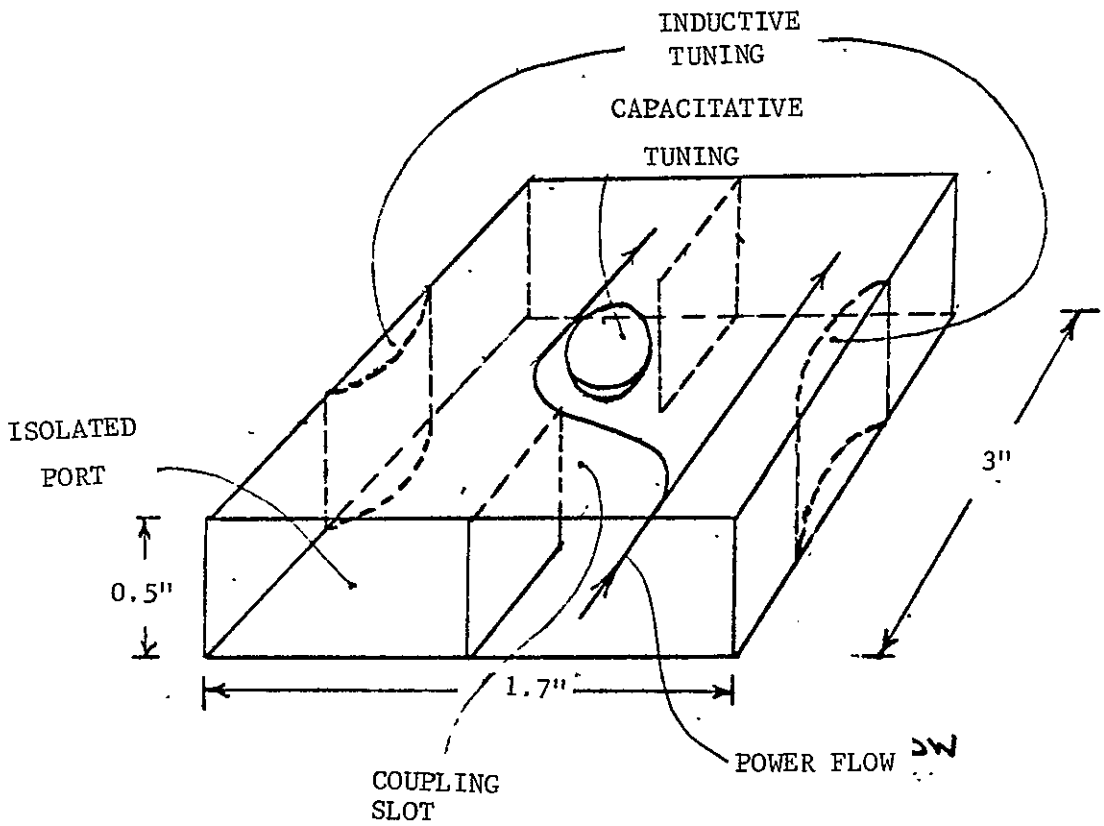

FIGURE 3-45 POWER DIVIDER

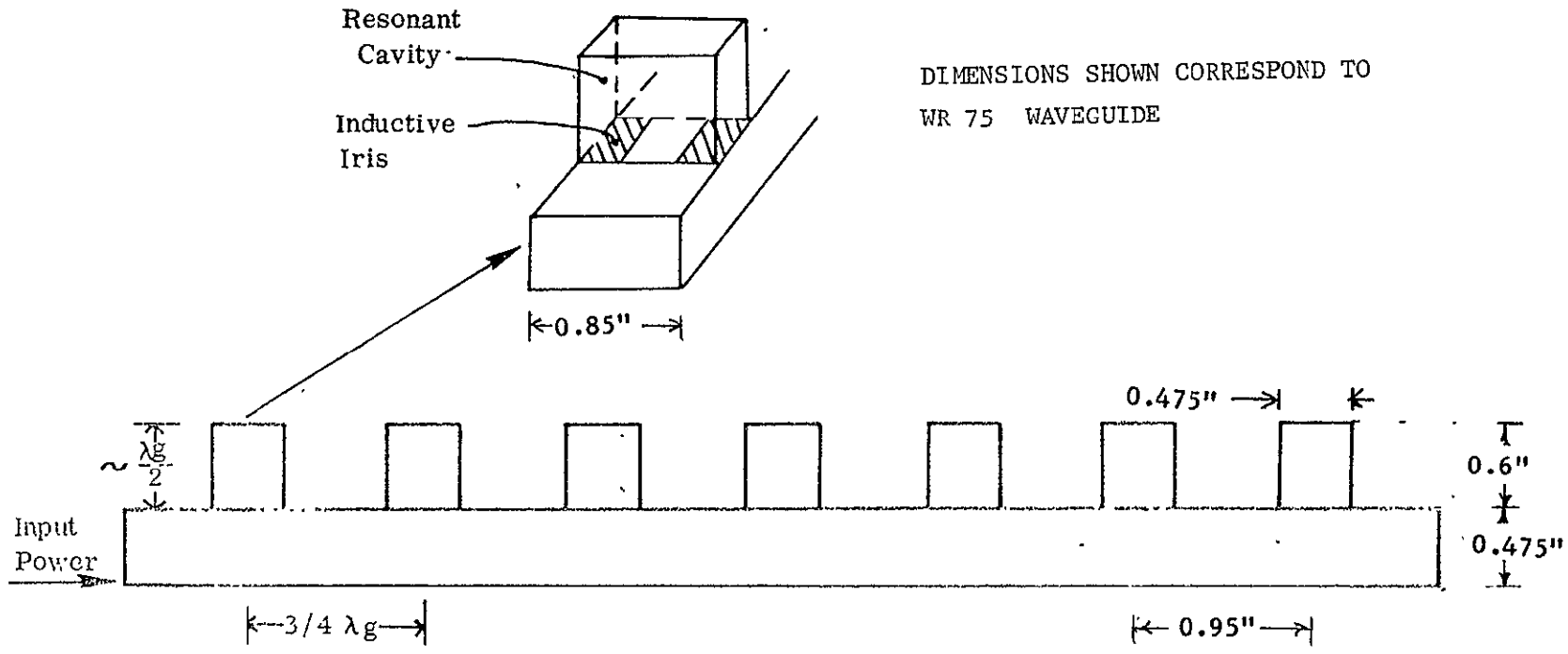

FIGURE 3-46 BAND-STOP FILTER DESIGN

A specimen filter with its stop-band centered on 12.2 GHz was then designed and its theoretical performance curves generated by means of a computational process. These curves are shown in Figures 3-47 and 3-48.

From Figure 3-47, it is seen that the required isolation characteristics can be achieved. It is also seen, however, that both the reflected wave for frequencies within the stop-band and the transmitted wave for frequencies more than 75 MHz outside it are attenuated by approximately 0.25 dB. Hence, each filter will contribute an insertion loss of this magnitude towards both of the channels that it handles.

The curve of Figure 3-48 plots the phase angle of the reflected wave as a function of frequency. From this, it is seen that the filter response complies with the requirements for phase linearity over a channel width.

3.4.2.5 Rotary Joints (Limited Motion)

In the candidate spacecraft configuration, rotary joints are required to circumvent the gimbal axes which control the pitch and roll motions of the despun antenna platform. A rotary joint is also required for switching the position of Beam 4.

In each case, however, the motion is limited to a few degrees and can, therefore, be readily achieved by means of flexible waveguide sections.

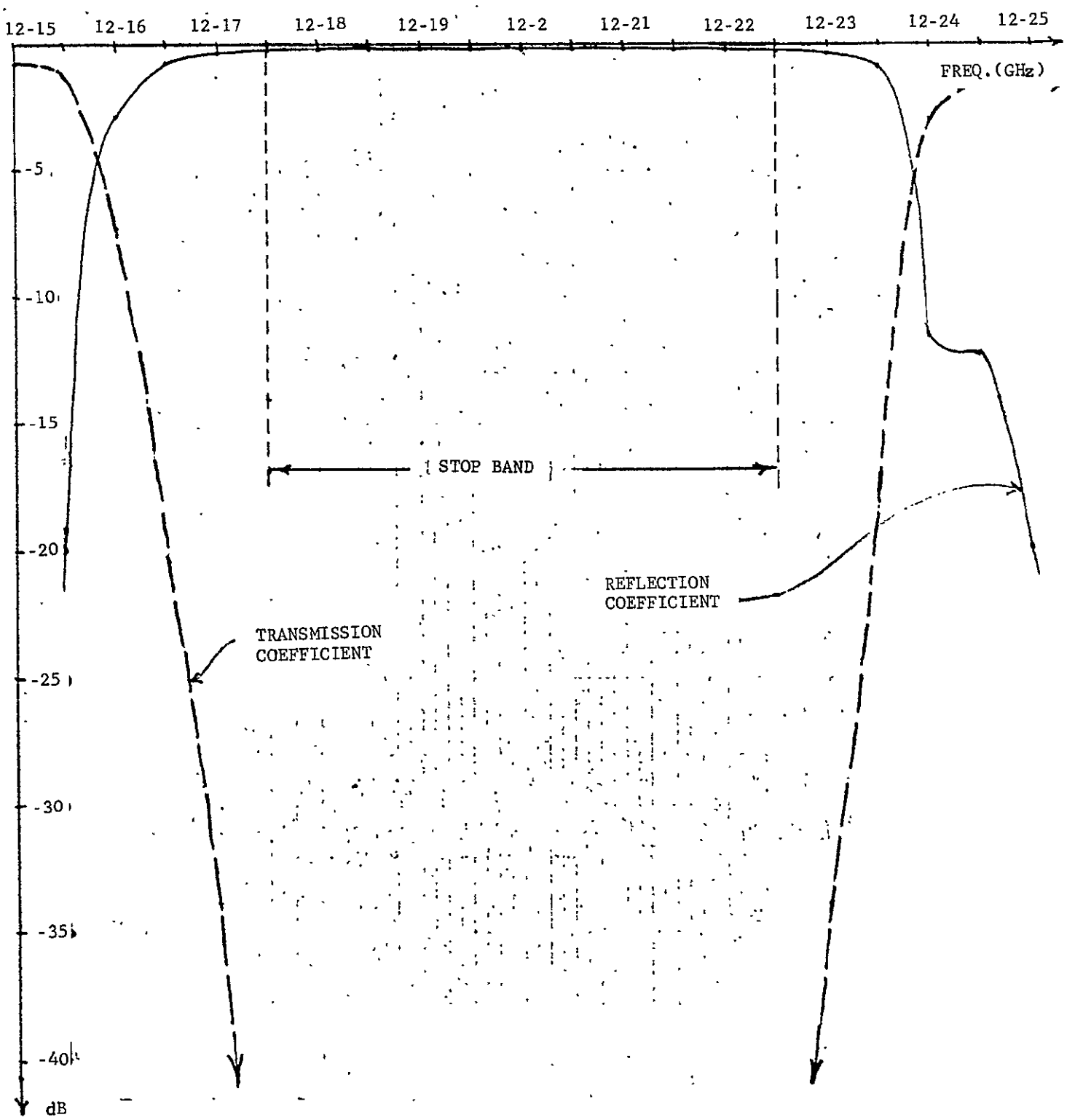

FIGURE 3-47 REFLECTION AND TRANSMISSION COEFFICIENTS FOR 7-ELEMENT BAND STOP FILTER

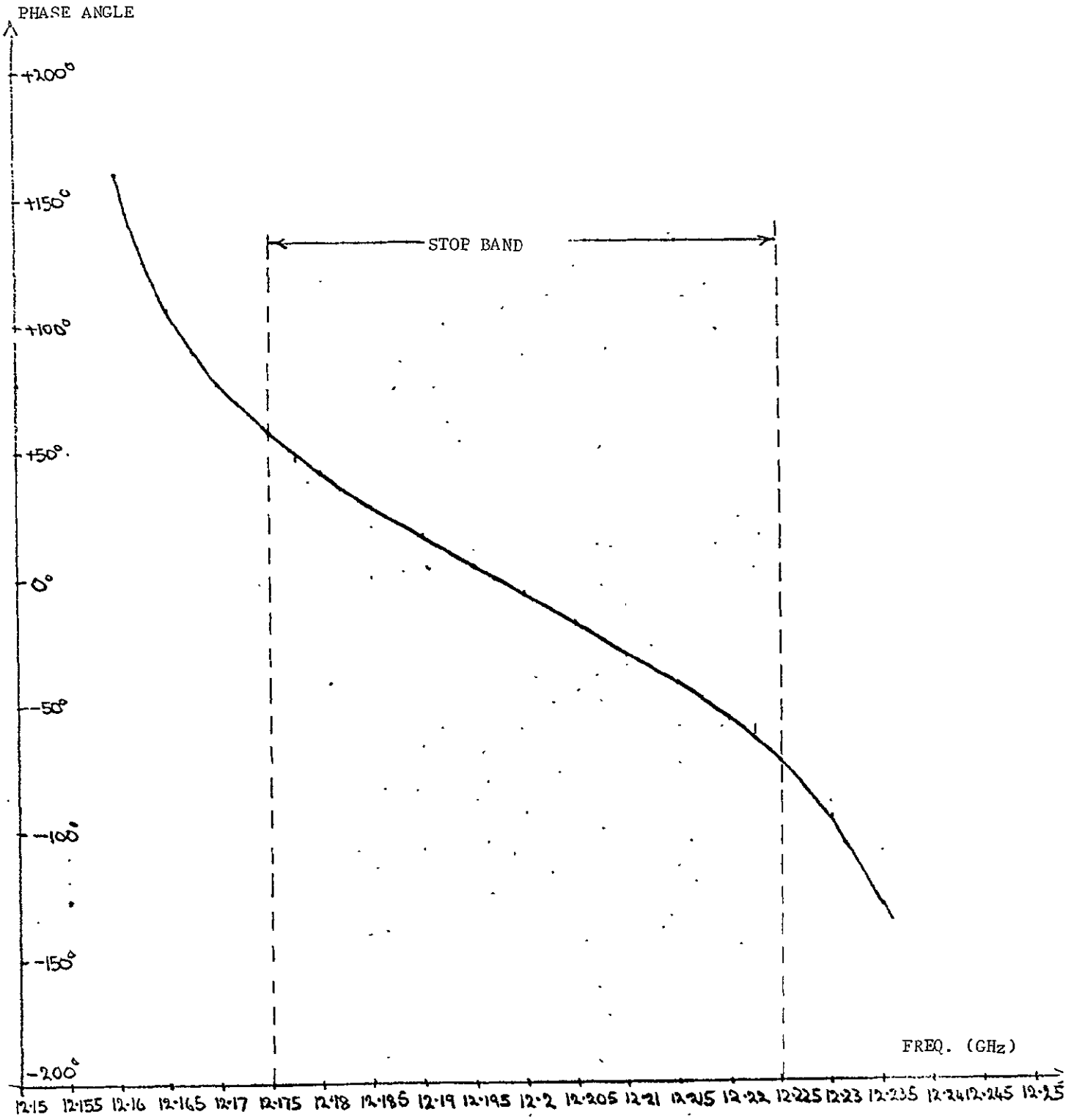

FIGURE 3-48 PHASE ANGLE OF REFLECTION COEFFICIENT OF BAND STOP FILTERS

3.4.3 Analysis of Integrated RF Subsystem

The main objective here was to define the power-handling capabilities of the integrated system. The bulk of the analysis was therefore devoted to investigating the problems associated with:

(a) High-power breakdown, and

(b) The effects of RF power dissipation within the structure.

3.4.3.1 High-Power Breakdown

When operating in a space environment, the system will be exposed to the following breakdown mechanisms:

(a) Multipaction

(b) Ionization in regions of localized gas entrapment

For both of these, the critical area is the coaxial waveguide choke sections of the rotary joint. Extensive calculations were therefore performed to determine the power levels required to initiate a breakdown in this area.

3.4.3.1.1 Analysis of Multipactor Breakdown*

General Description of Multipacting - Multipactor breakdown is a buildup of electrons near an electrode, in resonance with the RF electric field. For planar, parallel electrodes, separated by a gap, d, the time for electrons to cross the gap is an odd number of half-cycles of the radio frequency, f. The primary electrons must strike the electrode with sufficient energy to emit more than one secondary electron (on average). The secondary electrons then enter the discharge and maintain it. Present multipacting theories satisfactorily explain most of the observed experimental phenomena. The modes are described by an integer p = 0, 1, 2, etc., where (2p+1) is the number of half-cycles to cross the electrode gap.

Other important parameters for multipacting are: K^2, the ratio of primary electron energy to secondary electron energy; γ, the secondary emission coefficient, which is a function of primary electron energy; Φ, the starting phase of the electrons with respect to the RF electric field; and U, the primary electron threshold energy at which $\gamma = 1$. Figure 3-49 illustrates multipactor breakdown regions for the first three modes, assuming U = 50eV, K=3, Φ = -58.

The secondary emission coefficient also depends upon the electrode material, surface contaminants, and surface absorbed gases. Therefore, it can vary with time, and multipacting may start, quench itself, restart, and continue to flicker on and off. Alternately, it may not restart. Hence, the starting voltage for multipacting of surfaces is not necessarily the restriking voltage.

---

* Performed by SRI, Menlo Park, California

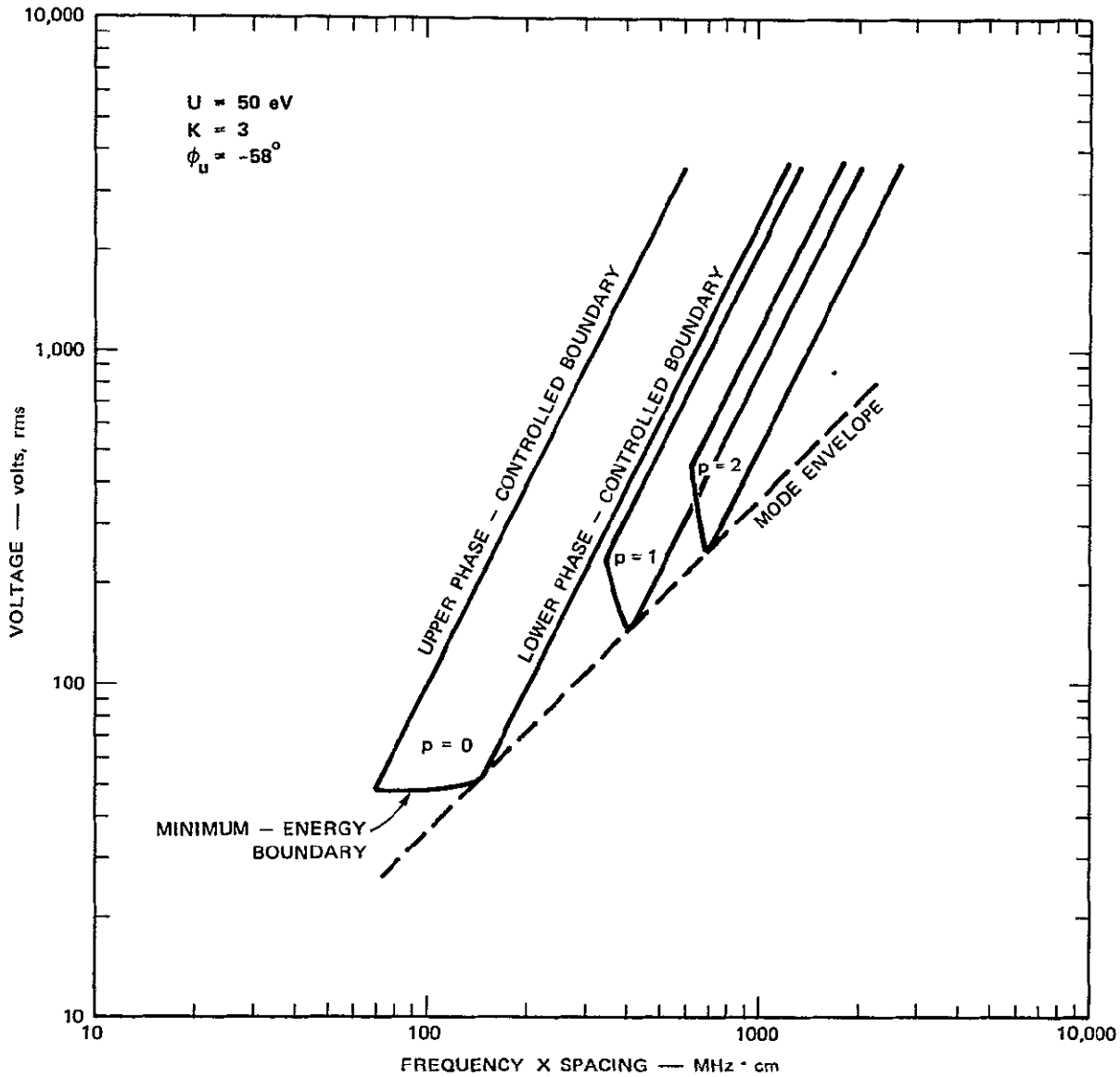

Figure 3-49 Multipactor Regions

Past experiments on multipacting of surfaces not previously outgassed by prior discharges have found that higher order mode breakdown tends to occur along a line parallel to and above the mode envelope, rather than showing dips and rises characteristic of the individual modes. After outgassing, the mode structure reappears, and U evidently increases.

Band and Channel Assignments - The four channels of the rotary joint are as follows:

I - Outermost coaxial channel, O.D.2·196 in, I.D.2·056in.

II - Central coaxial channel, O.D.1·652 in, I.D.1·488 in.

III - Innermost coaxial channel, O.D.1·288 in, I.D. 1·160 in.

IV - Rectangular waveguide channel, 0·375 in. by 0·750 in.

The four frequency bands, each 50 MHz wide, have center frequencies as follows:

1 - 12.050 GHz

2 - 12.150 GHz

3 - 12.250 GHz

4 - 12.350 GHz

There is an optimum assignment of frequency bands among the channels which minimizes multimoding in the coaxial channels. The longest wavelength or lowest frequency (Band 1) is assigned to the channel with the greatest circumference (Channel I), etc. The optimum assignment is therefore, I-I, 2-II, 3-III, 4-IV. This assignment was the only one used here. The likelihood of multipactor breakdown can be minimized by assigning the highest frequency (Band 4) to the channel having the highest field strength (Channel IV), etc., provided all other circumstances are the same. This assignment is therefore, identical with the one used above.

Higher Order Modes and Resonance Analysis - From this analysis it was concluded that, although multimoding is possible and the coaxial channel lengths are nearly resonant for some modes, no strong resonance can be excited, due to cavity loading. All mode effects were therefore neglected in computing voltages and fields in the various channels.

Voltage and Field Calculations - In calculating the voltages and fields, it was assumed that there were no mismatches within the channels. The rotary joint design incorporates eight probes from waveguides into each end of a given coaxial channel. The channel is short-circuited one quarter wavelength beyond each probe. Impedances are well matched. The geometrical layout is such that regions of high reactive field immediately about the probes are unlikely to multipact.

Channel IV fields were computed from waveguide theory. All three coaxial channels have the same impedance (6.25 Ohms), and so have the same gap voltage (79.1V) for 1 KW power transfer. Average gap fields were computed as voltage divided by gap spacing. To estimate choke fields, it was first assumed that each choke corresponded to an open-circuited line of quarter wavelength. The line current was assumed to be distributed sinusoidally from the open end of the choke, as on an antenna. The surface charge along the choke and the electric field were then derived. To zeroth order, the choke field at the open end is identical to the corresponding channel field. There are two minor corrections, one for a series expansion of the channel impedance, and one for a change in surface current density due to different diameters of choke and channel. These corrections lead to a field reduction for the outer diameter choke, and a field increase for the inner diameter choke, both by nearly the same amount.

Multipactor Calculations - Using existing theory, minimum voltage levels necessary to initiate multipacting between parallel plate electrodes can be predicted. The results also nearly hold for coaxial lines with outer/inner diameter ratios of 2.3, and are even more exact for smaller ratio such as the 1.11 used here

The aluminum used for the construction of the rotary joint quickly forms an A_2O_3 surface coating.* The value of U commonly quoted for this oxide is 20eV. A value of $k = 3$ is used, which is about the minimum value observed. With these two values, the mode envelope line is given by $V = 0.2555$ fd volts rms., where fd is the frequency-gap spacing product in MHz-cm. This is taken to be the minimum voltage required to initiate multipacting, but it is quite conservative, as the experimentally observed mode line is $V = 0.350$ fd for the 1/2-cycle mode, and $V = 0.402$ fd for higher order modes on gassy surfaces. Using this last value, a probable voltage required to initiate multipacting is obtained. These voltages are independent of mode number.

Within an individual mode, multipacting can begin at a higher voltage than on the mode line. The lower phase-controlled boundary of an individual mode depends only on K, and K=3 was used to determine that boundary.

Based on the initial probable voltage to initiate multipacting, Channel IV, the rectangular waveguide, had the lowest power rating, provided multipacting occurred in the p=42 mode. Multipacting has seldom been observed in modes higher than p=3. Usually electrons diffuse from the multipacting region so

* The aluminum is assumed un-anodized. Anodization would likely increase U above that observed for commercial aluminum.

rapidly that high order modes cannot be sustained, and multipacting must then take place in a lower order mode at a voltage well above the mode envelope voltage. The multipactor-initiate voltage then falls on the lower phase-controlled boundary.

Accordingly, a new probable starting voltage for the waveguide was calculated, by requiring the generation of one new secondary electron before the average secondary electron diffused to the waveguide sidewall. It was assumed that the secondary electrons had 5.55 eV energy, and that $\gamma = 1.27$, which should be characteristic of 50eV primary electrons on Ae_2O_3. The values have much uncertainty; however, the value of p was then limited to 22, and the waveguide probable breakdown power was raised about 8.5-fold.

With the waveguide calculation refined, it was found that the next three lowest power ratings were the inner choke, channel and outer choke for channel III, respectively. Of these, the two chokes would multipact in the p=1 or 3/2 mode, and so are less subject to diffusion effects, even though the high field region is at the choke end where the electrons can diffuse away. An incomplete analysis shows that gap electrons will raise the breakdown power only slightly, by shifting the breakdown region about one gap thickness inward from the choke edge. A fuller analysis is not warranted because Channel III itself can probably multipact at a slightly higher voltage as its mode number is only p=7.

Conclusions on Multipactor Breakdown - Table 3-9 lists the various channels and critical regions considered, with an estimate of their minimum and probable breakdown powers. Channel III is most likely to begin multipacting, with the inner choke the most critical location, followed by the channel itself. The minimum breakdown power is

TABLE 3-9

ROTARY JOINT POWER TO INITIATE MULTIPACTING

Location	*Electric Field V/cm rms	*Gap Voltage V rms	Gap Spacing cm	Frequency x Spacing MHx-cm	Minimum Breakdown Voltage V rms	Probable Breakdown Voltage V rms	Minimum Breakdown Power kW	Probable Breakdown Power kW
Channel I	306	79.1	.259	3120	795	1260	101	251
II	381	79.1	.208	2520	645	1020	65.2	200
III	489	79.1	.1625	1990	508	802	41.3	103
IV	733	697.0	.952	11700	3000	8800	18.6	159
Outer Choke I	284	14.4	.0508	611	156	246	118.	291
II	353	18.0	.0508	616	157	248	76.2	190
III	448	22.8	.0508	621	159	250	48.2	120
Inner Choke I	328	16.7	.0508	611	156	246	87.0	217
II	424	21.0	.0508	616	157	248	56.0	140
III	530	26.9	.0508	621	159	250	34.7	86.2
Coaxial Probe I	286	77	.539	3240	830	1300	116	287
II	286	77	.539	3270	836	1315	118	293
III	286	77	.539	3300	843	1330	120	298
Aperture into Channel I	348	90.3	.259	3120	795	1260	77.2	194
II	389	80.9	.208	2520	645	1020	63.3	158
III	441	71.5	.1625	1990	508	802	50.2	126

*Based on 1-kW power transfer per channel.

NOTE: Band-channel assignments are 1-I, 2-II, 3-III, 4-IV.

based on empirical data which covers the frequency-spacing range appropriate to the Channel III chokes, and so should be quite reliable. Diffusion effects are expected to slightly increase the choke breakdown power. Except for the chokes, which can multipact in the 3/2 mode, the lowest mode number for multipacting is p=7, or the 15/2 mode.

Multipacting probably limits the power-handling capability of the rotary joint not by direct power absorption, but by its consequences: Surface absorbed gas is released by bombardment of multipacting electrons, and thereby increases the local gas density. The combination of RF electric field and high local gas density can result in a gas discharge and/or an RF arc. Both of these can be physically destructive to the rotary joint, by overheating and structural failure, or by providing conducting deposits, sharp tips, or other electrical disturbances to the RF circuit. Naturally, high reflected RF powers may damage the RF power source, unless it is protected by limiting devices.

Although the lowest predicted probable power-handling capacity of any part of the rotary joint is 86 KW, it will be desirable to check its performance at lower power levels to ensure that the local gas pressure is not too high. This might occur due to heating of electrodes, or to slower-than-anticipated outgassing.

NOTE:

The results of the above analysis may be used directly to confirm that the band-stop filters do, in fact, have the required power-handling ability:

In this case, the critical region is the resonant cavity nearest the input to the device. However, from Table 3-9 it is seen that the probable breakdown voltage across the cavity is 8800 V rms, which corresponds to an input power of 57 KW CW to the filter. Hence, it is evident that the performance of these components is compatible with the system design goal of 1 KW CW per channel.

Analysis of Ionization Breakdown - The occurrence of ionization breakdowns in regions of localized gas entrapment is a potential hazard for any RF system operating in a space environment. In most cases, the increase in gas density can be mainly attributed to out-gassing of the metal surfaces of the RF components.

For the system being considered, the critical region in this respect was identified as the coaxial choke sections of the rotary joint. This region has a relatively high surface area-to-volume ratio and it also serves as a conductance path for the particles outgassing from the very thin annular volume adjacent to the rotary joints innermost cylinder. The rather high outgassing rate from the waveguide's aluminum surfaces, about 10^{-6} torr-liters sec^{-1} cm^{-2}, compared to about 10^{-7} torr-liters sec^{-1} cm^{-2}, for stainless steel, is of particular concern.

A detailed analysis was therefore performed with a view to obtaining a quantitative evaluation of the outgassing phenomena associated with this configuration. This analysis is presented in the following section.

Mathematical Treatment of Outgassing Phenomenon - The following problem was solved: given an outgassing rate for clean aluminum previously exposed to the atmosphere determine the maximum number density as a function of time in the region enclosed by the waveguide choke section; assume a reasonable initial pressure distribution.

Let $n(x,t)$ be a function which expresses the number of gas particles per unit length in a direction x which is parallel to the walls in the enclosed choke section and in a plane containing the central axis of the rotary joint (see Figure 3-50). Also, let $f(x)$ be the rate of surface outgassing per unit length along x. This one dimensional representation assumes that:

1. The radii of curvature of all surfaces is much greater than any of the gap distances.
2. There are no gradients in the number density or the outgassing rate in any plane perpendicular to the direction of x.

It is assumed that the following partial differencial equation applies:

$$\frac{\partial^2 n(x,t)}{\partial x^2} - a^2 \frac{\partial n(x,t)}{\partial t} = -a^2 f(x)$$

The boundary conditions are (see Figure 4-10):

$$n(o,t) = 0$$

$$\left.\frac{\partial n}{\partial x}\right|_{x = \frac{L}{2}} = 0 .$$

These boundary conditions are equivalent to $n(o,t) = 0 = n_x(\frac{L}{2},t)$ if $n(x,t)$ is symmetric about $x = \frac{L}{2}$. $n(x,o)$ is known and assumed equal to $n_o \sin(\frac{x\pi}{L})$. Further,

$$a^2 = \frac{2}{\overline{\ell^2}\, R}$$

where $\sqrt{\overline{\ell^2}}$ is the r.m.s. distance traveled by the gas particles along x between collisions (free molecule flow is assumed), and R is the mean collision frequency assumed that $f(x)$ = constant = r particles sec^{-1} cm^{-1}.

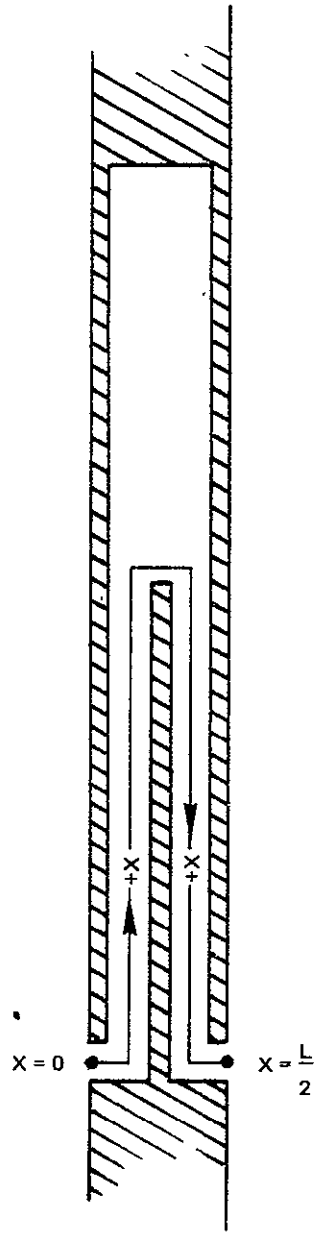

FIGURE 3-50 THE COORDINATE SYSTEM OF THE COAXIAL WAVEGUIDE CHOKE SECTION

The solution to the above partial differential equation can be obtained by standard Green's Function techniques; the solution is -

$$n(x,t) = \sum_{n=1}^{\infty} \frac{4a^2L^2r}{(2n-1)^3\pi^3}\left\{1-e^{-\frac{(2n-1)^2\pi^2 t}{L^2 a^2}}\right\} \sin\left\{\frac{(2n-1)\pi x}{L}\right\} + n_o \sin\left\{\frac{\pi r}{L}\right\} e^{-\frac{\pi^2 t}{L^2 a^2}}$$

This can be verified by direct substitution. (Note that

$$1 \doteq \frac{4}{\pi} \sum_{n=1}^{\infty} \frac{1}{(2n-1)} \sin\left\{\frac{(2n-1)\pi x}{L}\right\})$$

Using the following values of a, L, and r

$a^2 = 4.9\text{x}10^{-4}$ sec cm^{-2}

$R = 4.1\text{x}10^{-5}$ sec^{-1}

$\sqrt{\overline{\ell^2}} = 0.1$ cm

$L = 3.0$ cm

$r = 8.5\text{x}10^{13}$ particles sec^{-1} cm^{-1}

we obtain (using $\sum_{n=1}^{\infty} \frac{1}{(2n-1)^3} \doteq 1$

$$\lim_{t \to \infty} n\left(\frac{L}{2}, t\right) = 4.8 \times 10^{+10} \text{ particles cm}^{-1}$$

Since the minimum gap distance is 0.05 cm, the maximum number density is

$$\frac{4.8 \times 10^{10} \text{ particles cm}^{-1}}{(0.05 \text{ cm})\ (1 \text{ cm})} = 9.6 \times 10^{11} \text{ particles cm}^{-3}$$

and at 25° C this number density is equivalent to

$$(9.6\text{x}10^{11})\ (3.2\text{x}10^{16}\ \frac{\text{particles cm}^{-3}}{\text{torr}}) = 3\text{x}10^{-5} \text{ torr}$$

a. The Transformation of the Outgassing Volume

The outgassing volume is shown in Figure 3-50 the first step in the transformation and simplification of the outgassing volume is shown in Figure 3-51. Two, rather than one, enlargements are shown because in order to transform the boundary condition from $n(o,t) - 0 - n_x (\frac{L}{2}, t)$ into the more manageable boundary conditions $n(o,t) = 0 = n(L,t)$, it is necessary to ensure symmetry about $x = \frac{L}{2}$. These enlargements do not contribute significantly to the conductance along x but their surface area does contribute to the outgassing; this outgassing is assumed to be "smeared out" uniformly over x as stated in discussion of the outgassing rate.

b. The Outgassing Rate

The outgassing rate was assumed to be 10^{-6} torr-liters (at 25°C) per cm^2 per sec*. The surface area of the region of interest is 4.2 cm^2 per unit length perpendicular to the cross section shown in Figure 3-50 (including the enlargements shown in Figure 3-51; therefore, number of particles per unit length coming off the walls is -

$$3.25 \times 10^{+13} \text{ particles cm}^{-2} \text{ sec}^{-1} \times 4.2 \text{ cm}^2 = 1.36 \times 10^{+14} \text{ particles sec}^{-1}$$

Since the length of the region of interest is 1.5 cm:-

$$r = \frac{1.36 \times 10^{14} \text{ particles sec}^{-1}}{L/2} = 9.1 \times 10^{13} \text{ particles sec}^{-1} \text{ cm}^{-1}$$

c. The Relation $a^2 = \frac{2}{\ell^2 R}$

This relation can be derived from the a solution to the one dimensional random walk problem. The details will not be given here (see Kennard, Kinetic

* C. B. Barnes, "Cryogenic Vacuum and Space Simulation", CVI Corporation, Columbus, Ohio, May 1967, Figure 33.

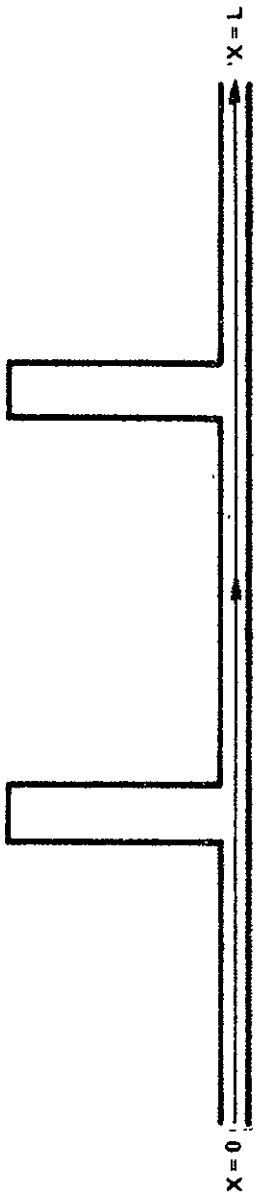

FIGURE 3-51 TRANSFORMED OUTGASSING VOLUME

Theory of Gases, beginning on Page 268). The value of $\ell_{r.m.s.}$ (the r. m.s. distance traveled by the particles along x between collisions) was estimated, assuming a cosing spacial remission distribution; the result was $\ell_{r.m.s.} = 2d$ where d is the gap distance. R (the mean collision frequency) was determined from $R = \frac{\bar{c}}{\bar{\ell}}$, where $\bar{c}$ is the mean speed of the gas particles at 25° C and $\bar{\ell}$ is the mean distance traveled between collision (not necessarily along x); $\bar{\ell}$ is equal to 2d. The particles' residence time on the walls between collisions is negligible; it is of the order of 5×10^{-12} sec *

d. The Boundary Conditions

At x = 0 in Figure 3-50, the conductance of all leakage paths increases several decades; the boundary condition at x = 0 can therefore be reasonably approximated by n (o,t) = 0. At $x = \frac{L}{2}$ in Figure 3-50, the conductance of the leakage path decreases, and there is some incoming particle flux at this point. This incoming particle flux comes from the outgassing of the inner shaft of the rotary joint. Under these circumstances, the boundary condition $n_x(L/2,t) = 0$ seems to be the most appropriate approximation.

e. The Time Constant

The time constant of the system is $-\frac{La}{\pi}^2 = 0.45$ milliseconds. Therefore, any reasonable initial number density decreases to a negligible value in an interval that is very short compared to the operational time scale.

---

* "The Dynamical Character of Adsorption", J. H. deBoar, The Clarendon Press, Oxford, 1953, pp 30, 35.

Conclusions of Ionization Breakdown - The preceding analysis shows that the venting path formed by a single rotary joint choke section has a time constant of approximately 0.45 milliseconds. It also shows that the maximum pressure in this region due to outgassing from a clean aluminum structure is 3×10^{-5} torr.

Since both of these parameters are proportional to (path length)^2, the corresponding figures for the complete rotary joint assembly (in which the venting path is through four such sections) are $(4)^2 \times 0.45 = 7.2$ milliseconds and $(4)^2 \times 3 \times 10^{-5} = 0.48 \times 10^{-3}$ torr.

Thus, if a rotary joint which has been thoroughly cleansed is placed in a space environment, the initial venting process will cause the pressure at the innermost choke section to drop within a few seconds to a level which is just below the ionization breakdown limit of 10^{-3} torr. (At 10^{-3} torr, the mean free path of an electron is commensurate with the inside dimensions of the coaxial waveguide channels. Hence, at pressures below this level, the avalanche process required to initiate an ionization breakdown cannot occur.) The pressure then falls off gradually from this level as the outgassing rate decreases.

If the unit has not been thoroughly cleansed, it is possible that the initial pressure due to outgassing will be above the critical level and hence there will be a period following launch (typically 10-20 hours) during which an ionization breakdown could occur.

It is therefore concluded that if such an occurrence is to be avoided, it will be necessary to -

(a) Specify a cleansing procedure which removes the metal surface impurities, and -

(b) Avoid switching on high RF powers in the early stages of the mission.

3.4.3.2 RF Power Dissipation

Estimation of RF Losses - The total RF losses were estimated by taking the mechanical layout and tracing the power flow through the system for each channel.

The worst case is depicted in Figure 3-52, which illustrates the path taken by the power in Channel 1 when it is switched into Beam 2. The insertion loss associated with each circuit element (including interconnecting waveguide runs) is shown, and adding these gives a figure of 1.55 dB. The value of 0.35 dB quoted for the rotary joint was arrived at in the following manner:

ITEM	INSERTION LOSS (dB)
Input Network	0.10
Rectangular-to-coaxial Waveguide Transition	0.05
Coaxial Waveguide	0.05
Coaxial-to-rectangular Waveguide Transition	0.05
Output Network	0.10
Total Insertion Loss	0.35

For a 1 KW input, this corresponds to a power dissipation of 300 watts and it therefore follows that there will be severe thermal control problems which must be overcome if the system is to operate successfully. These problems are discussed in the following section.

Effect of RF Power Dissipation on System Performance - A thermal analysis was performed which shows that, for an input of 1 KW CW per channel, the RF system has a steady-state operating temperature of 400-450°F. From this result, the dimensional changes and hence the performance degradation associated with the RF power dissipation were estimated. Two components were particularly vulnerable in this respect:

1. The band-stop filters
2. The coaxial choke sections of the rotary joint.

A first-order calculation showed that, in the case of the filters, the effect of the temperature variation would be to change the position of the stop-bands by approximately 20 MHz.

A similar calculation for the proposed rotary joint configuration revealed that dimensional changes of as much as 0.030 inch could occur in the region of the coaxial waveguide choke sections.

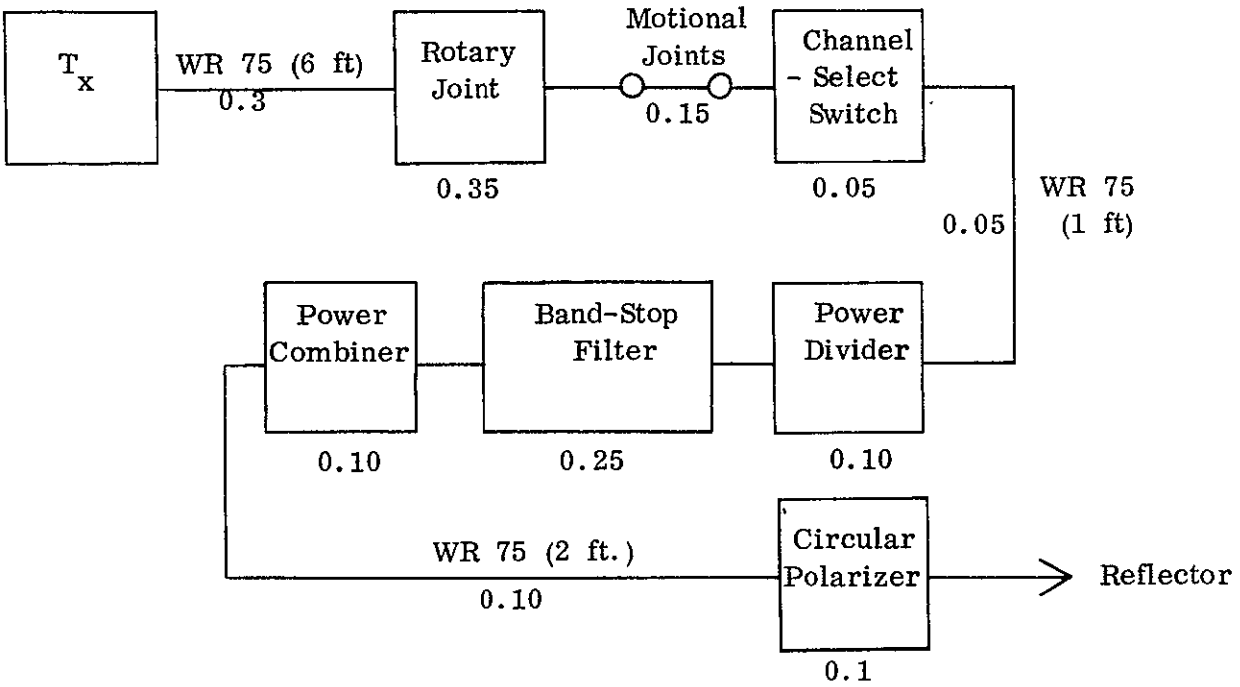

TOTAL LOSS = 1.55 dB

Figure 3-52 Worst-Case Insertion Loss for System Based on Aluminum WR75

Clearly, both of these effects are unacceptable to the system and it is therefore necessary to conclude that extensive thermal control mechanisms (e.g., external radiators) will be required if the design goals in terms of power-handling ability are to be realized.

Possible Techniques for Reducing RF Transmission Losses

RF transmission losses can be reduced (and hence the thermal control problem alleviated) by resorting to the following techniques:

1. Substitute WR-90 for WR-75 and fabricate, where possible, in OFHC copper instead of aluminum.
2. Use 0.9 inch (2.286 cm square waveguide for the 6-foot (1.8288 meter) runs from the transmitters to the rotary joint.

With these modifications, the attenuation constants become 2.96 and 1.65 dB/100 ft. (30.48 m) for the WR90 and 0.9-inch square waveguide respectively. The worst-case insertion loss is therefore reduced to 1.19 dB (see Figure 3-53). This corresponds to a power dissipation of 240 watts, which represents a substantial improvement on the original value of 300 watts.

3.5 RECOMMENDED DEVELOPMENT TEST PROGRAM

There are three areas which will require experimental investigation in order to verify the performance of the proposed RF system. These are:

a. Suppression of near-in side lobes of antenna radiation pattern.
b. Feasibility of the candidate design for the 12 GHz rotary joint.
c. Performance of the RF components (rotary joint in particular) at high power under environmental conditions.

The recommended test programs for each of these items are given in paragraphs 3.5.1 through 3.5.3.

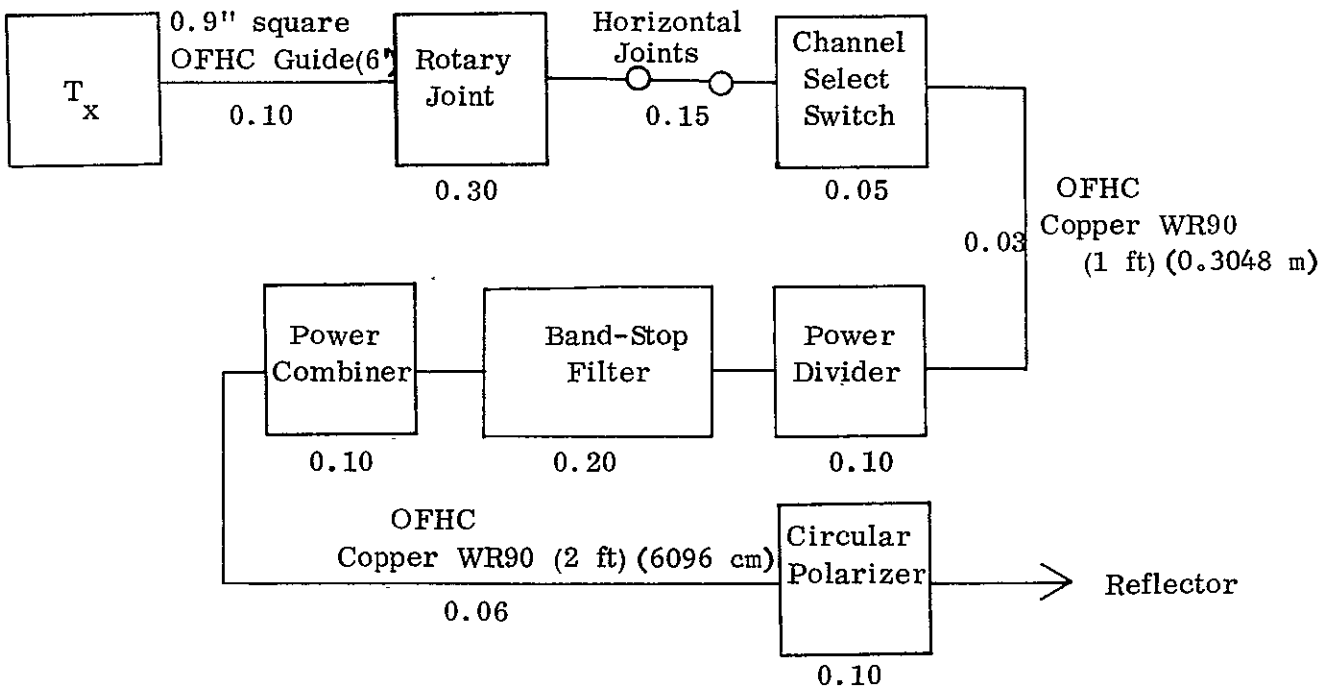

TOTAL LOSS = 1.19 dB

Figure 3-53 Worst-Case Insertion Loss for System Based on OFHC Copper WR90

3.5.1 Antenna Test Program

3.5.1.1 Objectives

The main purpose of this program should be to establish:

a. The extent to which the near-in side lobes of the antenna radiation can be suppressed by utilizing relatively simple aperture blockage compensation techniques in conjunction with a heavily-tapered aperture distribution.

b. The fraction of the input power which must be delivered to the blockage compensation element in order to achieve maximum suppression.

In addition to this work, a series of measurements should be carried out to evaluate the RF coupling between the high-power antennas and the interferometer elements of the direction-sensing system.

3.5.1.2 Test Plan

The antenna configuration, together with a block diagram of the required test set-up, is illustrated in Figure 3-54.

Since the blockage compensation technique, per se, does not depend on the use of circular polarization, the necessary tests could be carried out using linear polarization only. The principal stages of the program should, therefore, be as follows:

1. Procurement of main reflector

   This should be a precision dish having the required 28-inch (66.04 cm) diameter and f/d ratio (0.35).

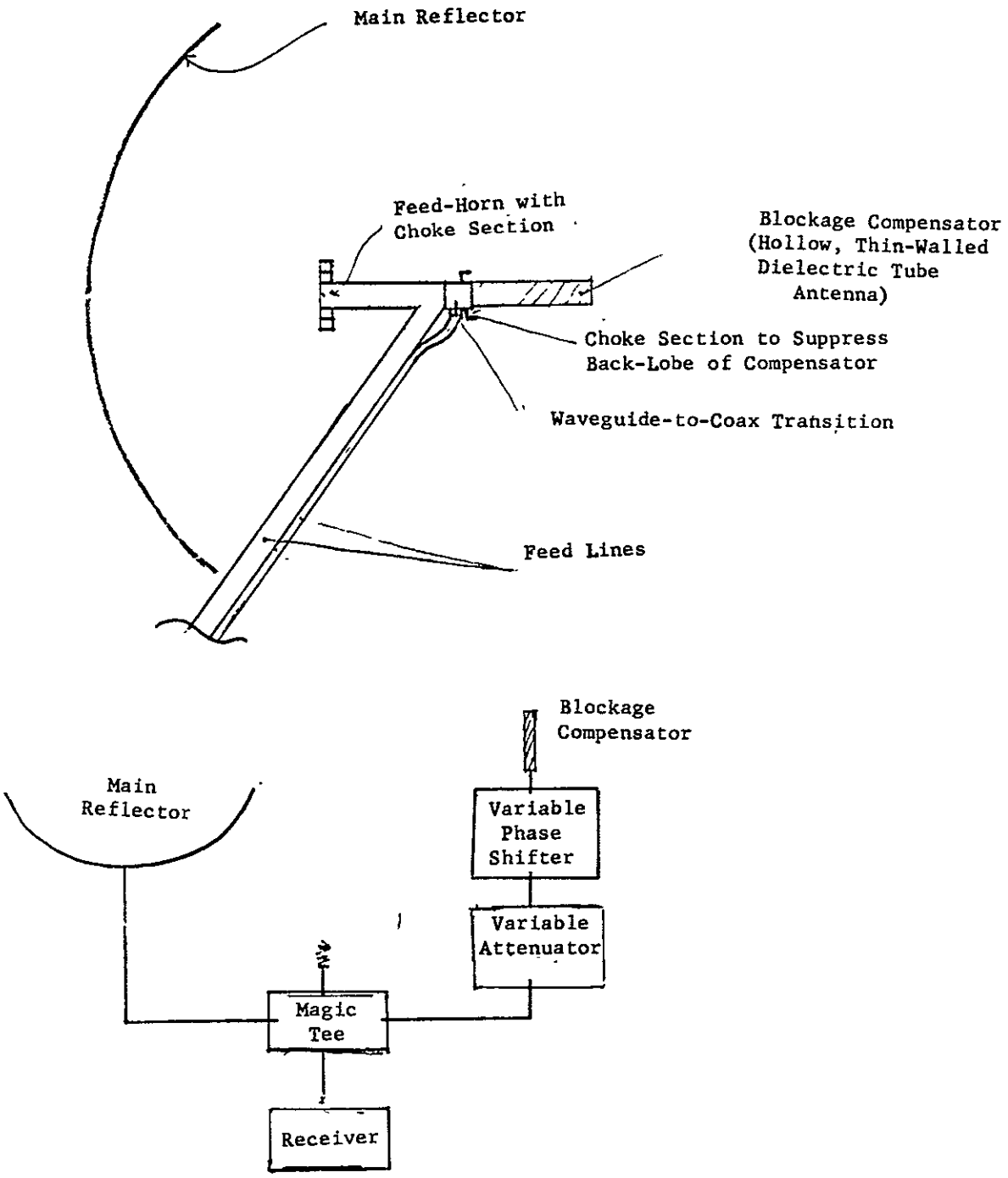

FIGURE 3-54 ANTENNA CONFIGURATION AND TEST EQUIPMENT FOR INVESTIGATION OF APERTURE BLOCKAGE COMPENSATION

2. Design, Fabrication and Testing of Prime Focus Feed-Horn

The horn dimensions needed to provide the required edge-directed aperture taper should be established experimentally.

Back-radiation from the horn could make a substantial contribution to the near-in sidelobe level of the secondary pattern. A double choke section of the type shown in Figure 3-54 should, therefore, be incorporated in the horn design so as to reduce this effect to an acceptable level.

3. Optimization of Prime Focus Reflector Antenna

The optimum feed position should be determined, after which measurement should be made of antenna gain, efficiency, beamwidth, near-in sidelobe level, back-to-front ratio and cross-polarization pattern.

4. Design, Fabrication and Testing of Dielectric Tube Antenna

As a first step in the development of this component, a suitable outside diameter should be chosen for the dielectric tube. Based on this dimension, a transition should be designed so that the antenna could be fed from coaxial cable. The dielectric tube parameters (i.e., length and wall thickness) so as to find the configuration which yields the optimum performance in terms of beamwidth, gain and sidelobe level. The final design should be modified by the addition of a choke section as shown in Figure 3-54. The function of this choke would be to suppress the backlobe of the tube pattern and hence minimize

the mutual coupling between the blockage compensator and the main antenna.

5. Optimization of Prime Focus Reflector Using Aperture Blockage Compensation

The blockage compensator should be positioned behind the prime focus feed-horn, as shown in Figure 3-54, and the phase and amplitude of the power delivered to it adjusted to achieve maximum suppression of the near-in sidelobes of the secondary pattern. The overall performance figures for this optimized configuration should then be obtained and compared with those for the basic prime focus reflector. In this way, the advantages to be gained by utilizing aperture blockage compensation for this project could be fully assessed.

6. Measurement of RF Coupling Between High Power Antennas and Interferometer Elements

The RF coupling between a single high-power antenna and the adjacent interferometer element should be measured using the test set-up shown in Figure 3-55. The coupled power could prove to be above an acceptable level when the interferometer element is in the position currently allocated to it. Should this be the case, a series of measurements should be performed to investigate the effectiveness of reducing the coupling by displacing the element, either laterally or axially, from its original position.

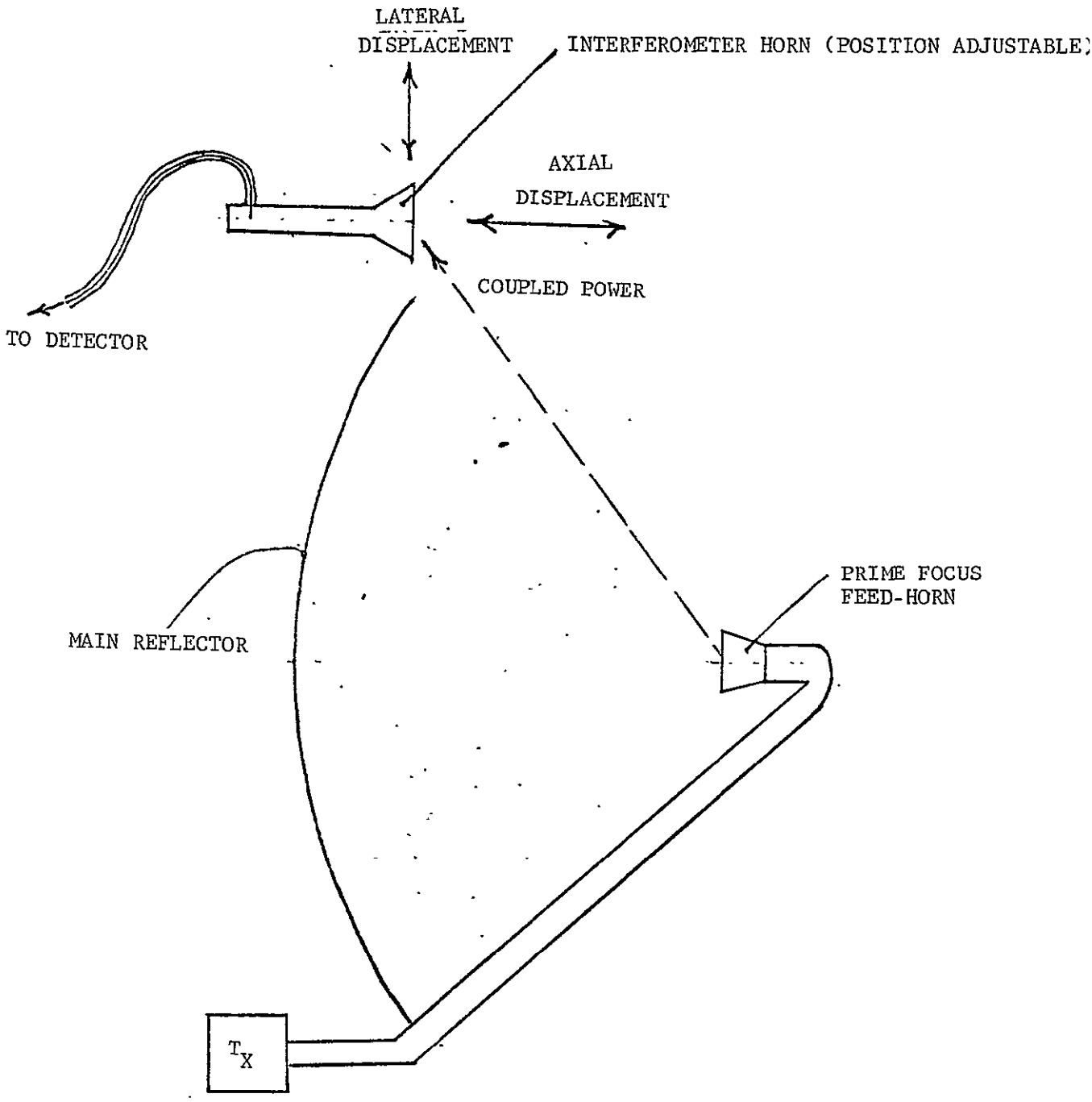

FIGURE 3-55 CONFIGURATION FOR INVESTIGATING RF COUPLING BETWEEN HIGH-POWER ANTENNAS AND INTERFEROMETER ELEMENTS

3.5.1.3 Expected Results

It is anticipated that the proposed antenna configuration near-in sidelobe level of approximately -30 dB. The power which must be delivered to the blockage compensation element to achieve this should represent a drop-in antenna efficiency of less than 3 percent.

3.5.2 Rotary Joint Feasibility Test Program

3.5.2.1 Objectives

This program should be directed toward demonstrating the feasibility of the candidate 12 GHz rotary joint. A complete single-channel device should therefore be fabricated and detailed measurements performed to evaluate its RF transmission properties.

3.5.2.2 Test Plan

The test plan should be divided into the following sections:

1. Design, Fabrication and Testing of Power Dividers for Feed Network

   The power dividers take the form of E-plane T-junctions and the object of this part of the program should be to develop a junction of this type which provides equal power-split with low input VSWR and insertion loss at the design frequency.

2. Design, Fabrication and Testing of Waveguide Bends for Feed Network

   The waveguide bends required for the interconnection of the E-plane power dividers should be determined from the final layout

of the feed network. These bends should then be designed with a view to minimizing their VSWR and the insertion loss.

3. Fabrication and Testing of Complete Feed Network

The design information gained in Sections (1) and (2) should be used as a basis for the fabrication of a complete feed network.

This network should be tested for insertion loss, input VSWR and equality of power split. The relative phase at each of the eight output ports should also be measured.

4. Design, Fabrication and Testing of Rectangular-to-Coaxial Waveguide Transitions

The special test equipment required to carry out this part of the program (such as coaxial waveguide slotted line) should first of all be designed and fabricated.

Measurements should then be carried out on a series of experimental transitions to establish the configuration which provides the best performance in terms of VSWR and insertion loss.

5. Design, Fabrication of Coaxial Waveguide Choke Section

A coaxial choke section which would provide a channel isolation of better than 40 db should be designed and fabricated.

6. Fabrication and Testing of Complete Single Channel Joint

A prototype single-channel unit should be designed and fabricated using the data gained in the previous segments of the

test program. An extensive series of VSWR and insertion loss measurements should then be conducted to evaluate the RF transmission properties of this device as a function of rotational angle.

A prime objective of the tests should be to detect any performance degradation caused by the generation of higher-order modes or spurious resonances within the coaxial waveguide section.

In the final part of the program, any modifications necessitated by these, or other, effects should be carried out.

3.5.3 Environmental Test Program

3.5.3.1 Objectives

The theoretical results of the high-power breakdown analysis (paragraph 3.4.3) indicate that the proposed rotary joint configuration will be capable of handling 1 KW CW power levels while operating in a space environment.

This test program should therefore be directed toward verifying these results experimentally and defining the thermal control mechanisms required to keep the operating temperature within acceptable limits.

3.5.3.2 Test Set-Up

RF Equipment - The RF test set-up is outlined diagrammatically in Figure 3-56. As shown, a pulsed source should be used. The peak power of this device at the design frequency should be in excess of 1 KW and the pulse should be of sufficient length

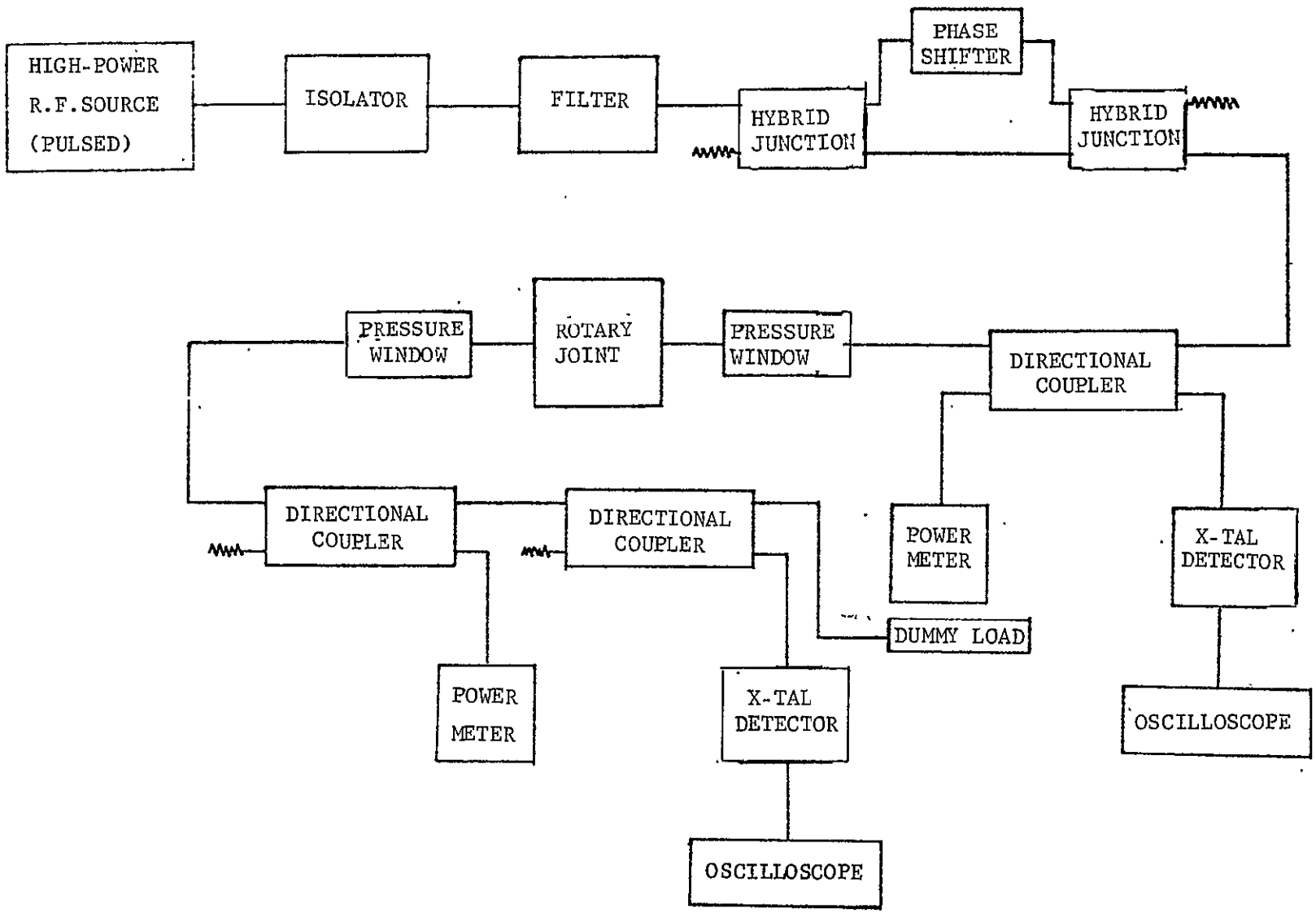

FIGURE 3-56 RF TEST SET-UP

to permit the build-up of any multipactor or ionization processes which might occur. (The RF power dissipation associated with a fully operational 4-channel rotary joint should be simulated by means of D.C. heating, so that the conditions under which the device must function would be accurately reproduced in the vacuum chamber.)

The source should be isolated from the effects of high-power breakdowns within the test circuit. Adequate filtering should be provided to reject any harmonics which might be generated by the source.

The power delivered to the test piece should be controlled by means of a phase-shifter/hybrid junction network. In this way, it should be possible to avoid the changes in pulse shape which would occur if the power level was varied electronically.

Provision should be made for the measurement of both incident and transmitted power levels. In addition, these parameters should be monitored continuously on oscilloscopes in order to detect any small, sporadic changes which might occur.

Low Pressure Equipment - The low-pressure tests should be performed using a stainless steel vacuum chamber which is equipped with the following:

1. Thermocouple feed-thru
2. Liquid nitrogen feed-thru
3. High-voltage and current feed-thru
4. Ordinary electrical leads
5. Rotary motion and linear displacement feed-thru's

A residual gas analyzer should also be utilized. The ultimate pressure of a vacuum system of this type should be a few times 10^{-10} torr, provided that all feed-thru's and other equipment inside the vacuum chamber are routinely cleaned in an ultrasonic cleaner.

3.5.3.3 Test Procedure

The power-handling capabilities of the rotary joint in a space environment should be evaluated by means of the following test procedures:

1. Cleansing of Test Item

The test item should be thoroughly cleaned prior to each set of low pressure measurements. Of the various cleansing methods available, the procedure associated with ASTM Designation B253-53* is considered to be the most satisfactory and practical for the aluminum surfaces in question. This treatment is advantageous in that it removes both the original oxide film and the surface microconstituents.

2. Checkout of Vacuum Facility

Each set of low-pressure measurements should be preceded by a test run with the empty chamber to ensure that the vacuum facilities are functioning satisfactorily.

3. Initial Investigation of Venting and Outgassing Rates

Preliminary tests should be carried out to evaluate the venting and outgassing rates associated with the basic rotary joint structure. These would merely involve placing the test piece in the vacuum chamber, pumping down, and monitoring the time required for the pressure within the joint to drop below the critical pressure of 10^{-3} torr. If it is felt to be necessary, the feasibility of introducing venting holes to increase the leakage rate should also be investigated.

---

* "Specifications and Tests for Electrodeposited Metallic Coatings", American Society for Testing Materials, July 1958, p. 69.

4. Investigation of Thermal Effects

The thermal conditions which will prevail when the 4-channel rotary joint is operating in the space environment should be simulated in the vacuum chamber by using DC heating in conjunction with a liquid nitrogen thermal shroud.

With zero heating, the internal pressure of the single-channel joint should be reduced below the critical value. Heating should then be applied (thereby simulating the switch-on of RF power), and the effect on the outgassing rate determined by measuring any pressure changes which occur. The results of this test should be used to define a switch-on procedure to ensure that the internal pressure remains below the critical level after the initial venting phase has been completed. Hence, the danger of ionization breakdown within the rotary joint during the early stages of high-power operation should be eliminated.

An additional test should be performed to evaluate the effect of thermal expansion brought about by RF power dissipation. The pressure should again be reduced below the critical value and the RF transmission properties of the rotary joint monitored using a low input power.

This power level should be kept constant as the temperature is increased to simulate the 1 KW CW per channel operating conditions. Any performance degradation due to the resulting dimensional variations should then be observed.

The results of this test should be used as a basis for defining the maximum permissible operating temperature and for specifying any thermal control mechanisms (such as external radiators) which might be required in the final system.

5. High Power Tests

The power handling capabilities of the rotary joint should be investigated using the techniques described in the previous sections to simulate the environmental operating conditions.

The general approach should be to observe a cautious switch-on procedure and then raise the input power to the maximum level that can be tolerated by the device.

If breakdown occurs before the required power level, steps should be taken to identify and eliminate the failure mechanism involved.

3.6 EFFECT OF VARIATIONS IN DESIGN

The following sections are devoted to considering various change in the system design parameters. In all cases, the primary objective will be to evaluate the effect of these changes on the performance of the antenna and RF subsystem.

3.6.1 Beam Separation of Up to 2 HPBW on All Patterns

In the proposed antenna system, a separate prime focus reflector is allocated to each of the four beams. Increasing the beam separations up to 2 HPBW, therefore, represents no mechanical or RF design problem since it only

involves making relatively small adjustments to the alignment of these reflectors.

To assess the effect of the increased beam separations on the system performance, it is necessary to consider separately the two modes of operation which are illustrated in Figure 3-57.

In the first, the four beams are "in-line" and the increased separation in no way compromises the antenna performance.

In the second case, however, increasing the "vertical" displacement of beam 4 will cause it to be intercepted by the solar panels. Unfortunately the situation cannot be alleviated by reorganizing the mechanical integration of the system, since the available shroud volume has already been fully utilized to provide maximum clearance between the panels and the high-power beams.

Therefore, with the present system, an upper limit (estimated as being approximately 1 HPBW) must be imposed on the "vertical" displacement of beam 4, if severe pattern degradation due to the presence of the solar panels is to be avoided.

3.6.2 Three Channels on Beam 3 and One on Beam 2

A slightly more complex RF subsystem is required to achieve the capability of combining three channels in a single beam.

The suggested configuration is illustrated in Figure 3-58. As can be seen from the diagram, it is a modified version of the original RF subsystem, and therefore presents essentially the same design problems.

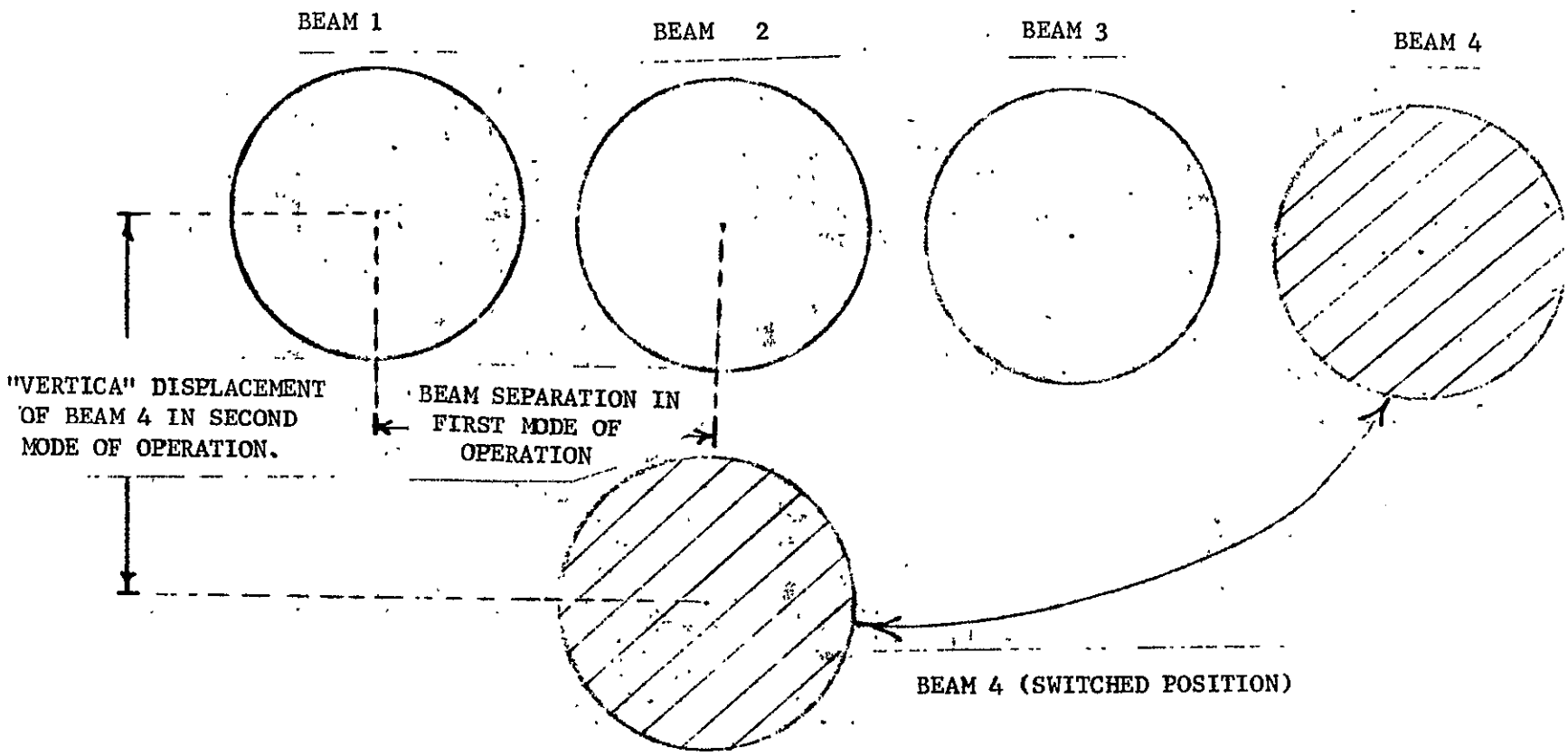

FIGURE 3-57 PATTERNS CONSIDERED IN ESTIMATING EFFECT OF INCREASED BEAM SEPARATION

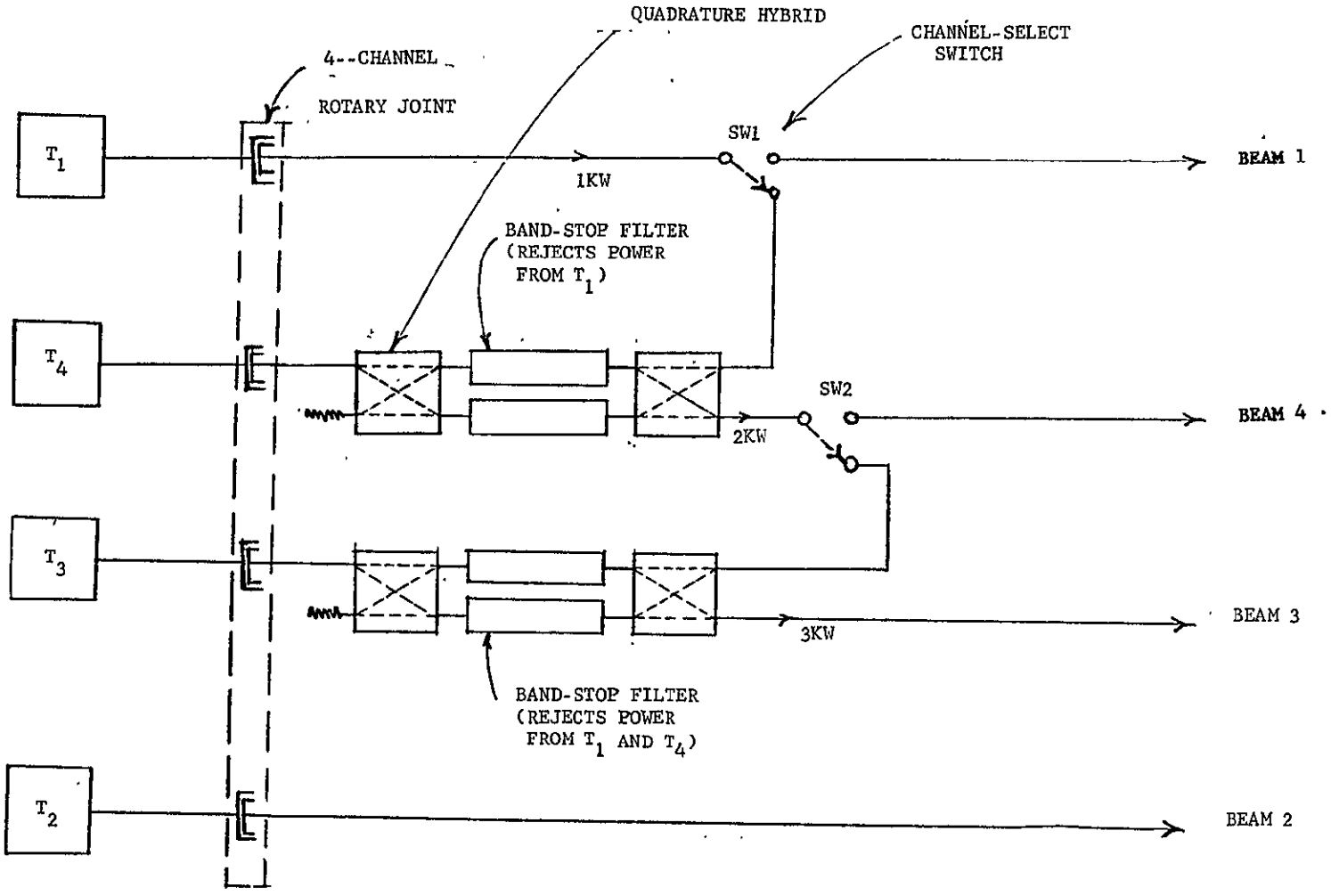

FIGURE 3-58 CONFIGURATION FOR TRANSMITTING 3 CHANNELS ON BEAM 3 AND ONE ON BEAM 2

There is, however, an additional problem of some significance in that the power rating of the second switch (SW2 in Figure 3-58) is increased to 2 KW CW. Hence, the successful operation of this system is contingent upon the development of a switch which is capable of handling power levels of this magnitude.

3.6.3 Power Transfer From Solar Panels to Transmitters by Means of D.C. Sliprings

The preferred satellite configuration for a system based on the concept of DC power transfer across sliprings is illustrated in Figure 3-59. From this, it is seen that the "North-South" alignment of the solar panels offers the immediate advantage of eliminating any interference between them and the beams from the high-power antennas.

In addition, by removing the need for a rotary joint and the 6 foot length of waveguide connecting it to the transmitters, a significant reduction in the RF power dissipation may be achieved. Calculation shows, in fact, that the overall insertion loss can be reduced by as much as 0.4 dB.

3.6.4 Variation of Channel Separation to 1.2 Channel Widths With a Relaxation in Channel Isolation to 20 dB

The proposed RF subsystem is such that a reduction in channel separation to 1.2 channel widths does not affect the system performance for the mode of operation in which a single channel is allocated to each beam.

However, for the mode in which the four channels are combined in two beams, the reduction in channel separation which may be achieved is limited due to the performance characteristics of the band-stop filters.

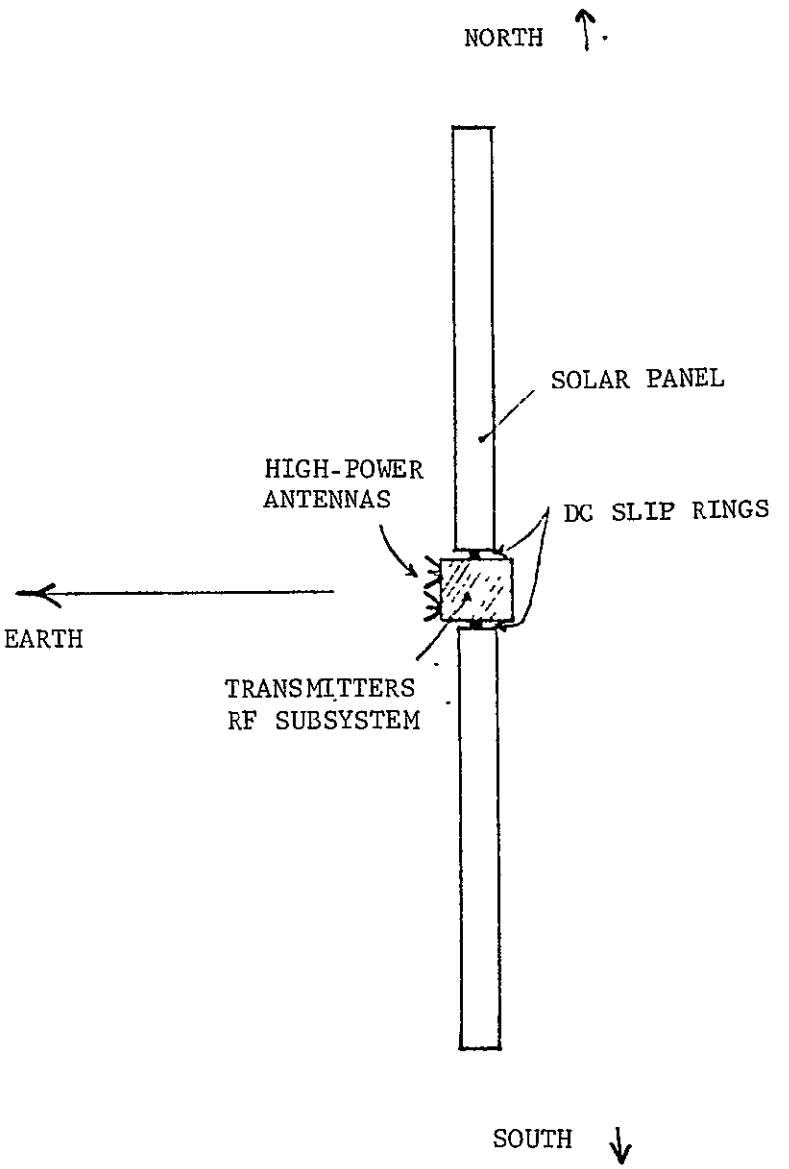

FIGURE 3-59 SATELLITE CONFIGURATION FOR SYSTEM BASED ON DC POWER TRANSFER FROM SOLAR PANELS

In this case, which is illustrated by Figure 3-60, the filters must reject one channel while transmitting the power from the adjacent channel with a minimum attenuation. Hence, as the channel separation is decreased, the "transmitted" channels move into the edges of the stop bands and consequently suffer an increase in attenuation.

An estimate of the lower limit which must be imposed on the channel separation may be obtained by considering the specimen filter which was designed to illustrate the feasibility of the proposed RF subsystem. This filter provides a 50 MHz stop band centered on 12.2 GHz. Therefore, the frequency corresponding to the center of the adjacent channel is of the adjacent channel:

$$fa = (12.2 + 0.050\ \delta)\ \text{GHz}, \text{ where } \delta \text{ is the channel separation in channel widths.}$$

From this, the frequency at the lower end of the adjacent channel is:

$$f1 = \left[(12.2 + 0.050\ \delta) - 0.022\right]\ \text{GHz}$$

i.e.,

$$f1 = (12.178 + 0.050\ \delta)\ \text{GHz}.$$

Using this relationship in conjunction with the theoretical curve for the filter transmission coefficient leads to the graph of insertion loss vs. channel separation which is shown in Figure 3-61.

If the maximum permissible transmission loss is nominally specified to be 0.5 dB, then it is seen from the graph that a lower limit of approximately 1.7 channel widths must be placed on the channel separation.

The transmission loss near the edge of the stop band could be reduced by relaxing the specification on the filter rejection from 40 dB to 20 dB.

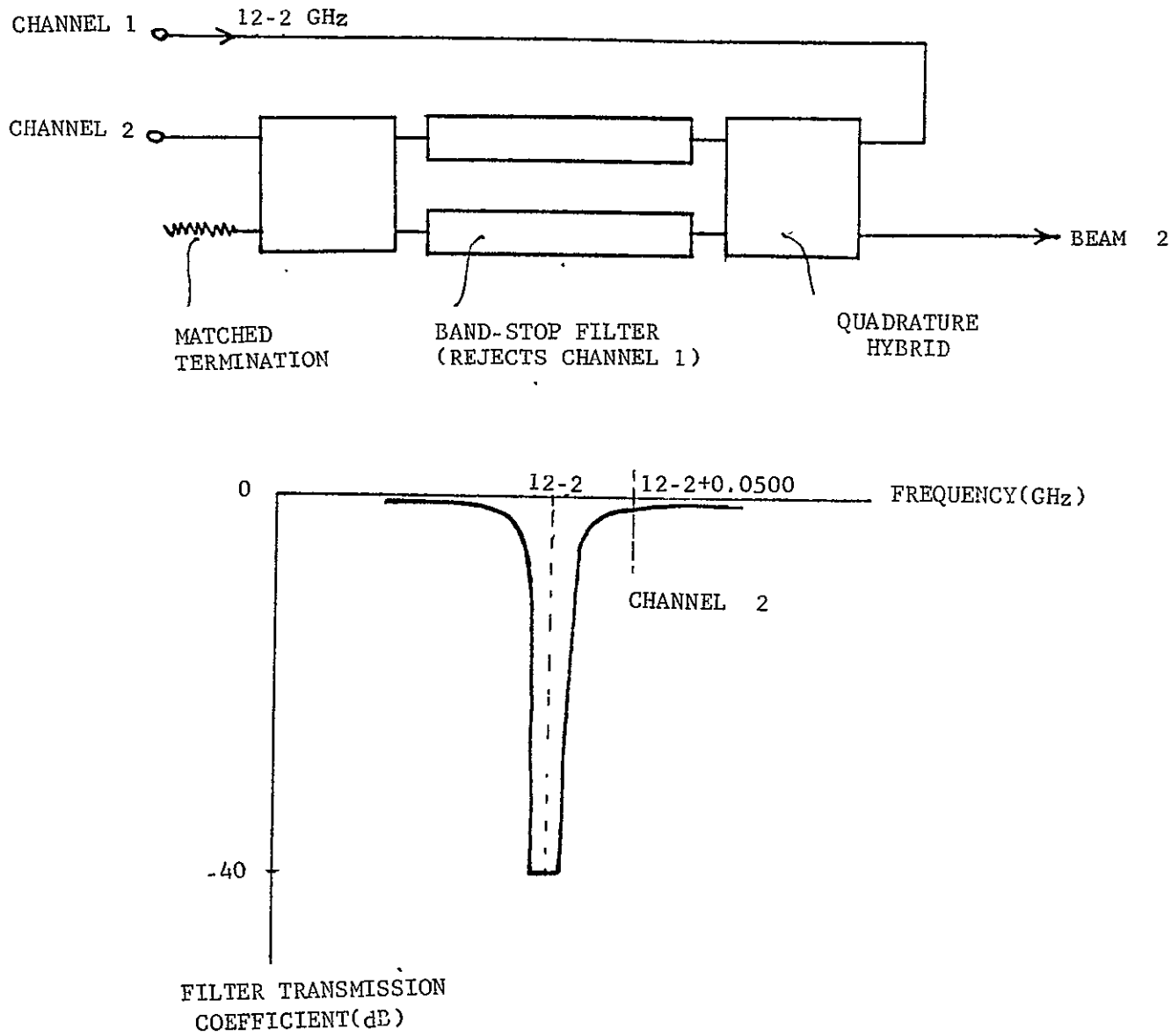

FIGURE 3-60 COMBINATION OF TWO CHANNELS IN A SINGLE BEAM

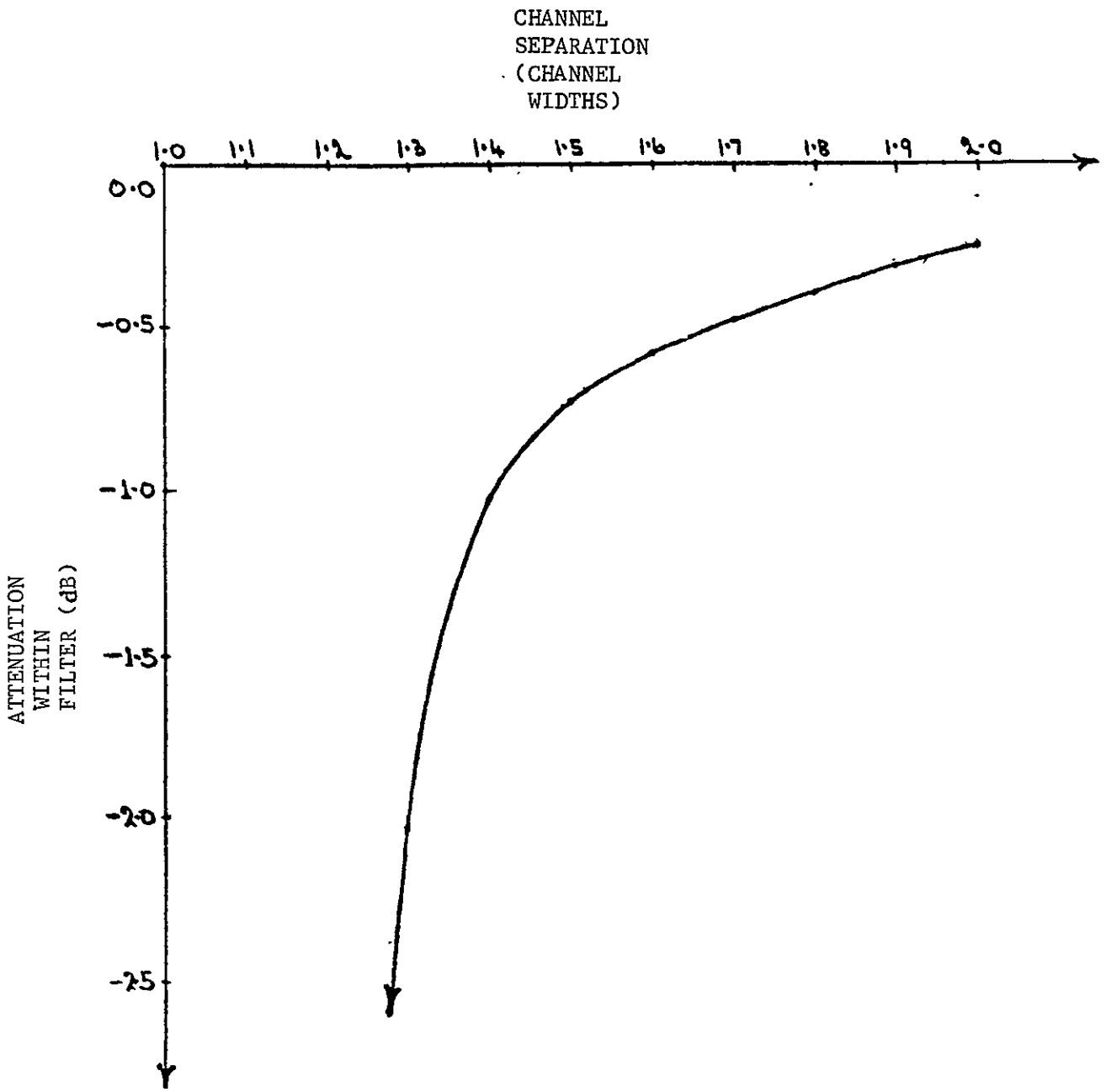

FIGURE 3-61 FILTER TRANSMISSION LOSS AS A FUNCTION OF CHANNEL SEPARATION.

This would not involve a corresponding decrease in the channel isolation since that parameter is determined by the properties of the rotary joint coaxial choke sections. However, there would be an increase in the power losses associated with the rejection process and, with a 1 KW input, it would be necessary to dissipate 10 Watts within the matched termination of the hybrid junction (see Figure 3-60).

Because of this effect, it is not possible to substantially reduce the lower limit on the channel separation by modifying the filter design.

A marginal improvement in the loss figures could be obtained by using WR 90 OFHC copper, instead of WR 75 aluminum waveguide. This would allow a separation of approximately 1.5 channel widths to be achieved. Any further reduction, however, would be accompanied by a sharp rise in the power dissipation within the filter. For this reason, it is necessary to conclude that a separation of less than 1.5 channel widths is not feasible for the mode of operation in which the four channels are combined in two beams.

3.6.5 Variations in Power Level to as High as 2.5 KW per Channel

There are three mechanisms which can seriously affect the performance characteristics of an RF system when it is operated at high CW powers in a space environment:

1. Multipactor breakdown
2. Ionization breakdown
3. Dimensional changes brought about by RF power dissipation.

For the system being considered, the critical region for both multipactor and ionization breakdown is the innermost coaxial choke section of the four-channel rotary joint. Analysis has shown, however, that multipaction cannot occur in this region until power levels in excess of 18 KW per channel are being transmitted. Furthermore, the choke dimensions are such that the avalanche process required to initiate an ionization breakdown cannot take place if the internal pressure is less than 10^{-3} torr.

Hence, it is concluded that an increase in power level to 2.5 KW per channel will not result in a multipactor or ionization breakdown, provided, of course, that a cautious switch-on procedure is observed.

Any performance degradation which occurs will, therefore, be related to the increased RF power dissipation. For a power level of 2.5 KW per channel, this effect gives rise to an operating temperature of approximately 600°F (see Thermal Analysis). It is therefore evident that if power levels of this magnitude are to be achieved, then external radiators must be employed to keep the system temperature within acceptable limits.

If adequate temperature control is not maintained, then it is possible that complete loss of mission will occur. In this event, the most likely failure modes are:

(1) Contact between adjacent coaxial choke sections, leading to complete malfunction of rotary joint.

(2) Change in position of filter stop bands, leading to very high power dissipation within matched terminations of power dividers.

SECTION IV

DIRECTION SENSING SUBSYSTEM

4.1 PURPOSE

The purpose of this part of the study is to develop alternative Direct Sensing Subsystem (DSS) concepts and select the best alternative to meet direct sensing requirements. A detailed error analysis is performed on the preferred design to determine DSS attitude measurement accuracy.

The DSS study has resulted in an attitude sensing system which meets the design requirements, objectives and constraints given in the Statement of Work. The system derived from the study reflects state-of-the-art techniques in RF direction sensing as it would be implemented for spacecraft. Tests required to confirm performance are recommended.

4.2 STUDY SUMMARY AND CONCLUSIONS

4.2.1 Preferred Spacecraft DSS Approach

The DSS is construed to be an integral link in the Attitude Control System (ACS) and the DSS with the ACS forms a complete, precision antenna platform attitude stabilization system. This system angle-locks to ground radio beacons, the attitude angle of lock being controlled by ground command. Upon changing of this command, the system seeks and acquires the new attitude stabilizing on it. In this way, the direction of and area of earth illumination by narrow beam satellite antennas is controlled.

4.2.1.1 DSS Requirements

The DSS requirements are derived from the overall antenna pointing requirements and are listed in Table 4-1. Included are important DSS requirements and constraints derived from study considerations.

TABLE 4-1

DIRECTION SENSING SUBSYSTEM (DSS) REQUIREMENTS

STATED REQUIREMENTS

- Simultaneous or Sequential Measurement (With Command Override) of:

  a. Signals from Ground Transmitters
  b. Signal(s) using Spacecraft Transmitting Antenna(s)

- Acquisition and Tracking Over: (Acquisition Time 15 Minutes)

  a. $\pm 20^{\circ}$ Longitude from Subsatellite
  b. $+45, -10^{\circ}$ Latitude

- Define Ground Equipment Characteristics for Evaluation and Analysis

DERIVED REQUIREMENTS AND CONSTRAINTS

- DSS Pattern Axes Location Error Allocation:

  a. $.05^{\circ}$ RMS Pitch and Roll — Relative Error for Spacecraft Measurement,
  b. $.5^{\circ}$ RMS Yaw — Absolute Error for Ground Measurement

- Ground Interferometer Beacon Transmitter Locations:

  a. 15° N. Latitude, 0° Longitude (From Subsatellite)
  b. Others Within the Tracking Area Boundary

- Reliability for a 5 Year Mission

- Minimum Impact on Transmission Antenna Design

4.2.1.2 Preferred DSS Configuration: Summary

The investigation of DSS design alternatives and error analysis has led to the following DSS configuration.

a. Orthogonal axes interferometer of 32-inch baseline (91.44 cm) with the horns mounted directly on the truss members running between the large aperture transmission antennas. Frequency is 8 GHz linearity-polarized "diagonal" horns are mounted on waveguide extensions to reduce coupling with the high power feeds. A second shorter baseline is omitted, the ambiguity resolution being performed initially by ground sensing of the beam position, and subsequently by phase tracking over the 2 transition in the receiver.

b. The interferometer receiver is located behind the center of the cross of the baselines and is coupled to the horns by non-rigid, thermally insulated, temperature compensated coaxial cable. The receiver input is isolated from 12 GHz signal coupling by waveguide filters which provide 105 dB rejection at 12 GHz. The receiver is switched between interferometer arms by means of PIN-diode RF switches at a 20 Hz rate. The receiver is a "pilot-tone" type to achieve negligible phase bias error in the receiver channel.

c. Three axis attitude measurement is provided by using two continuously transmitting ground beacons. The phase measurement circuit averages phase samples, which represent a beacon transmitter L.O.S. vector direction cosine in one axis for 1/80 second. The measurement circuit is then switched to the output of the alternate beacon signal detector to measure the second L.O.S. vector direction cosine. The receiver inputs are then switched to the other interferometer arm for measurements in the other axis.

d. The phase measurements are then presented to the ACS computer in the form of 4 11-bit binary numbers representing measurements with signal-to-noise ratios of 34 dB. The ACS computer derives antenna platform pitch, roll and yaw. The attitude determination contains $.038^{\circ}$ noise and $.023^{\circ}$ bias errors (both 3σ) for pitch and roll. Yaw noise error for a 10-second averaging period is less than 0.6° (3σ) for beacon L.O.S. vectors separated by more than 6° as viewed from the spacecraft.

4.2.1.3 Physical and Electrical Configuration

The physical configuration is shown in Figure 5-2.

The pilot tone receiver is shown in principle in Figure 4-1. Omitted from the drawing are the RF switches to alternate between the two interferometer axes, the switching between two envelope detectors and a standby redundant receiver and pilot-tone oscillator. The drawing illustrates the simplicity of the receiver design. There are no synchronous detectors or narrow-band tracking loops. The demodulators are conventional envelope detectors. The phase detector is an all-digital circuit that produces a phase estimate in the form of a digital number. The receiver design is detailed in paragraph 4.3.2.

4.2.1.4 Interferometer Attitude Measurement Performance

Table 4-2 itemizes the pitch and roll attitude errors due to the interferometer measurement. These figures are derived in paragraph 4.3.3. Note that the root sum square (RSS) of 3σ noise and bias error is $.032^{\circ}$, which is well within the $.05^{\circ}$ allocation for DSS. The figures for the yaw measurement are for a 10-second averaging time.

4.2.2 Preferred Ground DSS Function

4.2.2.1 Requirements

The DSS is required to perform the following functions not performed by the spacecraft functions. The DSS must:

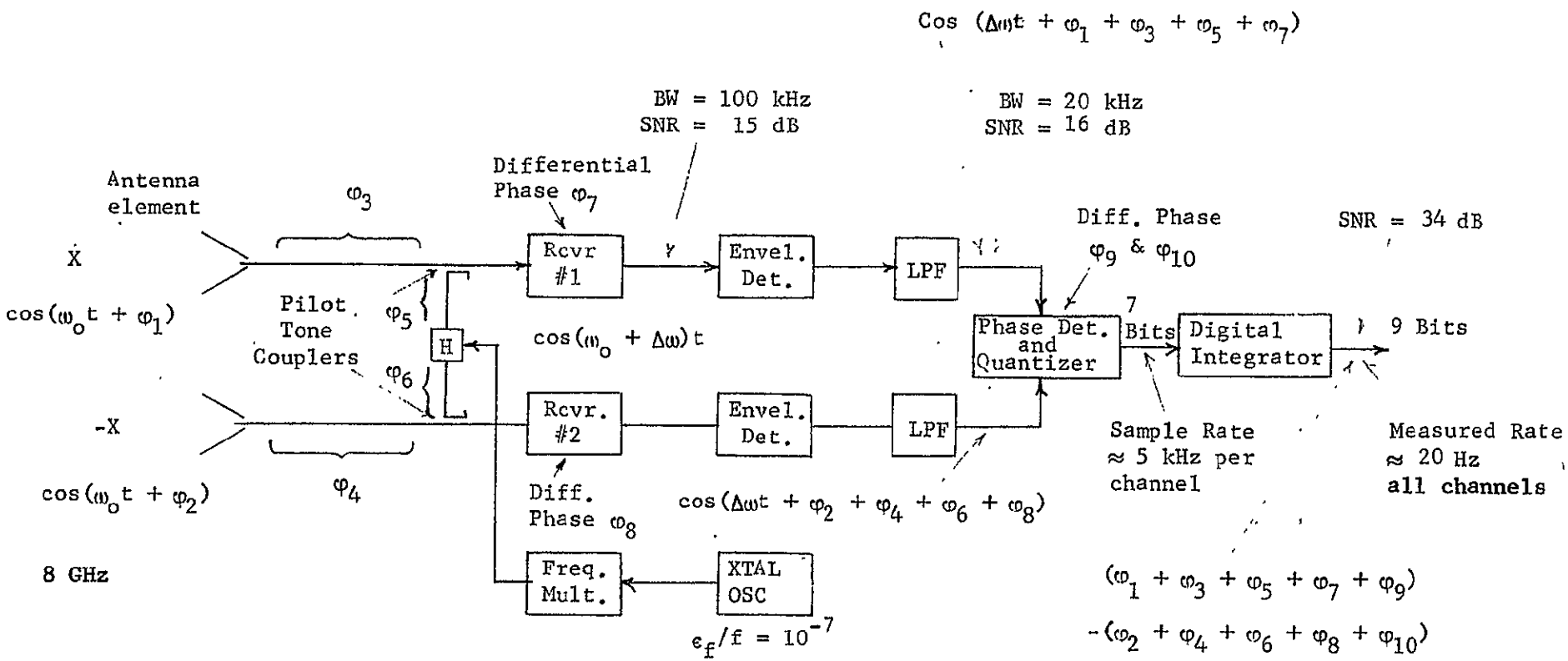

Fig. 4 - 1 Basic Pilot-Tone Interferometer Receiver

For $\Delta f = 2\pi\,\Delta\omega = 10$ kHz and a pilot tone stability of 10^{-7} (.1 ppm), a post-detection bandwidth of 20 kHz is practical.

TABLE 4-2 INTERFEROMETER ERROR BUDGET

ERROR SOURCE	RMS RANDOM ATTITUDE ERROR (DEG.)	BIAS & LONG-TERM RANDOM ATTITUDE ERROR (3σ) (DEG.)
Phase Quantization	.001	
Receiver Thermal Noise	.0086	
Scale Factor (Baseline Stability)		.0011
Zero Crossing Detector Bias		.001
RF Phase Bias		
Antenna Phase Center Motion (0.3° Diff.)		.0024
Antenna Polarization Error ($.1^{\circ}$ Element Alignment)		.001
Coax Diff. Phase (.50) (20°C Temp. Diff.)		.004
Directional Coupler Phase Diff.		.01
Rcvr. Diff. Phase ($.1^{\circ}$)		.001
Pitch and Roll RSS Total	.009 (1σ) .027 (3σ)	$.016^{\circ}$ (3σ)
Yaw (L.O.S. Vector Separation 6°)	$.6^{\circ}$ (3σ)	$.016^{\circ}$ (3σ)

a. Measure antenna platform attitude employing signal(s) which use the spacecraft large-aperture transmitting antennas.

b. Locate the beam pattern geometric center orientation with an absolute accuracy of $\pm .05^{\circ}$ in antenna platform pitch and roll and $\pm .5^{\circ}$ in yaw.

c. Convert the attitude measurements to attitude correction signals to be transmitted to the spacecraft attitude control system.

d. Provide spacecraft antenna platform attitude measurements simultaneously or in sequence with spacecraft interferometer attitude measurements.

e. Provide a means of redundant spacecraft antenna platform attitude measurement in event of spacecraft interferometer system failure or measurement interruption.

f. Provide a means of resolution of ambiguity of measurements made by the interferometer.

Requirements e and f above are derived from the preferred spacecraft DSS approach.

4.2.2.2 Selected Approach

The recommended technique of direction sensing employing signals which use the spacecraft transmission antennas is making direct measurements of the patterns at ground receivers. Other techniques were investigated. However, they in general involve additional feeds on the transmission antennas located close to the main feed. The resulting additional aperture blockage or feed mutual coupling would raise the sidelobe level above the -25 dB requirement placed on the design of the transmission antennas. Paragraph 4.4.2 compares the various approaches.

The recommended approach makes power measurements on the main transmitted signal (if angle modulation is used) with bandwidth up to 50 MHz. This is feasible with spacecraft ERP of 63 dBw or more. For operation with less ERP or if amplitude modulation is employed on the main beams, a constant power signal in a vacant area of the 12 GHz frequency spectrum must be used. In this case an ERP of 50 dBw provides the necessary attitude measurement accuracy if receiver bandwidth is equal or less than 2.5 MHz.

4.2.2.3 Accuracy of the Ground DSS Technique

Two approaches have been developed which measure beam pattern characteristics at ground receivers. The first approach utilizes the spacecraft antenna and ground receiver site effectively as an antenna range. (Refer to paragraph 4.4.3.)

Present simple antenna range practices permit definition of the location of the beam axis with an uncertainty of 1/50 of the HPBW. This corresponds to .05° for a 2.7° HPBW. Averaging data over several antenna pattern cuts reduces the uncertainty of the axis location. Table 4-3 lists errors in the axis location definition process.

TABLE 4-3

AXIS LOCATION UNCERTAINTY
(FULL PATTERN MEASUREMENT)

POWER METER RESOLUTION	PER MEASUREMENT ERROR (INCREMENT = .06°)	AXIS LOCATION UNCERTAINTY (ERRORS AVERAGED OVER -2.5° TO +2.5° PATTERN)
.01 dB	.051°	.0056°
.02 dB	.102°	.011°

It was found that error due to power meter resolution dominated error due to antenna platform stepper resolution.

A second approach uses small attitude increments in orthogonal or quadrature directions and measures the resulting power changes at a ground receiver located off the beam axis. (Refer to paragraph 4.4.7.) This technique requires the prior, accurate measurement of the antenna pattern. Figure 4-2 presents the estimated error for this DSS technique. It is seen from the curve that the attitude increment must be less than $.10^{\circ}$ for accuracy approaching the required $.05^{\circ}$. It should be noted that making a series of these measurements and averaging results should reduce error to less than that required.

4.2.3 DSS Integration into an On-Board Attitude Sensing and Control System

Figure 4-3 shows the DDS functions integrated into an on-board closed-loop attitude sensing and control system. The interferometer measures the direction of the line-of-sight (LOS) vectors of two transmitter beacons. From this information 3-axis attitude is measured and compared with the desired attitude in the computer. Offsets actuate the attitude control system. The attitude correction signals may come from the ground by command override. Ground receivers sense the beams to eliminate ambiguity in the phase measurement. The ground beam sensing may be used as a redundant DSS.

4.2.4 Required Development Tests

Table 4-4 itemizes simple labatory tests that should be performed to verify the interferometer stability and pilot-tone interferometer receiver performance. The first test requires assembly of an interferometer antenna array and measures the bias phase drift due to this area.

The second test will measure the bias error introduced by the receiver and the phase measurement circuit. The interferometer antenna array output is simulated by a dual signal source, which has the required phase stability; hence, the bias error due to the interferometer array is not present in the second test.

A third test which combines the above equipment to make an interferometer and receiver combined test might be considered.

Note that in the above tests standard lab receivers may be used, i.e. no receiver RF construction is necessary in either test.

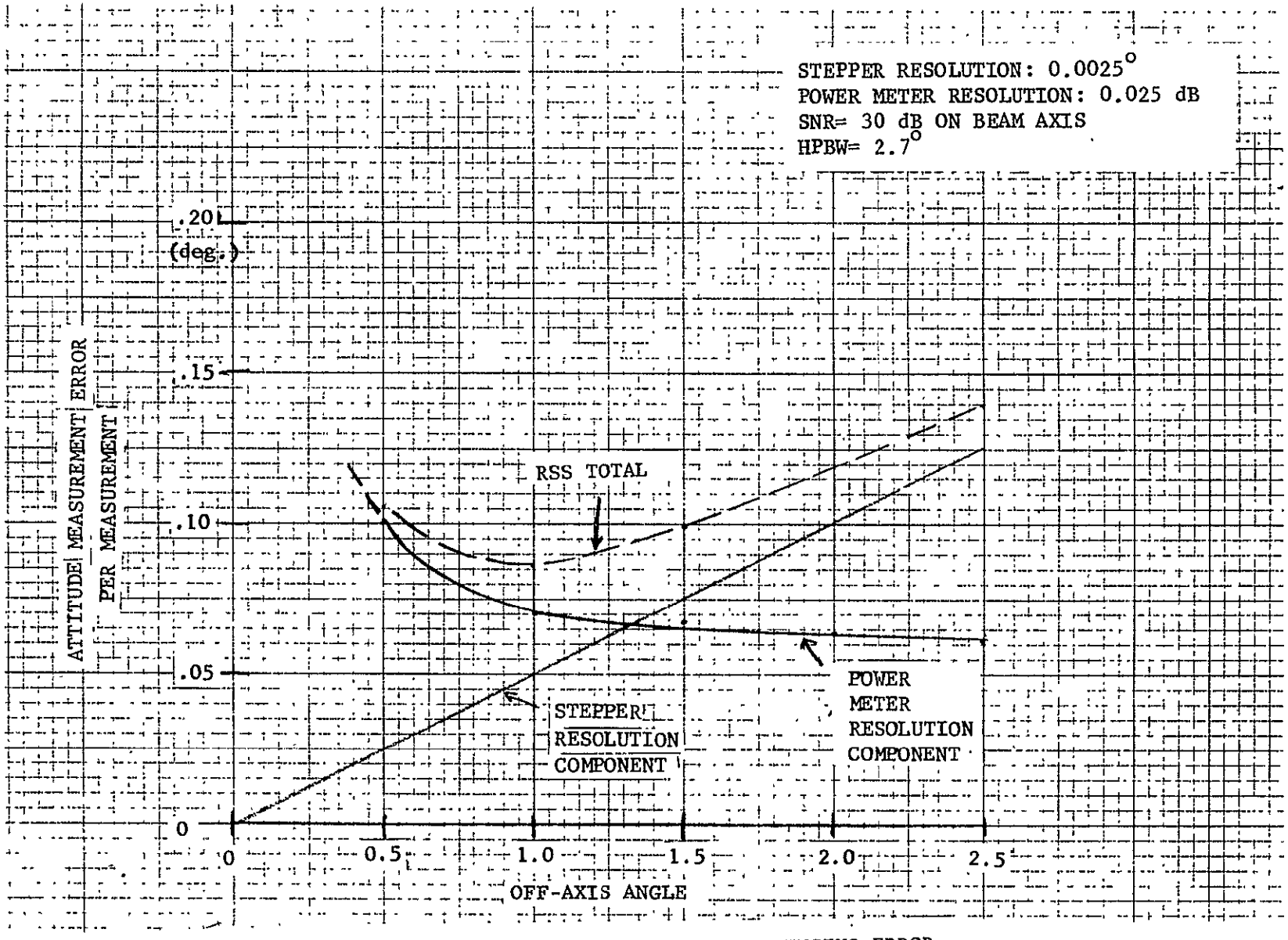

FIGURE 4-2 ANTENNA PLATFORM ATTITUDE SENSING ERROR FOR SENSING TWO RIGHT ANGLE, .05° STEPS

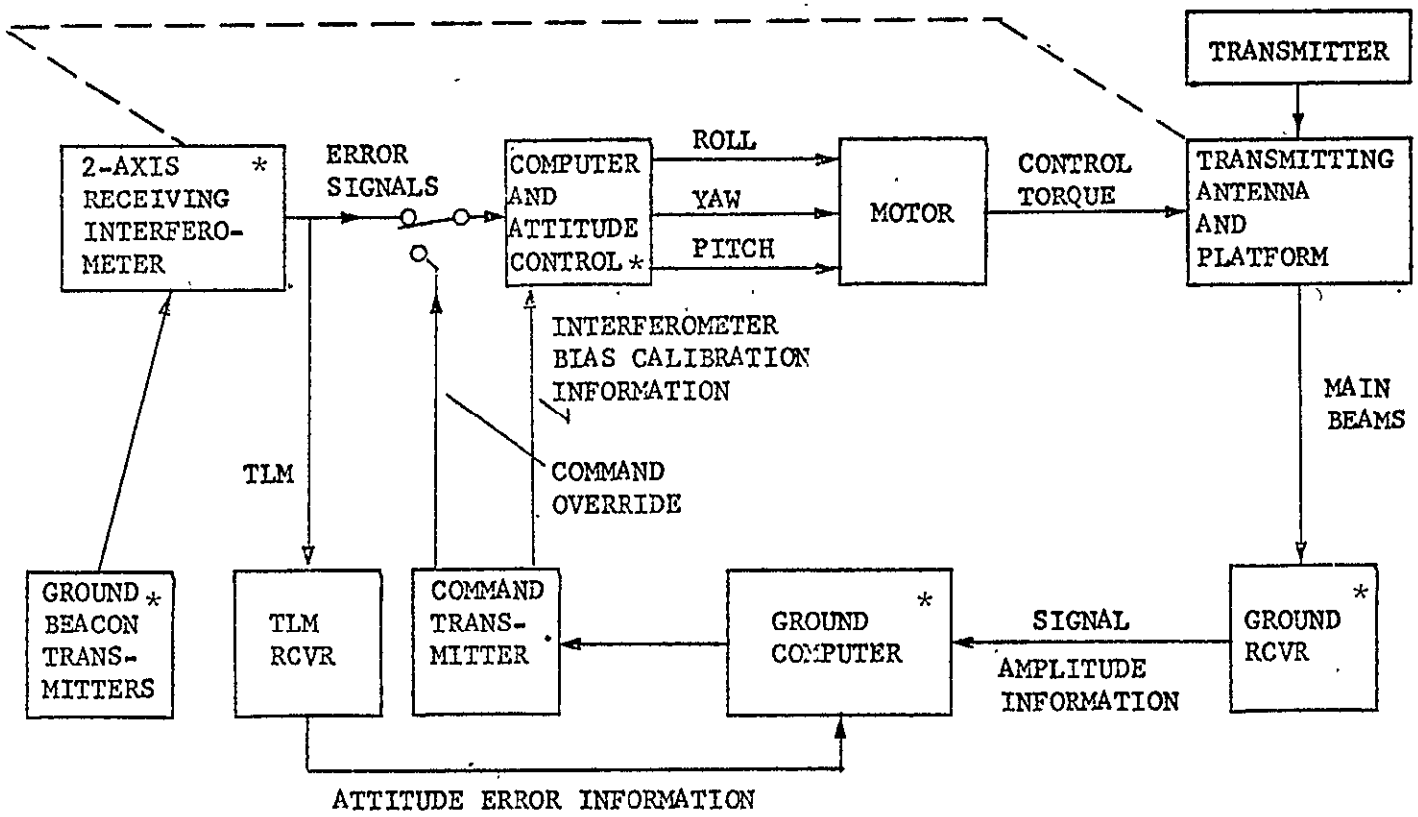

FUNCTIONS MARKED * ARE DSS BLOCKS OR PERFORM DSS FUNCTIONS

FIGURE 4-3 FUNCTIONAL BLOCK DIAGRAM OF ANTENNA DIRECTION SENSING AND CONTROL SYSTEM

TABLE 4-4

REQUIRED DEVELOPMENT TESTS

PILOT-TONE RECEIVER TESTS

1. INTERFEROMETER ARRAY, COAX CABLE LEAD-IN AND PILOT-TONE COUPLER PHASE STABILITY WITH TEMPERATURE VARIATION.

    - INTERFEROMETER ARRAY BREADBOARD
    - PILOT-TONE RF SOURCE (LAB SIGNAL GEN.)
    - TWO STANDARD RECEIVERS
    - LAB PHASE METER

2. RECEIVER & PHASE MEASUREMENT BIAS ERROR DETERMINATION.

    - DUAL SIGNAL SOURCE (SIMULATED IDEALIZED INTERFEROMETER & PILOT TONE OUTPUT)
    - TWO STANDARD RECEIVERS
    - PHASE MEASUREMENT CIRCUIT BREADBOARD

In addition, the tests may be simplified by omitting noise performance tests, the outcome of which are accurately predictable.

4.3 SPACECRAFT DSS

4.3.1 Spacecraft Direction Sensing: Summary

This section summarizes the spacecraft DSS selection considerations and describes the preferred design and accuracy performance. The system organization into which the spacecraft DSS function fits is introduced.

4.3.1.1 Approach Selection

The Statement-of-Work system requirements are re-iterated with study-derived requirements and constraints in Table 4-1. The DSS Requirements I state that the DSS will use two methods simultaneously or in sequence with command override of measuring antenna system orientation and transmission pattern location. This requirement implies the DSS coordinate system model illustrated in Figure 4-4. The ground station signals are received via one or more of the large aperture antennas, e.g., a monopulse receiver, or these signals are received via an indpendent direction measuring antenna, e.g., a radio interferometer. The coordinates thus measured have an alignment error θ, relative to the x, y, z coordinates of the actual transmission beam pattern geometrical centern. This alignment error is due to angular variations between the antenna platform and the beam patterns and is caused by mechanical or structural deformations which are time varying in nature and cannot be calibrated on earth.

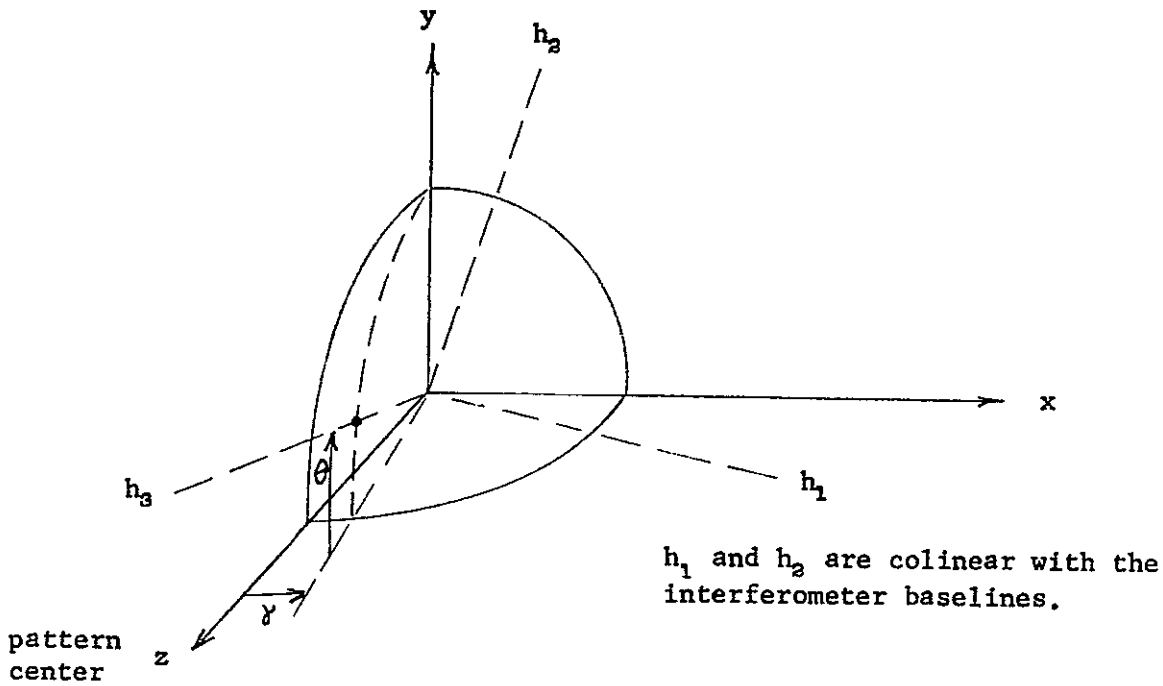

Figure 4-4 Model of Direction Sensing Subsystem Measurement Coordinates. The on-board direction sensing measurement has the coordinate system H_1, H_2, H_3. The plane (x, y) is normal to the actual beam pattern geometric center. The alignment error between on-board DSS coordinates and beam pattern coordinates is represented by angles and θ.

Since the overall accuracy of transmission pattern pointing must be better than $\pm$ 0.1 degrees rms, a DSS measurement accuracy of $\pm$ 0.05 degrees (3σ) will be taken as a design goal.

Measurement of Orientation by the On-Board DSS - Orthogonal baseline interferometers receiving from or transmitting to two or more ground stations are chosen to provide the required accuracy of measurement. Amplitude-sensing devices (e.g., monopulse receiver) will also serve this function but are ruled-out because a monopulse feed cluster in close proximity to the high-power feed would cause the sidelobe level of the main antennas to be above -25 dB, thus defeating those design attempts. If a monopulse receiver were used on an independent antenna, there would be the disadvantage that the ground beacon transmitter would be required to be located at the aiming point. A summary a interferometer-vs.-monopulse characteristics is presented in paragraph 4.3.1.4.

4.3.1.2 Spacecraft DSS Equipment Description and Performance

The selected interferometer configuration is described as follows:

a. Crossed-interferometer arms with superinsulated lead-in cables. The thermal isolation from the space environment will minimize thermal difference between lead-ins, minimizing phase differential. The cross configuration permits making equal the lengths of the RF coupling to each horn.

b. Linearly-polarized "diagonal" horns mounted on extensions to raise the horns above the large antenna surface so that coupling from the 12.2 GHz feed is reduced.

c. Interferometer receiver located on the antenna platform at the approximate center of the crossed arms. This receiver location minimizes RF cable lengths, keeping differential phase shifts small. The 12.2 GHz isolation filters are located within the superinsulation envelope. This is to cause the filter temperature to vary over a minimum range.

d. The coarse measurement (short baseline) horn has been omitted to simplify the interferometer receiver. Omitting this function is feasible because the ambiguity resolution may be performed by independent means. Attitude angle measurement ambiguity interval is 2.7° for the 32-inch baseline (81.28 cm) at 8 GHz. Initial ambiguity resolution may be accomplished by ground beam position measurements. Unambiguous measurements may then continue automatically by identifying the phase quadrant of each measurement.

e. The interferometer receiver has two separate downconverter channels, one for each antenna element of an interferometer arm. Differential phase error between the two channels is avoided by using a pilot tone injected by the receiver input. Phase is measured with respect to the pilot tone phase which undergores the same phase shifts as the signal.

f. The receiver is switched to the alternate interferometer arm by means of PIN diode RF switches. The switching rate between arms and hence the sample rate is 20 Hz.

g. Two ground beacons transmit continuously on adjacent frequencies in the 8 GHz band. The beacon signals are separated with bandpass filters at the receiver output.

h. The receiver phase measuring circuit is switched between output bandpass filters synchronously with the switching between interferometer arms.

i. Phase measurement samples are presented to the Attitude Control System (ACS) at a rate of 20 Hz. Each measurement consists of an 11-bit binary number and has a signal-to-noise ratio of 34 dB minimum.

j. The computer in the ACS (or on the ground) derives antenna platform attitude or attitude error from the samples. Yaw determinations should be averaged over 10 seconds to reduce noise error.

k. The attitude determination error due to DSS in $.038^{\circ}$ noise and $.023^{\circ}$ bias error (3σ) for pitch and roll. Noise error for yaw is less than 0.6° (3σ) for a 10 second averaging period and the ground beacon LOS vectors separated by more than 6°.

1. Spacecraft DSS receiver (without interferometer antenna structure) characteristics are:

   (1) Weight: 5 to 8 lbs. (2.27 to 3.63 kgm)
   (2) Power: 8 to 13 watts
   (3) Volume: 190 to 300 cu. in. (31100 to 49200 mm^3)
   (4) Probability of success for 5 years: .97

Figures 4-4 and 4-5 in paragraph 4.3.2.2 show the functional design of the receiver.

4.3.1.3 Interferometer-Amplitude-Sensing Monopulse Comparison

Comparison of the system integration utility of the RF interferometer versus the monopulse receiver for the purpose of antenna platform attitude sensing is given in Table 4-5. The interferometer approach has the advantages of generally better flexibility and least interference with the design of the large aperture antennas. The monopulse receiver has the advantage that the only significant causes of reference axes shift relative to the direction of the main pattern would be due to misalignment of the feeds and possible "squint" of the pattern due to operating on a different frequency. The interferometer system is chosen as the best for the DSS application.

Interferometer Direction Sensing Characteristics - The RF interferometer provides precise spacecraft attitude measurements by making relative phase measurements on a signal (beacon) which has propagated from a point source to two receiving antennas separated by a known, fixed distance. Two orthogonal baselines will provide three-axis attitude measurements if two or more ground stations illuminate the interferometer. Major error sources are due to random and bias errors arising in the phase measurement and errors originating in interferometer baseline length. Measurement errors include all errors that originate between the antenna elements and the attitude data readout and consists largely of differential phase shifts in the antenna couplers and receiver input circuits and random error. Random error (due to receiver noise and phase measurement quantization) in orientation angle is related to receiver SNR by;

$$\sigma_\alpha = \frac{1}{K(\alpha)} \sqrt{\frac{N}{S}}$$

TABLE 4-5

COMPARISON OF INTERFEROMETER AND MONOPULSE ATTITUDE SENSING

Consideration \ Approach	Orthogonal RF Interferometer Pair	Amplitude Sensing Monopulse Receiver
Effect on design of large aperture antenna.	Aperture blockage in same configurations.	Complicates feed design; aperture blockage.
Sensitivity to attitude change.	Proportional to arm length.	Fixed for a given beamwidth.
Ground Station transmitter location.	Angle lock may be achieved with arbitrarily located ground station.	At antenna pattern null only.
Attitude angle over which ground beacon may be acquired.	Restricted only by beam width of the interferometer antenna elements.	Less than 3° for a 2.7° beamwidth antenna.
Uncalibrateable error sources.	Offset of the high power transmission pattern relative to the interferometer axes.	Small boresight shift relative to the high power transmission pattern.
Can attitude measurement and beam position measurement functions be combined?	No	Yes

where K (α) is the scale factor or ratio of electrical-to-geometrical angular differentials and is a function of α . Bias errors arise from differential phase delay in the interferometer receiver, electrical phase bias error in the phase measurement and error in the effective baseline length. Phase bias error is the critical source of error for the pitch and roll axes. Yaw error is dominated by noise. Phase bias error is reduced to a low level by injecting a sinusoid as pilot tone of constant phase into the receiver inputs. Measurements are made relative to this reference.

Acquisition of the direction sensing and antenna platform control system is an important consideration. If the on-board DSS equipment is an interferometer, the ground station location is not restricted as it is the case ofa monopulse. The monopulse is a nulling device, hence the ground transmitter must be located at the position desired for the null. The phase-sensing interferometer, however, provides a unique phase measurement for any look-angle from the interferometer, once the measurement ambiguity is resolved.

Interferometers may either receive or transmit.* The transmitting interferometer simplifies the spacecraft (with the exception of a downlink reference channel being required) but rules out a self-contained radio-reference closed-loop attitude sensing-control system on the spacecraft. The receiving interferometer is more conventional and permits on-board angle lock with arbitrarily placed ground radio beacons.

The important desirable characteristics of the interferometer antenna elements are:

- Fixed phase center - phase center should be constant over the field of view and over the frequency spread of the received signals.

- Mutual coupling - coupling between antenna elements, which affects baseline length, should be a minimum.

---

* P. Wolfert, "The Transmitting Stabilized Interferometer Navigation System," Philco-Ford SRS interdepartmental technical notes, August 17, 1966 and September 12, 1966.

- Greater than earth-coverage beamwidth - antenna element beamwidth of 30 to 40° is desirable to provide superior properties near beam center and permit measurements with large (up to 15°) angular deviations.

- Low VSWR - should be less than 1.2:1 over the frequencies involved.

- Low sidelobes - reduces mutual coupling.

An antenna element which fits these requirements well is the diagonal horn.* This linearly polarized horn has a square mouth which provides identically tapered field distributions resulting in a fixed phase center. Sidelobes are 31 dB down and cross-polarization response is -33 dB.

Amplitude-Sensing Monopulse Characteristics - The attitude of the antenna array can be controlled to the required accuracy by angle tracking a ground transmitter with a receiving monopulse feed on the transmission antenna. Yaw axis orientation must either be provided by employing monopulse receivers on at least two of the beams, or by independent means. The monopulse receiver provides two-plane error signals proportional to the off-axis angle-of-arrival of a beacon signal from earth. The random errors of such a direction-sensing system can be reduced to a value much less than the pointing accuracy requirement of 0.1° with modest transmitter power. The monopulse receiver approach has the advantage that time-varying distortions and deflections of the associated transmitter antenna pattern are common to the monopulse beam. This is an advantage not provided by the interferometer approach. The major disadvantage of the monopulse receiver may be that the feed horns' location would interfer with the transmitter radiating element.

Bias error originates mainly from boresight shift due to reflections and feed phase error and slow time-varying feed misalignment due to thermally induced deflection. It is known that bias error due to mechanical tolerances and misalignment (exclusive of reflector distortions) may be reduced to much less than the required 0.1° by range and optical calibration.**

---

* Love, "The Diagonal Horn," Microwave Journal, Vol. 5, March 1962.

** "Errors Affecting Antenna Pointing Accuracy," IR/R Note No. 553-5, 118 dated June 5, 1968, Philco-Ford SRS Division.

Similarly, monopulse boresight shift residual after calibration due to uncalibrated reflections can be held to less than 0.5° if uncalibrated reflections are less than -40 dB relative to peak beam response.

Non-Bias Error - It can be shown* that for maximum slope of the monopulse difference pattern of an antenna of guassian amplitude variation, the sensitivity K_{Δ}, in $(\text{degree})^{-1}$ is

$$K_{\Delta} = 1.67/\theta_{HPBW} \qquad (4\text{-}1)$$

where θ_{HPBW} is the two-sided half-power beamwidth. The corresponding squint angle is greater than would be used on a power limited link, because compared to maximum theoretical gain, this pattern results in a 4.3-dB loss of reference channel gain on axis. In this system however, the small additional loss is compensated by the increased angular sensitivity.

Assuming equal noise temperature of sum and difference channels, the rms tracking error, E, for a square law monopulse receiver with large S/N is related to S/N by

$$S/N = \frac{5.6\ b/B}{E^2\left(K_{\Delta}\right)^2} \qquad (4\text{-}2)$$

where S/N = predetection SNR

B = predetection bandwidth

b = post-detection bandwidth

Assume $B = 2 \times 10^4$ Hz, which corresponds to a satellite oscillator long-term stability of 10^{-6} and an 8-GHz frequency. Also assume b = 10 Hz, which is a conservative estimate, since typical values may be nearer 1 Hz. The sensitivity constant for a beamwidth of 2.7° is $K_{\Delta} = 0.62$. If the rms noise error is to be held to 0.03°, then the required S/N is 16. A transmitter ERP of 50 dBW readily attains this S/N.

---

* "Tracking Receiver Design," Technical Note 1-582-3-VC-210, Philco-Ford SRS Division, May 12, 1967, Appendix A.

It is concluded that non-bias (random) errors of the monopulse system are readily reduced to a level much less than the required accuracy of 0.1 degree.

Bias Errors - Bias errors are introduced by:

- Mechanical tolerances
- Misalignment of feed
- Boresight shift due to reflections
- Time-varying alignment of monopulse beam axis relative to transmitter beam
- Feed and receiver phase shift

The first two errors can be reduced to small values by careful structure/thermal design and by range and optical calibration. Calibration in orbit may be achieved by use of an independent measurement technique on the transmitting beams, as described in Section 4.4. Reflections causing boresight shift can also be calibrated-out on the range. Residual uncalibrated reflection must be held to less than -40 dB relative to beam peak to maintain less than 0.03 degree of uncalibrated boresight shift. Distortions of antenna structures are largely self-calibrating in this approach because the monopulse uses the same reflector as the transmitter. Therefore, time-varying misalignments of the monopulse beam axis relative to the transmitter beam axis are largely due to feed axis motions. Hence, close mechanical coupling of the two feed structures is required.

4.3.2 Interferometer Direction Sensing Subsystem Functional Description

The function of the spacecraft DSS RF interferometer is to measure the attitude of the antenna platform. This is done by measuring the angles between the line-of-sight (LOS) vectors to two or more ground transmitters and the two interferometer baselines. From these measurements, the direction of the normal to the baselines may be computed. This direction is nominally the pointing angle of the transmission pattern geometric center, the offset being measured by ground beam position measurement.

4.3.2.1 Phase-Attitude Relationship

The interferometer receiver measures the relative phase of signal pairs received from pairs of antenna elements on orthongonal baselines. The measurements are converted to direction consines of the LOS to the ground transmitters according to the relation

$$\cos \theta_{ij} = \frac{\varphi_{ij}}{2\pi \, L_j/\lambda_i} \qquad (4\text{-}3)$$

where θ_{ij} is the angle from arm j to LOS vector to station i

L_j is the corrected electrical separation of the antenna element's phase centers on arm j

λ_i is the wavelength of the signal from station i

$\varphi_{ij} = \varphi'_{ij} + 2n\pi$ is the phase angle measured with ambiguities resolved by integer n.

Since the electrical phase angles measured may vary through several 2π radians, a large order of ambiguity exists. The resolution of the ground beam position measuring function is ample to determine the particular integer value of n, thus, eliminating any ambiguity. Once the ambiguity is resolved, a phase quadrant identification circuit provides unambiguous on-board measurement for any subsequent measurement, assuming no break in operation has occurred.

Previous studies* have shown that the most practical phase sensing interferometer receiver has the following design:

(1) frequency multiplexed signals from the two antenna elements of each arm;
(2) use of a common IF channel for the multiplexed signals;
(3) phase measurement with a zero crossing detector gating a stable clock to a counter;
(4) calibration of differential RF phase delay in the receiver circuits by injection of a common phase test signal.

---

* ATS-4 Study Program Final Report, Vol. 7, Fairchild Hiller Space Systems Division, SSD 102.3; December 1966.

Also, An Advanced Study of an ATS Mission, ATS-4 Final Study Report, Vol. 1, Book 1, General Electric Spacecraft Dept., Nov. 66.

4.3.2.2 Pilot-Tone Receiver

The principle of the pilot-tone receiver for making relative phase measurement of two signals S(X) and S(-X), is illustrated by Figure 4-1. The pilot tone is coupled into the two input circuits where the two signals, whose phase is to be measured, originate. Both the desired signal and the pilot tone, whose frequency differs from the signal by a small amount, are amplified in a common receiver channel. The signal with pilot tone are passed through a simple detector and low-pass filter which produces the difference frequency impressed with the phase information.

The relative phase of the A and B channel outputs is then measured giving the desired phase difference of the two signals S(X) and S(-X) plus some phase error components.

Phase error is due largely to effects in the input circuits. The phase of two two pilot-tone components at the couplers may be made nearly identical by placing the couplers where the input lines are in close proximity, i.e., at the center of the interferometer cross-arms.

The major error component due to differential phase shift in the A and B paths is due to non-tracking of the phase delay in the input circuits coupling the interferometer antennas to the centrally located receiver. This differential phase will be due to unequal temperatures of the two lead-in lines. The phase differential can be reduced by using temperature compensated coax and thermal super-insulation wrapped around the coax or the structure carrying the coax.

The pilot-tone receiver is developed in Figures 4-5 and 4-5a. The pilot tone is coupled to the input circuit of the 10 GHz low-pass filters (LPF) by means of hybrid power splitters (H). Phase drifts in the LPF and succeeding circuits are, therefore, of no consequence if the phase delay difference (ψ_7 or ψ_8 of Figure 4-1) of received signal and pilot tone is small. The standby redundant receiver includes components from the first mixer through the zero-crossing detector (ZCD). Output channels A and B separate and carry phase information from ground beacon transmitters A and B which transmit on slightly different frequencies (about 1 MHz apart).

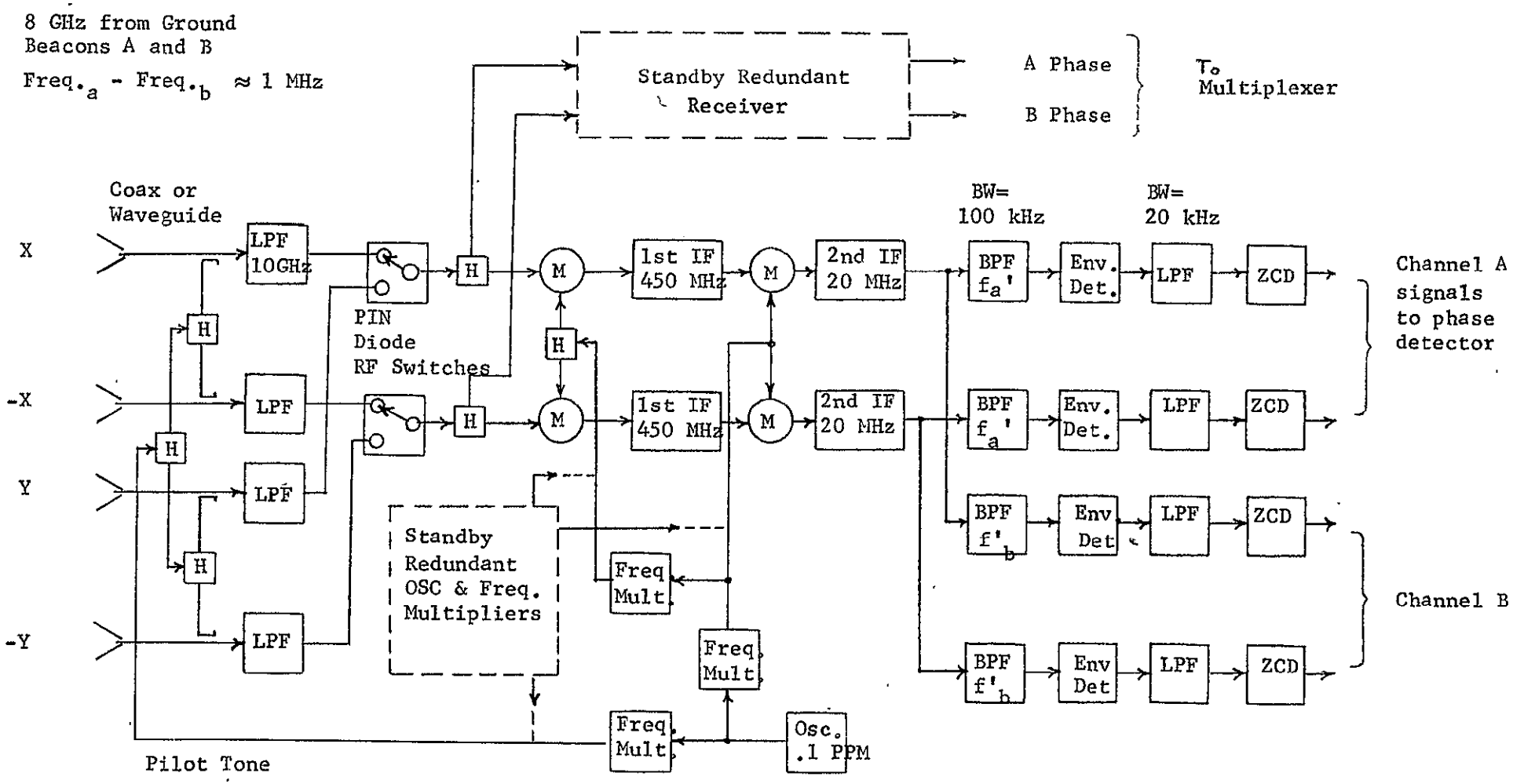

Fig. 4-5 Pilot-Tone Receiver for Interferometer. The receiver is switched between arms X and Y with PIN diode SPDT switches. Ground stations transmit continuously on frequency f_a and f_b which are separated at the 2nd. IF output by bandpass filters.

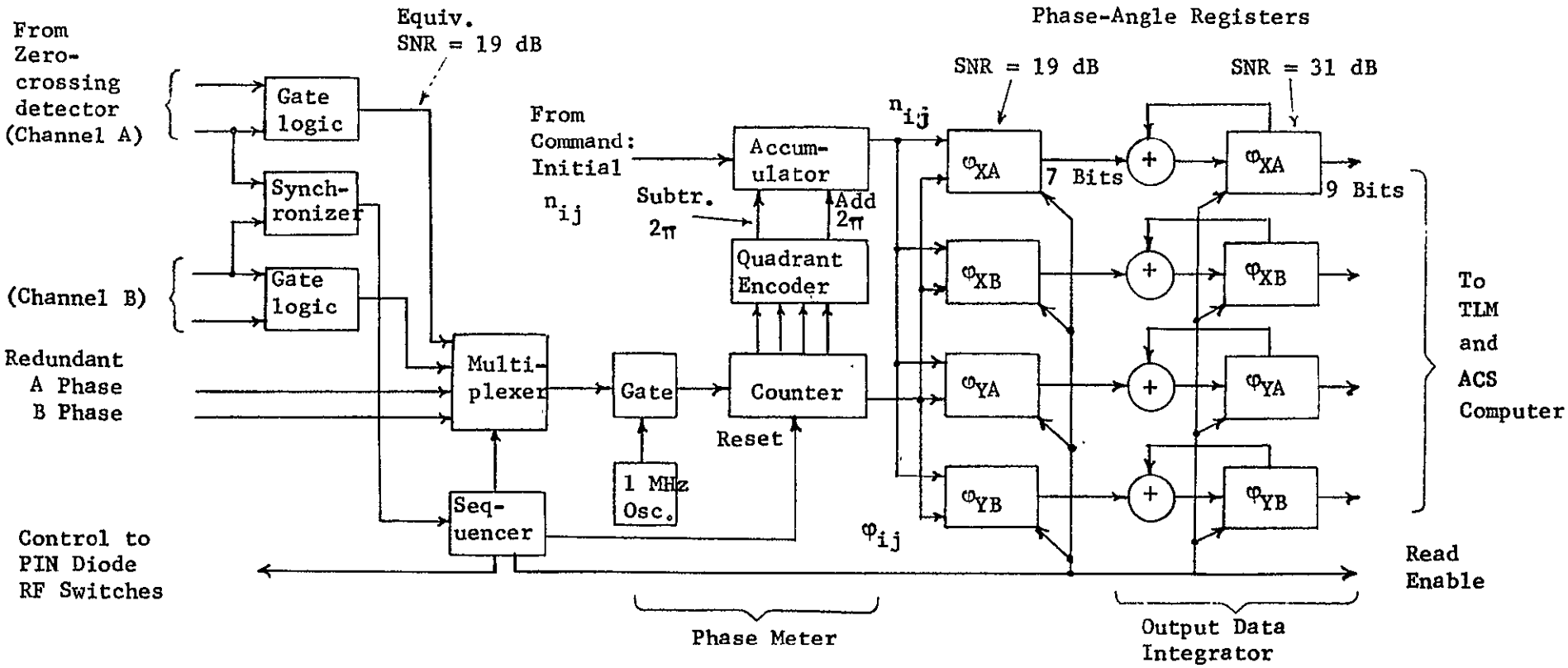

Fig. 4-5a <u>Phase Measurement and Output Averaging Circuit</u>. The sequencer samples signals A and B from each interferometer arm, X and Y.
For Δf = 10 kHz, the phase measurement quantization increment is 3.6°. If the output integrator averages over 64 samples, then the output rms phase noise components are $\sigma_{quan.} = .13^{\circ}$ for quantization noise and $\sigma_{noise} = 0.8^{\circ}$ for receiver thermal noise.
All circuits are digital.

Figure 4-5 is the phase measurement and measurment averaging circuit and comprises all digital logic circuits. Channel A or B (or redundant A or B) are gated to the phase meter in sequence. The phase meter also senses transitions over the 2 π radian boundary so that angles greater than 2 π may be tracked. The initial ambiguity of measurement is resolved by ground measurement as described in paragraph 4.4.6. The value of n (the number of whole cycles offset from zero phase reading) is put into the accumulator by command upon this initial ambiguity resolving operation. The phase meter then tracks the phase without further command unless a break in signal causes a loss of phase tracking. The measurement SNR is then improved by an output digital integrator which averages over 64 measurements.

One parameter of importance is predetection SNR. To avoid SNR degradation in the envelope (square-law) detector, it is necessary to maintain a predetection SNR greater than 10 dB. (A synchronous detector could be used to avoid degradation at low SNR, however the additional complexity is a disadvantage; also a synchronous detector would inject a phase error in presence of a frequency offset.) If received signal power is drecreased significantly, predetection bandwisth must be reduced to maintain a good predetection SNR. Due to the frequency drift characteristics of crystal oscillators of 1969 technology, frequency tracking will be required for the pilot tone oscillator to maintain an accurate frequency difference, $\Delta\omega$. If signal power is reduced by more than 5 or 10 dB, both bandwidth reduction and frequency tracking may be performed by replacing the envelope detectors by phase-lock loops and synchronous demodulators. This represents a reliability penalty of from .1 to .2λ. (.1 to .2% failure per 1000 hours. See Section 3.5 for reliability failure rate interpretation.)

The phase measurement circuit operates on the difference frequency, about 10 kHz. Readout and resetting of the digital counter requires that the detector sample, at most, every-other input cycle. This results in a maximum phase sample rate of 5 kHz. Since the noise bandwidth is 10 kHz, successive samples will contain noise components which are statistically independent.

Variation of difference frequency will require that the period of the input signal to the phase detector be measured. This will require an additional counter and a division function in digital computer located in the ACS.

Noise Spectrum Changes in the Detection and Phase Sampling Processes - The approximate noise and signal spectrum into the envelope detector and the resulting detector output spectrum is as in Figure 4-6.

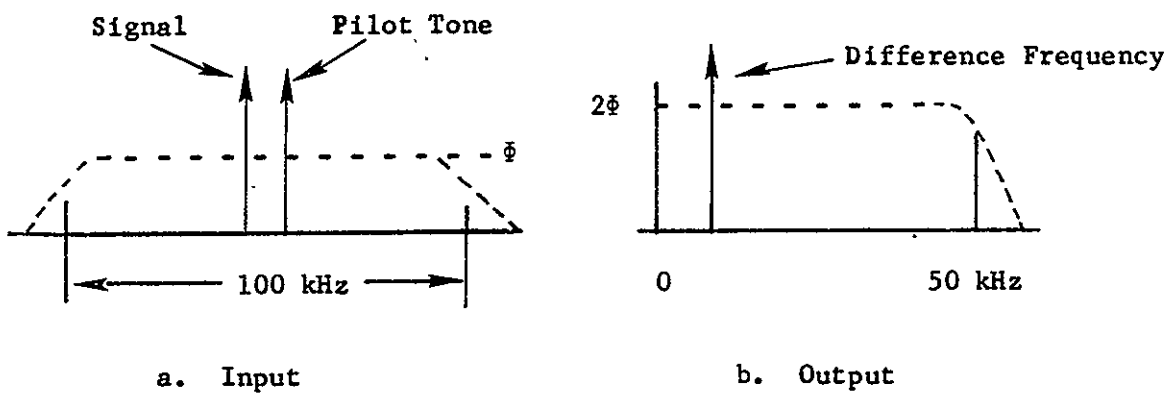

Figure 4-6 Envelope Detector Noise Spectra

We see that all the input noise is folded into a 50 kHz bandwidth. The envelope detector output is then passed through a 20 kHz low-pass filter. The relative phase of the difference frequencies of the two channels is then sampled by the phase detector. Assuming that the difference frequency is approximately 10 kHz, the entire noise into the phase detector (from both channels) will be folded into a 10 kHz bandwidth. This is sampled at a 5 kHz rate giving independent noise samples. The digital sample is then averaged over 128 samples giving an SNR improvement of 21 dB and 4 additional significant binary digits.

Choice of Interferometer Beacon Transmitting Frequency - The beacon frequency should be chosen so that it is at least 10% different from the satellite transmission frequency. This is so that the isolation filter may be readily realized. For this study the beacon frequency is chosen to be 8 GHz because of the availability of X-band transmitting equipment at NASA ground terminals.

4.3.2.3 Coupling Between the Interferometer and the High Power Transmission Feeds

Summary - Due to the proximity of the 12.2 GHz transmitter feed, a significant amount of power will be coupled to the interferometer antenna. This signal power would damage the receiver first mixer or mask the desired signal with cross-product interference. In specifying the rejection required of a receiver input filter, it is found that cross-product modulation causing background noise is the dominant issue. To reduce the level of this noise to the level of the receiver thermal noise, a low pass coaxial or waveguide filter with 105 dB attenuation at the satellite transmission frequency is required. This figure assumes a receiver IF of greater than 350 MHz. If the IF were 310 MHz or less, 135 dB of attenuation would be needed. It is preferred therefore, that the receiver first IF be greater than 350 MHz.

Isolation of the interferometer horns from the 12.2 GHz feed can be improved by positioning the horns in a low intensity part of the 12.2 GHz feed pattern and minimizing the horns' aperture. The best position is farthest from the 12.2 GHz reflector edge and raised from the surface. This factor favors a long baseline in the case of the square 12.2 GHz reflector array.*

RF Isolation of the 8 GHz Interferometer Receiver from the 12.2 (8.2 alternate) GHz Transmission - The interferometer receiver input circuit must provide the following functions:

1. A phase-stable passband at 8 GHz;**
2. Rejection of the 12.2 (8.2) GHz high power transmission to prevent saturation or damage to the receiver first mixer;
3. Rejection of spurious signals which would convert to the interferometer receiver IF amplifier passband.

---

* Mechanical Integration IRR #2, Dept. 553-5, APSS & SS MI-IRR-2, Dec. 12, 1968.

** It is assumed that uplink communications equipment will operate in the same band as the communications uplink.

The receiver input filtering specifications are derived according to the following assumptions:

1. High power transmission channel separation is 65 MHz (bandcenter to center) and a total of 5 adjacent channels each having a noise-like video signal.
2. The received interferometer signal level will be -140 dBW into the first mixer.
3. The interferometer receiver signal-to-noise density (S/N_o) is -201 dBW.

The major source of interference due to the high level transmission is through cross-product intermodulation producing a background noise-like interference. This assumes that mixer image frequencies and other first-order interferences are placed so that their levels can be made insignificant. The spectrum of the high power transmission must be examined to determine the magnitude of these intermodulation products. The spectrum is as in Figure 4-7 assuming 5-channels of 1.3 channel width separations. Figure 4-8 illustrates the signal path and associated power levels.

It is seen from Figure 4-7 that first-order cross-products will fall in the IF passband if the intermediate frequency is less than 310 MHz. Therefore it is concluded that, to avoid an unrealistic filtering requirement, the first IF center frequency should be greater than 350 MHz.

An IF amplifier center frequency of 375 MHz might be considered. This value has been proposed for Comsat application. Noting that significant cross-products will be produced by components only 65 MHz from band-edge of the signals represented in Figure 4-7 , it can be concluded that these components will be only about 30 dB down from 1.5 kw because steep-skirt filtering in the high power transmitter output is impractical for these components. These considerations lead to the cross-product level evaluations of Table 4-6.

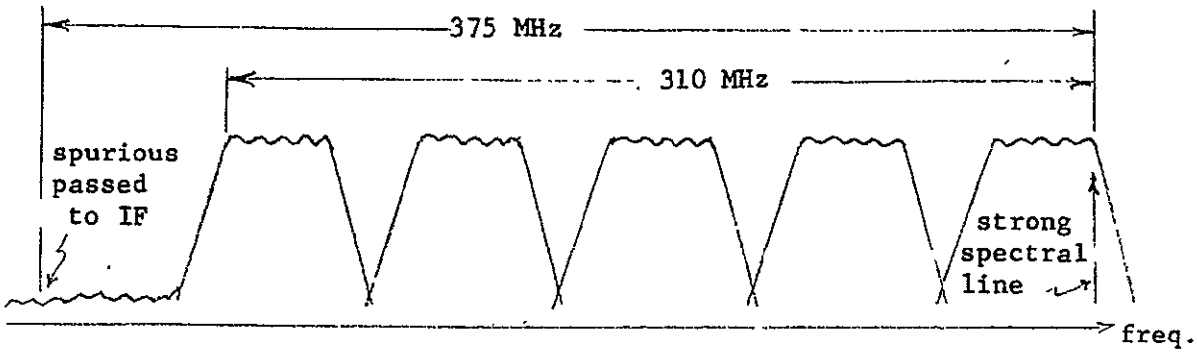

Fig. 4-7 High Level Transmission Spectrum Centered at 12.2 or 8.2 GHz. Each channel is approximately 50 MHz in bandwidth. The approximate location of the most significant spurious component is shown for the first IF of 375 MHz.

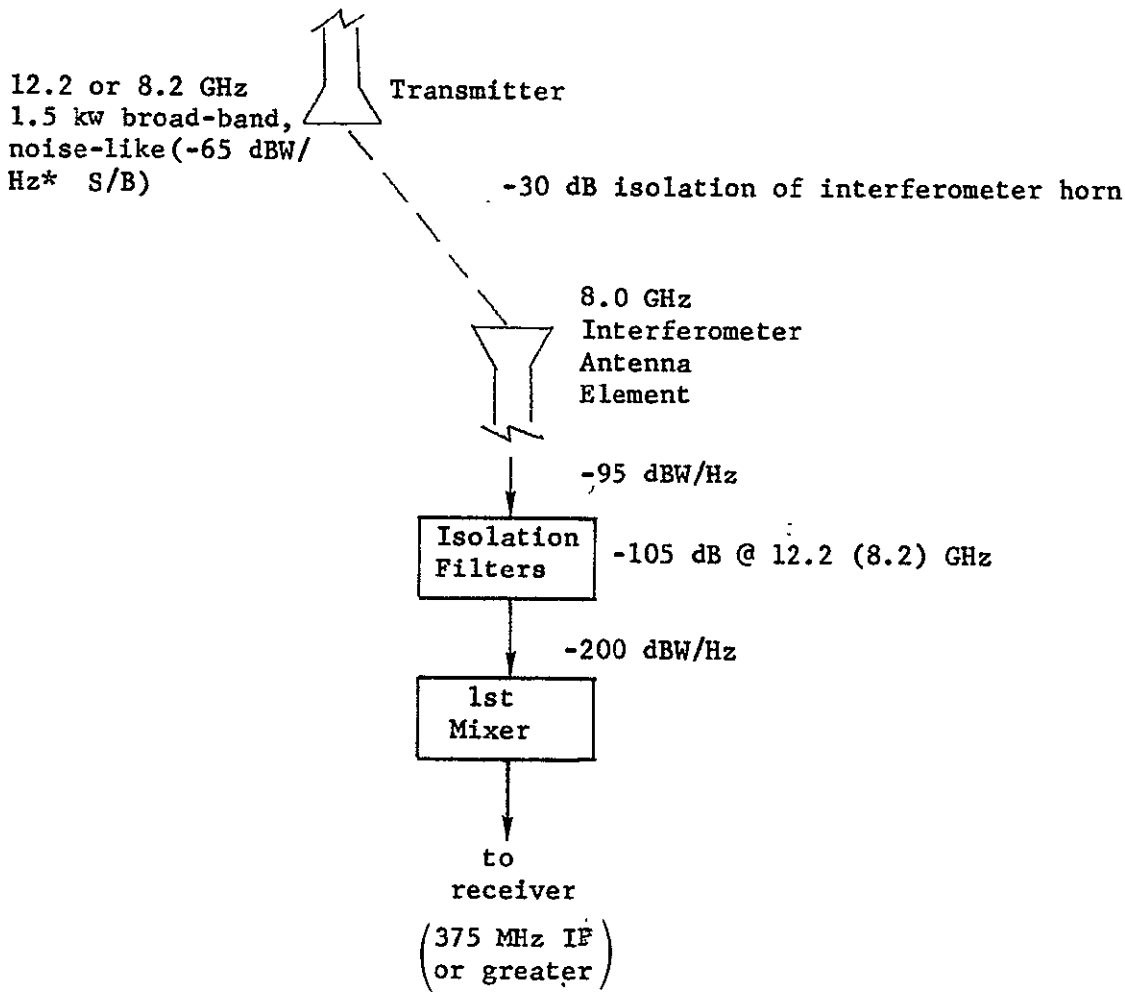

*Out-of-transmission band spurious components - down 30 dB from 1.5 kW. These out-of-band components are separated from in-band components by a frequency equal to the IF center frequency.

Fig. 4-8 First-Order Cross-Product Spectral Density Reduction to a Level Equal to Receiver Noise Density

TABLE 4-6

EVALUATION OF INTERFEROMETER RECEIVER INPUT FILTER REJECTION AT 12.2 (OR 8.2) GHz

FACTOR	REL. POWER SPECTRAL DENSITY	REMARKS
$S_{o_{peak}}$*	-35 dBW/Hz	TX P/Bandwidth
$P_{spurious}/P_T$	-30 dB	Spurious Level
$P_{spurious}$	-65 DBW/Hz	Spurious Density
Isolation of Interferometer Horn	-30 dB	Minimum
Spurious Power to Interferometer Receiver	-95 dBW/Hz	
Required Spurious Level**	-200 dBW/Hz	
Required Filter Isolation to First Mixer	105 dB	

* $S_o = 1500\ W/(5 \times 10^7\ MHz) = -45\ dBW/Hz$

Assume a signal contrast ratio of C = 20 dB

$S_{o_{peak}} = S_o + C/2 = -35\ dBW/Hz$

** Receiver Noise Density

From Table 4-6 we may conclude that 105 dB of rejection is required at 12.2 GHz.

It is now easily checked to determine if 105 dB attenuation protects the first mixer from saturation or damage. Total RF power is 28 dBW (four 1.5 kw channels) and isolation of the first mixer is 30 + 105 dB. Hence total power to the first mixer at 12.2 GHz is -97 dBW or -67 dBm. This number compares favorably with -10 dBm which is the upper limit to avoid mixer saturation effects.

Filter Realization - The above filter attenuation can be achieved using a lowpass, bandpass or bandstop characteristic. The effect of temperature variation will be to shift the transition frequency of the filter. Since phase shift effects are of fundamental importance, it is concluded that a lowpass filter is preferred. Several types of filter are applicable: coaxial, waveguide and interdigital filters. Their characteristics* pertinent to this application are given in Table 4-7. The coaxial filter would be smaller than the waveguide, having a diameter approximately equal to that of type N coax connector.

The alternate transmission frequency of 8.2 GHz would entail an alternate uplink frequency. The interferometer beacon would again be chosen in the uplink band to conserve ground station equipment. If the frequency between up- and downlinks is reduced below the 350 MHz assumed above, it may be necessary to include more sections (poles) in the isolation filter.

Coupling Between Antenna Feed-Horns and DSS Interferometer - To determine the magnitude of this effect, the coupling between a feed-horn and the adjacent interferometer element was estimated. For the purpose of the calculation, the geometry shown in Figure 4-9 is assumed, in which the interferometer lies flush with the reflector aperture.

Taking f/D = 0.35 defines the angle subtended at the feed-horn by the radiating aperture as 140°.

The semi-angle is therefore 70°, which has an associated space attenuation factor of 3.5 dB.

---

* Private communication with H. Gould of WDL.

TABLE 4-7

COMPARISON OF ISOLATION FILTERS

	COAXIAL (Lowpass)	WAVEGUIDE (Lowpass)	INTERDIGITAL (Bandpass)
Number of sections (poles) required for 105 dB rejection at 12 GHz	9-10	8-9	
Length	5-6"	5-6"	4-5"
Loss of 8 GHz	.3 dB	.1 dB	< 1 dB
Higher-order mode at 12 GHz?	No	May be eliminated by longitudinal slots or transform-down the width.	3rd harmonic passband
Phase sensitivity with temperature change	Small if frequency is well below cut-off	Same as coaxial	Sensitive for narrow bandpass

Now, required sidelobe level is approximately 30-35 dB. Therefore, required aperture taper is approximately 20 dB. Hence, feed-horn must have pattern which is (20-3.5)=16.5 dB down 70° off-axis. A circular horn of approximately 1.5 diameter will meet this requirement. Hence again of feed-horn is

$$G = 10.4 \text{ dB} \qquad (4\text{-}4)$$

If P_o = power radiated from feed-horn, then power density at interferometer element is:

$$P_I = P_o - \frac{1}{4\pi r^2} \text{ (in dB)} + 10.4 - 20, \text{ where } r = \text{distance from center of feed-horn to center of interferometer element} = 16.8'' \text{ (from scale drawing)} \qquad (4\text{-}5)$$

$$\therefore P_I = P_o - 35 + 10.4 - 20 = P_o - 44.6 \text{ dB}$$

Projected area of the 25 sq. in. interferometer element = 25 cos 74.5°
= 6.67 sq. in.

$\therefore$ Power intercepted by interferometer is approximately:

$$P = 6.67 \times P_I = P_I + 8.5 \text{ dB}$$

$$P = P_o - (44.6\text{-}8.5) \text{ dB}$$

$$\text{i.e., } P \doteq P_o - 36 \text{ dB}$$

Since P_o = 1 kw, $P \doteq 0.25$ Watt, and it will, therefore, be necessary to load the interferometer arms with band-pass filters whose rejection at the transmit frequency is sufficient to reduce this power to an acceptable level.

It should be noted, however, that the coupling can also be reduced by moving the interferometer elements forward of the reflector apertures so as to increase their angular displacement from the peak of the feed-horn radiation pattern.

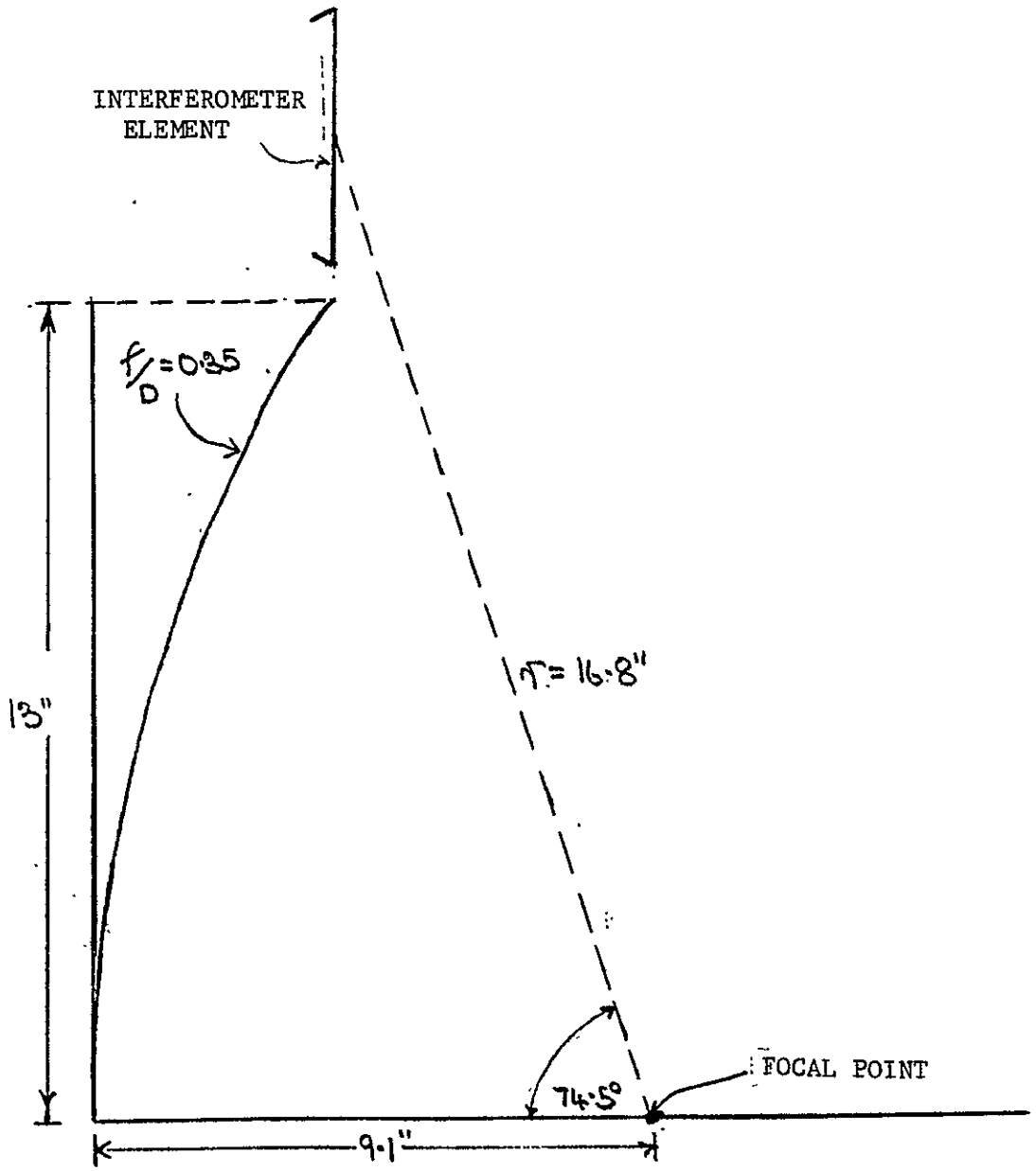

FIGURE 4-9. COUPLING BETWEEN FEED-HORN AND ADJACENT INTERFEROMETER ELEMENT

4.3.3 Interferometer Attitude Measurement Error

The investigation of attitude errors introduced by the interferometer receiver - attitude computation circuits is divided into two parts. The first deals with the noise-like and bias errors impressed on the direction cosine measurement. The second part investigates the propagation of these errors into the pitch, roll and yaw measurements. These two topics are developed in paragraph 4.3.3.2 with supporting analysis in paragraph 4.3.3.4. Paragraph 4.3.3.3 investigates the effect of multipath reception which may occur in the case of reflections from the solar panels when they are in the field of view of the interferometer antennas.

4.3.3.1 Error Magnitude Summary

Table 4-8 summarizes interferometer direction cosine errors, i.e., errors in the measurements that are the receiver output. Note that random error is given at the rms (1σ) value. Bias errors are worst case (probability $< 1\%$) and are here taken as 3σ values. The receiver configuration is the pilot-tone receiver of Figures 4-4 and 4-5. Antenna baseline 32 inches (81.28 cm). (Refer to paragraph 4.3.4.) Other link parameters and receiver characteristics are presented in Table 4-10 of paragraph 4.3.3.2.

Propagation of these errors into roll, pitch and yaw is summarized in Table 4-9. Pitch and roll computations result in the measurement errors being multiplied by approximately $\sqrt{2}$, depending upon location of ground beacon transmitters. (See Eq. 4-11, paragraph 4.3.3.4 and paragraph 4.3.3.2).

The propagation errors into yaw with the two ground beacon transmitter configuration is a special subject developed in paragraph 4.3.3.2. Table 4-9 shows that, while bias errors tend to cancel in the yaw computation, random noise is enhanced. To avoid undue yaw random error the beacons must be widely spaced in the spacecraft view. The propagation multiplier is so large, however, that averaging over a period of time is adviseable. The table shows results for an integration time of 10 seconds. This is not a disadvantage to the attitude control system since its response time in yaw is not required to be as small as for pitch and roll.

TABLE 4-8

INTERFEROMETER RECEIVER MEASUREMENT ERRORS

Error Source	RMS Random Direction Error (Deg.)	Bias & Long-Term Random Directions Error (3σ) (Deg.)
Phase Quantization	.001	
Receiver Thermal Noise	.0086	
Scale Factor (Baseline Stability)		.0011
Zero Crossing Detector Bias		.001
RF Phase Bias		
Antenna Phase Center Motion (0.3° Diff.)		.0024
Antenna Polarization Error ($.1^{\circ}$ Element Alignment)		.001
Coax Diff. Phase ($.1^{\circ}$) (20°C Temp. Diff.)		.004
Directional Coupler Phase Diff.		.01
RCVR Diff. Phase ($.1^{\circ}$)		.001
RSS	$.009^{\circ}$ (1σ)	$.016^{\circ}$ (3σ)

TABLE 4-9

PROPAGATION OF ERRORS INTO PITCH, ROLL AND YAW

COORDINATE	MULTIPLIER	NOISE ERROR	BIAS ERROR
Pitch or Roll	$\sqrt{2}$	038° (3σ)	$.023^{\circ}$ (3σ)

COORDINATE	BIAS MULTIPLIER	BEACON LOS VECTOR SEPARATION	MULTI.	NOISE ERROR*
Yaw	< 1	7.6°	15	$.04^{\circ}$ (3σ)
		5.7°	20	$.54^{\circ}$
		3.8°	30	$.81^{\circ}$

* Integration Time: 10 sec.

4.3.3.2 Error Sources and Magnitudes

This section itemizes noise-like and bias error contributions and lists design constraints necessary to minimize error magnitudes. The propagation of these two types of error into the yaw computation is derived. The results are summarized in Table 4-8.

Error in Attitude Measurement Due to Receiver Noise and Quantization Noise - The measured values of attitude will contain a rapidly varying random error (error value statistically independent from measurement to measurement) due to interferometer receiver thermal noise. The magnitude of this noise component relative to the required accuracy in dependent upon the following major beacon RF link parameters:

a. Beacon transmitter power and antenna gain.
b. Interferometer antenna element aperture.
c. Interferometer receiver noise temperature (including the noise temperature viewed by the antenna).
d. Measurement circuit output bandwidth (or integration time).

Other less important factor which may cause variation of only a few dB due to system design variation are:

a. System equipment RF losses ($\pm$ 1 dB).
b. Receiver noise temperature ($\pm$ 1 dB).
c. Predetection bandwidth variation effect (+0, -2 dB)

Factor c accounts for the eventuality where predetection SNR becomes as low as 0 dB. These numbers (factors 5 through 7) are given to indicate system design tolerance values which should be considered in broad systems - design considerations.

The interferometer uplink beacon parameters are chosen on the basis of existing NASA ground-satellite terminal equipment. Table 4-10 itemizes the beacon link power levels, gains, losses and output SNR for the interferometer receiver-measurement averaging circuits. Note that a transmitter power of 500 watts is assumed. This value is that available from 8 GHz equipment which is normally

TABLE 4-10

INTERFEROMETER BEACON POWER & RECEIVER SNR SUMMARY

PARAMETER	VALUE	REMARKS
Total Transmitter Power	27 dBW	½ K Watt
Transmitting Circuit Loss	-3 dB	Includes Rcvr Loss
Transmitting Antenna Gain	49 dB	15' Diam.
Space Loss @ 8 GHz, R = 38,000 kM	-202 dB	
Polarization Loss	-3 dB	Circular-to-Linear
Receiving Antenna Gain	10 dB	2" Aperture, 11° Off Axis
Receiving Circuit Loss	-3 dB	Redundancy Hybrid Ant. Noise ≪ Rcvr Noise
Net Circuit Loss	-152 dB	
System Adverse Tolerances	-3 dB	
Total Received Power	-128 dB	Worst Case
Receiver Noise Spectral Density (N/B) T System (T_s) = 3800°K	-193 dBW/Hz	Rcvr NF = 10 dB
Predetection Noise Bandwidth	50 dB-Hz	BW = 100 kHz
Predetection SNR	15 dB	
Detection SNR degradation	-3 dB	Spectrum Folding
Post Detection BW "Processing Gain"	4 dB	50 kHz/20 kHz
Degradation Due to Second Channel Noise	-3 dB	
Phase Sample SNR	13 dB	5 kHz Sample Rate
Digital Filter Processing Gain	21 dB	Avg. Over 128 Samples
Measurement Output SNR	34 dB	80 Hz Measurement Rate

used in conjunction with a 15-foot parabolic reflector. This may be more power than is desirable to allocate to this function. The 8 GHz link may be operated with less beacon station ERP by one means which involves changing spacecraft receiver design. (It is assumed that interferometer antenna gain and baseline are limited to their present values by the angular acquisition requirement.) This is by reducing effective measurement noise bandwidth at the digital integrator output. This, in general, results in a lower measurement rate. Receiver design complications may result to keep predetection SNR greater than unity. (Refer to paragraph 4.3.2.2.)

Table 4-10 shows that the interferometer receiver measurement-to-noise ratio is 34 dB or a factor of 2500. For large SNR, the following expression relates SNR to σ_φ , the rms phase noise.

$$\sigma_\varphi = \sqrt{\frac{N}{S}} \qquad (4\text{-}6)$$

For S/N = 2500, σ_φ = .02 radian = 1.15 deg.
From eq. (4-3) we have (D = 32", λ = 1.5")

$$\sigma_\theta = \sigma_\varphi / 134 = .0086^\circ$$

which holds for $\theta \leq 10^\circ$.

Quantization noise is determined as follows. For the 1 MHz oscillator in the phase detector circuit, phase quantization increment is $q_\varphi = 3.6^\circ$ if the difference frequency tone from the receiver envelope detector is 10 kHz. Since the quantization noise probability density is a uniform distribution, then $\sigma_q = q_\varphi / \sqrt{12}$. The effect of the second channel is to multiply σ_φ by $\sqrt{2}$. Therefore, after averaging 128 samples,

$$\bar{\sigma}_\varphi = \sqrt{2} \times 3.6 / (\sqrt{128} \times \sqrt{12}) = .13^\circ$$

Referred to attitude, the attitude error component due to quantization error is

$$\bar{\sigma}_{\theta(q)} = .13/134 = .001^\circ$$

Scale Factor Error: Bias Error Due to Baseline Length Variation - Direction error due to scale factor error is given by

$$\Delta \theta_{S.F.} = \cot \theta_{min} \Delta L/L \qquad (4\text{-}7)$$

where θ_{min} is the minimum angle between the beacon L.O.S. vector and the interferometer plane. (See derivation below.) The value of θ_{min} is that for conditions shown in Figure 4-13 is 79°. Therefore $\Delta\theta_{S.F.} = \cot (79^o)\Delta L/32$. The baseline length variation is (from thermal analysis) $\Delta L = .0040''$ in the x-direction and .0064" in the y-direction. The worst case direction error is therefore .002°.

The direction error due to scale factor error is derived as follows: The measured electrical phase is related to measured attitude by

(1) $\cos \theta = a\varphi \qquad (4\text{-}8)$

where $a = \frac{\lambda}{2\pi L}$ is the measurement scale factor. The differential of the scale factor is related to the differential of the length by

(2) $\partial a = -\frac{a}{L} \partial L \qquad (4\text{-}9)$

Taking the partial derivative of eq. (1) with respect to θ and using eq. (2), the differential of θ is then

(3) $\partial\theta = \cot \theta \; \partial L/L \qquad (4\text{-}10)$

This expression shows that the error is small for LOS beacon vectors near the boresight. The maximum error occurs for the maximum LOS angle off the boresight. The worst case geometrical situation is shown in Figure 4-10.

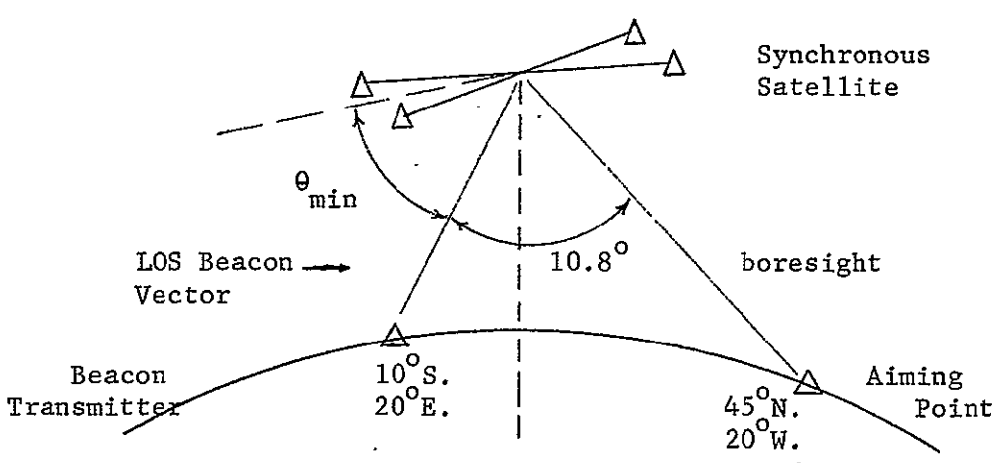

Figure 4-10. Beacon/Aiming-Point Geometry for Worst Case DSS Error due to Baseline Length Variation

Zero Crossing Detector Drift - The 2nd IF amplifier output should be as large as possible to reduce the effect of drift in amplifiers and the zero-crossing detector which follows the envelope detector. A 1-volt rms level is practical for IF amplifiers without introducing significant waveform distortion. The slope at the zero crossing of a 1 v rms sinewave is .025 v/deg. The input offset voltage drift of a good integrated circuit operational amplifier is 2.4 μv/^{o}C (RCA type CA3008A, worst case), or 0.12 mv for 50°C change. The input drift due to input offset current drift has about the same value for a 1 k-ohm source impedance (output impedance of the envelope detector).

The output of the envelope detector must be capacitively coupled to avoid the effect of detector output mean value variation with signal strength. The time constant of this coupling circuit must be high enough to result in low coupling of variations of the mean value of the detector output.

RF Bias Error Sources - Sources and magnitudes of bias error arising from RF circuit differential phase drift are as follows:

a. Antenna Phase Center Motion (0.3^{o}). Horn electrical phase center motion was measured by Cubic* by rotating the horn about its nominal phase center on the antenna range and measuring phase variation at the receiver. This was $\pm$ .3° peak over the full HPBW. There is no assurance that the two antennas would "track" or exhibit similar variational patterns, because of the random phase center motion exhibited in the experimental results.

b. Antenna Polarization Error (0.1^{o} phase). A previous study** has evaluated this source of error for the preferred polarization configuration where the ground antenna is circularly polarized and the spacecraft antenna is linearly polarized. For small angles of pitch and roll relative to the beacon L.O.S. vector, the worst case phase error due to antenna polarization misalignment is nearly

$$\Delta \varphi_p = 1.4 \, R_t \, B$$

where R_t = axial ratio of the transmitter antenna

B = tilt angle of interferometer elements

---

* Second Quarterly Report for RF Inferometer (1 May 1967 - 1 Aug. 1967), OR/111-2, Cubic Corporation.

** "ATS-4 Final Report," Vol. 7, F irchild Hiller, Dec. 1966

The 1.4 accounts for 2 random errors of value B. Assuming the axial ratio is 0.8 and the elements are aligned to 0.1°, then $\Delta\varphi_p = 0.1^{\circ}$.

c. Coaxial Cable Differential Phase (0.5° phase). Air-spaced dielectric temperature-compensated coax cable* is available which has a phase-temperature coefficient of less than 5×10^{-6} per $^{\circ}C$. Assume half the cable length is shadowed so that its temperature with insulation is $20^{\circ}C$ different from the other half. The differential phase shift is then

$(\lambda = 1.5")$:

$$\Delta\varphi_{coax} = \frac{L}{\lambda} 360 \; \Delta T \; C \qquad (4\text{-}11)$$

$$\Delta\varphi_{coax} = \frac{20 \text{ (inch)}}{\lambda \text{ (inch)}} \; 360 \text{ (deg.)} \times 20 \; (^{\circ}C) \times 5 \times 10^{-6} \; (^{\circ}C^{-1})$$

$$\Delta\varphi_{coax} = .5^{\circ}$$

This gives for attitude bias, $\Delta\theta_{coax} = .004^{\circ}$

d. Directional Coupler Phase Difference (1°). The pilot-signal directional couplers may show phase differential drifts of several degrees with temperature variation. The couplers must be before the lowpass input filters, hence a significant temperature difference may exist between them. It is assumed that the total effect will be a phase differential of 1°. It will be desirable to experimentally measure the magnitude of this error.

e. Receiver Differential Phase (0.1°). This source of bias is due to phase response variation due to the signal moving about in the receiver pass band. It is assumed that the receiver uses frequency control to maintain the signal-pilot tone difference at close to 10 kHz. This will ensure that post-detection filter differential phase response is constant. The main cause of receiver differential phase will then be in the most narrow-band predetection filter. This bandwidth is 100 kHz.

---

*"Variation of the Electrical Length of Coaxial Transmission Lines with Temperature," Tech. Bull. No. 6, Phelps Dodge Electronic Products, North Haven, Conn.

The phase characteristic of a second-order bandpass (simple L-C) filter is approximately linear near band-center with a slope of about 18° per 10 kHz in this case. If the filters in the two channels are made to track in phase, the differential error can be reduced to 1°. To avoid the major part of this error and make filter tracking design easier, it is advisable to use 2 or more pole-pairs in the bandpass filters. The phase slope can be made small at band-center and good linearity can be achieved. With these improvements, a differential phase variation (tracking error) of no more than 0.1° can be achieved with a frequency drift of 10% of the bandpass.

f. Other Bias Error Sources. Other RF differential phase variation effects will be observed due to:

1. connector VSWR changes with temperature -- can be made small.
2. horn antenna element thermal distortion -- use radomes.
3. input lowpass filter differential -- place cutoff well above the beacon frequency so that the phase characteristic is flat at the beacon frequency.
4. differential phase in hybrid-to-directional coupler lines -- use very short leads.
5. first and second IF amplifier differential phase variation -- keep bandpass much greater than 100 kHz.
6. post-detection lowpass filter differential phase variation -- keep bandpass at least twice the tone (10 kHz) frequency; use AFC on pilot tone oscillator (if necessary) to maintain the difference frequency within 10%; design post-detection filters to track in phase.

The above additional sources of error are deemed to contribute negligible bias error if the indicated design precautions are taken.

Propagation of Errors Into the Yaw Measurement - Phase measurement errors propagate into the attitude estimates according to characteristics depending on the type of error and the attitude axis. Error propagation into yaw is markedly different from that into roll and pitch. Random error propagation into yaw is greater by a factor of over 10 than propagation into roll and pitch. This is not true for bias error which tends to cancel in the computation of yaw. The particular propagation factors depend on the location of the ground beacon transmitters as defined in the antenna platform coordinate system.

The relations describing the propagation of errors of phase measurement into estimates of antenna platform coordinates are developed in Paragraph 4.3.3.4. Equation (4-11) expresses roll, pitch and yaw estimate errors in terms of electrical phase errors induced by baseline length errors, random (noise) errors and electrical phase bias errors. The interferometer arms along the roll and pitch axes propagate errors into roll and pitch attitude approximately as the RSS of the two error components. The propagation characteristic of main interest is that of errors into the yaw estimate.

Referring to Eq. (4-11), it is seen that the ratio of propagation of random noise into yaw and pitch is ($\delta_{\sigma 3}$ is yaw estimate error due to random noise, etc.)

$$\frac{\delta_{\sigma 3}}{\delta_{\sigma 2}} = \frac{(b_{31}\,\sigma_{11} + b_{33}\,\sigma_{21})F_1}{(b_{21}\,\sigma_{11} + b_{23}\,\sigma_{21})F_1}$$

where the b_{ij} are the elements of B^{-1} as defined in Eq. (4-8a). Assuming $\sigma_{ij} = \sigma_{2j}$, then since they will be uncorrelated,

$$\frac{\delta_{\sigma 3}}{\delta_{\sigma 2}} = \frac{|b_{31}| + |b_{33}|}{|b_{21}| + |b_{23}|} .$$

Substituting for b_{ij} and noting that r_{ij} are the direction cosines of the angles α_{ij},

$$\frac{\delta_{\sigma 3}}{\delta_{\sigma 2}} = \frac{\cos \alpha_{23} + \cos \alpha_{13}}{\cos \alpha_{12} + \cos \alpha_{22}}$$

For convenience in comparing noise-induced yaw and pitch errors, consider the case where the aiming point is ground beacon transmitter #1. This will make $\cos \alpha_{13} = 1$ and $\cos \alpha_{12} = 0$. (See Figure 4-11 for description of direction angles.)

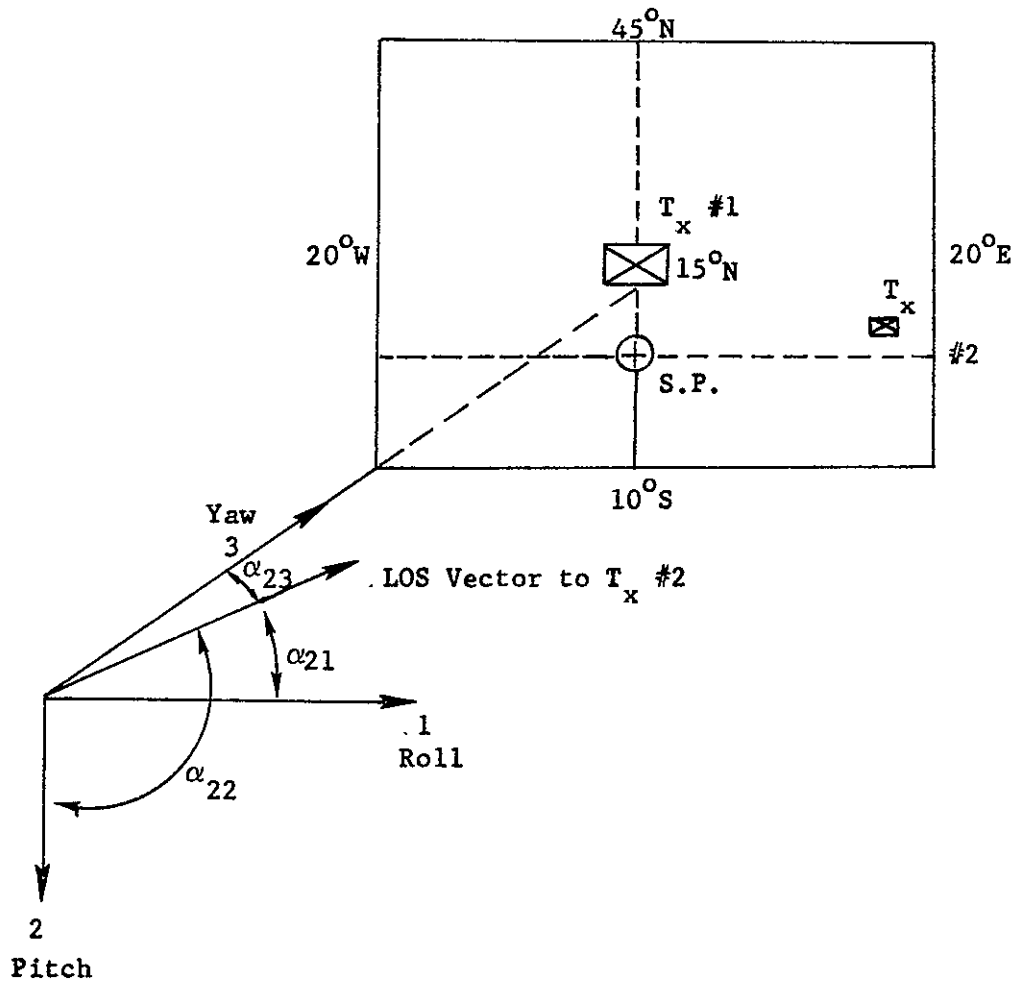

Fig. 4-11 Description of Direction Angles to LOS Vector to Ground Beacon Transmitted #2 When the Aiming Point (3-axis) is Aligned with Beacon #1.

The ratio of noise-induced yaw and pitch errors for the case where LOS vector #1 is colinear with the 3 axis is then

$$\frac{\delta_{\sigma 3}}{\delta_{\sigma 2}} = \frac{1 + \cos \alpha_{23}}{\cos \alpha_{22}}$$

Clearly, the random error in the yaw estimate becomes unlimited as α_{22} approaches $\pi/2$. This result agrees with results of antenna control subsystem computations, Section 6. As noted there, singularities in the solution of the yaw estimate may be avoided by proper choice of the three out of four equations contained in Eq. (4-18) for $i = 1,2$.

The above ratio is plotted for lines of constant yaw-to-pitch random error in Figure 4-12. This plot is for the special case where the yaw axis is aligned with the LOS vector to Beacon #1. Beacon #2 is off the yaw axis by angle α_{23} and at an azimuth angle relative to a north-south (pitch) plane. Values on this plot are within 10% of the correct value for the general case where $\alpha_{13} \neq 0$, i.e., for the yaw axis <u>not</u> aligned with the #1 beacon LOS vector. This is because the minimum value of α_{12} is about 84°, causing about a 10% change in values. The plot is symmetrical about the vertical axis. Also, the plot may be turned on its side to represent results for the case where Beacon #2 is located at azimuth greater than 45° from the pitch axis and the alternate set of equations as discussed above.

The data of Figure 4-12 has been applied to the case of Beacon #1 located 15° latitude and 0° longitude relative to the satellite subpoint. Restrictions for the location of Beacon #2 are given in Table 4-11. Only the case where Beacon #2 is located due north or south of Beacon #1 is considered.

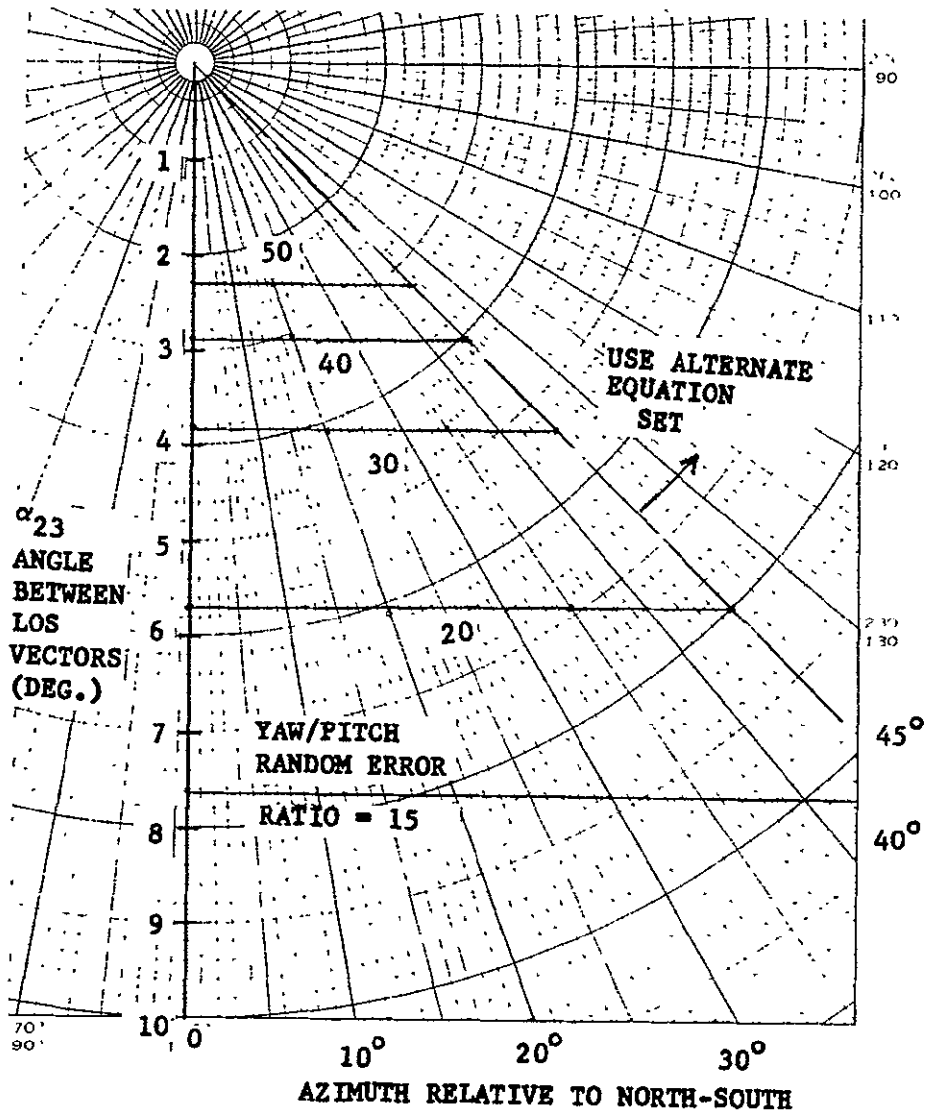

Fig. 4-12 Yaws/Pitch Random Error Ratio vs Angle Between LOS Vectors. The LOS Vector to Beacon #1 is Colinear with the 3-Axis.

TABLE 4-11

BEACON #2 LOCATION VS YAW/PITCH RANDOM ERROR RATIO. BEACON #1 IS LOCATED AT 15° LAT., 0° LONG. RELATIVE TO SATELLITE SUBPOINT

Yaw/Pitch Random Error Ratio	Beacon #2 Must be Located South of - or - North of	
20	18° S. Lat.	64° N. Lat.
30	7° S. Lat.	41° N. Lat.
40	2° S. Lat.	34° N. Lat.
50	2° N. Lat.	30° N. Lat.

4.3.3.3 Interferometer Errors - Supporting Analysis

The Interferometer Equation. The interferometer measures the direction cosine of the angle α between each baseline and the beacon LOS vector.

$$\cos \alpha_{ij} = M'_{ij} / (2\pi(L_j/\lambda_i) \qquad (4\text{-}12)$$

where

- i = 1,2 = beacon transmitter number
- j = 1,2 = roll or pitch - oriented baseline
- M' = the measured phase
- L/λ = baseline length in wavelengths
- L_j = baseline length of jth interferometer arm
- λ_i = wavelength of ith beacon sinusoid

The angle α is defined as being measured from one end (the +x or +y axis) of the interferometer arm. This is so that for $\alpha > 90$, $\cos \alpha < 0$.

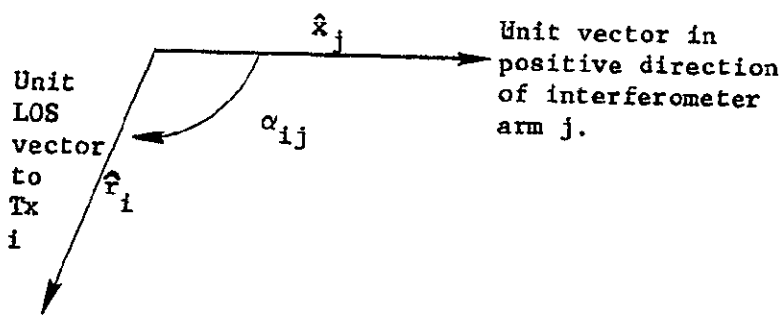

Figure 4-13 Direction Angle from Interferometer Arm j to LOS Vector to Transmitter i.

The beacon LOS unit vector $\hat{r}_i$ may be expressed in measured attitude coordinates and desired coordinates by the matrix product.

$$\hat{r}_i = \begin{bmatrix} r_{i1} & r_{i2} & r_{i3} \end{bmatrix} \begin{bmatrix} x_1 \\ x_2 \\ x_3 \end{bmatrix} = \begin{bmatrix} r'_{i1} & r'_{i2} & r'_{i3} \end{bmatrix} \begin{bmatrix} x'_1 \\ x'_2 \\ x'_3 \end{bmatrix}$$

where

$$\left.\begin{array}{l} r'_{iu} = \text{components of } \hat{r}_i \text{ in the } x'_u \text{ direction} \\ r_{iu} = r'_{iu} \text{ in required direction } x_u \text{ of } x'_u \end{array}\right\} u = 1,2,3$$

$\left[\quad\right]$ = column matrix of unit vectors.

Or, the vector $\hat{r}_i$ can be expressed in matrix notation by

$$\hat{r}_i = R_i^T X = (R'_i)^T X' \tag{4-13}$$

where R_i and R'_i are the row matrices and X and X' are the column matrices defined above.

The unit vectors x'_1, x'_2, x'_3 of the measured attitude can be rotated into the required set x_1, x_2, x_3 by rotations defined by matrices T_1, T_2, and T_3 where

$$T_a = T_a(\theta) = \{t_{ij}(\theta)\}$$

and

$$t_{aa} = 1, \; t_{ja} = t_{aj} = 0$$

$$t_{ii} = \cos\theta$$

$$t_{ij} = \pm\sin\theta$$

Error analysis deals with the condition where attitude variations from the required are small. The coordinate rotation $T_1T_3T_2^T$ for small angular offsets d_i gives the following approximate relation between actual and required coordinate orientations.

$$X = AX' \tag{4-14}$$

where

$$A = \begin{bmatrix} 1 & d_1 & -d_2 \\ -d_1 & 1 & d_3 \\ d_2 & -d_3 & 1 \end{bmatrix}$$

Substituting for X from eq. (4-14) into (4-13) gives

$$R_i'^T X' = R_i^T AX' \tag{4-15}$$

Eq. (4-4) indicates that

$$R_i'^T = R_i^T A \tag{4-16}$$

To form the difference between measured and required direction cosines, subtract R_i^T from Eq. (4-16). After transposing the resultant, it may be written as

$$R_i' - R_i = B_i D \tag{4-17}$$

where

$$B_i = \begin{bmatrix} 0 & r_{i3} & -r_{i2} \\ -r_{i3} & 0 & r_{i1} \\ r_{i2} & -r_{i1} & 0 \end{bmatrix}, \quad D = \begin{bmatrix} d_1 \\ d_2 \\ d_3 \end{bmatrix}$$

If the interferometer arms are exactly aligned with the coordinate system X', then

$$r'_{ij} = \cos \alpha_{ij} \ , \ j = 1,2$$

Eq. (4-6) then becomes (the measurement of α_{i3} is not available since the interferometer has no third arm)

$$C_i - [1 \quad 1 \quad 0] R_i = \begin{bmatrix} 1 & 0 & 0 \\ 0 & 1 & 0 \\ 0 & 0 & 0 \end{bmatrix} B_i D \tag{4-18}$$

where

$$C_i = \begin{bmatrix} \cos \alpha_{i1} \\ \cos \alpha_{i2} \end{bmatrix}$$

The left hand side of Eq. (4-18) represents the difference between measured direction cosines, C_i, and required direction cosines. Since D consists of three variables the method of solving Eq. (4-18) is either to furnish a value for one of the variables (e.g., the yaw offset d_3) or make a second pair of measurements using a second ground beacon along a new LOS vector $\hat{r}_2$. Assuming the more general case, measurements on the second beacon provide a total of four equations. Using three of these in the form of Eq. (4-17), the solution for the offsets is

$$D = B^{-1}(C-R) \tag{4-19}$$

where

$$C = \begin{bmatrix} \cos \alpha_{11} \\ \cos \alpha_{12} \\ \cos \alpha_{21} \end{bmatrix} \ , \quad R = \begin{bmatrix} r_{11} \\ r_{12} \\ r_{21} \end{bmatrix}$$

$$B = \begin{bmatrix} 0 & r_{13} & -r_{12} \\ -r_{13} & 0 & r_{11} \\ 0 & r_{23} & -r_{22} \end{bmatrix}$$

A solution exists for Eq. (4-8) if B^{-1} is not singular. This is the case if det $B \neq 0$.

$$\det B = r_{13}(r_{12}\, r_{23} - r_{13}\, r_{22}) \neq 0$$

Therefore $r_{13} \neq 0$ and $r_{12}\, r_{23} \neq r_{13}\, r_{22}$. These relations mean that the beacon LOS vector must have a 3-axis component, i.e., the vector cannot lie in the plane of the interferometer arms. Also, $r_{12} \neq r_{22}$ and $r_{13} \neq r_{23}$, i.e., the beacon LOS vectors must be distinct.

The inverse of B is

$$B^{-1} = \frac{r_{13}}{\det B} \begin{bmatrix} -r_{11}\, r_{23}/r_{13} & (r_{13}\, r_{22} - r_{12}\, r_{23})/r_{13} & r_{11} \\ -r_{22} & 0 & r_{12} \\ -r_{23} & 0 & r_{13} \end{bmatrix} \qquad (4\text{-}20)$$

Eq. (4-19) may be called the interferometer equation and provides the basis from which error analysis may be developed.

Error Analysis

The error components in the measurement of attitude angle offsets may be expressed by

$$\begin{bmatrix} d_1 + \delta_1 \\ d_2 + \delta_2 \\ d_3 + \delta_3 \end{bmatrix} = B^{-1} \begin{bmatrix} k(M_{11} + \sigma_{11} + \eta_{11})(F_1 + \epsilon_1) - r_{11} \\ k(M_{12} + \sigma_{12} + \eta_{12})(F_2 + \epsilon_2) - r_{12} \\ k(M_{21} + \sigma_{21} + \eta_{21})(F_1 + \epsilon_1) - r_{21} \end{bmatrix} \qquad (4\text{-}21)$$

where Eq. (4-12) has been substituted for C in Eq. (4-8) and the following substitutions have been used;

$M' = M + \sigma + \eta$ = the phase estimate

$\frac{1}{L} = F + \epsilon$ = the inverse baseline length estimate

$k = \lambda / 2\pi$

Expanding products and dropping second-order terms, Eq. (4-21) gives

$$D + \begin{bmatrix} \delta_1 \\ \delta_2 \\ \delta_3 \end{bmatrix} = B^{-1}(C-R) + kB^{-1} \begin{bmatrix} M_{11}\ \epsilon_1 \\ M_{12}\ \epsilon_2 \\ M_{21}\ \epsilon_1 \end{bmatrix} + kB^{-1} \begin{bmatrix} F_1(\sigma_{11} + \eta_1) \\ F_2(\sigma_{12} + \eta_2) \\ F_1(\sigma_{21} + \eta_1) \end{bmatrix} \qquad (4\text{-}22)$$

The errorless part of Eq. (4-22) can be removed by subtracting Eq. (4-19). The remaining error portion may be written as the three antenna platform coordinate errors δ_1, δ_2 and δ_3 in the matrix form.

$$\delta = kB^{-1}(M\epsilon + F\sigma + G\eta) \qquad (4\text{-}23)$$

where

$$\delta = \begin{bmatrix} \delta_1 \\ \delta_2 \\ \delta_3 \end{bmatrix}, \quad \epsilon = \begin{bmatrix} \epsilon_1 \\ \epsilon_2 \end{bmatrix}, \quad \sigma = \begin{bmatrix} \sigma_{11} \\ \sigma_{12} \\ \sigma_{21} \end{bmatrix}, \quad \eta = \begin{bmatrix} \eta_1 \\ \eta_2 \end{bmatrix}$$

$$M = \begin{bmatrix} M_{11} & 0 \\ 0 & M_{12} \\ M_{21} & 0 \end{bmatrix}, \quad F = \begin{bmatrix} F_1 & 0 & 0 \\ 0 & F_2 & 0 \\ 0 & 0 & F_1 \end{bmatrix}, \quad G = \begin{bmatrix} F_1 & 0 \\ 0 & F_2 \\ F_1 & 0 \end{bmatrix}$$

The first term on the right of (4-11) is the scale factor error due to baseline length errors ϵ_j . The second term is random, noise-like error due to receiver thermal and quantization noise. The third term is receiver electrical bias error and has two terms, one for each arm and its receiver channel.

Equation (4-11) can be readily developed into an equation for the covariance matrix of attitude errors

$$P = \{ \sigma^2_{\delta_i \delta_j} \} = U P_\epsilon U^T + V P_\sigma V^T + W P_\eta W^T \tag{4-24}$$

where

$$U = k B^{-1} M \qquad P_\epsilon = \begin{bmatrix} \sigma^2_{\epsilon 1} & 0 \\ 0 & \sigma^2_{\epsilon 2} \end{bmatrix}, \text{ etc.}$$

$$V = k B^{-1} F$$

$$W = k B^{-1} G$$

This formulation assumes that the random variables are independent and that over a long period of measurements, the average error of the bias components is fixed (stationary random process). Equation (4-24) may be used in computer evaluation of error propagation into pitch, roll and yaw measurements.

Nonorthogonality of Interferometer Arms

To examine the effects of nonorthogonality of interferometer baselines it is necessary to inject into Eq. (4-17)a term relating measurements made by the nonorthogonal measurement system to the LOS vector expressed in the orthogonal coordinate system.

Consider the case where arms 1 and 2 are misaligned in the plane of the arms by angles β_1 and β_2 as in Figure 4-14.

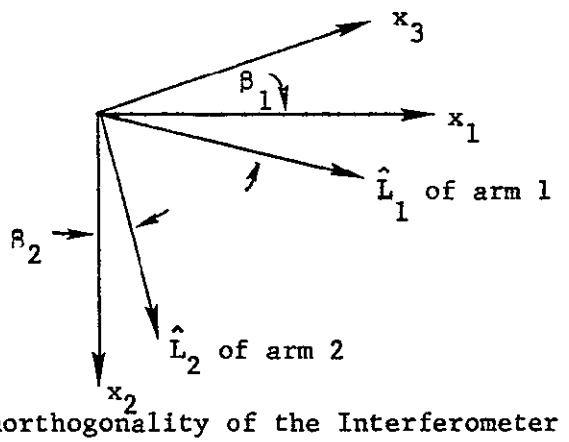

Figure 4-14. Nonorthogonality of the Interferometer Arms

The measured direction cosines are related to the LOS vector expressed in coordinate system X' by

$$\begin{bmatrix} \cos \alpha_{i1} \\ \cos \alpha_{i2} \end{bmatrix} = \begin{bmatrix} \cos \beta_1 & \sin \beta_1 & 0 \\ \sin \beta_2 & \cos \beta_2 & 0 \end{bmatrix} \begin{bmatrix} r'_{i1} \\ r'_{i2} \\ r'_{i3} \end{bmatrix}$$

or in matrix notation.

$$C_i = TR'_i$$

Multiplying Eq. (4-17) by T produces

$$T(R_i' - R_i) = T\ B_i\ D$$

or

$$C_i - TR_i = T\ B_i\ D \tag{4-25}$$

Equation (4-25) may be used to determine the effect of misalignment of the interferometer arms. To determine the effect of non-orthogonality, arm 2 may be assumed to be perfectly aligned and the total orthogonality error be contained in angle β_1.

Matrix T then becomes (for $\beta_1 \ll 1$)

$$T = \begin{bmatrix} 1 & \beta_1 & 0 \\ 0 & 1 & 0 \end{bmatrix}$$

By following the procedure of the error analysis above, D becomes the true offset plus the error, i.e., D becomes D + δ and C becomes C + (measurement errors). The error part is (second row only)

$$-r_{i3}\ \delta_1 + r_{i1}\ \delta_3 + \beta_1\ r_{i2} = k(M_{12}\ \epsilon_2 + F_2\ \sigma_{i2})$$

The effect of error component $\beta_1 r_{i2}$ compared to the effect of random noise error may be expressed by

$$\frac{\partial\delta_1/\partial\beta_1}{\partial\delta_1/\partial\sigma_{i2}} = \frac{r_{i2}}{kF_2}$$

For small angular offsets $r_{i2} \approx r_{i2}' = \cos\alpha_{i2}$. Substituting for kF from Eq. (4-21).

$$\frac{\delta_{orthog.}}{\delta_{noise}} = \frac{2\pi\lambda}{L}\cos\alpha_{i2} \tag{4-26}$$

Equation (4-26) reveals that the non-orthogonality-induced error is maximum for minimum α. Also, this result shows that the attitude error due to non-orthogonality of interferometer baselines decreases with increasing baseline length.

4.3.3.4 Interferometer Measurement Error Due to Spacecraft Solar Panels

Summary. The geometry of the DSS ground beacon transmitter - solar panel - interferometer antenna signal path has been investigated. It is concluded that a reflection from the solar panel can cause a significant error when the solar panel is downward. Furthermore, shadowing of the small-aperture interferometer antenna can occur for some ground transmitter locations and the anticipated antenna mast height.

Recommendations include:

1. reduce reflection-induced error by increasing interferometer baseline length;
2. avoid using flat surfaces on the solar panel edges to cause a diffuse reflection;
3. restrict ground beacon transmitter location to places north of 10° S latitude (antenna platform assumed to be on north end of despun axis) to reduce the minimum mast height required to avoid shadowing of the interferometer by the solar panels.

It is not recommended that either antenna mast height or interferometer beamwidth be reduced to reduce the effect of the reflection. This is because the magnitude of the error can be reduced by other means listed above. In addition, there is a large degree of uncertainty concerning the error magnitude. Beamwidth reduction would increase the aperture which would increase interference power from the near-by 12.2 GHz source. Furthermore, beamwidth reduction below 30° would be required for anticipated antenna mast heights, which would violate the constraint that reception will be from uplink stations which view the spacecraft with greater than 25° elevation.

The solar panels will probably cause significant measurement error due to reflections of the interferometer beacon signal as the solar panels pass through the interferometer patterns. A rough estimate gave an attitude error on the order of $.05^{\circ}$ or greater. Increasing antenna mast height or decreasing interferometer beamwidth is not recommended since an extreme amount of either change would be necessary. The attitude measurement error due to reflection can be decreased by increasing the interferometer baseline length. It is recommended that the solar panel edge structure should not be flat but should have a shape which causes the reflection to be as diffuse as possible in character.

It can be shown that shadowing of the interferometer antenna elements by the solar panels can occur for beacon transmitters in the southern hemisphere. It is felt mast height should not be required to be extended for the DSS function. Instead, the location of DSS beacon ground transmitters should be restricted to a maximum southern latitude of about 10° for a mast height of 5.7 feet (1.74 meters) and a spacecraft attitude tolerance of $\pm 5^{\circ}$.

4.3.4 Preliminary Interferometer Physical Configuration

4.3.4.1 Summary. Reference to the ATS-4 study* provides the following physical configuration characteristics and the pertinent rationale. See Figures 4-15 through 4-17.

1. Crossed-interferometer arms of superinsulated lead-in cables. The thermal isolation from the space environment will minimize thermal difference between lead-ins, minimizing phase differential. The cross configuration permits making equal the lengths of the RF coupling to each horn. Mounting points are at each end to minimize horn motion along the earth-vector. Mounting points must accommodate thermal extension of the length due to truss thermal flexure. This configuration is most appropriate for the quad configuration of the large aperture antennas.** The T-configuration may require an L-shaped alternate to the crossed-arm configuration interferometer.

2. Linearly-polarized diagonal horns mounted on extensions to raise the horns above the large antenna surface so that coupling from the 12.2-GHz feed is reduced. Horn out-of-plane motion due to thermal distortion, etc., must be less than .004 inch for 1° of electrical phase error.

3. Interferometer receiver located on the antenna platform at the approximate center of the crossed arms. This receiver location minimizes RF cable lengths, keeping differential phase shifts small. The 12.2 GHz isolation filters are located within the superinsulation envelope. This is to cause the filter temperature to vary over a minimum range. The receiver and RF lines must be isolated

---

*ATS-4 Study Program Final Report, Vol. 7, Fairchild-Hiller Space Systems Division, December 1966.

**Mechanical Integration IRR #2, APSS & SS, Department 553-5, MI-IRR-2, December 12, 1968.

from the 12.2 GHz feed transmission lines. Thermal isolation of the receiver should maintain a receiver temperature range of 0.to 40° C. Note that the receiver will dissipate approximately 5 watts.

4. The coarse measurement (short baseline) horn has been omitted to simplify the interferometer receiver. Omitting this function is feasible because the ambituity resolution may be performed by independent means. Attitude angle measurement ambiguity interval is 2.7°.for the 32-inch (81.28 cm) baseline at 8 GHz. Initial ambiguity resolution may be accomplished by ground beam position measurements. Unambiguous measurements may then continue by identifying the phase quadrant of each measurement.

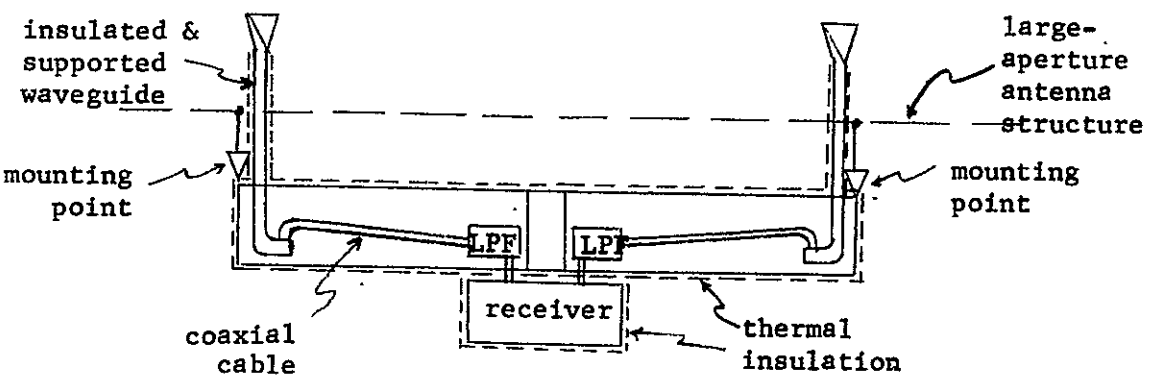

Figure 4-15. Crossed-Arm Interferometer Configuration (sketch)

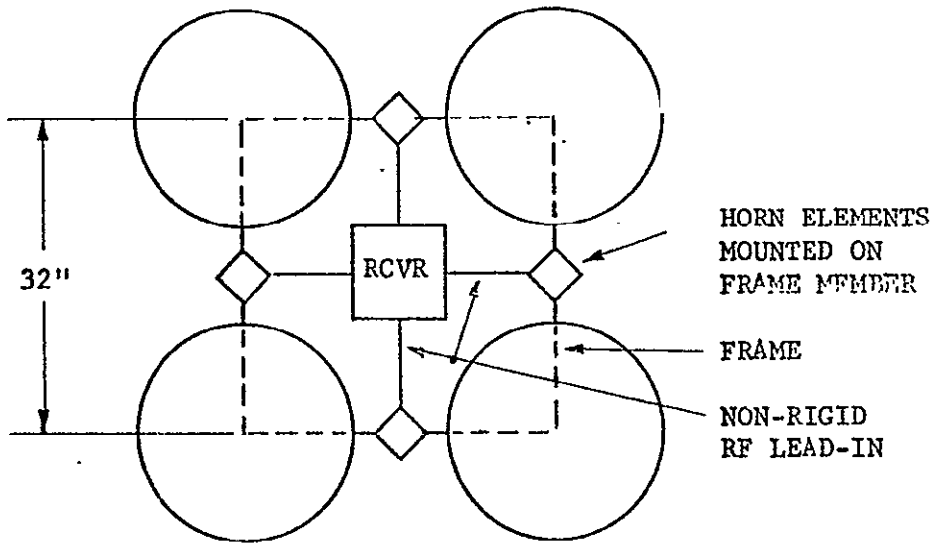

FIGURE 4-16. INTERFEROMETER HORN ANTENNA ELEMENT MOUNTING LOCATION, PLAN VIEW

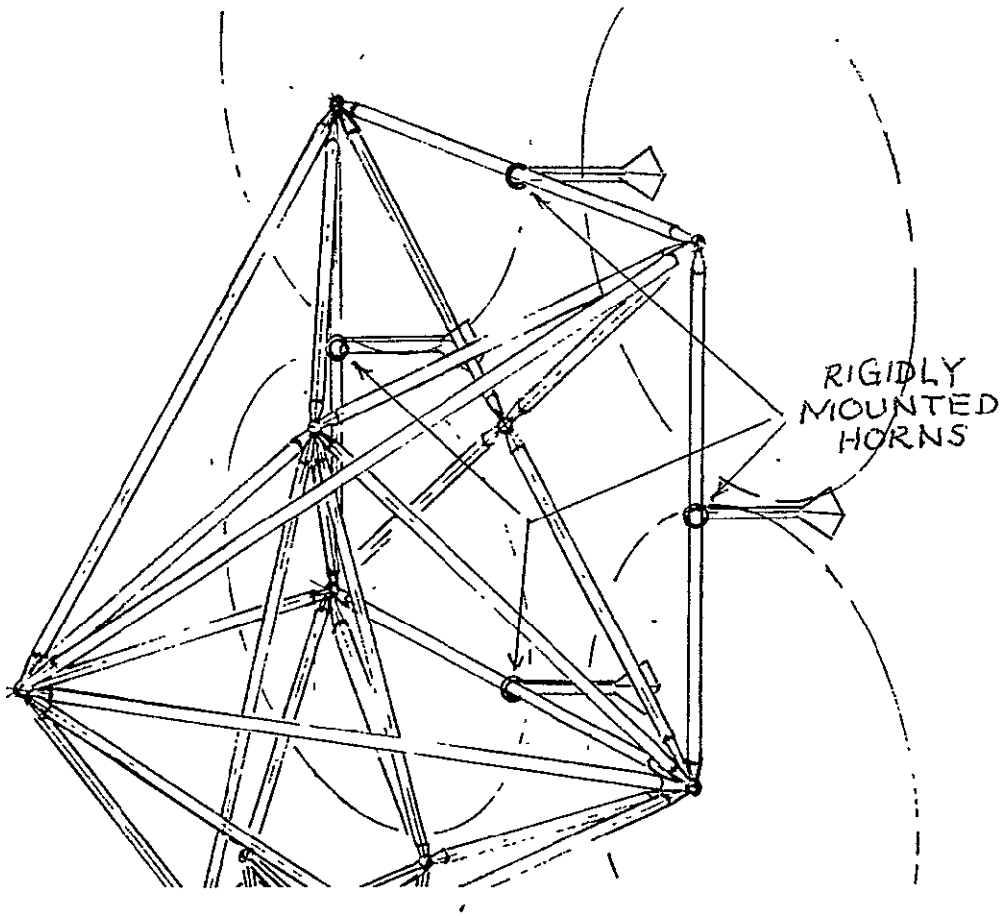

FIGURE 4-17. HORN MOUNTING, ISOMETRIC VIEW

4.3.5 RELIABILITY ANALYSIS OF INTERFEROMETER RECEIVER

The interferometer receiver with various configurations for switching the receiver input between interferometer arms and switching to a redundant receiver has been evaluated for reliability. The input switching arrangement with the best reliability was selected and overall receiver probability of success for 5 years was evaluated.

4.3.5.1 Summary. Of five configurations analyzed, a receiver system using a standby redundant receiver with PIN-diode switching between interferometer arms and a hybrid power-splitter to couple to the redundant receiver has the highest probability of success over a five-year mission period. The computed probability of success for the dual local oscillator receiver up through the phase detector but not including the subsequent digital averaging circuits is .97 over 5 years. It should be noted that the reliability evaluation was performed for the dual-local oscillator type of receiver. The pilot-tone receiver is, however, the preferred receiver design. The circuits are very similar in parts content by function: the dual local oscillator (L.O.) is replaced by the first L.O. and pilot tone oscillator of the preferred design; the preferred design contains an addition 2nd IF amplifier, but this addition will decrease the probability of success by only .004. The additional circuitry of the digital filter will add only a small additional failure rate because of the high reliability of digital integrated circuits. Adding a redundant L.O. and pilot tone oscillator would cut the failure rate in approximately half as may be seen from the calculations in Figure 4-19. Therefore we may conclude the following approximate reliability for the interferometer receiver and digital filter:

Configuration: (Pilot Tone Receiver)

a. PIN diode switching between interferometer arms

b. Hybrid coupling of signal to standby redundant receiver.

c. Redundant local oscillator and pilot tone oscillator - multiplier chain.

Probability of success at 5 years: .97

4.3.5.2 Reliability Analysis. Several receiver input configurations using the receiver block as a failure rate constant were evaluated for their relative probability of success. The receiver itself was analyzed from a parts-count itemization first and the results used in the overall configuration model. The receiver input switching configuration with the greatest probability of success over a five-year mission was then determined.

Functional block diagram for the receiver is shown on Figure 4-18 and the reliability block diagram is on Figure 4-19. It appears obvious from the total total failure rate for the Local Oscillator and the Double-Local Oscillator that these two units will require some sort of redundancy. However, for the purpose of this study, the receiver will be as shown.

Of the five configurations analyzed, the receiver system using the standby receiver with PIN-diode switching and the hybrid to couple to the redundant receiver has the highest probability of success over a five-year period.

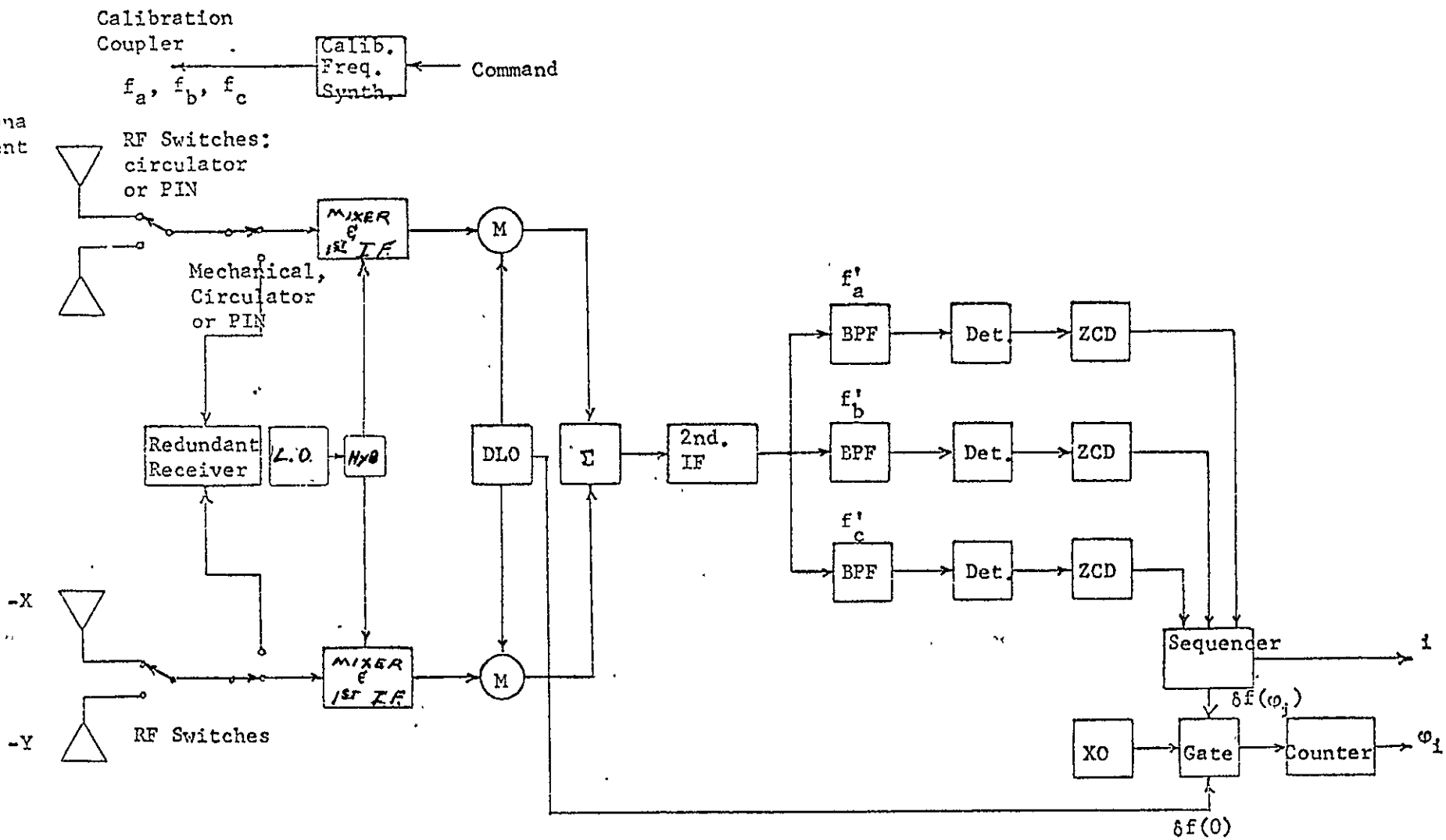

Figure 4-18. Multiple Frequency, Single Receiver Approach. Ground stations transmit continuously on frequencies f_a and f_b. The receiver is switched between arms X and Y with circulator or PIN diode RF switches.

TABLE 4-12. CONSOLIDATED RELIABILITY ANALYSIS - INTERFEROMETER RECEIVER

	CONFIGURATION	PROBABILITY OF SUCCESS at 5-Year	RANK
A	Circulator Switching-Standby	0.8158	4
B	Pin Diodes S_1, S_1' Circulator Standby S_2, S_2'	0.8664	2
C	Pin Diodes S_1, S_1' Hybrid Power Splitter Standby S_2, S_2'	0.9197	1
A	Circulators-Active	0.6732	5
B	Pin Diodes-Active	0.8574	3

The reliability of the approach using PIN diode switches and a standby redundant receiver was recomputed for the case where each receiver has a standby redundant local oscillator - pilot tone multiplier chain. This configuration is preferred because the oscillator presents the largest reliability penalty of any single block in the receiver. Using standby redundant oscillators, the receiver probability of success is increased from .74 to .88. The receiver system P_s is then raised from .92 to .97.

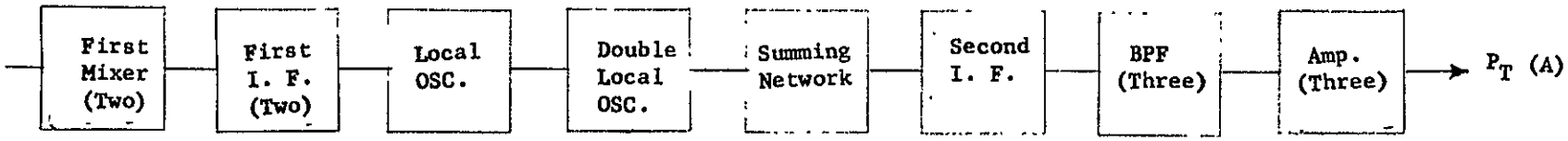

λ (Unit)	.0220	.0414	.3005	.1298	.0015	.0298	.0020	.0029	%/1000 Hr
λ (Total)	.0440	.0828	.3005	.1298	.0015	.0298	.0020	.0029	%/1000 Hr
λ (Total)	.5933								%/1000 Hr

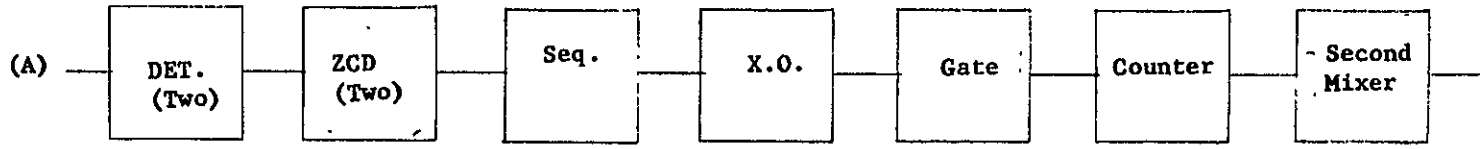

λ (Unit)	.0027	.0093	.0045	.0317	.0045	.0045	.0230	%/1000 Hr
λ (Total)	.0071	.0186	.0045	.0317	.0045	.0045	.0230	%/1000 Hr
λ (Total)	.0939							%/1000 Hr

$\lambda t = \underline{.6872}$

$P_s(5\ yR) = .7401$

LO Redun. $P_s(5\ yR) = (2P_3 - P_3^2)\ P_1P_2 \sum_4^{15} P_i(t) = .8313$

LO & D. LO Redundant $P_s(5\ yR) = (2P_3 - P_3^2)\ (2P_4 - P_4^2)\ P_1P_2 \sum_5^{15} P_i(t) = .8772$

FIGURE 4-19. RELIABILITY BLOCK DIAGRAM - RECEIVER ONLY

4.4 SENSING THE DIRECTION OF SATELLITE NARROW ANTENNA-BEAM AXES BY PATTERN MEASUREMENT AT GROUND RECEIVERS

The DSS is required to perform the following additional function not performed by previously developed spacecraft functions. The DSS must

a. Measure antenna platform attitude employing signal(s) which use the spacecraft large-aperture transmitting antennas;

b. Locate the beam pattern geometric center orientation with an accuracy of $\pm$ .05° in antenna platform pitch and roll and $\pm$ .5° in yaw.

c. Convert the attitude measurements to attitude correction signals to be transmitted to the spacecraft attitude control system.

d. Provide spacecraft antenna platform attitude measurements simultaneously or in sequence with spacecraft interferometer attitude measurements.

In addition the following requirements are derived from the preferred DSS approach derived in paragraph 4.3.

e. Provide a means of redundant spacecraft antenna platform attitude measurement in event of spacecraft interferometer system failure or measurement interruption.

f. Provide a means of resolution of ambiguity of measurements made by the interferometer.

The sections below develop a preferred DSS technique which makes direct measurements of the patterns of the spacecraft transmission antennas. The required ground receiving equipment is developed to a functional level and special receiver characteristics and ground computation requirements are described. Error analysis of the developed DSS technique is presented.

4.4.1 Direction Sensing by Beam Pattern Measurements on the Ground: Summary

The recommended technique of direction sensing employing signals which use the spacecraft transmission antennas is making direct measurements of the patterns at ground receivers. Other techniques were investigated. However, they in general involve additional feeds on the transmission antennas located close to the main feed. The resulting additional aperture blockage or feed mutual coupling would raise the sidelobe level above the -25 dB requirement placed on the design of the transmission antennas. Section 4.2 compares the various alternate approaches.

The recommended approach makes signal power measurements on the main transmitted signal (if angle modulation is used) with bandwidths up to 50 MHz. This is feasible with spacecraft ERP of 63 dBW or more. For operation with less ERP or if amplitude modulation is employed on the main beams, a constant power signal in a vacant area of the 12 GHz frequency spectrum must be used. In this case an ERP of 50 dBW provides the necessary attitude measurement accuracy if receiver bandwidth is equal or less than 2.5 MHz.

Two approaches are developed for spacecraft antenna platform attitude measurement by measuring beam pattern characteristics at ground receivers. The first approach utilizes the spacecraft antenna - ground receiver site effectively as an antenna range (see paragraph 4.4.3). Since reflections at the ground receiver are negligible for a dish antenna, then pattern measurement accuracy is limited only by the accuracy of receiver relative power measurement equipment and attitude actuator or stepper resolution. Present simply antenna range practices permit location of the beam axis within 1/50 of the HPBW. This corresponds to $.05^{\circ}$ for a 2.7° HPBW. Averaging data over several antenna pattern cuts should reduce the uncertainty of the axis location.

A second approach uses small attitude increments in orthogonal or quadrative directions and measures the resulting power changes at a ground receiver located off the beam axis. (See paragraph 4.4.7.) This technique requires the prior, accurate measurement of the antenna pattern. Figure 4-20 presents the estimated error for this DSS technique. It is seen from the curve that

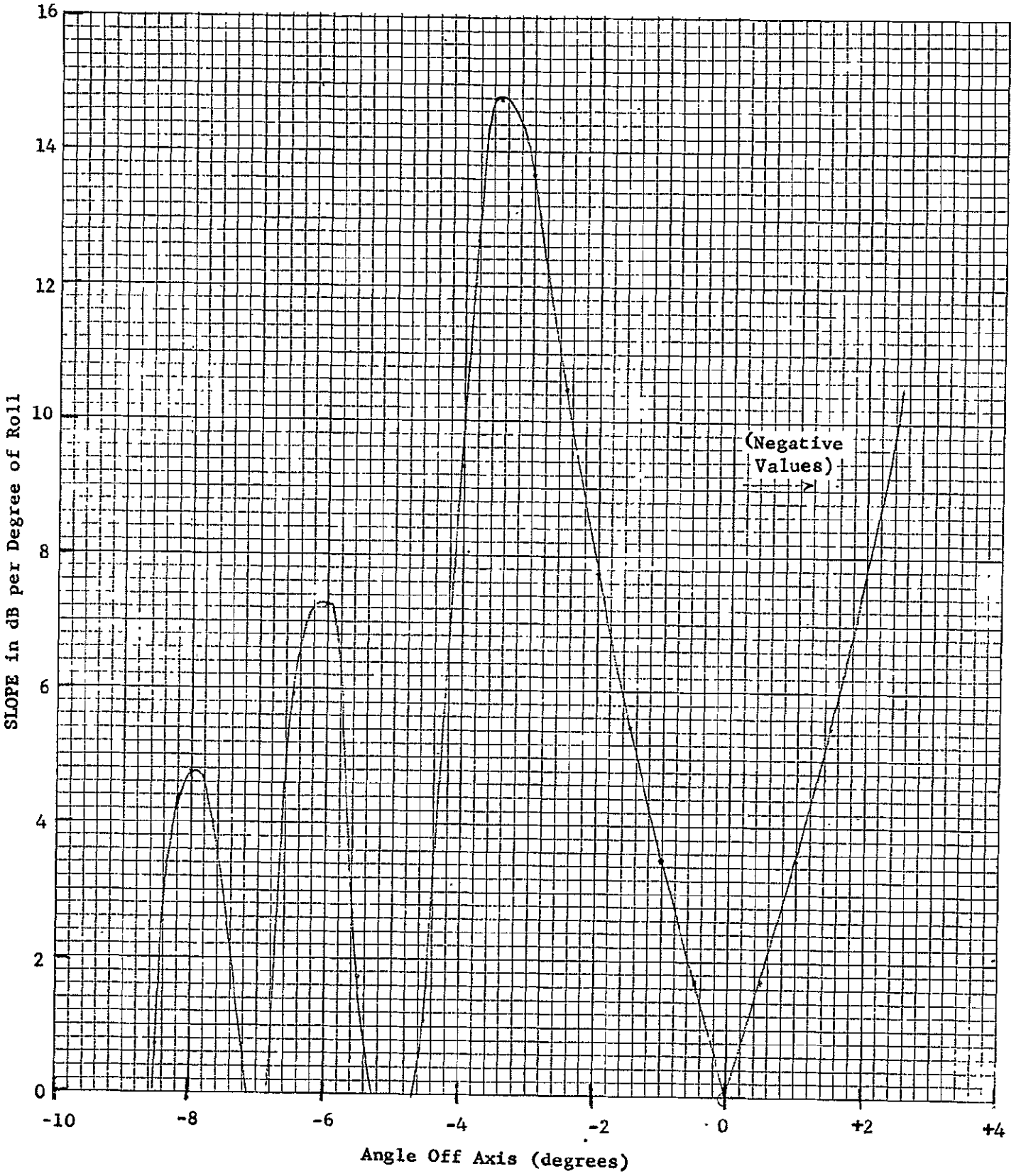

Figure 4.20 Antenna Pattern Slope (Prime Focus Feed, 28" Diam. with Blockage, 40° Azimuth)

the attitude increment must be less than $.10^{\circ}$ for accuracy approaching the required $.05^{\circ}$. It should be noted that making a series of measurements (incrementing attitude in a square pattern) should reduce the error.

Paragraph 4.4.4 develops error analyses for the relative power pattern measurement techniques. Paragraph 4.4.6 itemizes the procedure to resolve ambiguity in the spacecraft interferometer measurement using the ground receiving equipment.

4.4.2 Direct Beam Pattern Measurement Techniques

To measure antenna patterns while in orbit, the spacecraft antenna platform, antennas and ground receiver terminal may be used in a manner similar to the antenna pattern-measuring range. The antenna platform attitude is adjusted in two degrees of freedom in 0.06 degree steps. These relative positions are telemetered to the ground in terms of the number of steps. An error in attitude exists for each step position due to stepper resolution. At the ground receiver, power change is measured in a constant gain receiver. The power measurement is made relative to the on axis, beam peak power value, hence absolute accuracy of the power meter is unimportant. The important factor is resolution of the meter which may be expressed in terms of the power measuring device's differential linearity.

The beam pattern is measured by the following procedure. The antenna platform is moved in one degree of freedom until a maximum signal level is found. The platform is then stepped through the orthogonal degree of freedom from beam edge to edge and power readings are made at each step. This process may be repeated in the perpendicular direction to get a right-angle pattern cut, where the two cuts intersect near the beam peak. Additional parallel pattern cuts may be made off beam peak. Pattern data may be smoothed by computer curve fitting. Pattern measurement cuts may be repeated to average error due to stepper resolution and power meter resolution.

The above procedure provides a definition of pattern axis location. The technique is called the sequential power measurement method and is developed in paragraph 4.4.3. The accuracy parameter of interest in this case is the

repeatability or uncertainty of the experimental location of the beam axis. Paragraph 4.4.4 investigates the value of uncertainty associated with this definition.

A second sequential power measurement technique estimates the location of the beam axis as defined above by making relative power measurements over a small area near the beam periphery. This may be achieved using one ground receiver, if subsequent increments are made in the perpendicular direction. This technique does not have the accuracy of the method above where the whole pattern is sampled; however, accuracy does approach the required $.05^{\circ}$. This technique is of interest because the attitude need be stepped an amount less than the overall 0.1° system accuracy requirement. This procedure is termed the sequential orthogonal incrementing technique and is developed further in paragraph 4.4.7. Paragraphs 4.4.4.2 and 4.4.4.3 discuss error sources peculiar to this technique.

Reference Signal Power Technique. In this method a reference signal of low power is transmitted on an earth-coverage antenna which transmits equal or a known relative power level to all ground stations. The necessary reference SNR at the receiver is obtained by achieving a narrow bandwidth by use of a phase-lock loop. Transmission on an adjacent frequency channel is desirable to reduce differential gain and noise density effects between the main and reference receiver channels.

A disadvantage of the reference power technique is that variations (drift) of the above parameters over a period of several hours may exceed the 0.1 to 0.2 dB stability required. The added complexity of a low-gain antenna and 12 GHz source on the spacecraft is also objectionable compared to the simplicity of other methods.

4.4.3 Sequential Power Measurement Technique

In the sequential power measurement techniques, power measurements are made relative to previous power measurements with a fixed- or known-gain receiver. The basic sensitivity requirement of the ground receiver is set by the Statement of Work in the RFP* which states that operation must be feasible at ERP's of 50 dBw per channel. As is shown below, the on-axis receiver SNR required to meet the accuracy requirement is greater than 30 dB.

---

* RFP C-360742Q, Exhibit A, Section 10.7

The ground beam tracking receiver may use a constant gain receiver "front-end" plus a commercially available broad-band power meter. An alternative approach is to measure the output of a calibrated AGC detector and with knowledge of the receiver gain vs AGC voltage, and compute the received power. If the spacecraft transmission is FM or PM, the entire signal bandwidth must be measured to obtain constant power at a given link gain. As an alternative, a low power beacon may be transmitted on an adjacent band in the case of FM or PM. This signal requires little additional circuitry since it can be amplified by the same 12 GHz power source. If the transmission is AM, total transmitted power varies as a function of the modulation. In this case the power in a portion of the spectrum containing a constant power component may be measured.

4.4.3.1 Relative Signal Strength Measurement Receiver Requirements

To make relative power measurements the receiver will be required to

a. make a measurement of power at the receiver.

b. maintain a constant or accurately known gain for a period of time until

c. a second power measurement is made.

The simplest technique of signal power measurement is shown in the receiver model of Figure 4-21. Here a precision wide-band power meter measures the signal plus noise power at a point in the receiver where the receiver bandpass has been established. As is suggested in Figure 4-21 , the first stages of amplification are of constant gain. These stages do not need the usual AGC feature because signal dynamic range will be approximately 35 dB. Any gain control required for adjusting signal level (e.g., for the purpose of signal demodulation and monitoring) can be accomplished in subsequent amplifier stages. It should be noted that pne advantage of the constant gain approach is that the noise power component is constant for a constant receiver equivalent noise temperature (receiver thermal noise plus antenna noise temperature). This fact is useful if the noise power can be measured separately. The noise power (watts) could then be subtracted from the power reading.

An alternate technique is to use a non-precision power measuring device such as a simple detector plus lowpass filter. This approach is usually restricted to a narrow range of measured signal power because of the restricted range over which most detector devices retain their desirable characteristics. To accommodate the wide range of signal powers the output of the device may be used as an AGC voltage. The device input level variation ratio would then be reduced by a factor equal to the gain variation ratio. Measured AGC voltage could then be related to received power by use of accurate knowledge of amplifier gain A(v) vs AGC voltage, v. The receiver output power S_o is related to the dc amplitude out of the square-law detector $y = Kx^2$ by

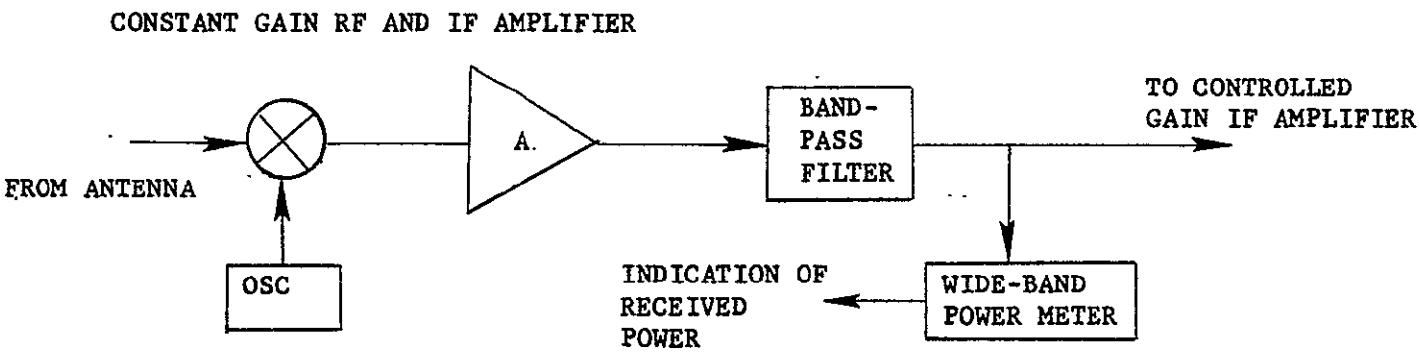

Figure 4-21. Measurement of the Total Power of an Angle-Modulated Signal

$$S_o = v/K$$

and thus the received power is given by

$$S_i = S_o/A(v) = v/KA(v)$$

In calibrating the detector it will be found that K is also a function of v, i.e., the gain constant will not be fixed over v. The accuracy required of the detector is less than .25 dB error for 0.05^o error in the antenna off-axis angle measurement as is shown in paragraph 4.4.4.

The techniques of signal power measurement discussed above require that the signal power in the passband is not a function of modulation waveform. If the signal is FM (or angle modulation in general), the bandwidth must be great enough to pass all significant sidebands. The signal power will then be constant at a fixed point on the beam. In the case of an AM signal, the received power (sum of entire signal spectrum) will vary with the modulation waveform. In this case, the power of a single, but fixed component of the spectrum may be sampled. This can be a sync component which is always present. Rather than attempt to select a narrow portion of the IF spectrum, it is more practical to translate to baseband (detect) and select the signal component as is shown in Figure 4-22. The variation of the power of this signal component may then be related to angle of antenna beam center. Note that AGC will be required to provide an adequate signal into the detector, therefore AGC voltage must be sampled to determine receiver gain.

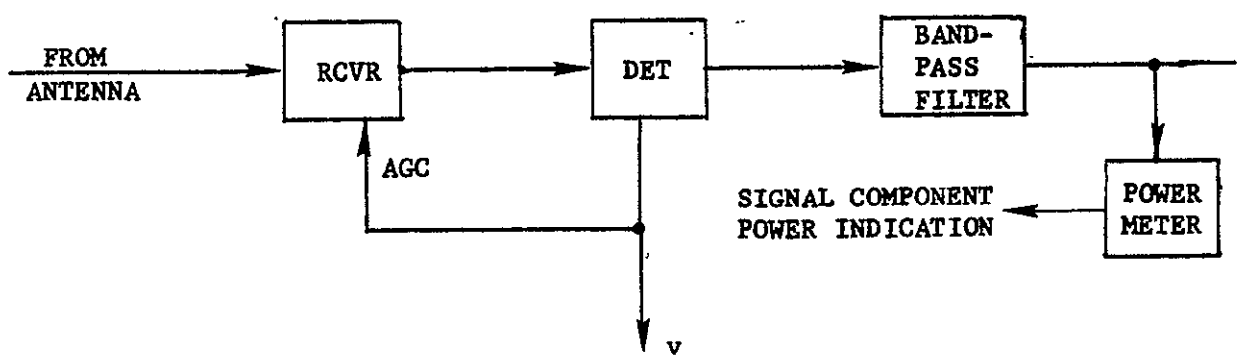

Figure 4-22. Measurement of Power of a Fixed Spectral Component

4.4.3.2 Receiver Noise and Satellite ERP

Table 4-14 itemizes the link conditions for the spacecraft-to-pattern measuring ground terminal. The power budget is carried out for variable transmitter power P and receiver bandwidth B. Two cases are of interest. One (a) is where measurements are made on the entire wideband angle-modulated signal (ERP $>$ 50 dBw). The second case (b) is where ERP is restricted to 50 dBw as per the RFP. For case

a. P = 27 dBw (500 watts)
   B = 77 dB-Hz (50 MHz)
   Hence S/N = 20 dB.

b. ERP = 50 dBw
   P = 14 dBw (25 watts)
   B = 64 dB-Hz (2.5 MHz)
   Hence S/N = 20 dB.

Note that in case (a), the SNR of 20 dB is marginal and little can be done about it other than increasing receiver G/T by about 10 dB.

TABLE 4-13. Downlink Power Budget for Beam Axis Direction Sensing

NO	PARAMETER	VALUE	SOURCE
1	Total Transmitter Power	P dBw	---
2	Transmitting Circuit Loss	-1 dB	
3	Transmitting Antenna Gain	36 dB	
4	Transmitting Antenna Pointing Loss	—	
5	Space Divergence Factor @ 12.2 GHz, R = 38,000 kM	-206 dB	
6	Polarization Loss	—	
7	Receiving Antenna Gain	49 dB	10' diam
8	Receiving Antenna Pointing Loss	—	
9	Receiving Circuit Loss	-1 dB	
10	Net Circuit Loss	-123 dB	
11	Total Received Power	P-123 dBw	
12	Receiver Noise Spectral Density (N/B) T System (T_s) = 3800° K	-193 dBw/Hz	NF=10 dB
	Signal-to-Noise Density S/No	P + 70 dB/Hz	
	Bandwidth	B dB-Hz	
	Signal-to-Noise Ratio S/N	P + 70 - B dB	

Case (b) is equally marginal; however, the bandwidth can readily be reduced 20 dB to 25 kHz. This is because the low power beacon may be a sinusoid leaving the minimum bandwidth set only by frequency uncertainty, which, for a 10^{-6} oscillator, is 8 kHz.

It is concluded therefore that if the additional 12 GHz signal source and multiplier chain are not objectionable, then the following spacecraft configuration is preferred for ground beam sensing purposes.

Spacecraft Transmitter Additional Circuit	RF Power Out	Ground Receiver Bandwidth
12 GHz driver added to existing pre-power amplifier circuits	10 to 25 watt	10 to 25 kHz

4.4.4 Error Analysis of Beam Axis Location by Pattern and Partial Pattern Measurement

Two problems are considered in this section:

a. Determining the repeatibility in locating (defining) the beam axis by making complete pattern measurements.

b. Finding the error in estimating the orientation of the beam axis by partial-pattern measurements.

Problem (a) is the antenna range problem. This has been studied for spacecraft application in detail by groups in the past*,**. These studies indicate that antenna range error sources are largely associated with mechanical devices and the resolution in reading them. Since problem (a) is concerned with random errors of zero mean, the bias errors are of no concern. This leaves only

---

* "Error Analysis for Mariner Mars 69," JPL MESA East Antenna Range Report No. 3678-68-009 Tech Memo, Feb. 19, 1968.

** "Error Analysis for NATO Communication Antenna," by G. H. Schennum, Philco-Ford WDL Div., 9 Oct. 68.

mechanical and electrical resolution values (random error values) to be of concern. These studies show that the random error sources for the ground beam-sensing DSS are

a. antenna platform attitude stepper resolution,
b. ground receiver power meter resolution.

In addition, the following sources of error have been found to be significant.

c. the effect of the noise component in the power measurement,
d. distortion of the pattern due to thermal distortion of the reflector.

The effects of these error sources are brought out in paragraph 4.4.4.1.

4.4.4.1 Summary of Error Magnitudes

The techniques of pattern measurement for beam axis location definition and beam axis orientation sensing by partial pattern measurement are developed in paragraph 4.4.2. This section investigates the repeatibility in the axis-defining procedure and the error in sequential-orthogonal partial pattern measurement procedure. Results of the error analysis are provided in Table 4-1 .

TABLE 4-14. Axis Location Uncertainty (Full Pattern Measurement)

Power Meter Resolution	Per Measurement Error (increment = .06°)	Axis Location Uncertainty (Errors averaged over -2.5° to +2.5° pattern)
.01 dB	.051°	.0056°
.02 dB	.102°	.011°

It was found that error due to power meter resolution dominated error due to antenna platform stepper resolution.

4.4.4.2 Repeatibility in or Uncertainty of Beam Axis Location by Pattern Measurement Data Integration. As noted above, the major sources of random error contributing to uncertainty in the definition of axis location are

a. antenna platform stepper resolution
b. power resolution of receiver power meter.

Antenna platform stepper resolution is estimated to be 5 to 10% of the 0.06 degree step size for the Lewis antenna. The rms uncertainty in the axis location may be determined by considering the displacement of the axis definition caused by each measurement error, then averaging over the number of measurements required to make one complete pattern cut. Assume that the parabolic shape of the pattern is prior knowledge. Then one measurement relative to a zero-error measurement would cause an axis location error equal to the value of stepper angular error on that test. Assuming the stepper error is statistically independent from step to step with an rms value (normal density) of e_s, the net contribution to axis location error is $e_s/\sqrt{n}$, where n is the number of measurements. Therefore, for measuring the pattern from -2.5 to + 2.5 degrees, the following uncertainty in axis location definition results (step size is $.06^\circ$):

rms stepper resolution	number of measurement steps	rms uncertainty in axis location definition due to stepper resolution
5% or $.003^\circ$	83	$.00033^\circ$
10% or $.006^\circ$	83	$.00066^\circ$

It is expected that pattern shape irregularity will make curve fitting more difficult, thus increasing the values given here. In addition, the direction of stepping may introduce a correlation between the step error in successive steps. This would tend to eliminate the averaging effect of taking many measurements. The final error can, however, be concluded to be much less than the $.05^\circ$ accuracy requirement.

The effect of power resolution of the receiver power meter is the other major factor in causing uncertainty in beam axis location. It is assumed that for the axis location definition operation a power measurement circuit SNR of greater than 20 dB will be obtained. It can be shown that for large SNR, the power measurement error is nearly equal to the power meter resolution.

(The error is greater than power meter resolution for low SNR). Assuming the slope is a linear function of off-axis angle β , (this is a good approximation; see Figure 4-20) then the slope m is given by

$$m = k\beta = \Delta G/\Delta\beta \qquad (4\text{-}29)$$

where $\Delta\beta$ is the nominal attitude increment.

The variation of computed β relative to variation in measured gain change ΔG is then

$$k\partial\beta = \partial(\Delta G)/\Delta\beta \qquad (4\text{-}30)$$

The variation in ΔG is identified as the power meter resolution, E. The per-measurement error in β is then

$$e_\beta = E/k\Delta\beta$$

Since k and $\Delta\beta$ are constant, then e_β has the same value irrespective of off-axis angle. For the 2.7° HPBW antenna, k = 3.29 dB/(deg.)^2. The following axis location definition uncertainty results for stepping the attitude from -2.5° to $+2.5^\circ$. Attitude increment $\Delta\beta$ is $.06^\circ$.

Power Meter Resolution E	Per-Measurement Error e_β	Axis Location Uncertainty (83 measurements)
.01 dB	$.051^\circ$	$.0056^\circ$
.02 dB	$.102^\circ$	$.0112^\circ$

The values of power meter resolution given above are representative of two types of equipment. The Scientific Atlanta Wide Range Receiver with Model 1630/40 series bolometer has a resolution of .01 dB. The Hewlett-Packard Model 432A or 437A Wide Band Power Meter has a differential linearity better than .01 dB.* Its response time is less than one second.

* Private communication with B. Peterson of Hewlett-Packard Microwave Division.

Measurement Sensitivity as a Function of Off-Axis Angle

Computer calculation of antenna pattern characteristics in a plane approximately normal to the roll axis has been used to plot slope of the pattern in Figure 4-20. Made from this plot is the table of sensitivities below.

Angle Off Boresight	Slope in dB per 0.1 degree change in roll
1°	0.35 dB/0.1°
2	.78
3	1.37
4	.93
5	(negative)

This table and the plot show that good sensitivity is available on off-axis angle equal to the full beamwidth at half-power points. However, the sensitivity drops off rapidly beyond 3.5° as the first null is approached. Ground stations should not be located beyond the 3° angle because a roll rotation of slightly more than 1° will result in an abrupt loss of sensitivity to rotation.

4.4.4.3 The Error in Estimating the Orientation of the Beam-Axis by Partial-Pattern Measurements. In this technique (for example the sequential, orthogonal technique of paragraphs 4.4.2 and 4.4.7) a number of measurements are made on a limited area of the pattern. The technique essentially measures the pattern slope to obtain off-axis angle. Orthogonal increments can be made to determine azimuth of a single ground receiver.

Antenna platform stepper resolution has a major effect in this technique. The error due to stepper resolution is determined as follows: As seen below, the slope of the pattern is nearly linearly increasing in magnitude from beam center to 3° off axis. Let step resolution be ϵ_{step} and pattern slope m. Let the error in the determination of off-axis angle be called $\epsilon\beta$ Then the off-axis angle β is computed from

$$m = k\beta = \Delta G/\Delta\beta$$

where ΔG is the measured gain change and $\Delta\beta$ is the nominal step size. Introducing the error in step size and β we have

$$\beta + \epsilon_\beta = \frac{\Delta G}{k\,(\Delta\beta + \epsilon_{step})} \qquad (4\text{-}31)$$

$$\approx \frac{\Delta G}{k\,\Delta\beta}\,(1 - \epsilon_{step}/\Delta\beta)$$

The error part is

$$|\epsilon_\beta| = \beta\epsilon_{step}/\Delta\beta$$

The error in determining off-axis angle is seen to be proportionate to off-axis angle β and the fractional step error or step resolution. This result is plotted in Figure 4-23.

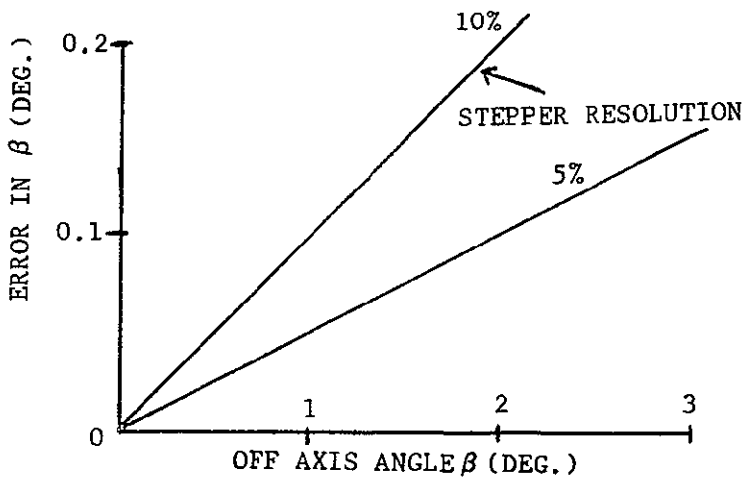

Figure 4-23. Error in Determining Off-Axis Angle vs. Off-Axis Angle.

Error due to power meter resolution and receiver noise is investigated in paragraph 4.4.7. Those results and the above error component are combined in Figure 4-2. It is seen that error due to stepper resolution dominates for off-axis angle greater than 1.5°. Also, power meter resolution causes an increase in error as off-axis angle approaches zero. The best receiver location is therefore 1 to 1.5° off beam axis. Note that the -3 dB point on the pattern is 1.35° from the axis.

4.4.4.4 Pattern Asymmetry and Thermal Distortion Errors. Computer-derived patterns of the worst case thermally distorted antenna were obtained from the antenna design task. Thermal distortion causes a change in pattern shape which was found to cause significant error in the method of locating the beam axis by partial pattern measurements. Therefore, the pattern must be measured for the distorted condition. Since distortion will vary periodically with a 24-hour period, a set of two or more complete pattern measurements representing distortion extremes should suffice.

Pattern asymmetry due to aperture blockage causes a complication of the partial pattern measurement axis location technique. This will require an iterative procedure to determine axis location. The first computation will assume circular symmetry. The second computation will inject a correction term using the results of the first computation. This one iteration should suffice because the effects of asymmetry is slowly varying with aximuth (yaw).

4.4.5 Derivation of Antenna Pattern Geometric Center Location in Earth Coordinates

The analysis of the ground beam sensing subsystem is broken up into the following two basic problems.

1. Measurement of the position of the antenna patterns' geometric center (derivation problem, noiseless case);

2. Prediction of error in the measurement of geometric center location in presence of system noise and bias error (tracking problem).

The first problem is developed in this paragraph; the error analysis appears in paragraph 4.4.4.

4.4.5.1 Summary

The analytical development below derives expressions for

1. The spacecraft-to-ground receiver vector in antenna platform coordinates using two ground receiver off-axis antenna angle measurements;

2. The antenna platform coordinate system-to-earth coordinate system linear transformation from the results of 1. above.

3. The beam pattern geometric center location on the earth in earth coordinates using the results of 2. above.

It is shown that the measurement of the spacecraft-to-ground receiver vector provides redundant information which may be used to measure antenna axis alignment error. Ambiguity of solutions exists for some of the expressions; however, the antenna platform orientation will be known approximately from spacecraft attitude and gimbal data.

4.4.5.2 Derivation of Spacecraft-to-Ground Receiver Vector from Ground Off-Axis Angle Measurements

The geometrical relationships between antenna platform coordinate system XYZ, the boresight vector $_k$ of antenna pattern #k and the spacecraft to receiver vector $\bar{r}_1$ is shown in Figure 4-24. It is shown below that if the boresight vector is known in XYZ coordinates and the off-axis angle is measured, then the vector $\bar{r}_1$ can be determined by either

1. Making off-axis angle measurements on two beams with one ground receiver location, or

2. Making off-axis angle measurements on one beam with two ground receiver locations.

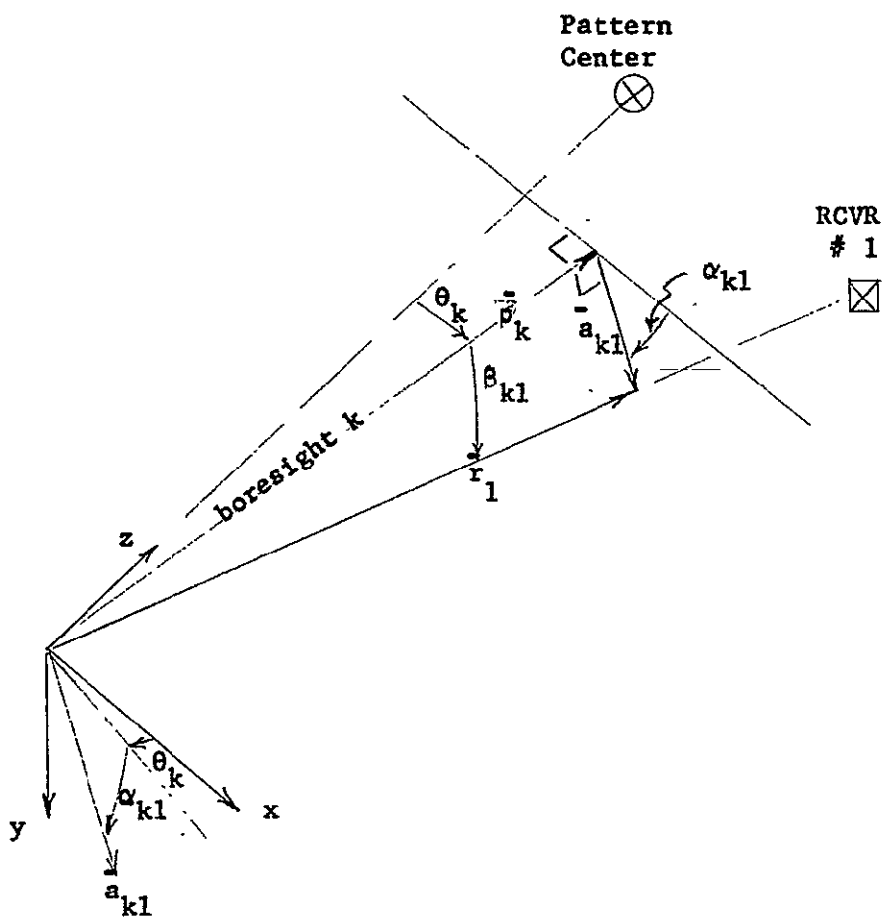

Figure 4-24. Beam Boresight and Ground Receiver Vector in Antenna Platform Coordinates

From the vector diagram it is seen that the vector to ground receiver #1 is given by

$$\bar{r}_1 = \bar{\rho}_k + \bar{a}_{k1} \tag{4-35}$$

The kth boresight vector is known in xyz coordinates; it is

$$\bar{\rho}_k = |\bar{\rho}_k| \, T_2(\theta_k) \, \hat{3} = \begin{bmatrix} \sin\theta \\ 0 \\ \cos\theta \end{bmatrix} \tag{4-36}$$

where T_2 is a linear transformation representing rotation about the 2-axis (y-axis) and

$$T_2(u) = \begin{bmatrix} \cos u & 0 & \sin u \\ 0 & 1 & 0 \\ -\sin u & 0 & \cos u \end{bmatrix}$$

and

$$\hat{3} = \begin{bmatrix} 0 \\ 0 \\ 1 \end{bmatrix}$$

The vector $\bar{a}_{k1}$ is

$$\bar{a}_{k1} = |a_{k1}| \, T_2(\theta_k) \, T_3' \, (\alpha_{k1}) \, \hat{1} \tag{4-37}$$

where T_3' is the transpose of T_3 and is a rotation about the 3-axis:

$$T_3'(u) = \begin{bmatrix} \cos u & -\sin u & 0 \\ \sin u & \cos u & 0 \\ 0 & 0 & 1 \end{bmatrix}$$

and

$$\hat{1} = \begin{bmatrix} 1 \\ 0 \\ 0 \end{bmatrix}$$

Noting that $|\bar{a}_{k1}| = |\bar{\rho}_k| \sin\beta_{k1}$, then

$$\bar{r}_1 = |\bar{\rho}_k| \; T_2(\theta_k) \left(\hat{3} + \sin\beta_{k1} \; T_3'(\alpha_{k1}) \; \hat{1} \right) \qquad (4\text{-}38)$$

Defining the unit vector $\hat{r}_1$ by

$$\hat{r}_1 = \bar{r}_1 / |\bar{r}_1|$$

where

$$|\bar{r}_1| = |\bar{\rho}_k| / \cos\beta_{k1}$$

then the expansion of equation (4) yields

$$\hat{r}_1 = \cos\beta_{k1} \begin{bmatrix} \sin\theta_k + \sin\beta_{k1} \cos\theta_k \cos\alpha_{k1} \\ \sin\beta_{k1} \sin\alpha_{k1} \\ \cos\theta_k - \sin\beta_{k1} \sin\theta_k \cos\alpha_{k1} \end{bmatrix} \qquad (4\text{-}39)$$

In equation (4-39) the value of α_{k1} is unknown. It can be determined by measuring β_{m1}, i.e., the off-axis angle to beam #m at the same receiver. Then

$$\hat{r}_1 = \cos\beta_{m1} \; T_2(\theta_m) \left(\hat{3} + \sin\beta_{m1} \; T_3'(\alpha_{m1}) \; \hat{1} \right) \qquad (4\text{-}40)$$

Equating equation (4-39) and (4-40) gives three equations in two unknowns. The values of α may then be determined from any two of the resulting equations. Note that there is a dual ambiguity in the solution which may be resolved

by a second set of solutions after a rotation in roll. The difference between successive solutions must be consistent with the direction of rotation. The redundant equation from (4-40) and (4-39) above may be used to solve for θ, the antenna boresight alighment in pitch. The general development of boresight orientation calibration (in orbit) must include pitch and roll offsets and hence requires further analytical consideration. This is left to the error analysis problem to be considered later.

Coordinate Transformation

From Figure 2 it is seen that

$$T_a(\eta, \mu, \psi)\ \bar{r}_1^{(xyz)} = (\bar{R}_1 - \bar{\rho}_o)^{(E)} \qquad (4\text{-}41)$$

which, once $\bar{r}_1$ has been determined by the one ground receiver approach, may be solved for η, μ and ψ .

An alternate measurement procedure to determine the spacecraft-to-receiver vector, solves simultaneously for angles α_{ki} and the linear transformation angles relating Earth coordinates to antenna platform coordinates. This procedure requires the off-axis angle θ_{ki} measurement by two ground receivers (i = 1, 2) sensing the same beam (one value of k). Figure 4-25 shows the geometrical model.

The second ground receiver defines vector $\bar{r}_2$ where

$$\bar{r}_2 = \bar{\rho}_{k2} + \bar{a}_{k2}$$

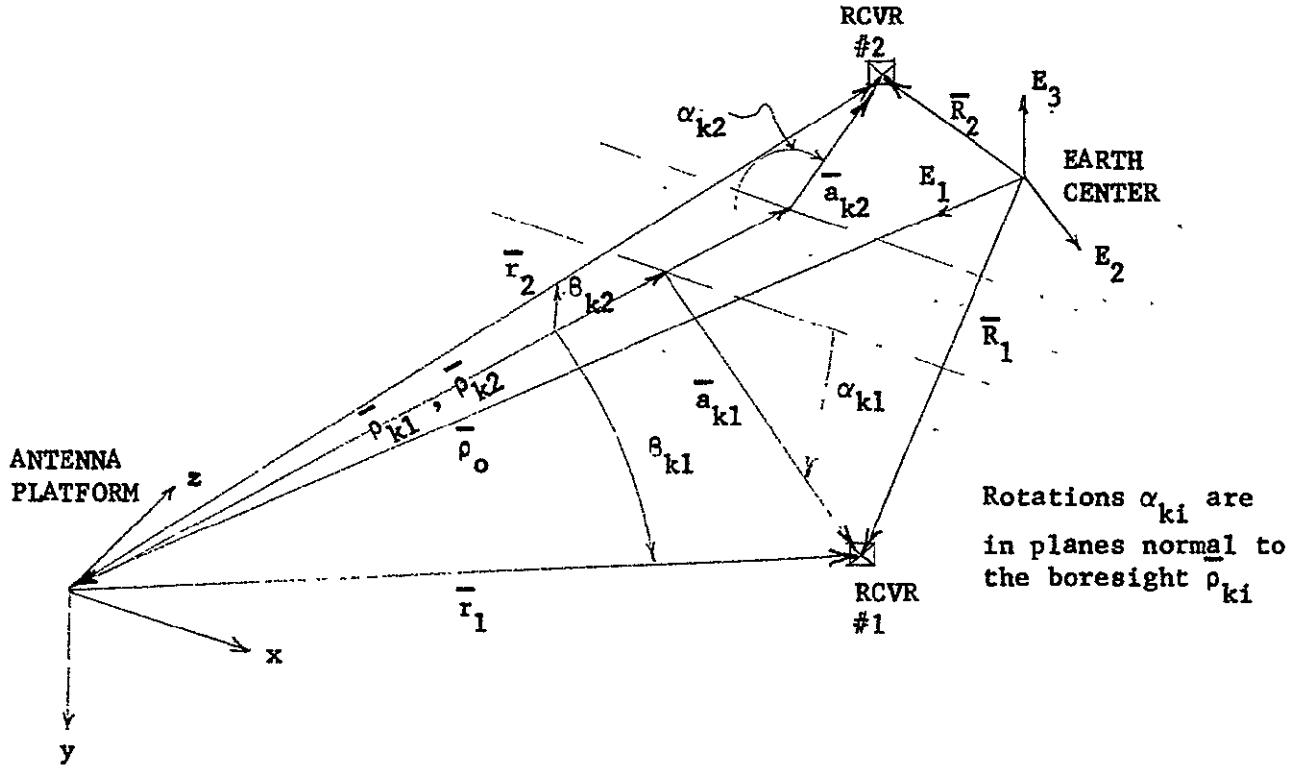

Figure 4-25. Two Ground Receivers Sensing One Beam

As before, expressions for $\hat{r}_1$ and $\hat{r}_2$ are derived yielding six equations in eight unknowns. But, in addition, the vectors $\bar{r}_i$ may be expressed in terms of the satellite and receiver station vectors.

$$\bar{r}_i = (\bar{R}_i - \bar{\rho}_o)^{(xyz)} = T_a^{-1}(\eta,\mu,\psi)(\bar{R}_i - \bar{\rho}_o)^{(E)}, \quad i = 1,2$$

where the superscript indicates the coordinate system and $T_a(\eta,\mu,\psi)$ is a linear transformation which translates vectors from earth coordinates to antenna platform coordinates. Then we have

$$\hat{r}_i = \frac{1}{|\bar{r}_i|} T_a^{-1}(\bar{R}_i - \bar{\rho}_o)^{(E)} = \cos\beta_{ki} \begin{bmatrix} f_1(\alpha_{ki}) \\ f_2(\alpha_{ki}) \\ f_3(\alpha_{ki}) \end{bmatrix}$$

where

$$r_i = \bar{r}_i / \bar{r}_i$$

which for $i = 1, 2$ gives six equations in five unknowns. The values of α and the linear transformation may be determined assuming $_{ki}$ are known. Ambiguity in the solution may be resolved by use of approximate values of antenna platform orientation.

Location of the Beam Pattern Center in Earth Coordinates

From Figure 4-26 we see that the location of the beam center in Earth coordinates is the vector sum

$$\bar{R}_c = \bar{R}_1 - \bar{r}_1 + \bar{r}_c$$

where $\bar{r}_c$ is colinear with the antenna platform z-axis. Since

$$\bar{r}_c^{(E)} = T_a \, \bar{r}_c^{(xyz)} = T_a \, |\bar{r}_c| \, \hat{3}$$

then

$$\bar{R}_c^{(E)} = \bar{R}_1^{(E)} + T_a(-\bar{r}_1^{(xyz)} + |\bar{r}_c| \, \hat{3})$$

where $|\bar{r}_c|$ is unknown but may be obtained from the fact that $|\bar{R}_c| = R_o$, the Earth radius.

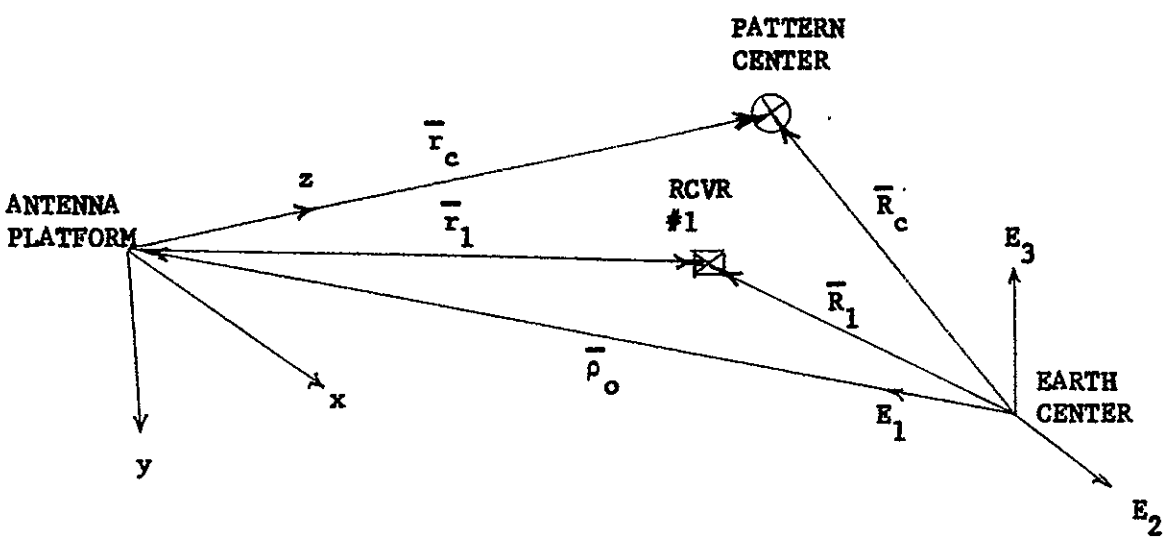

Figure 4-26 Pattern Center Vector Geometry

4.4.6 Use of the Ground Beam Position Measurement to Resolve Ambiguities in the Spacecraft Interferometer Measurement.

During initial in-orbit calibration of the interferometer attitude sensing equipment there is a multiple ambiguity in attitude measurement. This is because the electrical phase measurement traverses 2π radians while the angle being measured goes through 2.7° (32-inch baseline, 8 GHz). Since the ground beam position measurement will be available for redundant attitude measurement, this subsystem may be used to make the initial ambiguity resolution computation. The procedure is simply:

1. attain the approximate spacecraft antenna orientation through the command channel (command override);
2. rotate the spacecraft antenna in pitch and roll until the pattern is acquired at the ground receivers;
3. make an initial, reduced accuracy attitude computation using the receiving station outputs and the preflight-measured antenna patterns. Since the non-ambiguous attitude range is 2.7°, the initial accuracy must be better than $\pm (1.4^{\circ} - \epsilon_{\theta})$ where ϵ_{θ} is the maximum expected interferometer boresight drift (offset from antenna pattern center);
4. compare the ground-sensing computed attitude with the ambiguous set of solutions derived from data telemetered from the spacecraft. The telemetered data should be the phase measurement outputs φ'_{ij} where the true phase is

$$\varphi_{ij} = \varphi'_{ij} + 2n_j\pi \qquad \begin{array}{l} i = 1, 2 \ldots \\ j = 1, 2 \end{array}$$

and n is to be determined. (See paragraph 4.3.2)

5. after selecting the proper values of integers n_j, these numbers are commanded into the spacecraft interferometer phase-measurement quadrant-encoder accumulator.
6. the ground beam-sensing function may be used periodically to check the spacecraft attitude measurement function for failure.

4.4.7 Use of the Ground Direction Sensing Function as a Redundant DSS

4.4.7.1 Redundant DSS By Ground Sensing of Beam Orientation. It is clear from the derivation procedure for antenna platform attitude as developed in Section 4.5 that beam axis orientation can be calculated from signal strength measurements made by ground receivers located within the beam. If the measurement procedure does not interrupt service (does not reduce SNR in the service area below requirements), then that method of ground direction sensing can act as a redundant DSS in event of satellite DSS malfunction or outage. Any signal strength measurement and beam-axis direction computation procedure will require that accurate pattern measurement records be available. The pattern uncertainty considerations of Section 4.4 state that the main source of error in on-orbit measurements will be due to platform attitude stepper resolution. This resolution is about $.006^{\circ}$. Since this is the magnitude of calibration error which reflects directly on any axis-location procedure using the patterns measured on-orbit, then it is concluded that such a direction sensing technique is feasible provided that a suitable power measurement procedure is available.

The only power measurement procedure which will provide the necessary accuracy is a relative power measurement as discussed in paragraph 4.4.2. Of the techniques introduced there, the most simple and direct is method of sequential power measurements while incrementing the antenna platform. An approach which provides all the information needed while requiring only one ground receiver site will be called the method of sequential orthogonal attitude increments. While other techniques using more ground receivers might be considered, this approach provides accuracy representative of any sequential power measurement procedure; therefore, only this procedure will be analyzed.

4.4.7.2 Method of Sequential Orthogonal Attitude Increments. The principle behind this technique is as follows: Consider a ground receiver at azimuth angle α and off-axis angle β relative to one of the beam axes. Let the antenna platform attitude be incremented $\Delta\theta_1$, along the 0° azimuth axis and $\Delta\theta_2$ orthogonal to this axis. See Figure 4-27 for illustration.

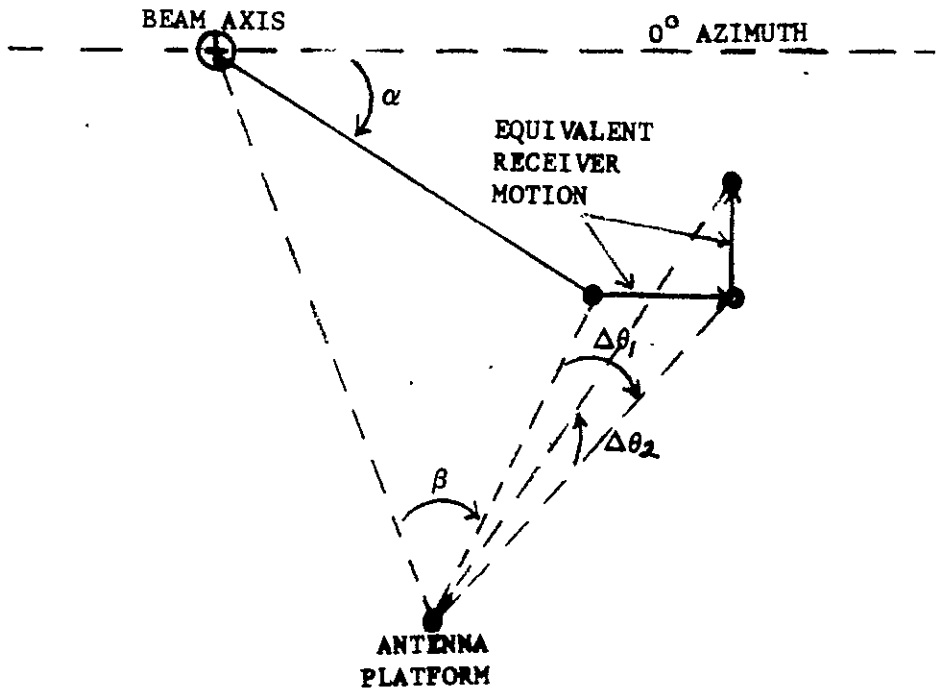

Figure 4-27: Increment Angles $\Delta\theta$, Off-Axis Angle and Azimuth

The two power changes measured at the receiver are then approximately

$$\Delta G_1 \approx s_1 \Delta\theta_1 \cos\alpha_1$$
$$\Delta G_2 \approx s_2 \Delta\theta_1 \sin\alpha_2$$

where s_1 is pattern slope. If now $s_1 \approx s_2$ and $\alpha_1 \approx \alpha_2$ which holds for increments small compared to the half-power beamwidth, then by letting $\Delta\theta_1 = \Delta\theta_2$, the azimuth may be determibed from

$$\alpha \approx \tan^{-1} \frac{\Delta G_2}{\Delta G_1}$$

Since, in the determination of antenna platform attitude from α, errors in α are multiplied by sin β, then relatively large errors in α can be tolerated. It can be shown that for an idealized pattern (Gaussian) and $\Delta\theta = .05^\circ$, attitude error due to the constant pattern slope assumption is less than $.01^\circ$ for $\beta > 0.5^\circ$. After estimating α, the off-axis angle can be determined from calculating the slope from the gain expressions above. The expression corresponding to the larger ΔG should be used to minimize error in

In addition to errors due to the constant slope assumption, the following sources of errors contribute to the attitude determination error.

1. Power meter resolution plus noise effect: $\widehat{\Delta G} = \Delta G + \epsilon_p$

2. Attitude stepper resolution: $\widehat{\Delta\theta} = \Delta\theta + \epsilon_{\Delta\theta}$

3. Pattern slope error: $\hat{s} = s + \epsilon_s$

A closed form solution of error in the estimate of antenna platform attitude is difficult if the ground direction sensing function is to be closely approximated. Therefore, a computer simulation of the technique is a more economical way of determining performance characteristics of this beam axis direction sensing approach.

4.4.7.3 Simulation Results. The simulation assumes exact attitude incrementing (zero stepper resolution) and computes beam-axis direction from the simulated measurements. Error in the measurements consists of error components introduced by ground receiver power meter resolution and thermal noise.

Results of the simulation are presented in Figure 4-28.

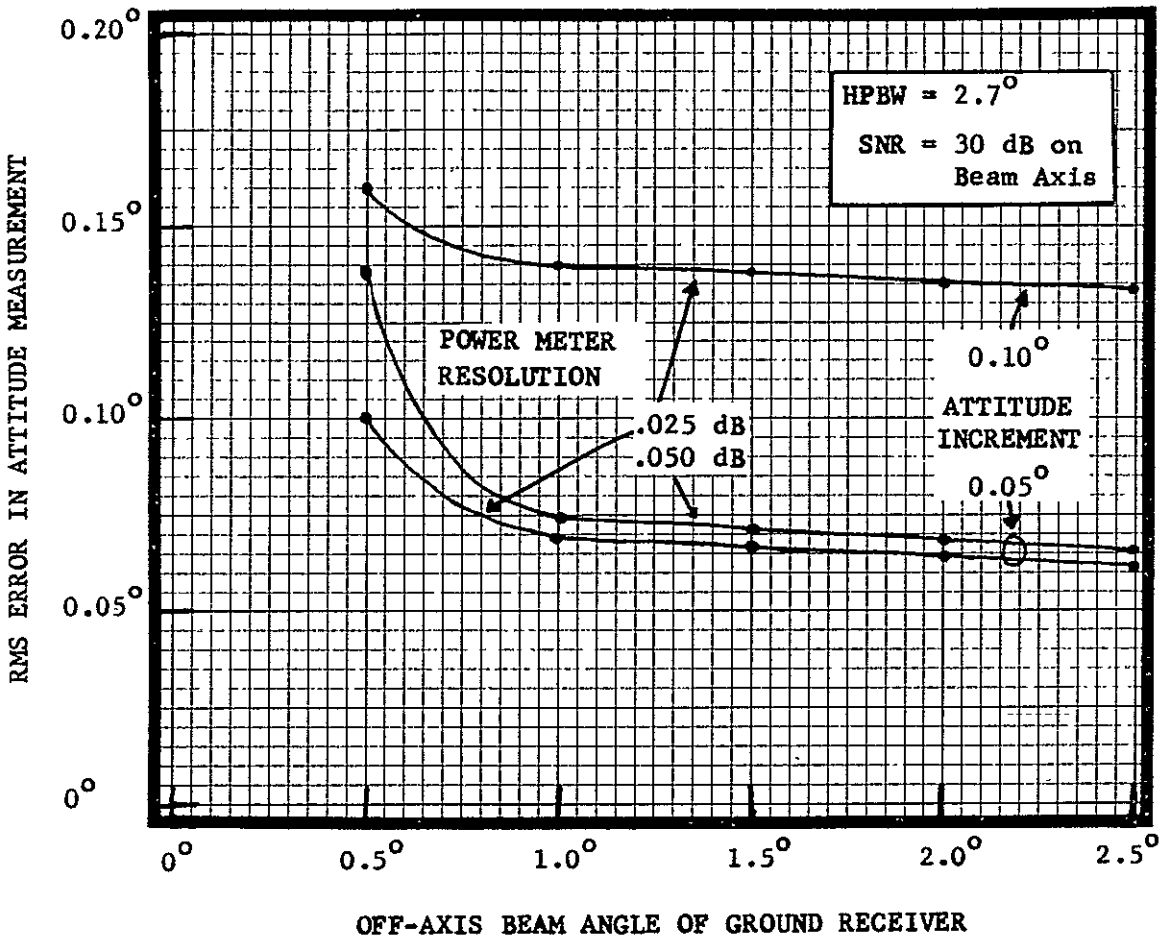

FIGURE 4-28. ANTENNA PLATFORM ATTITUDE SENSING ERROR VS. OFF-AXIS BEAM ANGLE OF GROUND RECEIVER

SECTION V

MECHANICAL DESIGN ANALYSIS AND INTEGRATION

5.1 CONFIGURATION

R.F. trade offs resulted in the selection of four prime focus parabolic reflectors mechanically despun with respect to the spacecraft and had the following physical characteristics:

a.	Relfector diameter	28.0	(71.12 cm)
b.	F/D ratio	.35	
c.	Focal Length	9.8	(23.892 cm)

Based on this selection mechanical design and integration trade offs were performed which initially addressed the packaging of the four antennas within the physical constraints imposed by the basic system requirements specified in the NASA/LeRC Statement of Work, and those derived from RF/considerations. The imposed and derived requirements and constraints may be summarized as follows:

a. The spacecraft body and solar array are sun oriented in a geostationary orbit.

b. Minimum field of view angle over solar array is 4°.

c. System requires a four channel RF rotary joint, for 360° continuous rotation in pitch.

d. Antenna gimbaling is required in roll ($+12^{\circ}$, -6°) and yaw ($\pm 5^{\circ}$).

e. One reflector requires two position capability.

f. Packaging is required within the envelope of the Atlas Centaur shroud.

The selected antenna packaging arrangement resulting from the initial investigations was further examined in parallel with the structural and thermal analyses. Based on the requirements generated by the analysis efforts a conceptual design was developed which includes the antenna reflectors, the mechanically despin motor drive assembly (integrated with the four channel RF rotary joint), the support truss structure and a method of providing antenna gimbaling. This conceptual design is described in paragraph 5.3.

5.1.1 Configuration Trade Offs

Based on the solar array criteria provided by NASA-Lewis (array area 350 sq. ft. and aspect ratio 6:1) the height of the antenna array was determined as a function of pointing error. Figure 5-1 shows a plot of aspect ratio versus antenna height above the spacecraft solar array for a pointing angular range of 6.61° and 10.61°. The maximum height possible within the fairing constraints is 6.3 feet indicating that the maximum attitude error of the spacecraft must be maintained at 1.0° or less and the height of the antenna array must be less than 6.3 feet to avoid interference of the RF beam by the solar array when deployed.

In order to maximize the height of the antenna array above the solar array, a configuration was considered that permitted the use of the upper narrow portion of the fairing for storage purposes. This configuration is shown at the left in Figure 5-2. However, when compared to the configuration shown at the right it was decided that this arrangement was the least desirable of the two for the reasons noted.

The selected arrangement permits sufficient separation between lowest antennas and the solar array to avoid interference with the RF beam.

5.1.2 Description of Proposal Design

A conceptual layout of the design is shown in Figure 5-3. Views 1 and 2 show profile and back views. No attempt has been made to show detail at the Array/Spacecraft interface. Computer models of the structure, both thermal and structural, were constructed

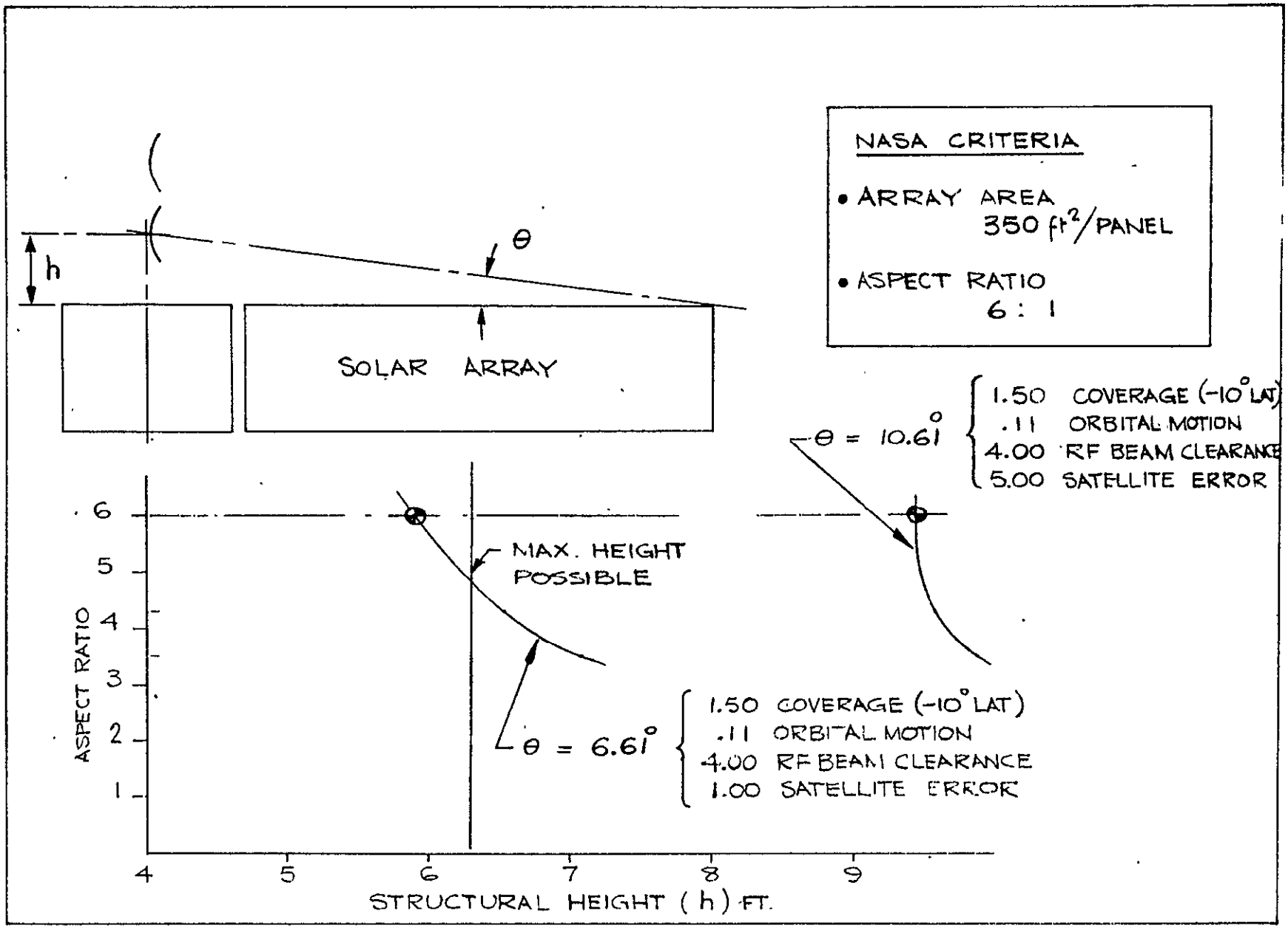

Figure 5-1 Influence of Solar Array on Antenna Configuration

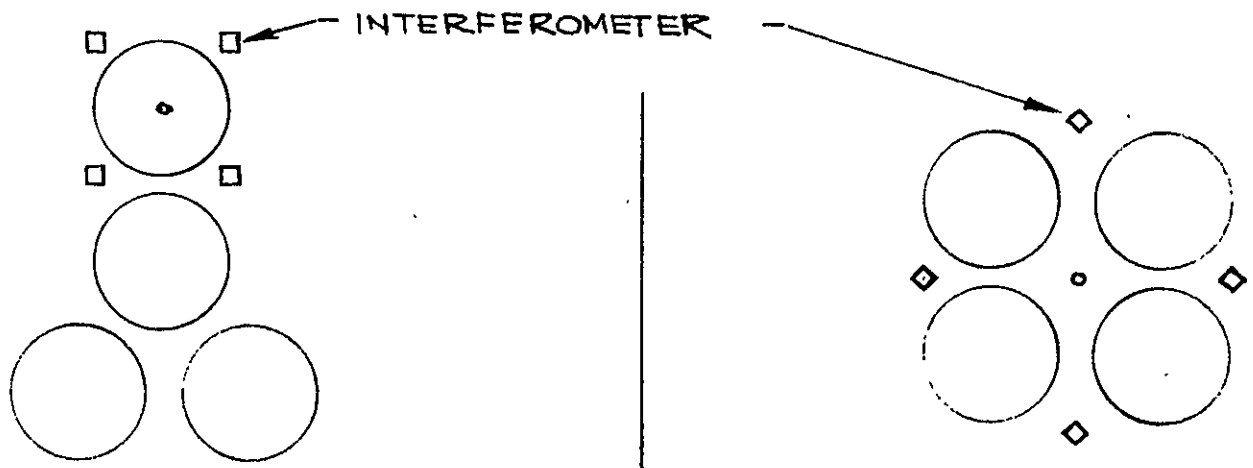

- PERMITS MAXIMUM HEIGHT ABOVE SPACECRAFT
- LEAST EFFICIENT STRUCTURAL SUPPORT
- NON SYMMETRICAL WAVEGUIDE ARRANGEMENT
- INTERFEROMETER DOES NOT ALLOW USE OF SELECTED SIDE LOBE SUPPRESSION TECHNIQUES.

- LOWEST STRUCTURAL SUPPORT WEIGHT
- WAVEGUIDE SYMMETRICAL
- COMPATIBLE WITH SIDE LOBE SUPPRESSORS.
- • SELECTED CONFIGURATION

Figure 5-2 Antenna Configuration Trade-Off

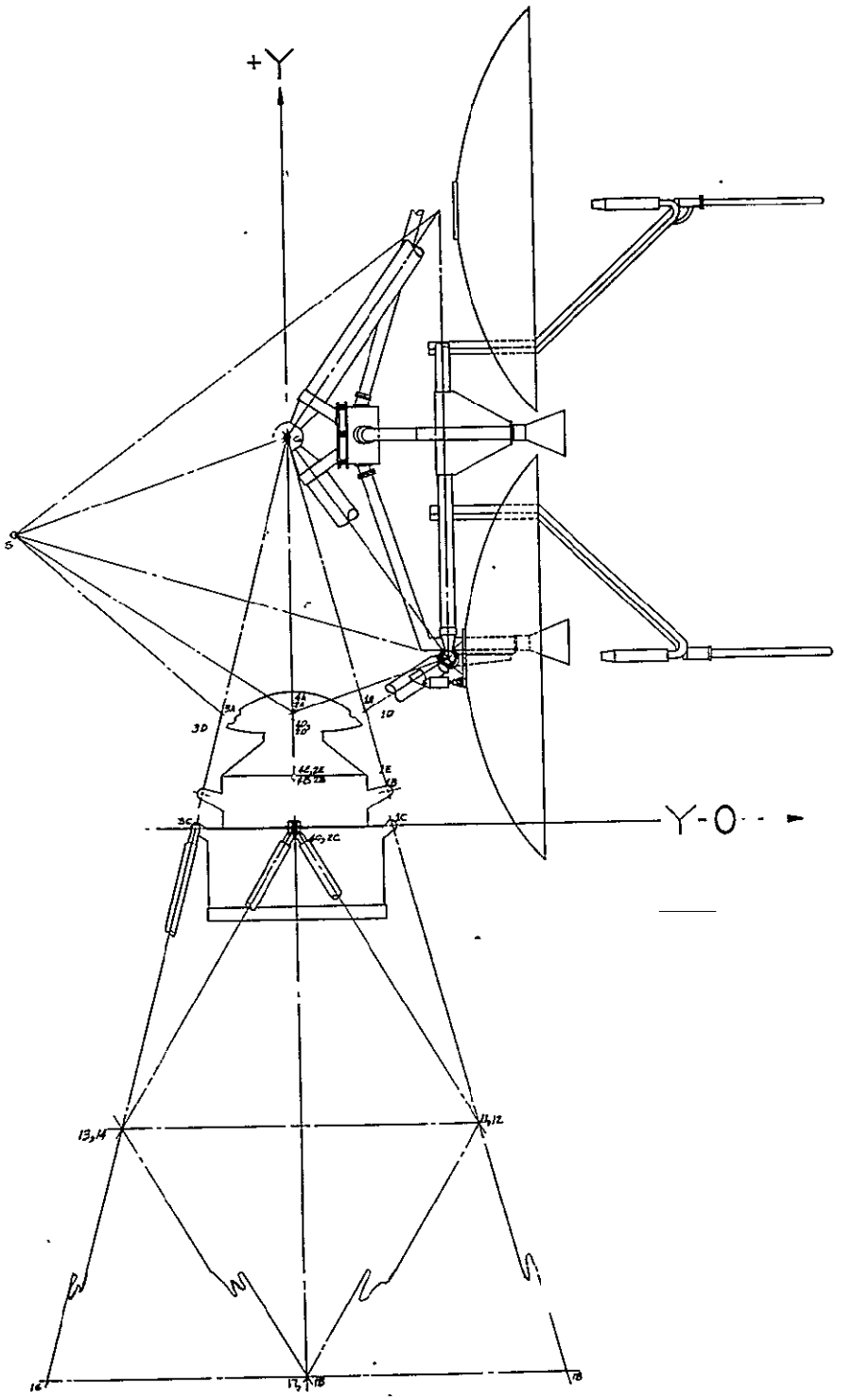

Figure 5-3 ANTENNA LAYOUT DESIGN, PROFILE OF REFLECTORS AND STRUCTURES (View 1)

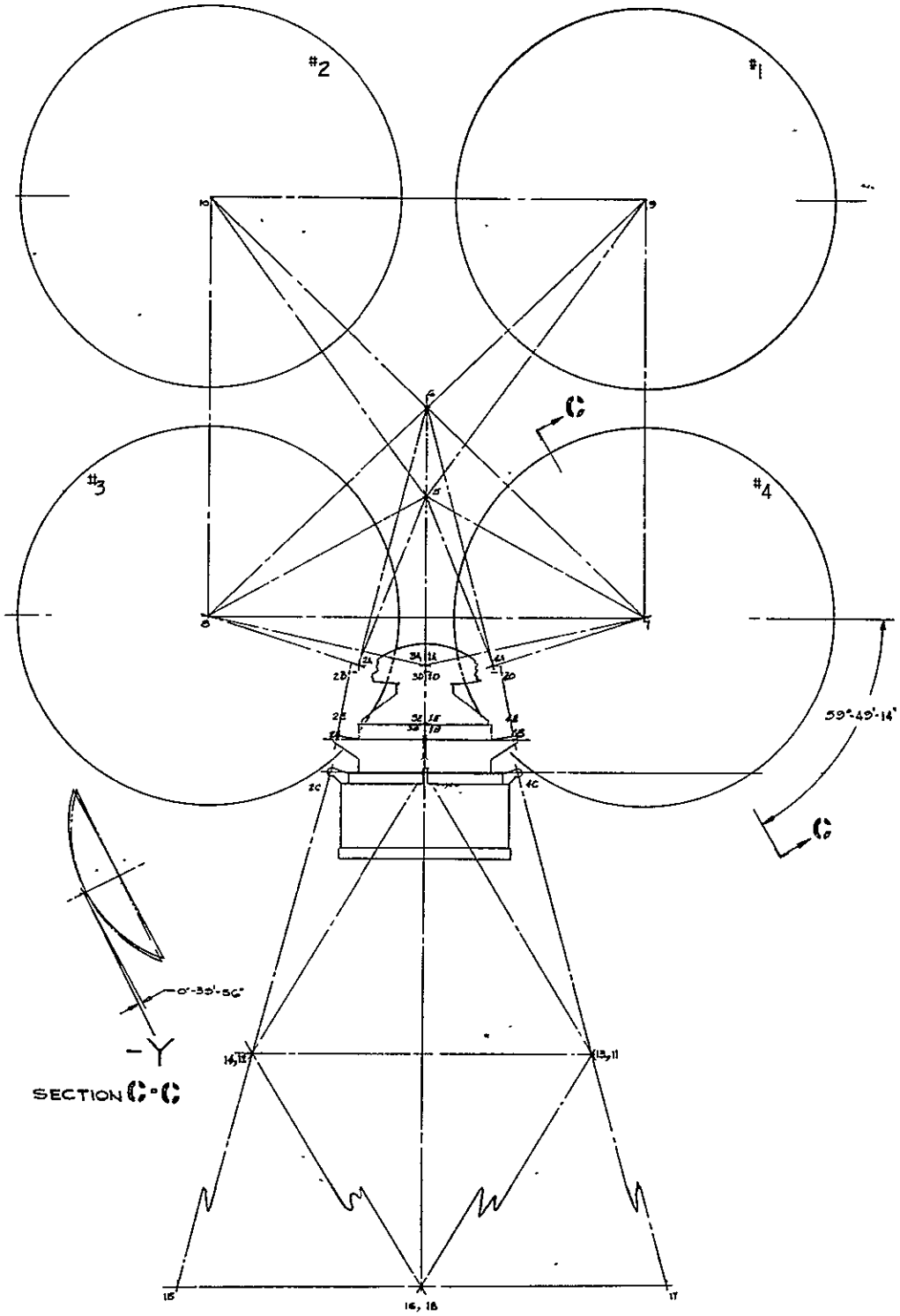

Figure 5-3 ANTENNA LAYOUT DESIGN, BACK OF REFLECTORS AND STRUCTURE (VIEW 2)

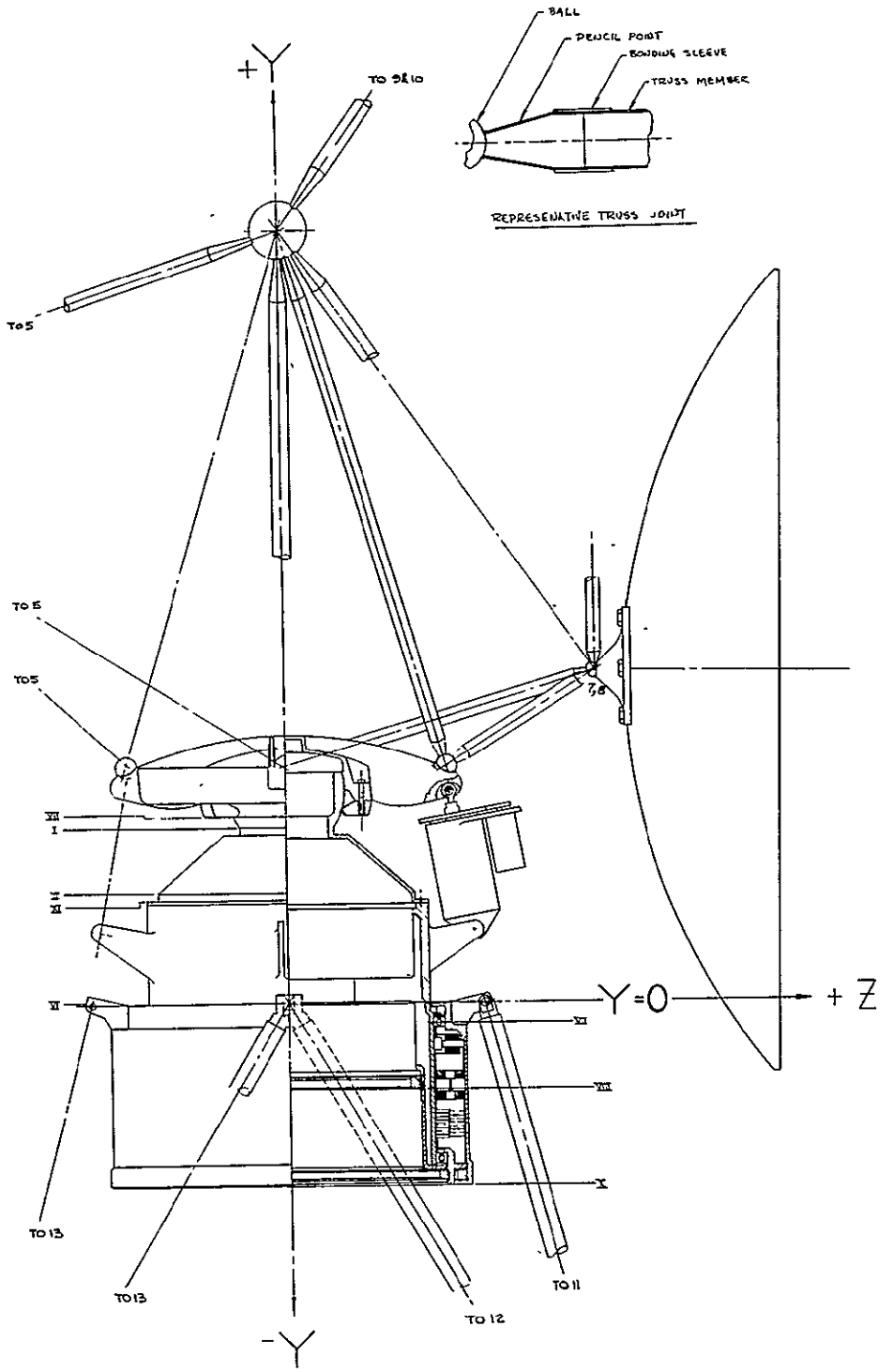

Figure 5-3 ANTENNA LAYOUT DESIGN, MOTOR DRIVE AND GIMBAL ASSEMBLIES (View 3)

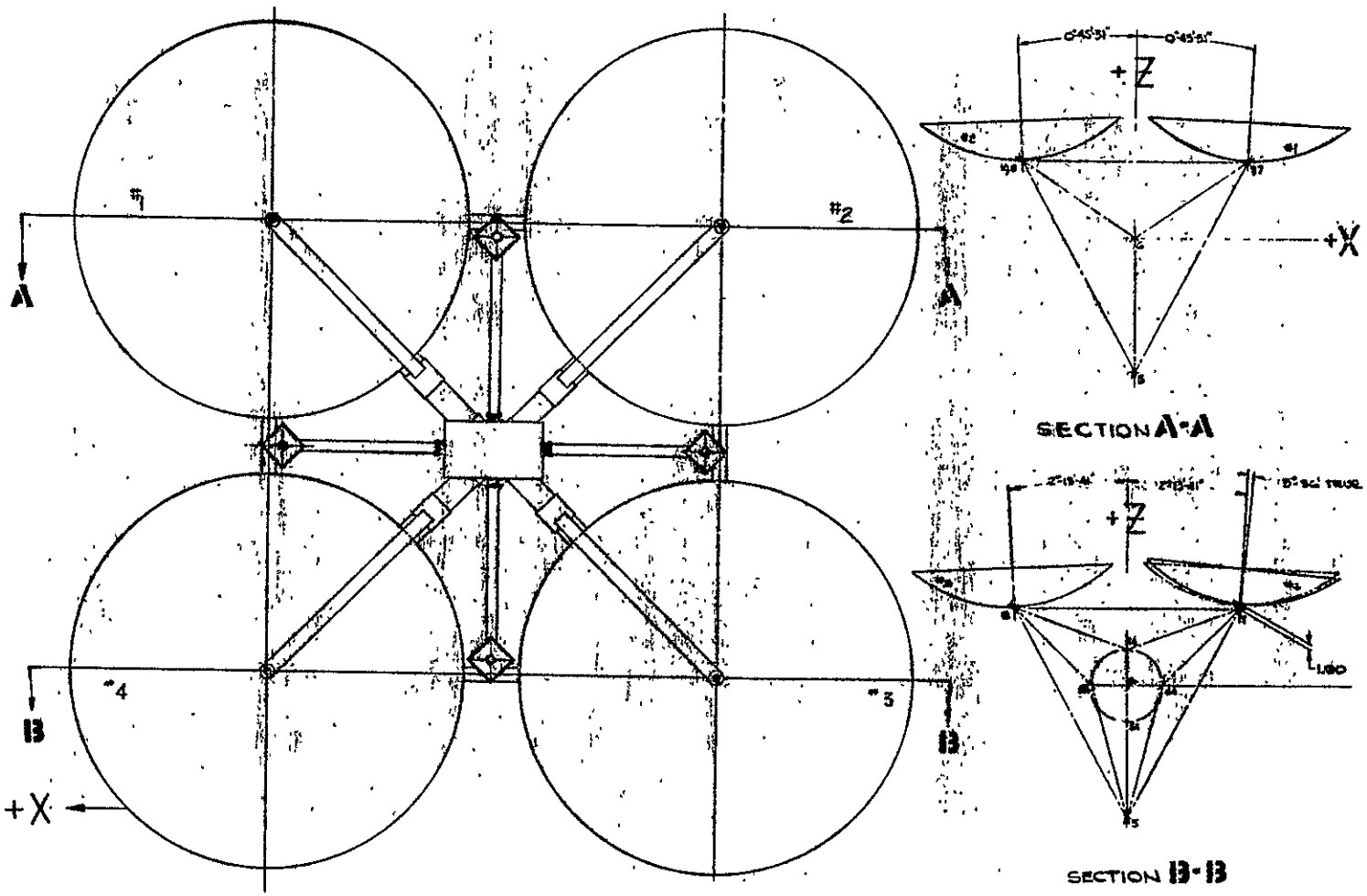

Figure 5-3 ANTENNA LAYOUT DESIGN INTERFEROMETER AND REFLECTOR ASSEMBLIES (View 4)

early in the program. As the layout/design developed changes were made in the structural geometry (i.e. R.F. rotary joint sizes became somewhat larger than original estimates forcing a change in the structure). Each of these changes were reviewed and judgment made as to their effect on the analysis. When the changes tended to make the analysis conservative (i.e. reduce the frequency response, stress, etc.) the changes were not reflected in the computer models.

5.1.2.1 Antenna Reflector Construction

In order to provide a stable R.F. reflective surface on Invar honeycomb construction is selected. The reflectors consist of .003 face sheets brazed to a core of .001 invar honeycomb 1.04 lb./in.^{3} density.

The reflective surface (a paraboloid of revolution, 28 inches in diameter with focal length 9.8 inches) will be pre-formed to the required shape placed on a tool with the reflective surface in contact with the tool and furnanced brazed. This fabrication technique will permit surface accuracies in the range of .005 RMS well within the accuracy limits specified in the R.F. design.

5.1.2.2 Truss Construction

Both the upper and lower trusses will be manufactured from Graphite Epoxy tubing (HY-E-1101). Truss joints will be of two types:

a. Ball joints, used where truss members intersect.
b. End fittings where the truss is joined to other components.

The ball joint (a) is constructured of a 2219 aluminum alloy ball to which is welded a "pencil point." The pencil point is a frustrum of a cone, the small dia end of which is welded to the ball and is sized to provide a stress well within the elastic limit of the material. The large end of the cone is made to be the same size of the tube to which it connects. A bonding sleeve is then placed around the tube end and the pencil point and a high temperature bond affected (See Figure 5-3, View 3).

End fittings are attached to the tubes in the manner of the pencil points but are configured to meet attachment requirements.

Construction in this manner will provide a very light weight, strong and very stiff nearly text book perfect truss. Philco-Ford has used this technique for launching groups of satellites very successfully.

5.1.2.3 Gimbaling

Roll and yaw gimbaling motions ($\pm 12^{\circ}$ and $\pm 5^{\circ}$) are provided for thru a large diameter spherical bearing the outer race of which forms the lower terminus of the upper truss. Machined integral with this ring are the attach points for the gimbal actuators (See Figure 5-3, View 3).

Linear actuators have been designed for this application. Four actuators are used, two each for roll and two each for yaw. The actuator pair centerlines are placed out of plane with each other approximately 10° in order to resist the rorsional loads which will occur during launch.

The basic elements of the linear actuators are shown in Figure 5-4 and consist of a motor, gear, ball nut and screw, and an anti-rotation device all contained within a housing. The motor is a reversible brushless stepper motor which drives a gear which is firmly attached to a ball nut. The ball nut is supported and restrained in the housing thru the use of two ball bearings. The ball screw is prevented from rotating as the ball nut turns by the anti rotation rods located in and firmly attached to the housing. Rotation of ball nut causes the ball screw to move in or out of the housing which changes the length of the actuator assembly. This change in length provides the necessary motions about the roll/yaw axes. The required ratio between input and output of the actuator can be changed by selection of a suitable gear ratio or by the lead of the ball nut/screw combination. The design shown in Figure 5-4 provides a ratio of 375:1 that is 375° rotation of the motor causes a 1° rotation of the axis being drive.

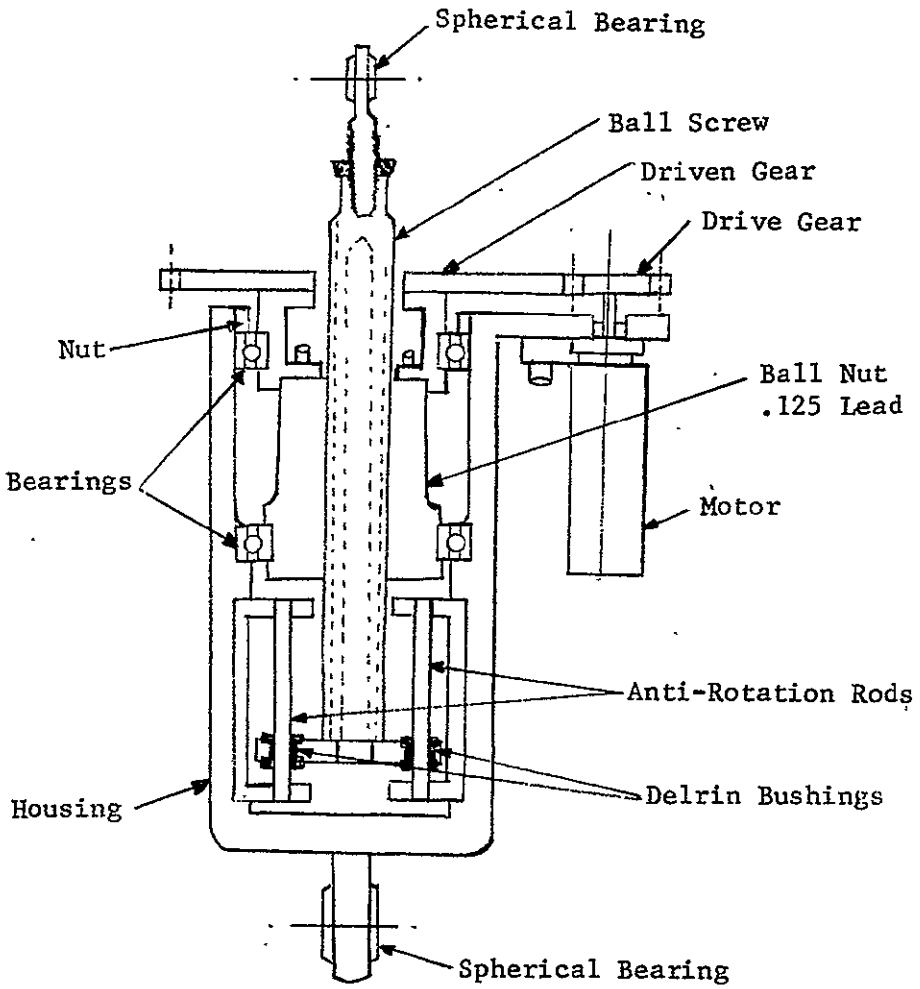

1 inch Linear Travel = 10° Antenna Array Rotation

FIGURE 5-4

ROLL/YAW ACTUATOR

Lubrication of this actuator will be by moly disulfide impregnation on the bearing surfaces of all moving parts. This lubrication technique has been used successfully on several successfull space probes:Ranger, Pioneer, LSM as examples.

5.1.2.4 Motor Drive Assembly

A conceptual motor drive assembly has been designed for motion on the Pitch axis. This unit consists of the following basic components (see Figure 5-3 View 3):

1. Outer housing.
2. Inner support.
3. Two angular contact ball bearings.
4. Brushless motor.
5. Resolver.
6. Slip rings.

The outer housing is designed to support the outer races of the two bearings and

the upper terminus of the two bearings. The upper terminus of the lower truss provides for support of the stationary portion of the R.F. rotary joint.

The inner support provides for support of the rotating portion of the R.F. rotary joints, the inner races of the two bearings and the ball half of the yaw/roll spherical ball bearing.

The outer housing and inner support are fabricated of aluminum alloy treated with a high emissivity coating and with steel inserts impregnated with moly disulfide for the spherical ball bearing on the yaw/roll axis.

The radial space between the inner support and the outer housing contains a brushless motor, a magnetic resolver for position detection and a set of slip rings for carry thru of power and signals to the rotating members.

A set of angular contact ball bearings provide the rotating elements. These bearings are specially manufactured of 52100 steel of the highest quality to insure accurate long time service. Lubrication is provided by Ball Brothers Research Corp Vac-Kote process.

5.1.2.5 Interferometer Mounting

During the structural design study thermal distortion analysis were performed in order to determine the pointing errors between the interferometer horns and the antenna reflectors. In order to maintain the angular error between the RF axis and the axis of the interferometer horns to less than 0.05 degrees it was determined that the interferometer horns had to be structural support separate from the interferometer receiver.

Therefore, the results of the design study of the interferometer as shown in the layout drawing is summarized as follows (See Figure 3, View 4):

1) Orthogonal axis interferometer of 32 inch baseline with the horns mounted directly on the truss members running between the large aperture transmission antennas.

2) The interferometer receiver is located behind the center of the cross of the baseline and is coupled to the horns by non-rigid coaxial cable.

A complete description of the results of parametric study relating to the interferometer mounting in order to reduce alignment errors is contained in the Structural Design Study portion of this report.

Mass Properties - Estimates of weight are shown in Table 5-1.

TABLE 5-1

SYSTEM WEIGHTS

	Weight, Lbs.	
Antennas - 4 ea. @ 2.97	11.90	
Feed Horns - 4 ea. @ 2.00	8.00	
Interferometer Horns - 4 ea. @ 1.26	6.00	
Low Pass Filter - 4 ea. @ 0.4	1.60	
Receiver	8.00	
Structure	20.00	
#4 Antenna Drive Mechanism	3.00	
Wageguide Switches - 2 ea. @ 3.7	7.40	
Waveguide	30.00	
Thermal Control	16.00	
Thermal Finishes	8.00	
Inteferometer Structure	5.00	
Interferometer Waveguide (Coax)	2.00	
Miscellaneous Brackets and Hardware	10.00	
Interferometer Probe	1.00	
Subtotal		137.90
Rotary Joint (R.F.)	9.50	
Pitch Axis Motor & Resolver	3.00	
Pitch Axis Bearings & HSG	13.00	
Roll Axis Gimbal	5.00	
Yaw Axis Gimgal	5.00	
Roll/Yaw Actuators	6.00	
Miscellaneous Electronics	15.00	
Subtotal		56.50
Total Weight, Lbs.		194.40

5.2 THERMAL DESIGN STUDIES

The thermal design studies covered three basic areas: (1) reflector temperature distribution, (2) truss structure temperature distribution, and (3) RF losses and component temperatures. Reflector and truss structure temperature distribution results were used as inputs in the structural design studies which determined the corresponding deflections and distortions. The results from the component thermal analysis were used to recommend minimum surface areas required to radiate the RF losses associated with each component and section of waveguide to maintain temperatures within the preferred range.

The following discussion describes the thermal models used in these design studies, describes conditions analysed, and presents the most pertinent results.

5.2.1 Reflector Thermal Analysis

As the reflector array moves around the earth in its synchronous orbit, the reflectors are subjected to extremely non-uniform solar heating conditions at various times during an orbit. Figure 5-5 shows solar angle as a function of position in orbit. The non-uniform solar heating conditions occur when the solar vector is normal to the reflector axis ($\theta = 0^{\circ}$ or $\theta = 180^{\circ}$). A shadowing problem between reflectors also occurs for these values of θ. Note that at $\theta = 0$ (at equinox) one reflector completely shadows its adjacent reflector. Thus, shadowing effects also cause non-uniformity in solar heating.

To determine reflector temperature distribution as a function of solar angle and shadowing two thermal models were established, an isolated reflector model and a dual reflector model.

Both of these models are based on steady-state analyses. The validity of this approach is discussed in Section 5.2.4 (Reflector Transient Analysis).

The reflector considered is a parabolic dish 28 inches (71.12 cm) in diameter with an F/D ratio of 0.35. The reflector consists of a 1/4 inch (6.35 mm) invar honeycomb core 2.7 lb./ft.^{3} density and 1/4 inch cell size, (4.32 kgm/meter^3 density and 6.35 mm cell size) with 0.003 inch (76.2 micrometer) invar facesheets. All external surfaces were assumed to be coated with a black paint ($\alpha_s = 0.90$ and $\epsilon = 0.90$).

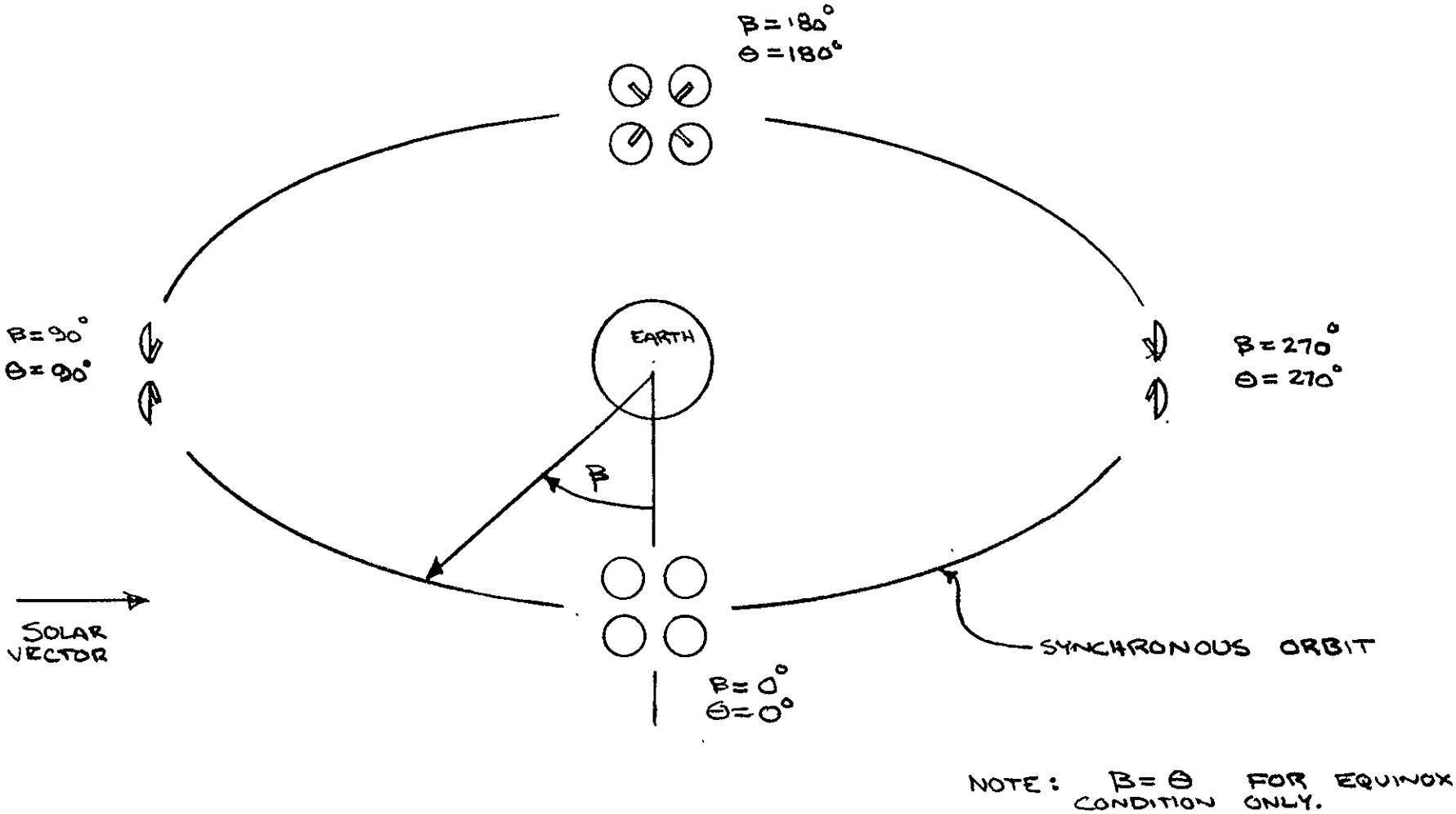

FIGURE 5-5 SOLAR ANGLE AS A FUNCTION OF POSITION IN ORBIT

5.2.2 Isolated Reflector Model

The primary objective of this model was to determine reflector steady-state temperature distribution as a function of solar angle (orbital position) without complicating the analysis by including shadowing by the adjacent reflectors. A 38-node model was created which had the capability of analysing axial, circumferential, and radial conduction effects (refer to Figure 5-6). Note that only half of the reflector is modeled. By defining the solar vector in the X-Z plane, the temperature distributions on either side of the X-axis are symmetrical.

Five solar vector orientations were analysed: (1) $\theta = 90^{\circ}$ - solar vector and reflector axis coincide, (2) $\theta = 54^{\circ}$ - solar vector is normal to point on reflector surface near the reflector edge, (3) $\theta = 10^{\circ}$, (4) $\theta = 0^{\circ}$, solar vector axis is normal to reflector axis, and (5) $\theta = -10^{\circ}$.

From the results of these cases the maximum temperature difference between any two nodes and maximum temperature gradient were determined and plotted as a function of solar angle in Figure 5-7. The maximum temperature difference and maximum temperature gradient occur when $\theta = 0$ and $\theta = -10^{\circ}$ and are presented in Figures 5-8 and 5-9. The results indicated that the axial temperature difference across the core is relatively small (less than $2^{\circ}F$) and can be neglected in future analyses.

5.2.3 Dual Reflector Model

The dual reflector model is shown in Figure 5-10. Due to the negligible affect of axial thermal resistance found from the isolated model results, the nodes on each side of the reflector structure were combined reducing the total number of nodes per reflector by a factor of two. Other than this simplification each reflector in the dual reflector model is identical to the isolated reflector model.

Since reflector #1 completely shadows reflector #2 when $\theta = 0$, the steady-state approach is not realistic because reflector #2 would go to absolute zero. Instead of analysing for $\theta = 0$, $\theta = \pm 5^{\circ}$ solar angle conditions were analysed for steady-state. The solar heat rate inputs to reflector #2 (the partially shadowed reflector) were determined graphically.

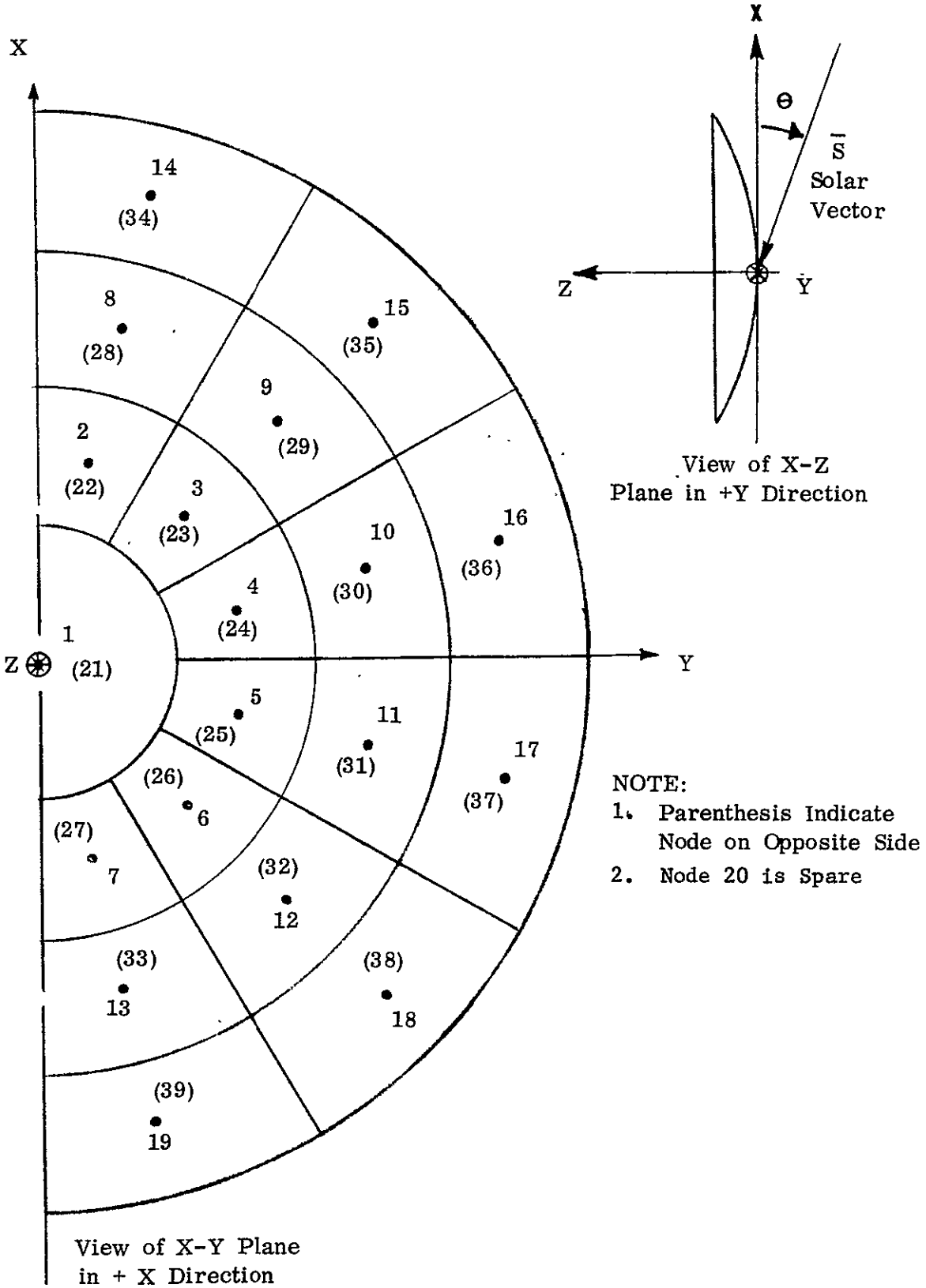

Figure 5-6 Nodal Breakdown for Isolated Reflector Model

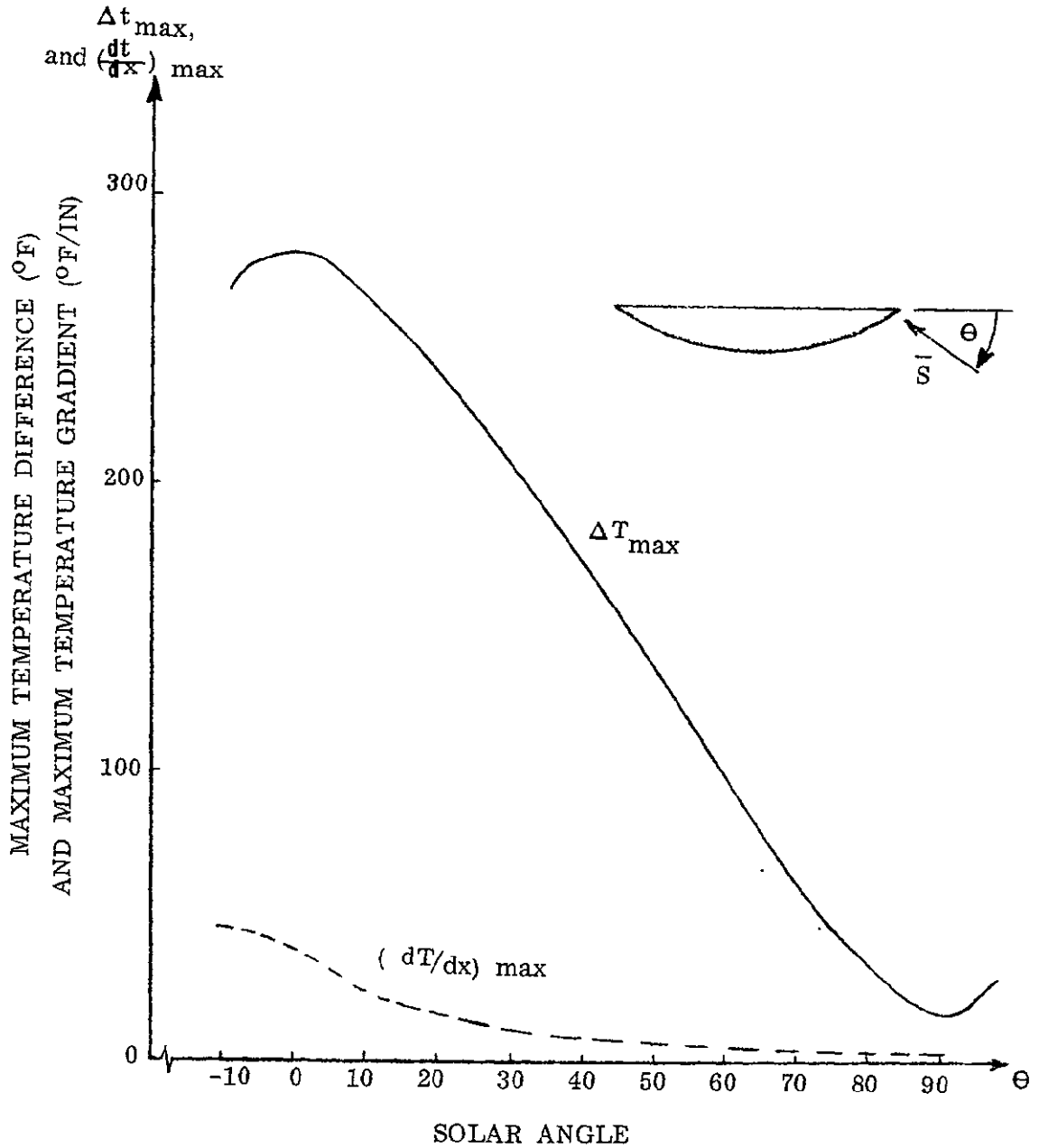

Figure 5-7 Maximum Temperature Difference and Maximum Temperature Gradient Versus Solar Angle

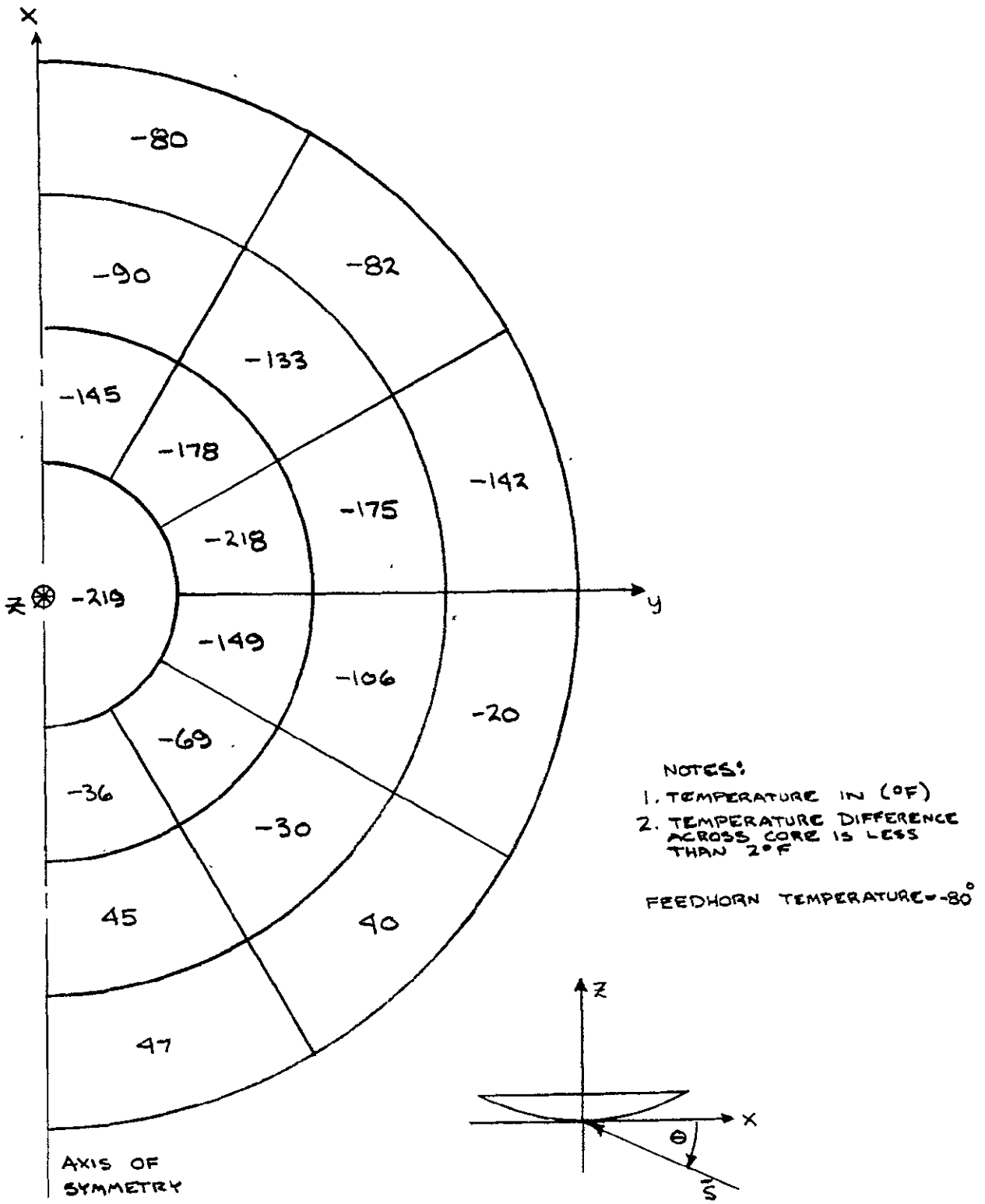

Figure 5-8 Reflector Temperature Distribution for $\theta = 0^{\circ}$

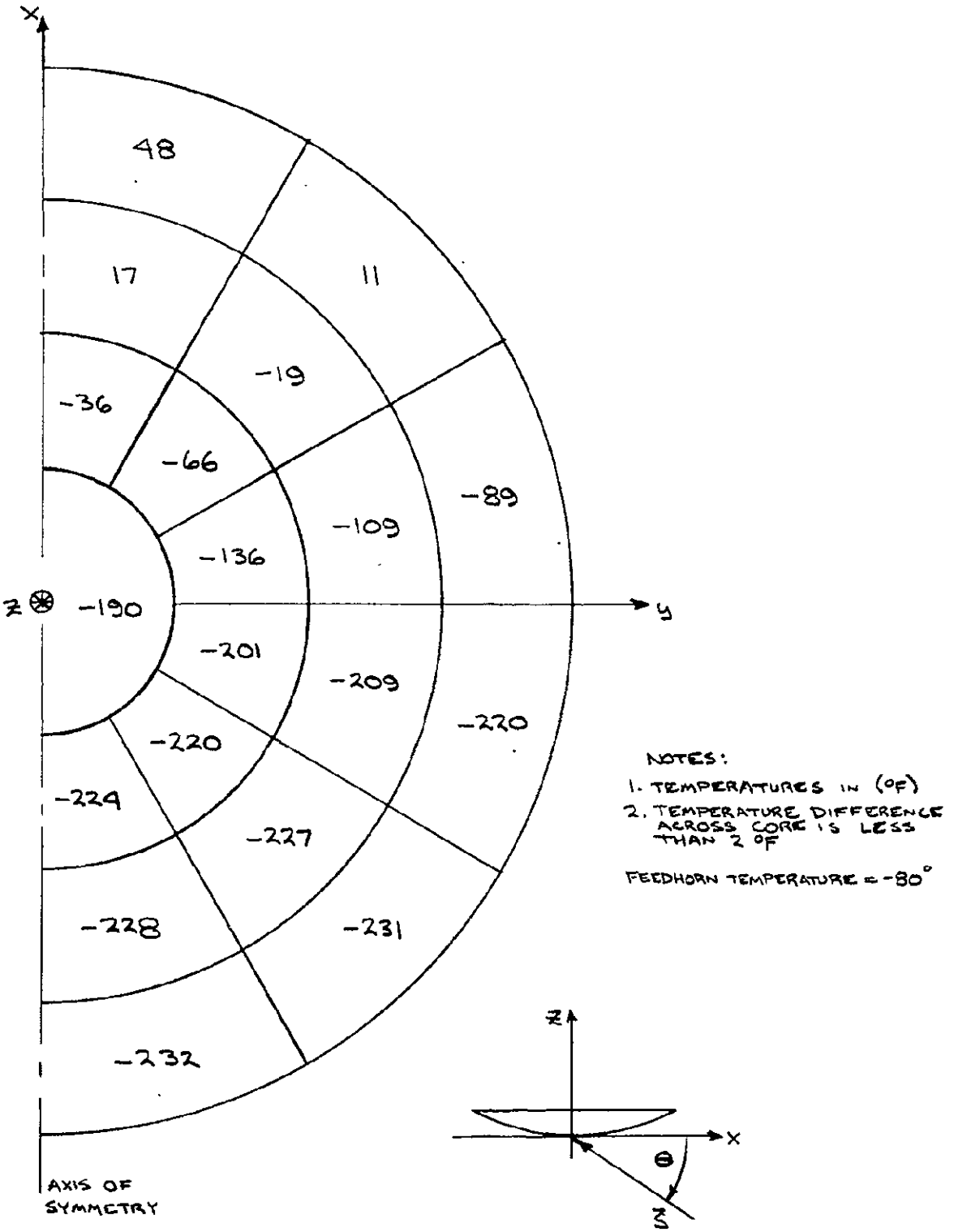

Figure 5-9 Reflector Temperature Distribution for $\theta = 10^{\circ}$

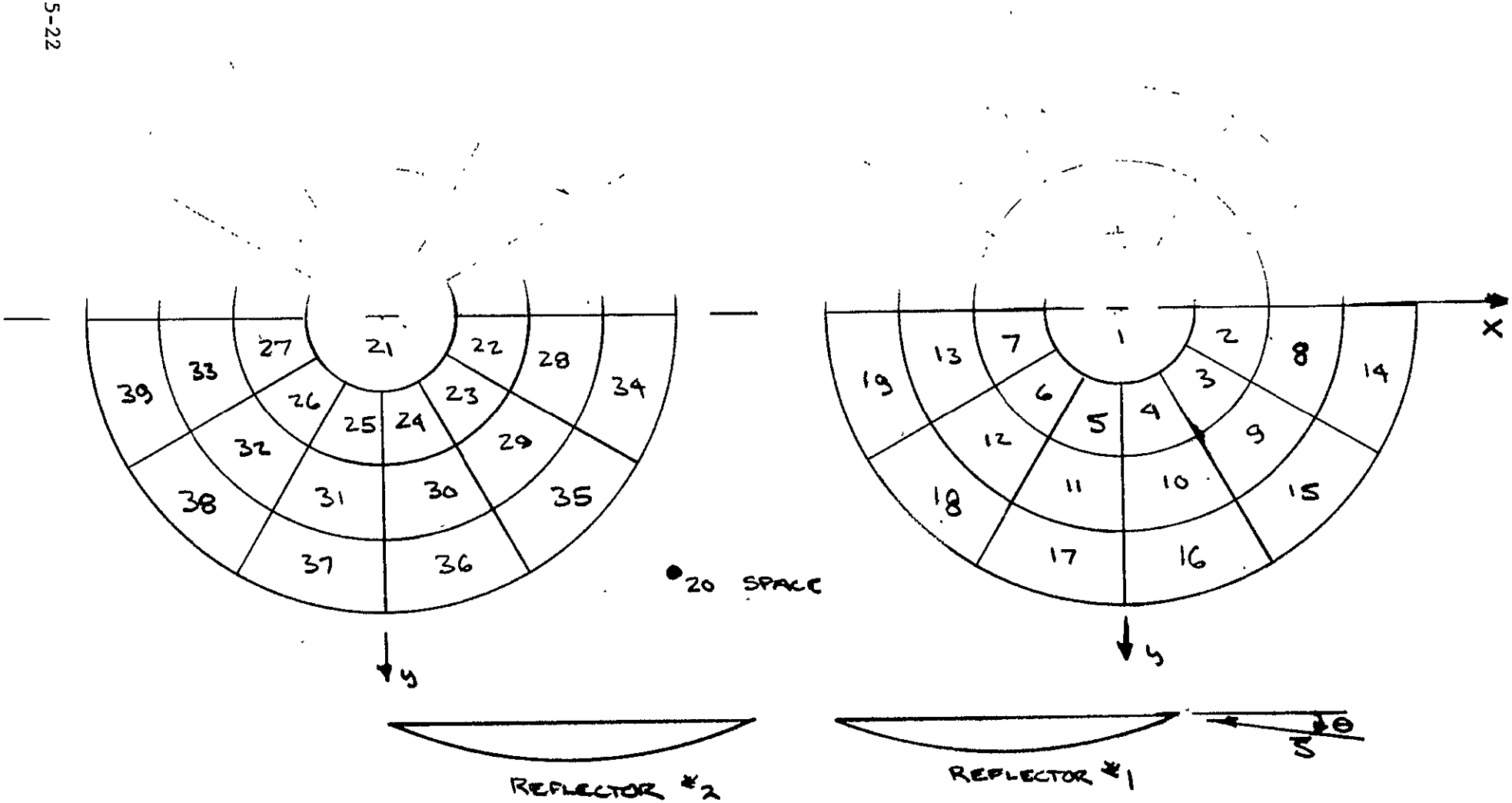

FIGURE 5-10 NODAL BREAKDOWN FOR DUAL REFLECTOR MODEL

The temperature distribution for reflector #2 appeared to be more severe for the $\theta = -5^{\circ}$ orientation than for the $\theta = +5^{\circ}$ orientation. The temperature distributions for $\theta = -5^{\circ}$ are shown in Figure 5-11. The maximum temperature difference of 279°F for reflector #2 ($\theta = -5^{\circ}$) is comparable to the maximum temperature difference found for a reflector with no shadowing at $\theta = 0^{\circ}$ (see Figure 5-7). Note that the $\theta = -5^{\circ}$ temperature distribution for reflector #1 (reflector on sun side) agrees with the temperature distributions for $\theta = 0^{\circ}$ and $\theta = -10^{\circ}$ cases (Figures 5-8 and 5-9) using the isolated reflector model.

5.2.4 Reflector Transient Analysis

A transient analysis was performed for an isothermal section of reflector to gain insight on the validity of the steady-state assumption used for all previous analyses and to determine reflector temperatures at the end of an eclipse period. The reflector temperature response for a shadow condition (no solar heating) with an initial temperature of 140°F (333.5°K) is presented in Figure 5-12. The major conclusion drawn from this figure is that for reflector temperatures above -200°F the time constant is on the order of minutes and for temperatures below -300°F (88.8°K) the time constant is on the order of hours with temperatures between -200°F (144.5 °K) and -300°F (88.8°K) being the transition region. This behavior is due to the third power temperature dependence of radiation resistance terms.

Since the solar angle is changing at 0.25° per minute and at orientations where $\theta > 10^{\circ}$ the time constant is on the order of minutes for the corresponding temperature levels, the steady-state analysis gives an accurate temperature estimates. For $-10^{\circ} < \theta < 10^{\circ}$ some of the reflector temperatures are below -200°F (144.5 °K). Below -200°F (144.5 °K) capacitance effects become significant so the steady-state temperature predictions are on the conservative side.

Note that no drastic temperature drop occurs when one reflector is completely shadowed by another. From Figure 5-12 the temperature drop of a region initially at -220°F (133.5 °K) is approximately 40°F (278°K) for a time duration of 20 minutes which corresponds to a change in θ from 5° to 0°.

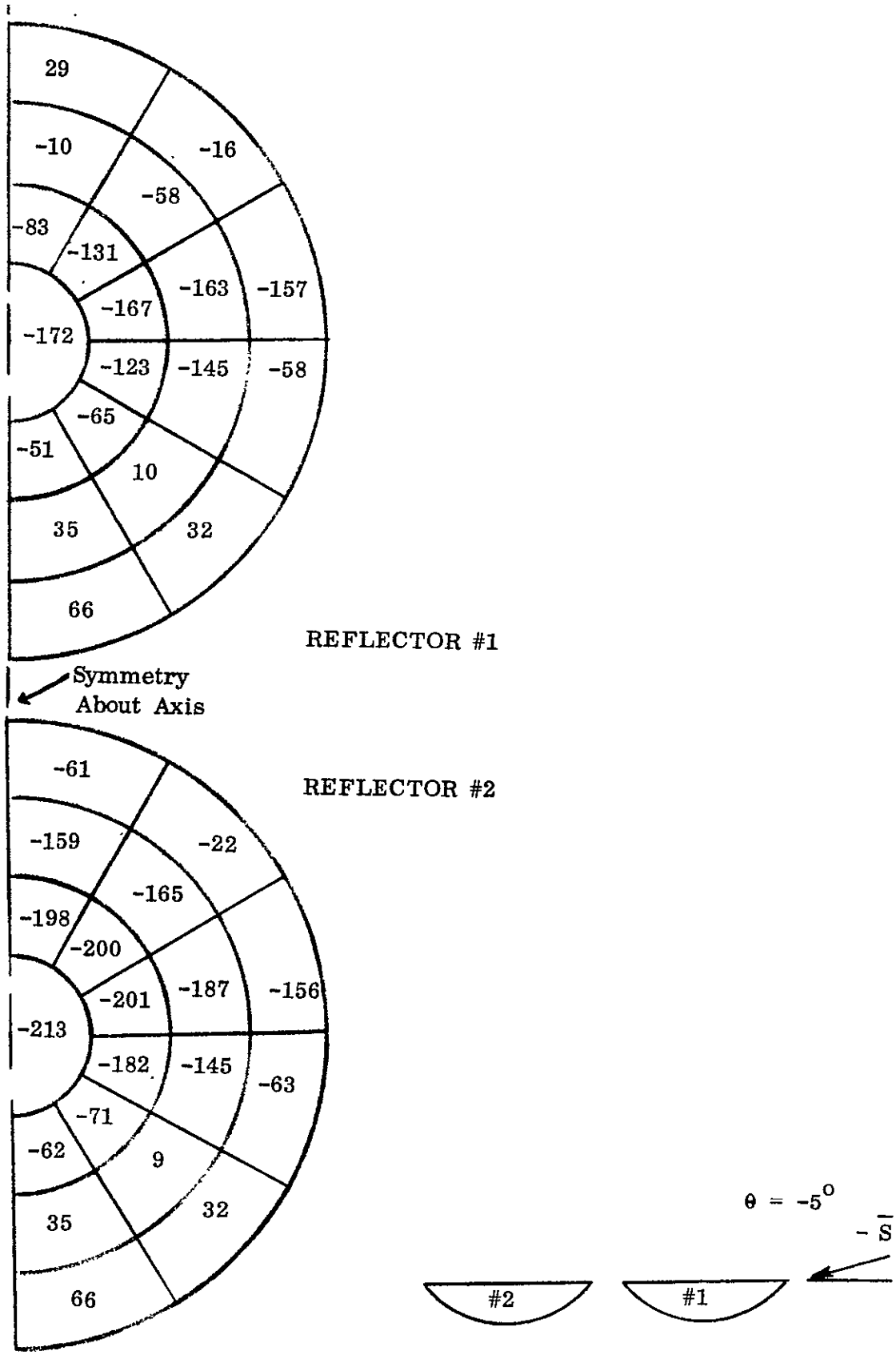

Figure 5-11 Dual Reflector Temperature Distribution

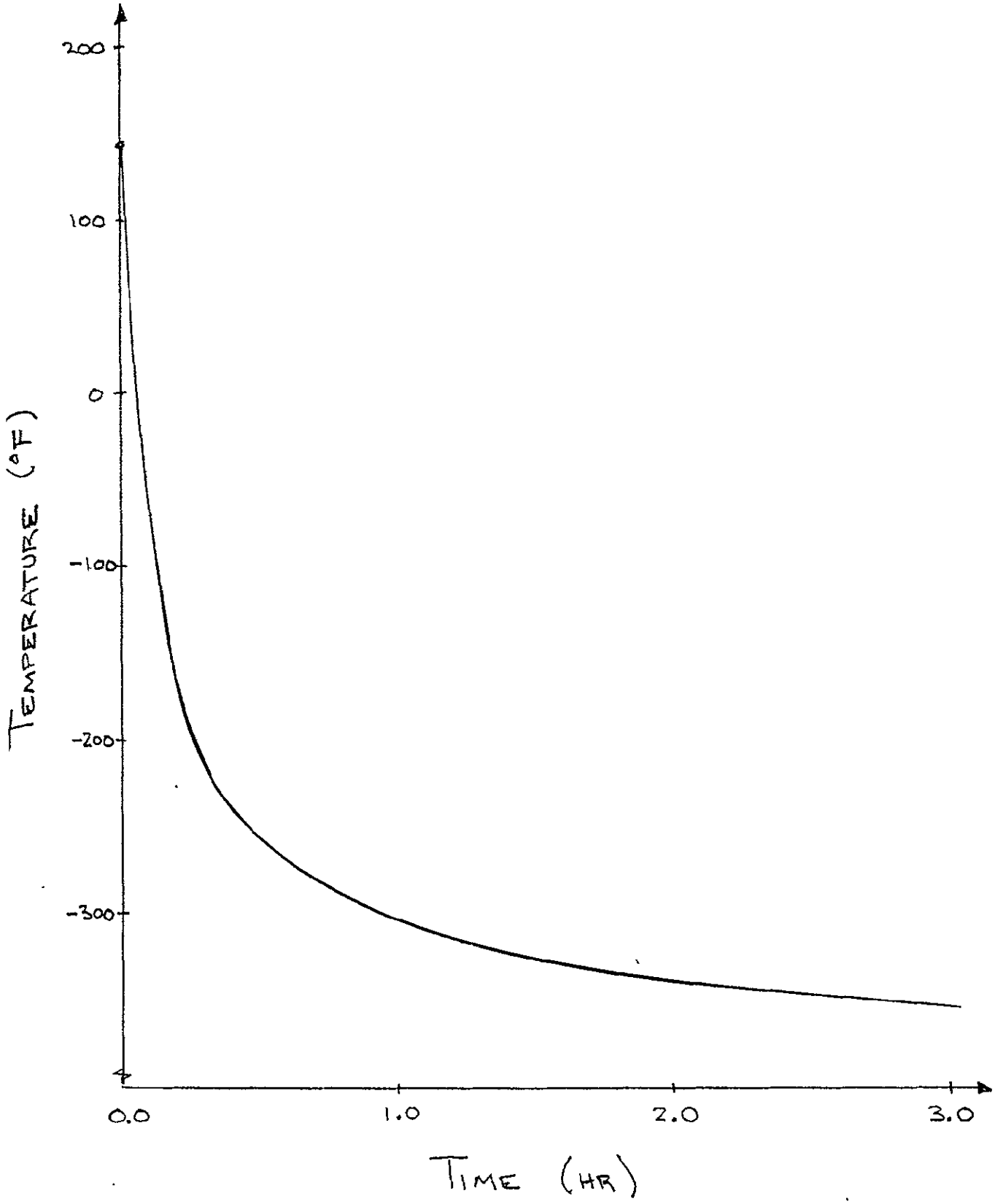

Figure 5-12 Temperature Response of an Idealized Isothermal Reflector

At the end of a 1.2 hour synchronous orbit eclipse the reflector is expected to be virtually isothermal at a temperature of -315°F (80.5° K).

5.2.5 Truss Structure Thermal Analysis

Thermal analyses were performed to determine temperature distributions on the reflector truss structure for various truss member materials and thermal control coatings. Truss member materials recommended for analysis were aluminum, invar, and graphite/epoxy laminates. Three types of thermal control surfaces were considered:

	α_s	ϵ	α_s/ϵ
White Paint	0.30	0.90	0.33
Aluminum Paint	0.25	0.25	1.00
Polished Aluminum	0.15	0.05	3.00

These three thermal control surfaces are practical candidates which cover a wide range of α_s/ϵ.

To gain insight regarding the steady-state temperature levels of the truss members as a function of solar angle, at first the members were assumed to be independent isothermal rods. Figure 5-13 shows the steady-state rod temperatures as a function of solar angle for the three thermal control surfaces. Two conclusions were drawn from Figure 5-13: (1) the higher α_s/ϵ is the greater the total temperature range, and (2) between solar angles of 0° and 60° the decrease in absolute temperature for all three coatings is approximately 18%. Since a majority of the truss members have solar angles less than 60° regardless of orbital position of the spacecraft, the temperature range for the majority of the truss members is within 18% of the maximum absolute value ($\theta = 0°$) with two exceptions: (1) the few members with $\theta > 60°$, and (2) those members which are shadowed by the reflectors. With conduction effects included the low temperature extremes for these two exceptions are reduced.

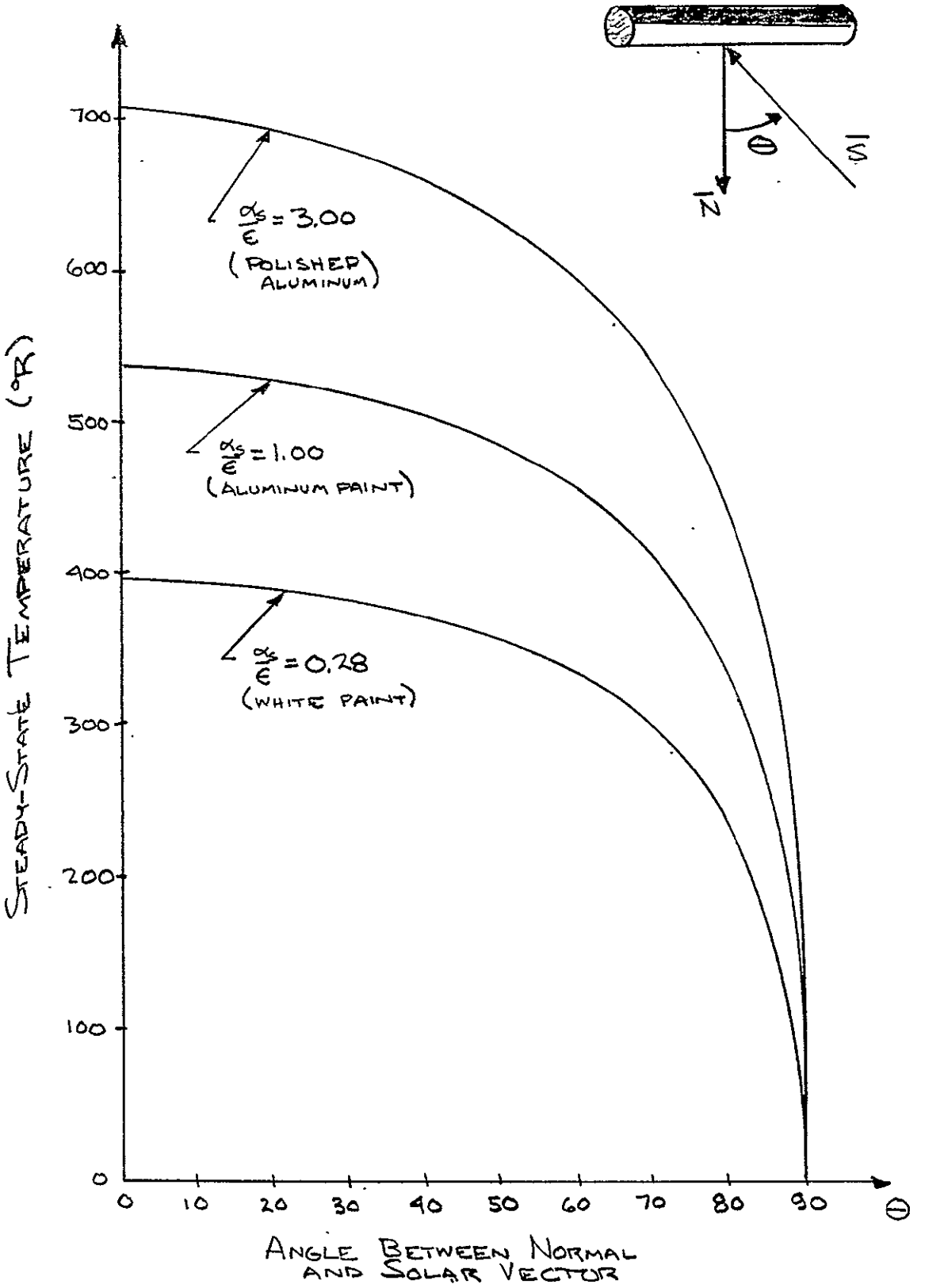

Figure 5-13 Temperature versus Solar Angle for Isothermal Rod Model

5.2.5.1 Truss Thermal Model

To predict the temperature distribution for the truss structure when partial shadowing of the reflectors occurs and conduction effects are included, a 33-node model was developed (refer to Figure 5-14). Each joint and member were represented by a node. Conduction through the members and joints was considered. Only radiation from the members to space was considered because radiation between the members and between the members and reflectors was assumed to be negligible. Due to the large number of cases (combinations of materials and surface coatings), only the most severe shadowing case (by reflectors) was analysed using this model. For this case a few members received solar radiation with $\theta \geq 20^{\circ}$ and the remaining members are totally shadowed by the reflectors (refer to Figure 5-15).

5.2.5.2 Truss Temperature Distribution

The resulting temperature distributions are listed in Table 5-2 and summarized in Table 5-3. No conclusions regarding the optimum combination of material and thermal control coating can be reached from a thermal standpoint. The case with the maximum temperature difference between members does not necessarily produce the largest distortion because the coefficient of thermal expansion and material stiffness must also be included. Thus, the temperature results served as inputs to the truss distortion analysis which is discussed in a separate section of this report.

5.2.6 RF Losses and Component Temperatures

5.2.6.1 Thermal Design Criteria

The preferred temperature range of the RF components, such as the rotary joint, circular polarizer, and connecting waveguide is 20° to 120°F (266.5° K to 322.5°K). This preferred temperature range is based on the required dimensional stability of the RF chokes.

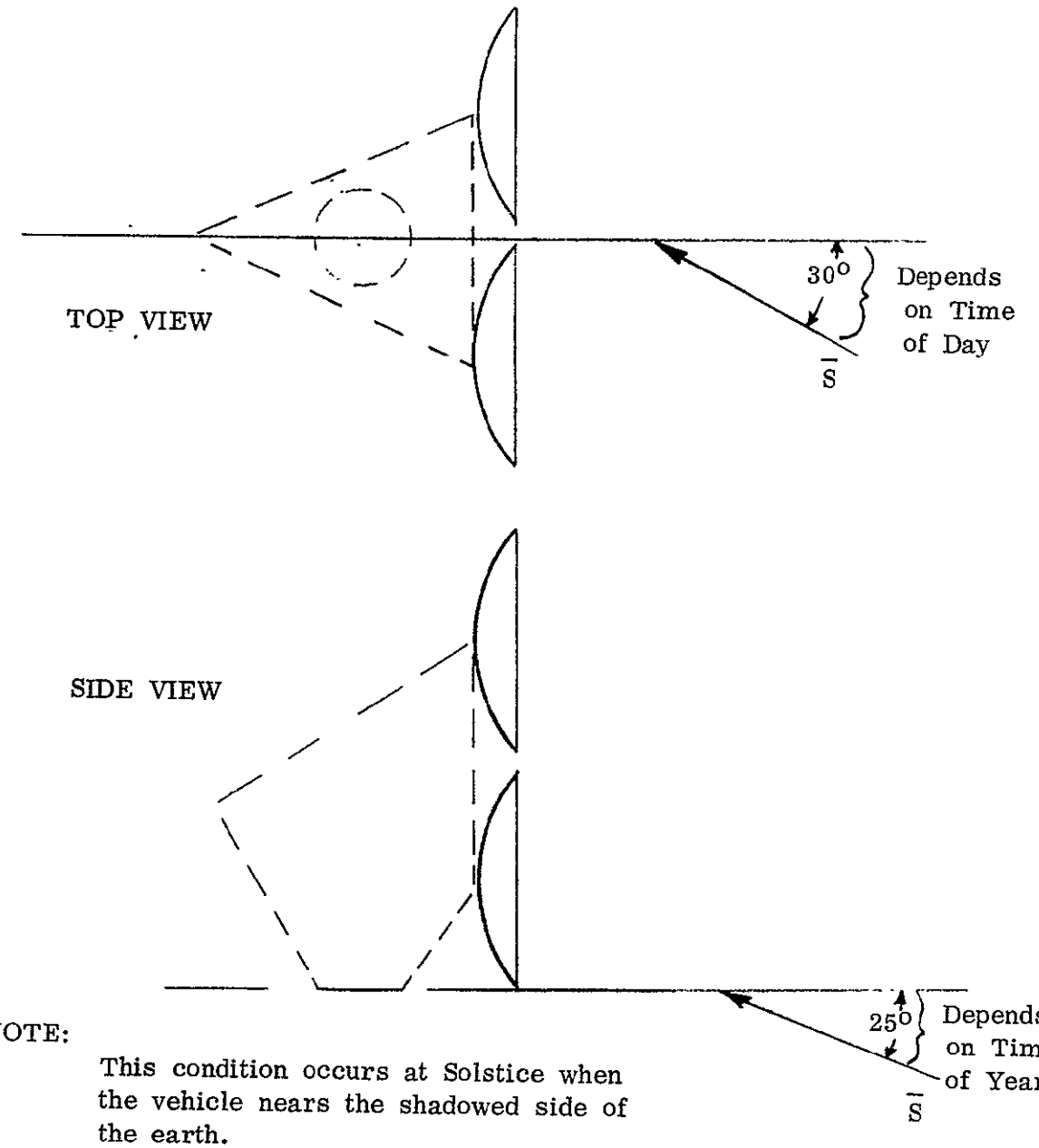

NOTE:

This condition occurs at Solstice when the vehicle nears the shadowed side of the earth.

Figure 5-14 Solar Vector Orientation For Most Severe Temperature Distribution

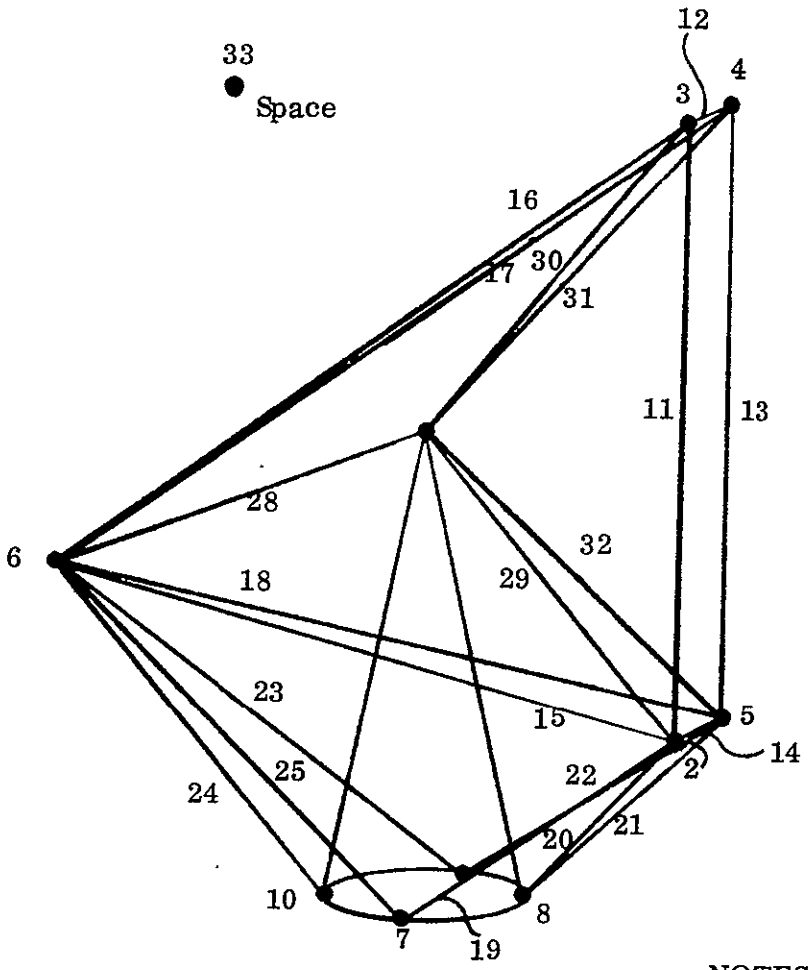

TYPICAL CIRCUIT:

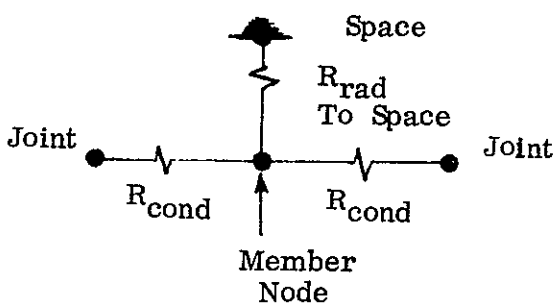

NOTES:

1. Lower portion of structure is not included in model.

2. Node 1-10 are joints, the remaining nodes are members.

Figure 5-15 Analytical Model Nodal Breakdown

TABLE 5-2

REFLECTOR TRUSS STRUCTURE TEMPERATURE (°F)
DISTRIBUTIONS FOR WORST CASE ORIENTATION

Node	White Paint	Al. Paint	Polished Al.	White Paint	Al. Paint	Polished Al.	White Paint	Al. Paint	Polished Al.
1	-216	-144	-47	-248	-177	- 70	-269	-206	-103
2	-239	-173	-67	-305	-252	-152	-266	-231	-160
3	-194	-129	-41	-186	-114	- 21	-142	-101	- 36
4	-153	- 80	- 4	-123	- 50	51	-120	- 69	9
5	-224	-160	-60	-235	-173	- 86	-187	-129	- 50
6	-235	-167	-62	-202	-234	-131	-343	-302	-223
7	-243	-177	-69	-318	-266	-163	-366	-332	-256
8	-229	-163	-61	-253	-187	- 97	-263	-200	-101
9	-234	-169	-64	-285	-234	-132	-358	-326	-247
10	-236	-165	-60	-308	-250	-139	-355	-314	-227
11	-153	-124	-52	-125	- 99	- 52	-126	-101	- 58
12	-138	- 99	-28	-128	- 87	- 10	-123	- 93	- 37
13	-143	-107	-35	-124	- 95	- 40	-124	- 94	- 40
14	-158	-133	-59	-126	-101	- 57	-127	-102	- 60
15	-245	-179	-70	-322	-271	-168	-354	-320	-242
16	-209	-136	-43	-205	-125	- 25	-203	-121	- 16
17	-160	- 75	8	-145	- 47	77	-143	- 43	88
18	-231	-164	-61	-245	-180	- 95	-240	-172	- 86
19	-243	-177	-69	-318	-267	-164	-361	-328	-254
20	-237	-171	-66	-295	-238	-138	-320	-273	-179
21	-221	-155	-57	-193	-118	- 47	-171	- 81	21
22	-231	-167	-63	-271	-221	-121	-335	-309	-226
23	-239	-173	-66	-306	-253	-148	-367	-331	-254
24	-243	-174	-65	-321	-267	-160	-366	-328	-247
25	-243	-176	-67	-318	-265	-161	-368	-333	-257
26	-280	-160	-58	-286	-223	-115	-332	-283	-183
27	-282	-162	-57	-302	-243	-131	-348	-305	-213
28	-240	-171	-68	-315	-259	-151	*	*	*
29	-238	-170	-64	-312	-257	-149	-347	-306	-219
30	-202	-131	-40	-196	-115	- 16	-193	-110	- 4
31	-154	- 75	- 2	-114	- 8	113	-109	0	141
32	-220	-151	-53	-225	-153	- 61	-221	-146	- 49

*Member deleted.

TABLE 5-3

TRUSS TEMPERATURE SUMMARY

Material	Surface Finish	Temperature, °R		
		Max.	Nominal	Min.
Aluminum	White paint	322 (12)*	244	215 (15)
	Aluminum paint	385 (17)	311	281 (15)
	Polished aluminum	468 (17)	408	390 (15)
Invar	White paint	346 (31)	218	138 (15)
	Aluminum paint	452 (31)	278	189 (15)
	Polished aluminum	573 (31)	374	292 (15)
Hy-E Laminate	White paint	351 (31)	204	92 (25)
	Aluminum paint	460 (31)	254	127 (25)
	Polished aluminum	601 (31)	338	203 (25)

* Number in ( ) refers to nodes of thermal model Figure 5-15.

5.2.6.2 Preliminary Thermal Analysis

Since RF losses occur in these components, heat rejection capability must be considered in the thermal control analysis.

Assuming a thermal control coating of white paint ($\alpha_s = 0.30$, $\epsilon = 0.90$), the temperature of a cylindrical surface was calculated as a function of solar illumination and power density and is presented in Figure 5-16. These results show that the power density must be maintained between 24 to 38 watts/ft.^{2} for the component to be within the preferred temperature range of 20°F to 120°F (266.5 $^\circ$K to 322.5 $^\circ$K). The power density of each component was computed based on its RF loss and surface area. For some components the power density exceeded the 38 watts/ft.^{2} maximum, in which case, the minimum area to obtain 38 watts/ft.^{3} was calculated. The resulting RF loss distribution minimum surface area, and component temperatures are shown in Figure 5-17. A total of 12.7 square feet of additional surface area must be added for a truss type structure in order to dissipate the RF power losses and maintain the RF components within the preferred temperature range of 20°F to 120°F (266.5 $^\circ$K to 322.5 $^\circ$K).

5.3 STRUCTURAL DESIGN STUDY

The structural design study for the Antenna Pattern Shaping, Sensing and Steering Study included three specific efforts: truss structural analysis, truss distortion, and reflector distortions.

5.3.1 Truss Structure

A preliminary structural analysis was performed for the proposed antenna pattern shaping, sensing and steering study antenna configuration to assure that weight requirements could be met and that structural performance met all requirements.

A truss was chosen for the upper support structure to fulfill geometric requirements and to reduce shadowing on the reflectors. A truss and shell were considered for the lower support structure. Of the two lower support structures, the one used will greatly depend on the mounting structure provided on the satellite.

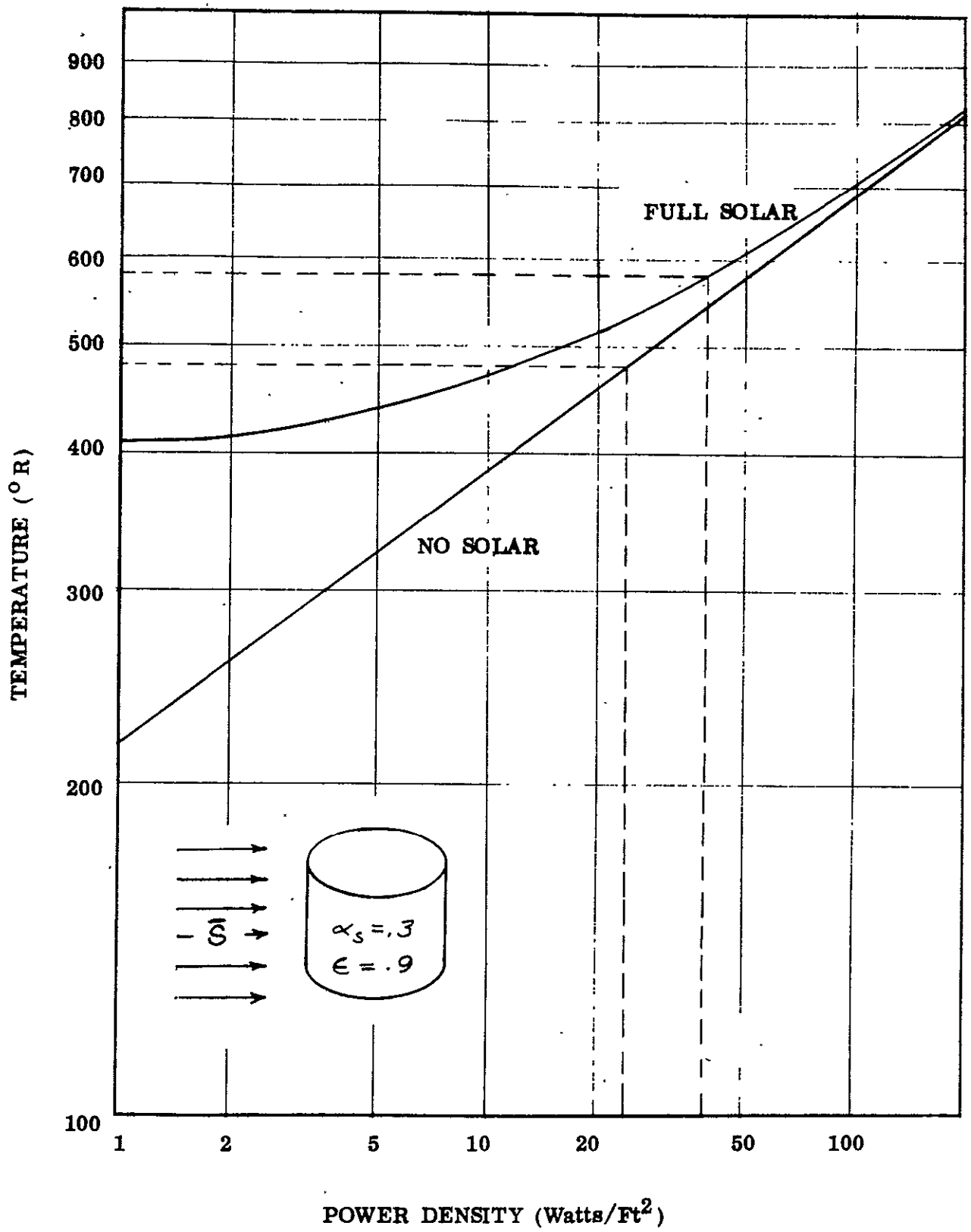

Figure 5-16 Cylinder Temperature As A Function Of Solar Illumination and Power Density

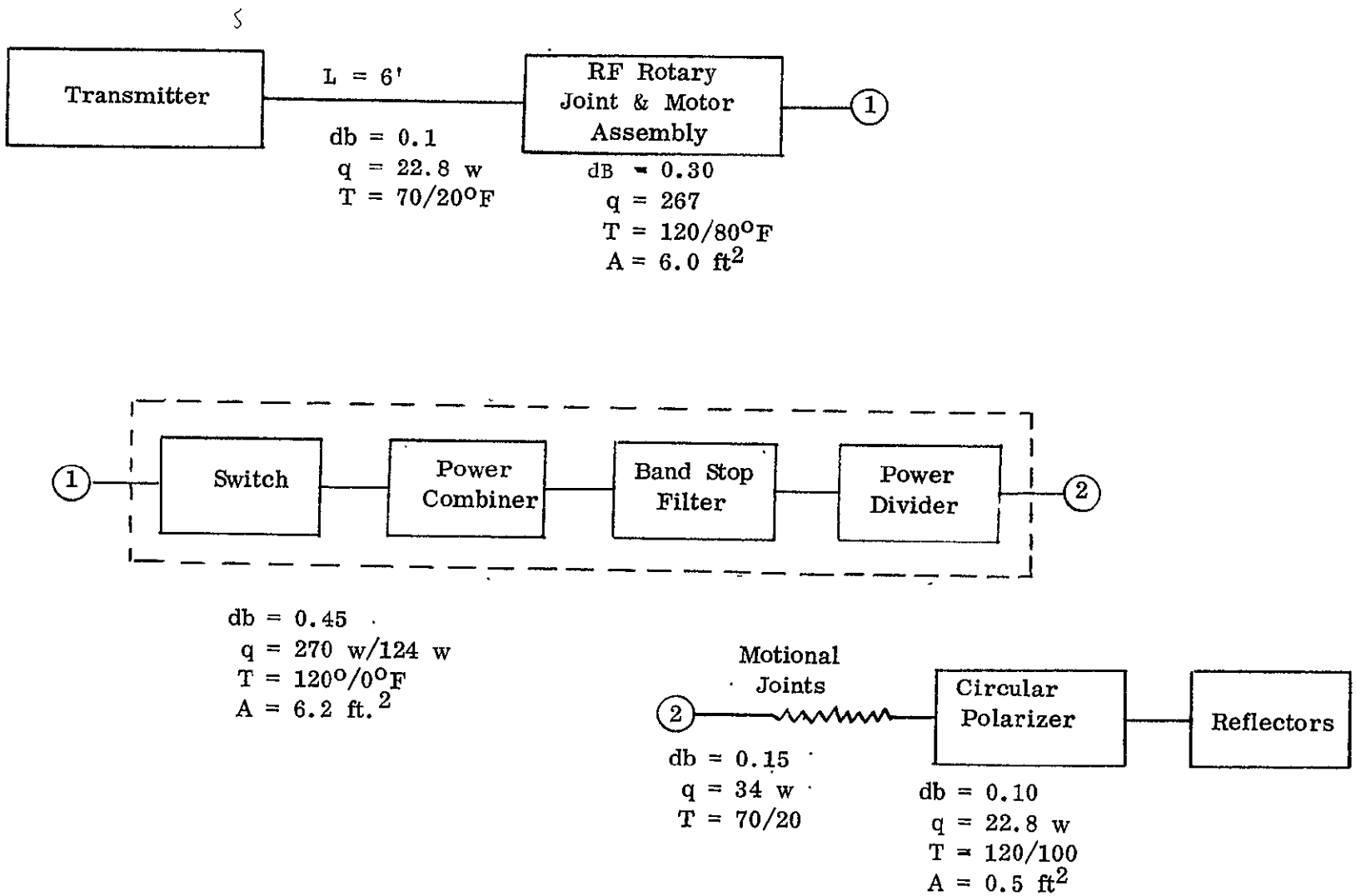

Figure 5-17 RF Loss Distribution and Component Temperatures

The truss support structure was analyzed using computer techniques supplemented by hand calculations. The shell was analyzed using hand calculations.

Truss member areas were determined by stiffness criteria. The inertias were selected to satisfy column buckling criteria. The face sheets of the shell were sized for stress and intracell buckling criteria.

5.3.2 Truss Distortion

Pointing errors between the interferometers and antenna reflectors due to thermal distortions of the antenna support structure were investigated. The thermal distortions result from shadowing part of the antenna support structure during a critical sun orientation. Results were obtained for a graphite epoxy support structure and an aluminum support structure. The maximum pointing error calculated using the graphite epoxy support structure was 0.018 degrees and was well within the budgeted error of 0.05 degrees. For the aluminum structure the error was from 0.041 to 0.099 degrees and is dependent on the surface finish of the truss members.

5.3.3 Reflector Distortions

A fininte element model of an antenna reflector and feed support was developed in order to predict structural distortion of the antenna for worst-case, space-environment, temperature conditions. This model is used, in conjunction with the computer routine entitled "Structural Analysis and Matrix Interpretive System" (SAMIS), to predict thermal distortion of the reflector and feed support.

The reflector material was assumed to be honeycomb construction with 0.003 inch (0.762 mm) thick invar face sheets with 0.250 inch (6.35 mm) thick invar honeycomb core. The feed support was also assumed to be fabricated from invar, with dimensions of 0.375 in. x 0.750 in. x 0.020 in. (9.525 mm x 19.05 mm x 0.508 mm). A three point support on a 6-inch (15.24 cm) diameter circle was assumed.

Based on the worst-case, sun angle ($\theta = 0$), temperature distribution, distortion of the antenna reflector is a maximum of $\pm$ 0.002" (0.05 mm) in the plane of the antenna aperture. Predicted distortion of the antenna is nominal and can be related as a rigid body rotation of the reflector aperture.

5.3.4 Structural Design Study Requirements

The structural design study requirements were derived from the mechanical layout design which in turn is based on the RF design requirements for the antenna system. Basically the structure consists of two parts; an upper structure supporting the four reflectors from the gimbal and RF rotary joint platform and a lower structure supporting upper structure, gimbal and RF platform to the satellite.

The structural design load criteria is based on the assumed launch environment for a vehicle.

The thermal distortion tolerance of the antenna structure, reflector assembly, and interferometer support are based on the RF performance and steering requirements of the study.

5.3.4.1 Structure Definition

Figure 5-18 shows the proposed upper support structure. A truss is chosen because (1) a minimum of shadowing occurs on the reflectors minimizing thermal distortions; (2) it is judged that cantilevering a truss structure from the lower support structure is more efficient (greater stiffness/weight ratio) and can more easily adapt to the geometry needed to satisfy RF systems requirements; (3) computer programs required to analyze the structure in detail are much easier to use when the structure is a truss; and (4) the capability of fabricating a truss in-house, thus reducing cost, is greater.

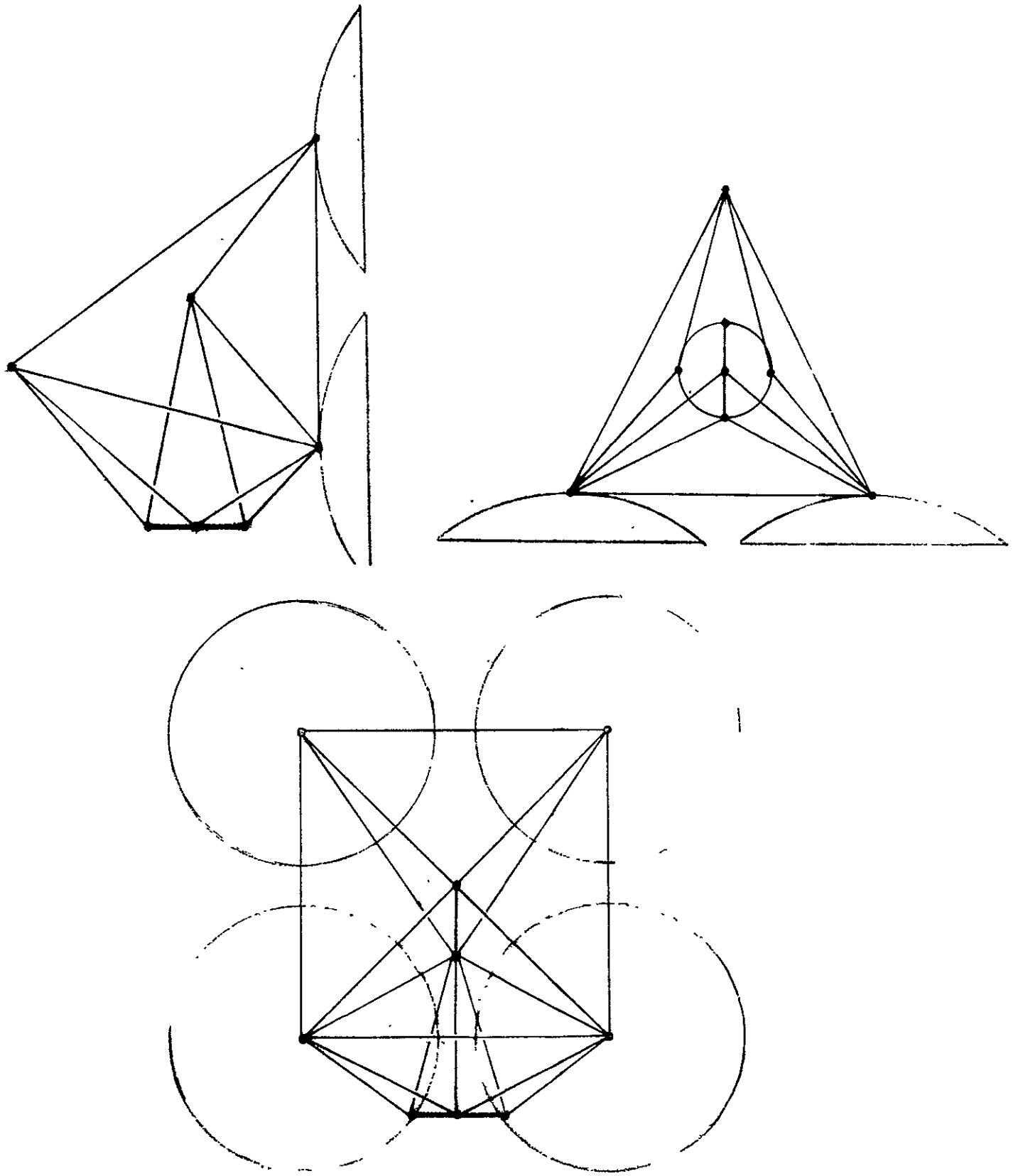

Figure 5-18 Upper Truss Support Structure

Figures 5-19 and 5-20 are proposed lower support structures. Figure 5-19 shows a truss structure while 5-20 is a honeycomb shell. It is felt the two structures will not differ greatly in weight. The structure to be chosen will depend on the satellite/antenna interface which is undefined at this time.

Figure 5-21 is the computer model used to analyze the truss structure. The shell will be analyzed by hand calculations due to difficulty in using SAMIS.

5.3.4.2 Design Criteria

The structural design criteria for the structural design study is summarized in Table 5-4 and discussed in the following paragraphs

Strength - The following flight load factors will be used:

(1) -6.8 g on longitudinal axis and ±2.3 g laterally.
(2) +1.8 g on longitudinal axis and ± 2.3 g laterally.

In general condition (1) is worst case.

It is assumed that the ground handling of the antenna is sufficiently controlled such that the loads experienced during fabrication and transportation will not exceed the flight loads.

In addition, the structure is required to carry loads due to response of the masses of the antenna during an RMS sine vibration of 1.0 g in the frequency range 10 to 60 Hertz and 2.0 g in the range of 70 to 2000 Hertz.

Thermal distortions will produce internal loads which must be carried by the structure. In general, these loads will be much less than the above load criteria.

Stiffness - With the antenna on a fixed base no structural resonance shall be lower than 14 Hertz in a lateral direction.

Factors of Safety - Structural components shall be designed to reflect a 1.0 factor of safety against yield stress and a 1.25 factor of safety against ultimate stress and buckling.

NOTE:
DASHED LINES ARE NOT
REQUIRED FOR STABILITY

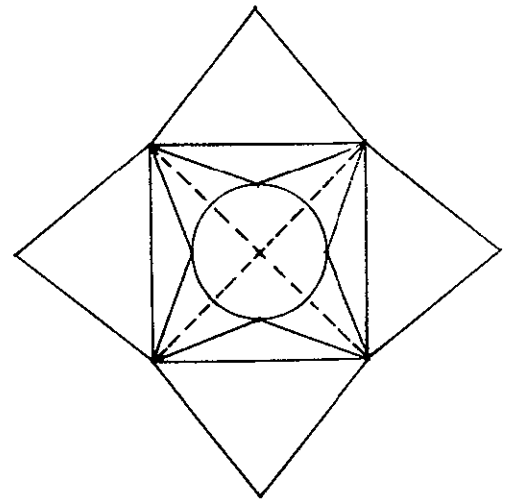

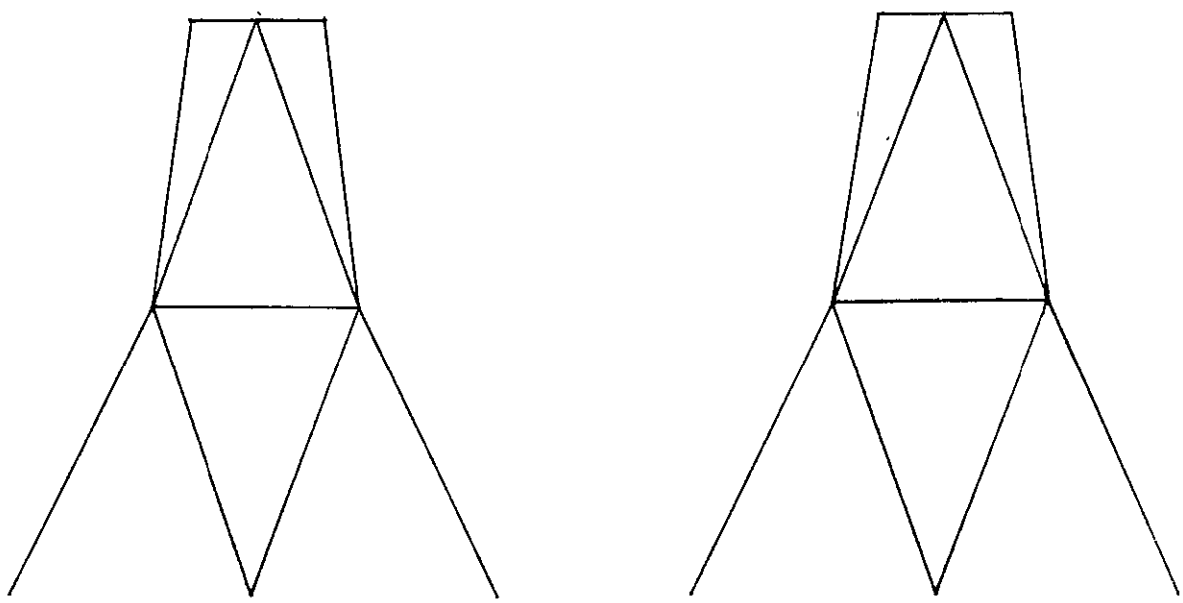

Figure 5-19 Lower Truss Support Structure

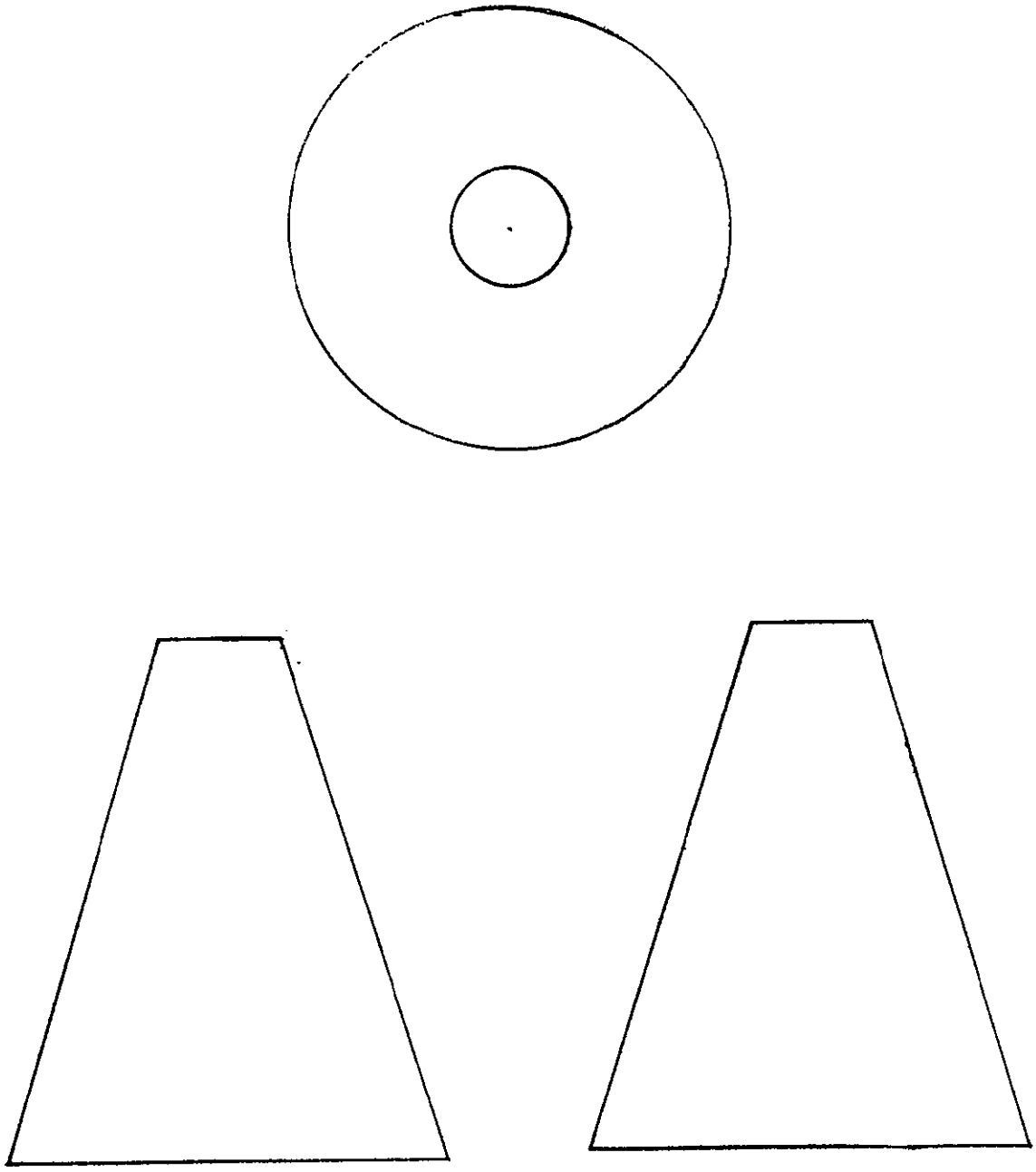

Figure 5-20 Alternate Tower Support Structure

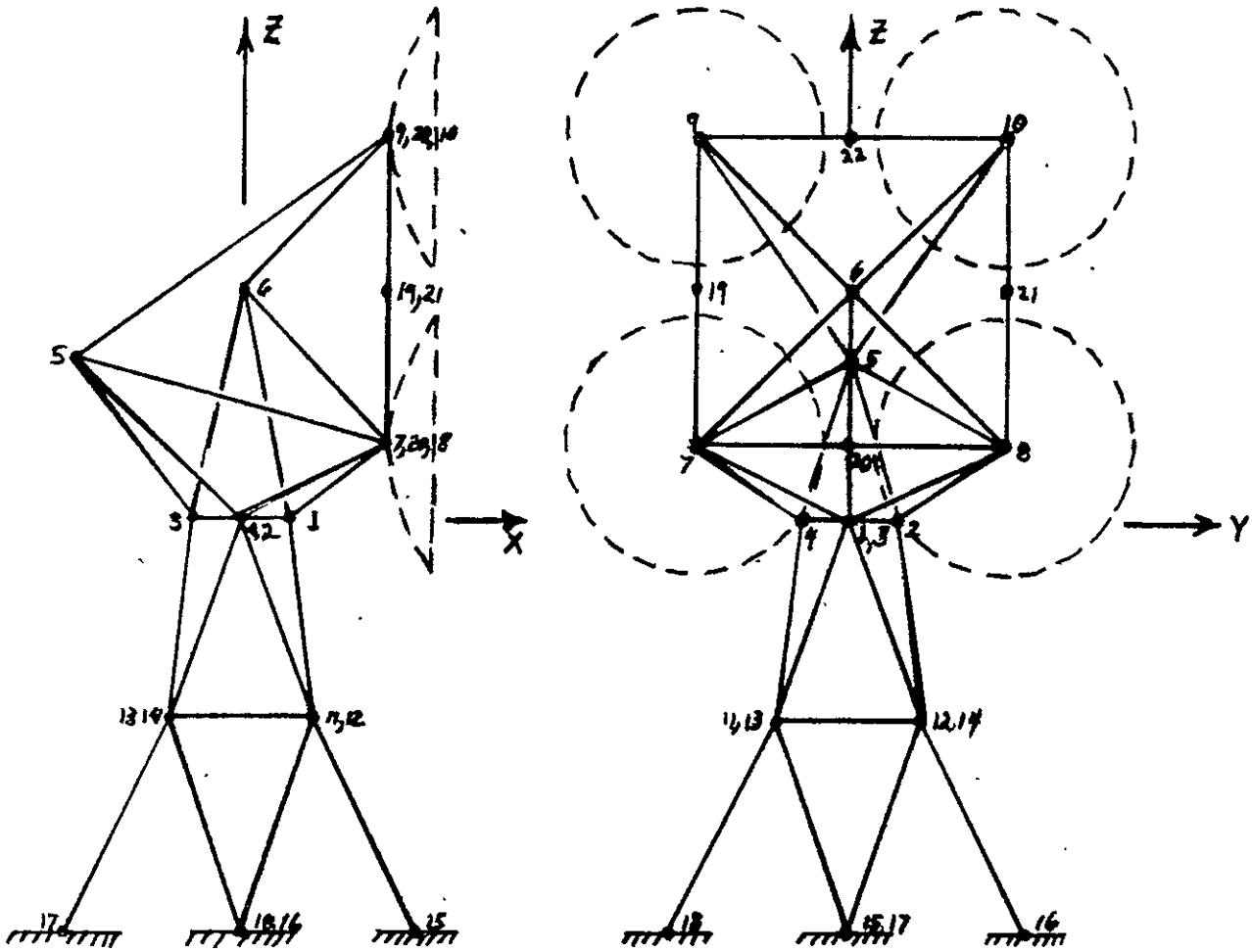

Figure 5-21 TRUSS COMPUTER MODEL

TABLE 5-4

STRUCTURAL DESIGN CRITERIA

- Sustained Acceleration

  -6.8 g Longitudinal (Z Axis)

  +1.8 g Longitudinal (Z Axis)

  ±2.3 g Lateral (X and Y Axis)

- Vibration

  1 g Sinusoidal Input

- Factors of Safety

  1.0 Limit

  1.25 Ultimate

- Stiffness

  No Structural Resonance in Lateral Direction Less Than 14 cps (Fixed Base)

- Thermal Distortion

  0.05 Degree Maximum Pointing Error Between Reflectors and Interferometer

5.3.4.3 Weight Distribution

The weight of the RF system for the structural analysis is represented by six concentrated masses: one for each of the four antennas, the interferometer receiver and the RF rotary joint. The weight summary for each of these six dumped masses is presented in Table 5-5.

5.3.5 Structural Design Analysis

The truss structure, Figure 5-21, was designed on an existing truss design program TDPREL. The input data includes a materials table, joint coordinates, member cards, and dynamic design criteria.

The materials table includes Young's modulus and density for aluminum, Hy-E Material 1101, and Boron Fiberglass. A structure is designed for each of these materials.

The dynamic design criteria consists of unit loads at the cg of each mass for each dynamic degree of freedom and a mass matrix relating forces to accelerations. For preliminary dynamic analysis a simplified two node mass model is used. One mass represents the four reflectors, interferometers, and miscellaneous electronic equipment as if mounted to a thin plate. The other mass represents the rotary joint. The weights used in the calculation of the mass and interia terms are those presented in Table 5-4.

5.3.5.1 Preliminary Truss Design Analysis

Preliminary design analysis were performed to define an efficient truss support configuration, to optimize its stiffness to weight ratio, and to compare the performance of different truss materials. This initial analysis was performed with a computer routine referred to as TDPREL which is represented in block diagram in the upper portion of Figure 5-22. This program permits automated design of hyperstatic truss structure subject to alternate resonant frequency requirements.

TABLE 5-5

WEIGHT DISTRIBUTION

Weight Lumped at Each Reflector	
Reflector	2.975
Side Lobe Suppressor Horns	3.000
Antenna Drive Mechanism	.750
Structure	1.000
Thermal Finishes	2.000
Misc. Brackets	1.000
	10.725#

Weight Lumped at Receiver	
Low Pass Filter	1.60
Receiver	8.00
Structure	6.00
Waveguide Switches	7.40
Thermal Control	8.00
Interferometer Wave Guide	2.00
Interferometer Probe	1.00
Misc. Brackets & Hardware	6.00
Interferometer Horns	6.00
Interferometer Structure	5.00
	51.00#

Weight Lumped at Rotary Joint	
Structure	10.00
Thermal Control	8.00
Rotary Joint	6.50
Pitch Axis Motor & Resolver	3.00
Pitch Axis Beakings & Housing	13.00
Roll Axis Gimbal	10.00
Yaw Axis Gimbal	10.00
Misc. Electronics	15.00
	75.50#

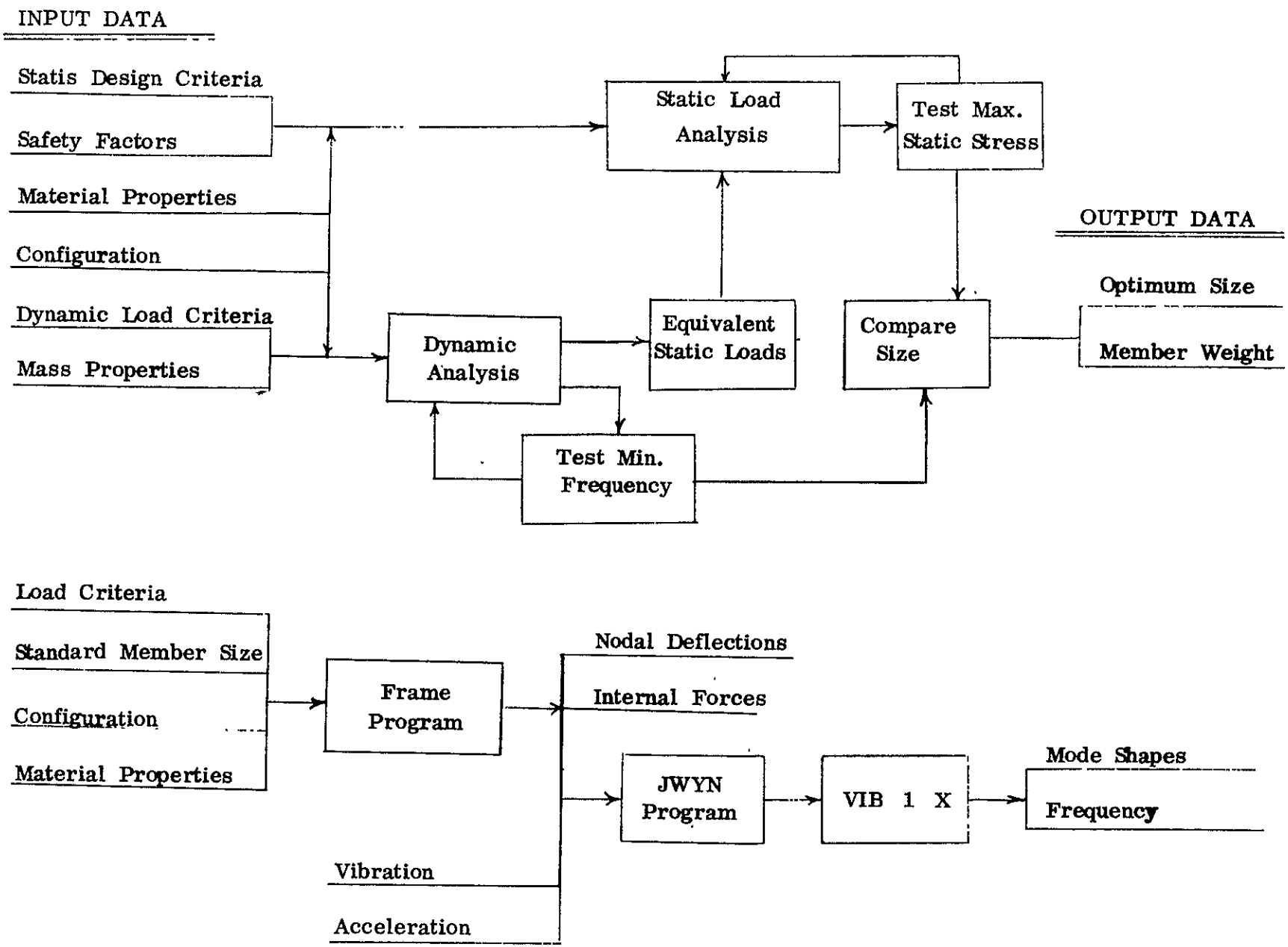

Figure 5-22 Truss Structural Analysis

The input data for TDPREL consists of static design and dynamic load criteria, safety factors, configuration and joint coordinates, and material and mass properties. The truss design criteria used for the study included: (1) a minimum allowable lateral resonant frequency of 14 Hertz and (2) static load factors of 6.8 g's longitudinal and $\pm$ 1.8 g's lateral. Several different basic truss configurations were studied. In addition, joint locations in each of the basic configurations were varied arbitrarily to assist in defining the optimum location for each joint. The performance of three different truss member materials were compared. These included aluminum, graphite-epoxy and baron/epoxy.

The output of TDPREL is optimum member size and weight. The optimum member size is obtained through an iterative static and dynamic analysis in which maximum static stresses and minimum design frequency are tested in each member.

The model of the selected truss configuration used for the structural analysis is shown in Figure 5-23. A list of truss member sizes and weights for both the upper and lower structures and corresponding to three different materials included in the study, aluminum, graphite epoxy, and boron epoxy, are given in Tables 5-6, 5-7, and 5-8, respectively. As previously noted, these members were sized to meet specified minimum frequency and static load design requirements. These members will change slightly following more detailed buckling analyses and dynamic response analysis as discussed in the following section.

It is apparent from a comparison of the data in Tables 5-6, 5-7 and 5-8 that a significant weight savings can be realized through the use of high modulous composite materials. The final selection of a proposed material, however, must await the results of additional analyses such as the analyses to predict the thermal distortion of the truss and the response of the antenna assemblies to dynamic excitations.

Based on the preliminary truss analysis an optimum structural configuration is obtained. The optimum size of truss members are converted to standard tube sizes and further, more detailed dynamic and stress analysis of the truss structure are performed. A flow diagram of the method and computer programs utilized for the detailed analysis is shown in the lower portion of Figure 5-22. Details of the dynamic and stress analysis are discussed in the following sections.

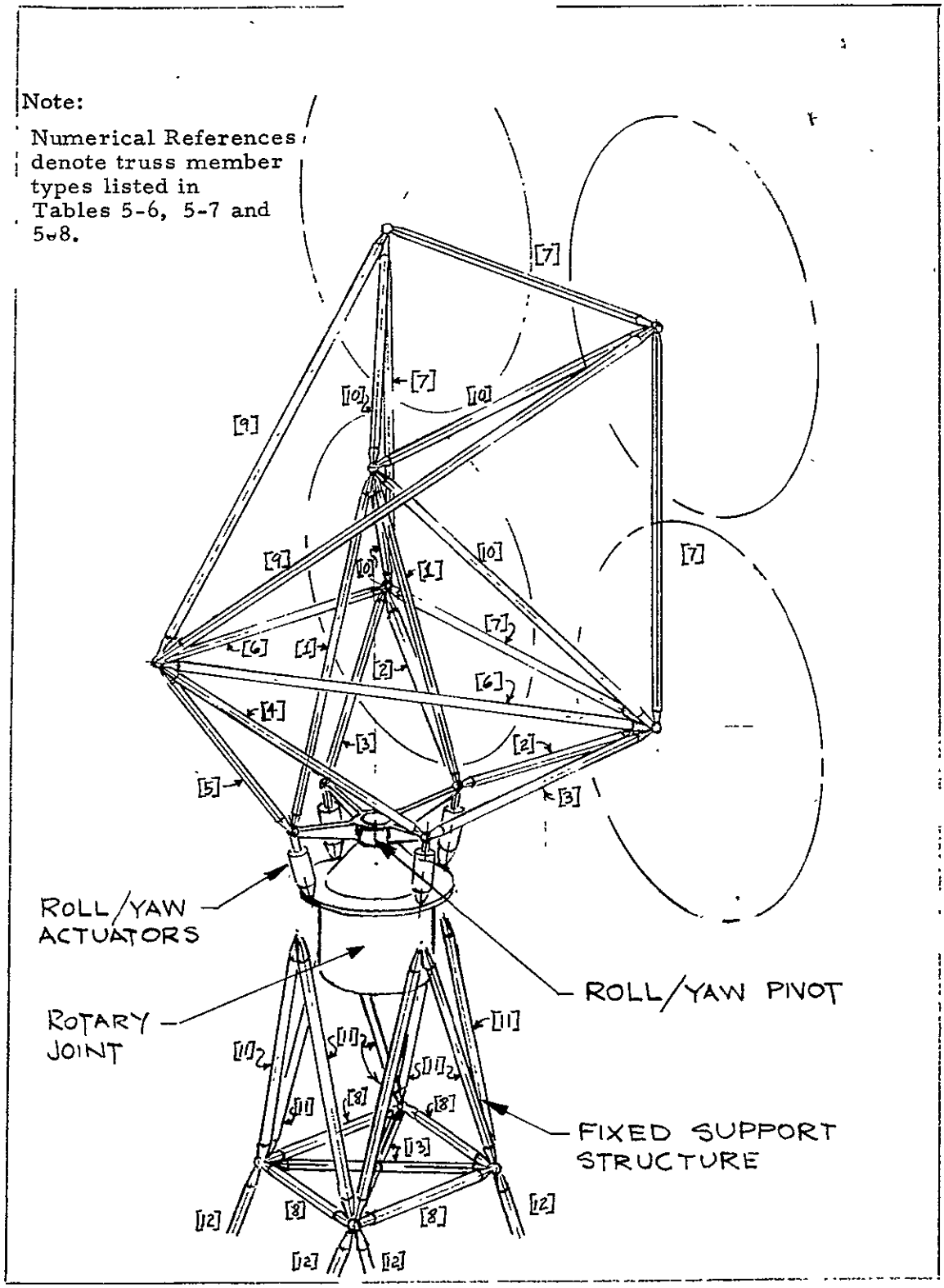

Figure 5-23 Proposed Structural Design

TABLE 5-6

TRUSS MEMBER SIZES AND WEIGHTS, MATERIAL - ALUMINUM

Member Type	Diameter (In.)	Wall Thickness (In.)	Area ($In.^2$)	Intertia ($In.^4$)	Weight (Lbs.)
1	1 1/4	.058	.2172	.03867	.533
2	1 3/8	.095	.3820	.07867	.749
3	1 1/4	.156	.5362	.08184	1.009
4	1 5/8	.120	.5674	.16170	1.474
5	1	.028	.0855	.01011	.188
6	1 1/4	.095	.3447	.05787	1.272
7	1	.028	.0855	.01011	.274
8	1 3/8	.035	.1473	.03309	.240
9	1 1/2	.028	.1295	.03508	.551
10	1 5/8	.035	.1748	.05528	.456
11	2	.095	.5685	.2586	1.319
12	1 1/2	.058	.2628	.06841	.657
13	1	.028	.0855	.01011	.197

Weight of Upper Truss	14.284 Lbs.
Weight of Lower Truss	17.162 Lbs.
Total Truss Weight	31.446 Lbs.

Joint Weight Not Included

TABLE 5-7

TRUSS MEMBER SIZES AND WEIGHTS
MATERIAL-GRAPHITE/EPOXY (HY-E 1101)

Member Type	Diameter (In.)	Wall Thickness (In.)	Area ($In.^2$)	Inertia ($In.^4$)	Weight (Lbs.)
1	1	.035	.1061	.01237	.146
2	1 1/2	.035	.1611	.04324	.177
3	1 1/2	.049	.2234	.05885	.235
4	1 1/2	.049	.2234	.05885	.325
5	3/4	.028	.06351	.004145	.078
6	1	.049	.1464	.01659	.303
7	1	.049	.1464	.01659	.262
8	3/4	.028	.06351	.004145	.058
9	3/4	.028	.06351	.004145	.151
10	3/4	.035	.07862	.005036	.115
11	1 1/2	.049	.2234	.05885	.290
12	1	.035	.1061	.01237	.149
13	3/4	.028	.06351	.004145	.082

Weight of Upper Truss	4.260 Lbs.
Weight of Lower Truss	3.908 Lbs
Total Truss Weight	8.168 Lbs.

Joint Weights Not Included

TABLE 5-8

TRUSS MEMBER SIZES AND WEIGHTS

MATERIAL - BORON EPOXY

Member Type	Diameter (in)	Wall Thickness (in)	Area (in^2)	Inertia (in^4)	Weight (lbs)
1	3/4	.028	.06351	.004145	.112
2	7/8	.035	.09236	.008161	.130
3	7/8	.049	.1272	.01088	.172
4	3/4	.065	.1399	.008278	.262
5	3/4	.025	.06351	.004445	.104
6	7/8	.035	.09236	.008161	.245
7	3/4	.028	.06351	.004145	.146
8	3/4	.028	.06351	.004145	.074
9	3/4	.028	.06351	.004145	.195
10	3/4	.028	.06351	.004145	.119
11	3/4	.065	.1399	.008378	.234
12	3/4	.028	.06351	.004145	.114
13	3/4	.028	.06351	.004145	.105

Weight of Upper Truss . . . . . 3.393 lbs.

Weight of Lower Truss . . . . . 3.290 lbs.

Total Truss Weight (excluding Joint Weights) . . . . . 6.683 lbs.

5.3.5.2 Truss Dynamic Analysis

In this section modeshapes, frequencies, and modal participation factors for the structure are predicted. Using the modeshapes, frequencies, and modal participation factors responses in g's are calculated for each mass during the first three modes of vibration. The responses are converted to static loads and applied to a stiffness model of the support structure. The internal loads distribution is thus obtained for use in the stress analysis.

Flexibility Matrix - The stiffness model is shown in Figure 5-21. The truss elements are given inertia and torsional properties to include secondary stiffness effects in the flexibility matrix. These properties are given in Table 5-7. A 3-D frame analysis program "frame" is used to form a stiffness matrix for the structure.

The flexibility matrix is formed by applying unit actions, corresponding to the degrees of freedom of the inertia model, to the stiffness model. The deflections due to these unit loads are calculated. The flexibility matrix is then determined by:

$$F = A^{*T} D^{*}$$

where A^* = The matrix of applied unit actions.
F = The flexibility matrix.
D^* = The matrix of corresponding displacements.

The flexibility matrix relates displacements to actions in the following matrix equation.

$$D_i = F A \qquad (5\text{-}1)$$

Inertia Matrix - The inertia model is represented by six nodes: one for each of the four reflectors, the interferometer receiver, and the RF rotary joint. The mass of each node is calculated from the lumped weights given in Table 5-5.

Assuming thin disks for the four reflectors, the inertia of each reflector node id calculated by the following equations:

$$I_{nx} = \frac{Mnr^2}{2}$$

$$I_{ny} = I_{nz}^{\ 2} = \frac{Mnr^2}{4}$$

The inertia of the rotary joint is calculated assuming a cylinder with uniform mass distribution.

$$I_x = I_y = \frac{M\ (3r^2 + l^2)}{12}$$

$$I_z = \frac{Mr^2}{2}$$

where
- I = inertia
- M = mass
- r = radius
- l = length
- n = node identification
- x, y, z = coordinate axis

The mass matrix relates actions to accelerations in the following matrix expression.

$$A = -M\ D$$

where
- M = The inertia matrix.
- D = The matrix of accelerations.

Noting that for harmonic motion

$$D_i = -\ W_i^{\ 2}\ D_i$$

where W = The natural circular frequency

Therefore,

$$A = W_i^{\ 2}\ M\ D_i \qquad (5\text{-}2)$$

The inertia matrix $\underset{\sim}{M}$ is a diagonal matrix which consists of the submatrices for the reflectors, receiver and rotary joint of the following form:

$$\underset{\sim}{Mn} = \begin{matrix} Mn & O & O & O & O & O \\ O & Mn & O & O & O & O \\ O & O & Mn & O & O & O \\ O & O & O & Inx & O & O \\ O & O & O & O & Iny & O \\ O & O & O & O & O & Inz \end{matrix}$$

Modeshapes, frequencies, and modal participation factors combining equations (1) and (2) we obtain the following matrix equation.

$$\underset{\sim}{F}\ \underset{\sim}{M}\ \underset{\sim}{Di} = \frac{1}{W_i^2}\ \underset{\sim}{D}_i$$

then,

$$\underset{\sim}{F}\ \underset{\sim}{U}^T\ \underset{\sim}{U}\ \underset{\sim}{Di} = \frac{1}{W_i^2}\ \underset{\sim}{U}\ \underset{\sim}{Di}$$

let $\quad \underset{\sim}{F}_T = \underset{\sim}{U}\ \underset{\sim}{F}\ \underset{\sim}{U}^T \quad$ and $\quad \underset{\sim}{D}_{Ti} = \underset{\sim}{U}\ \underset{\sim}{Di}$

then,

$$\underset{\sim}{F}_T\ \underset{\sim}{D}_{Ti} = \frac{1}{W_i^2} \cdot \underset{\sim}{D}_{Ti}$$

The matrix $\underset{\sim}{F}_T$ is the dynamic matrix and is symmetrical. An Eigenvalue computer routine is used to solve the above equation for the Eigenvalues $(\frac{1}{W_i^2})$ and Eigenvectors $(\underset{\sim}{D}_{Ti})$. Each of the Eigenvectors is normalized for unit vector length and stored column-wise in Matrix $\underset{\sim}{V}$.

$$\underset{\sim}{D}_i = \underset{\sim}{U}^{-1}\ \underset{\sim}{D}_{Ti}$$

which gives

$$\underset{\sim}{V}_N = \underset{\sim}{U}^{-1}\ \underset{\sim}{D}_{Ti}$$

where $\underset{\sim}{V}_N$ is a matrix of modeshapes which are normalized for unit generalized mass. That is,

$$\underset{\sim}{Y}_N^T \underset{\sim}{M} \underset{\sim}{Y}_N = I$$

which can be shown to be true if $\underset{\sim}{D}i$ is normalized for unit vector length.

The modeshapes $\underset{\sim}{V}_N$ are then normalized so the largest term in each column (mode) is unity. The frequencies are obtained from the Eigenvalues.

$$f = \frac{1}{2\pi} \quad \frac{1}{\frac{1}{W_i^2}}$$

The first 6 modes occur at natural frequency of 17.1, 21.2, 28.9, 31.6, 33.7 and 37.0 Hertz.

The modal participation factors are calculated from the following expression.

$$\underset{\sim}{P} = \underset{\sim}{V}_N^T \underset{\sim}{M} \underset{\sim}{H}$$

where: $\underset{\sim}{H}$ = A matrix of dimensionless distribution functions which correlate a given direction of base acceleration with the resulting inertia forces.

Table 5-9 contains the modal participation factors for the first ten modes of this problem.

Response to 1g RMS sine input the equation of motion of the j normal mode of a structure due to a base excitation assuming damping exists is:

$$\ddot{D}^*_{Nj} + 2\,(DC)_j\, S_{Nj}^{1/2}\, \dot{D}^*_{Nj} + S_{Nj}\, D^*_{Nj} = Pj\, f\,(t)$$

where: $\ddot{D}^*_{Nj}$ = Acceleration relative to the base in normal coordinates.

(DC)j = Decimal fraction of critical damping.

$S_{Nj} = W_j^2$

TABLE 5-9

MODAL PARTICIPATION FACTORS

Mode	X - Base Motion	Y - Base Motion	Z - Base Motion	θx - Base Motion	θy - Base Motion	θz - Base Motion
1	0	.45004	0	-.68339	0	.33375
2	.47732	0	-.12455	0	.61574	0
3	.087621	0	.028355	0	-.44940	0
4	0	.057308	0	-.89853	0	-.41670
5	0	-.11365	0	.83749	0	1.2003
6	.15173	0	.074847	0	-.86382	0
7	0	-.12375	0	-1.7534	0	-.44362
8	0	.20496	0	1.5875	0	-.38043
9	.15185	0	.091980	0	-.96046	0
10	-.10658	0	-.066255	0	.71290	0

$\dot{D}^*_{Nj}$ = Velocity relative to the base in normal coordinates.

D^*_{Nj} = Displacement relative to the base in normal coordinates.

Pj = Modal Participation factor for j^{th} mode.

$f(t)$ = Forcing Function.

Let $f(5) = F_o e^{iWt} = \ddot{D}_B$

The solution of the equation is as follows:

$$D^*_{Nj} = \frac{Fo\ Pj}{S_{Nj}} Hj\ (W)\ e^{iWt}$$

$$Hj(W) = \frac{1}{1 - \left(\frac{W}{Wj}\right)^2 + i\ 2\ (DC)j \left(\frac{W}{Wj}\right)}$$

$$\left| Hj\ (W) \right| = \frac{1}{\sqrt{\left[1 - \left(\frac{W}{Wj}\right)^2\right]^2 + \left[2(DC)j\ \left(\frac{W}{Wj}\right)\right]^2}} \qquad \text{(Magnification Factor)}$$

$$\ddot{D}^*_{Nj} = S_{Nj}\ D^*_{Nj} = Fo\ Pj\ Hj\ (W)\ e^{iWt}$$

$$\ddot{\underset{\sim}{D}}^* = \underset{\sim}{V}_N\ \ddot{\underset{\sim}{D}}_{Nj}$$

Let i be a particular degree of freedom in the inertia model.

$$\ddot{D}_i = \sum_{j=1}^{n} V_{Nij}\ D^*_{Nj}$$

$$D_i = Fo \sum_{j=1}^{n} V_{Nij}\ Pj\ Hj\ (W)\ e^{iWt}$$

The calculations of the response of several degrees of freedom for the first three modes were made and are presented in Table 5-10. In these calculations $e^{iWt} = 1$ which assumes the contributions of each degree of freedom to the total response are in phase with each other. This assumption results in conservatively high numbers.

TABLE 5-10

NODE RESPONSE TO 1g RMS SINE INPUT

Node	Direction	Response, g's Mode 1	2	3
Top Antennas	X	5.1	18.0	2.9
	Y	19.5		0.3
	Z	0.9	2.5	1.2
Receiver	X		11.5	2.1
	Y	9.4		
	Z			
Despin Drive	X		2.5	
	Y	1.5		
	Z			
Lower Antennas	X	1.6	5.5	
	Y	5.7		
	Z	0.4	1.7	

5.3.6 Truss Stress Analysis

Based on the preliminary truss analysis the graphite epoxy tubes were selected for further stress analysis.

Utilizing the weight distribution the flight load factors and the response load factors calculated in previous paragraph, static loads were calculated using the following expression:

$$P = \text{Weight} \times \text{Load Factor}$$

The flight loads were applied to the stiffness model in the directions described in paragraph 5.3.5.1. The loads from vibration response were applied according to the modeshapes which are sketched in paragraph 5.3.4.1. The internal loads distribution was obtained for each load case using a 3-dimensional frame analysis program FRAME.

The worst loads on each set of members was determined from the static loads computer output. The stresses resulting from these loads were calculated using factors of safety as described in paragraph 5.3.4.1. Bucking of the tubes was based on Euler theory. Since no experimental data is available to compare with the assumed buckling theory, an additional 50% margin of safety is maintained.

The properties of graphite/epoxy, HY-E 1101, are as follows.

Tensile Strength	130,000 psi
Young's Modulus	24×10^6 psi
Compression Strength	80,000 psi
Shear Strength	7,000 psi

Based on the tube sizes listed in Table 5-6, on the material properties for graphite/epoxy and the static loads, the stresses in each truss member were calculated and compared to their allowable stress. The ratio of allowable to calculated stresses determined the margin of safety.

TABLE 5-11

TRUSS MEMBER CHANGES BASED ON STRESS ANALYSIS

Member Type (1)	Member (2)	Previous Tube Size		Present Tube Size	
		O.D. Inch	Wall Inch	O.D. Inch	Wall Inch
6	5-7	1	0.049	1 1/2	0.035
6	5-8	1	0.049	1 1/2	0.35
9	5-9	3/4	0.028	1	0.028
9	5-10	3/4	0.028	1	0.028
10	6-7	3/4	0.035	1	0.028
10	6-8	3/4	0.035	1	0.028
10	6-9	3/4	0.035	1	0.028
10	6-10	3/4	0.035	1	0.028

(1) Refer to Table 5-7 and Figure 5-23.

(2) Refer to Figures 5-21 and 5-23, numerical references is to joint coordinates at end of each member.

Based on these stress analyses it was determined that tube sizes for a total of 10 truss members have to be increased over the sizes calculated from the preliminary truss analysis (TDPREL). The ten truss members are composed of three tube sizes and the recommended increase in sizes are listed in Table 5-11.

5.3.6.1 Alternate Lower Support Structure.

In this section is presented the results of a structural analysis for an alternate lower support structure. The structure consists of a shell with the geometry of a frustrum of a cone. The base diameters of the cone frustrum are 36 and 10 inches and the height is 43 inches. The cone is assumed to be honeycomb fabrication with aluminum skins and core. The core is assumed to be 1/2 inch thick with a 3/16 inch cell size. The minimum facesheets thickness is to be determined from the results of the analysis.

The structural design study for the alternate lower support structure includes a dynamic and stress analysis and are presented in the following two sections, respectively.

Dynamic Analysis - The dynamic analysis assumed a rigid upper support structure with mass distributions similar to the truss design analysis. Influence terms in lateral bending for the cone are obtained by equating the work done to the strain energy and the influence term for torsion is found using the method of virtual work. Shear and bending stresses are carried by the facesheets of the honeycomb, the core being used for stability of the facesheets. Therefore, the properties of aluminum are used in calculating the influence coefficients.

For the vibration analysis the lowest lateral mode is assumed to occur in the Y-Z plane. Vibration in this plane couples translation of the mass in the Y-direction, rotation of the mass about the x-axis, and rotation of the mass about the Z-axis. The flexibility matrix is calculated using the influence coefficients calculated for the aluminum honeycomb cone.

After combining the equations relating actions to displacements by 1) the inertia matrix, and 2) the flexibility matrix, iteration results in an equation relating face-sheet thickness to the lateral frequency of vibration. This express is stated as follows:

$$t_f = 2\pi^2 f^2 (0.81 \times 10^{-6})$$

The facesheet thickness, f, is plotted on Figure 5-24as a function of the lateral frequency. Based on the dynamic analysis and for an assumed lower natural frequency of 14 cps, the minimum facesheet thickness is 0.003 inches.

Strength Analysis - The stresses in the conical shell are calculated using the method developed by Flugge and reported in "Handbook of Engineering Mechanics". The loads are developed on the shell from the 6.8g axial load factor and a 1.8 g lateral load factor. The combined loads and the equivalent point load and moments are shown in Figure 5-25. Based on the equivalent point loads and moment, the membrane forces and in turn the membrane stresses are calculated as a function of the total skin thickness and presented as follows:

$$J_c = -135.3/t \text{ psi}$$

$$= 10.82/t \text{ psi}$$

where:

J_c = membrane stress in compression
= membrane stress in shear
$y = 2t_f = 2$ (Thickness of one facesheet)

In addition to the flight loads there are loads resulting from the response of the antenna, receiver and RF rotary joint masses to a 1g sinusoidal base input. The responses calculated for the pure truss structure are used in order to calculated combined and equivalent point loads and moments for the shell structure. The equivalent point loads and moment of the shell for the 1g sinusoidal base input are shown in Figure 5-26.

The membrane stresses for the 1g sinusoidal base input are calculated as a function of the total skin thickness and presented as follows:

$$J_c = 394.7/t \text{ psi}$$

$$= 59.4/t \text{ psi}$$

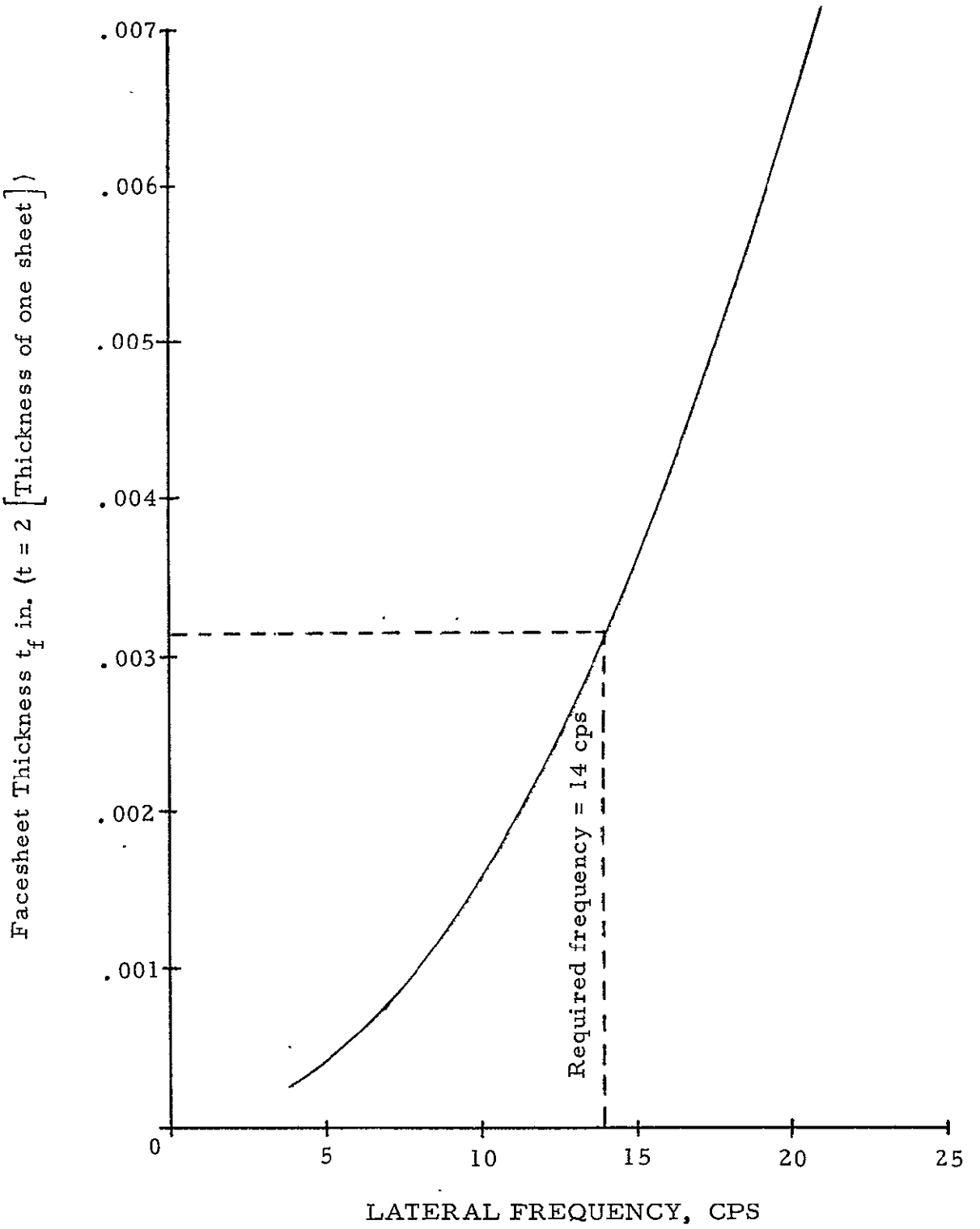

FIGURE 5-24

Facesheet Thickness as a Function of Lateral Frequency

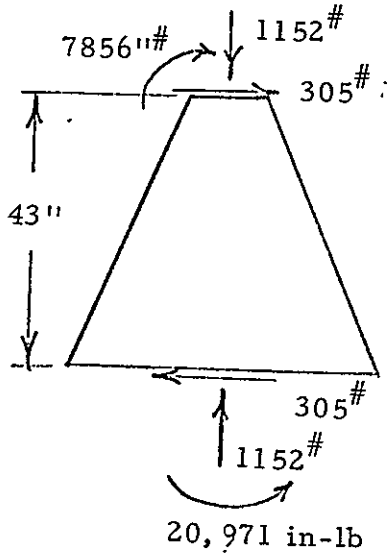

Combined Loads

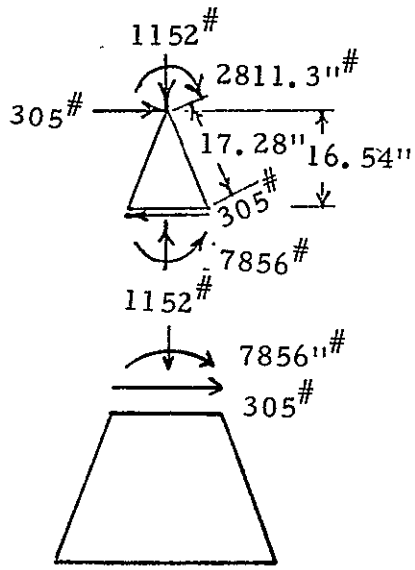

Equivalent Point Load and Moment

FIGURE 5-25 COMBINED LOADS AND EQUIVALENT POINT LOAD FOR FLIGHT LOAD FACTORS

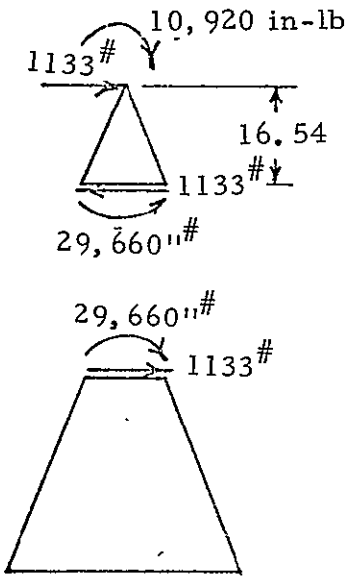

FIGURE 5-26. EQUIVALENT POINT LOADS AND MOMENT FOR 1g SINUSOIDAL BASE INPUT

The total shear stress is the sum of the stresses resulting from the moment and torques applied to the top of the shell resulting from response to the sinusoidal base input.

$$\text{Total} = \frac{59.4}{t} + \frac{42.0}{t} = 101.4/t$$

The total shear is sufficiently low enough that its effects are neglected from further considerations.

A more detailed investigation is required to determine the effects of the compressive stress on intracell buckling of the honeycomb core of the proposed conical shell structure. Intracell buckling, which is a local instability of the skins, is analyzed by applying the method developed by Buchn and reported in "Analysis and Design of Flight Vehicle Structures". The computations are made for the compressive stresses only because the shear stresses are relatively lower. Because the analysis relies heavily on graphs in the referenced literature, only the method of analysis is outlined and the results presented in Figure 5-27.

The method of analysis is outlined as follows:

1) Calculate S/t_f
2) Obtain $Fci/_n$ from Figure C12.5.2a on page C12.8
3) Obtain Fci from Figure C12.5.2b on page C12.8

where

$t_f = t/2$ = facesheet thickness

S = cell size

F_{ci} = compressive stress in skin.

For the assumed core and facesheets (2024-T4 Aluminum)

S = 3/16"

F_{cy} = 42,000 psi

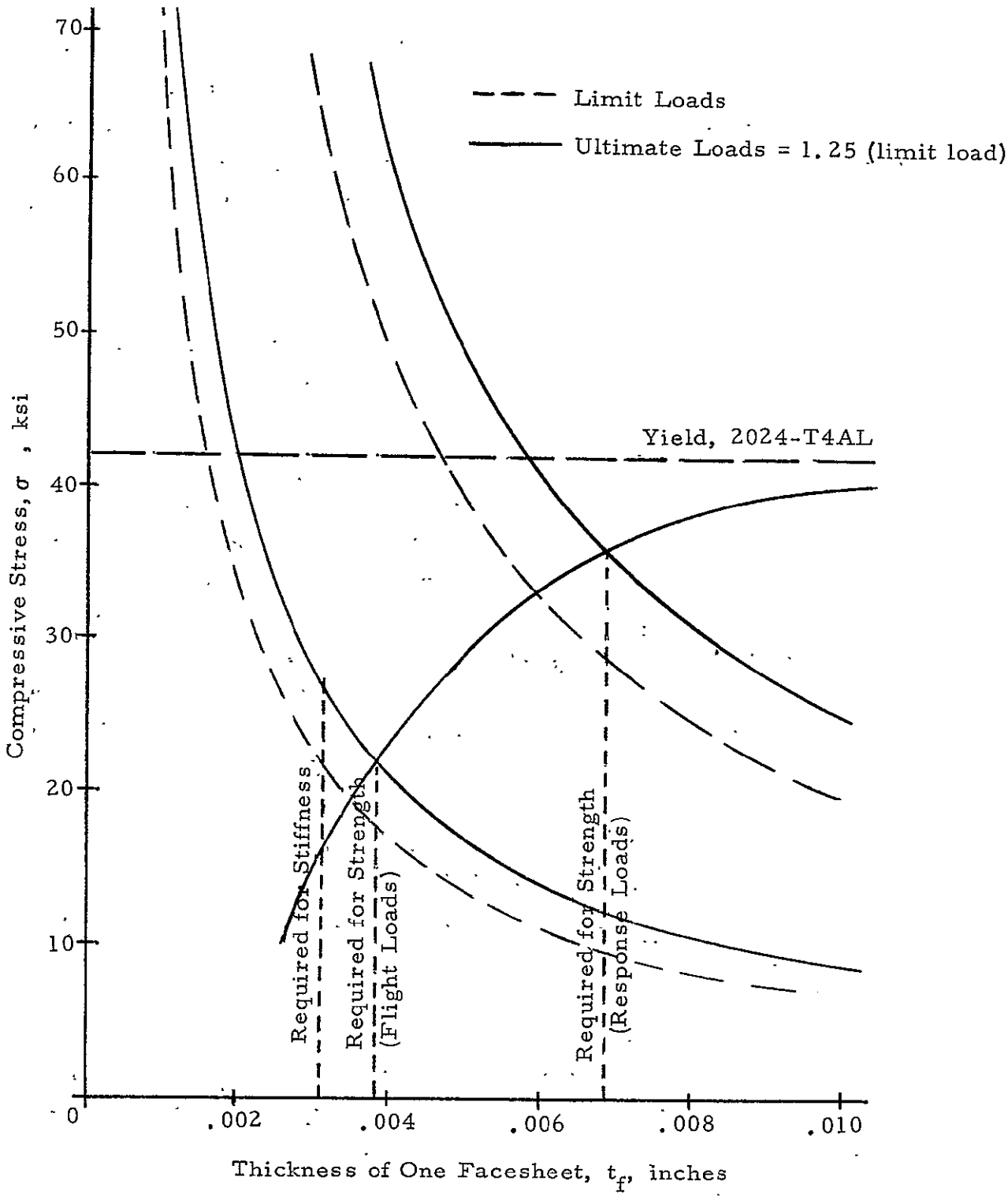

FIGURE 5-27

COMPRESSIVE STRESSES FOR THE CONICAL SHELL

The results of the strength analysis for the alternate lower support structure, a conical honeycomb shell, are summarized in Figure 5-27. The compressive stress in the shell is presented as a function of the facesheet thickness for the flight loads, response loads, and for the intracell buckling criteria assuming an aluminum facesheet material with a compressive yield strength of 42,000 psi, it is shown in Figure 5-27 that the minimum facesheet thickness of 0.007 inches is determined based on the intracell bucling criteria rather than the yield strength of the material.

Weight Analysis - The weight of the conical shell of aluminum honeycomb construction is presented in Figure 5-28 as a function of facesheet thickness. The weight analysis is based on an aluminum core 1/2 inches thick and with a density of 3.0 lb/ft^3.

It was determined from the dynamic analysis that the facesheet thickness must be greater than 0.002 inches to provide a minimum frequency response of 14cps. From the stress analysis to prevent intercell buckling the minimum facesheet thickness was determined to be 0.007 inches. Therefore, a conical shell structure for the lower support of the RF system would weigh approximately 7.0 pounds for a facesheet thickness of 0.007 inches as determined from the results presented in Figure 5-28. This weight for the conical structure does not include structural attachment rings between the base of the cone and the spacecraft.

For a graphite/epoxy lower support truss structure the weight was determined to be 3.9 lbs. as reported in Table 5-7. Thus, assuming that both structures are of equal strength or stiffness, the truss structure fabricated from graphite/epoxy tubes would be a more efficient structure from a weight standpoint.

5.3.7 Truss Thermal Distortion Analysis

The purpose of the truss distortion study is to determine the pointing errors between the interferometer horns (4) and the antenna reflectors. The objective is to maintain the error to less than 0.05 degrees as budgeted in the interferometer error analysis.

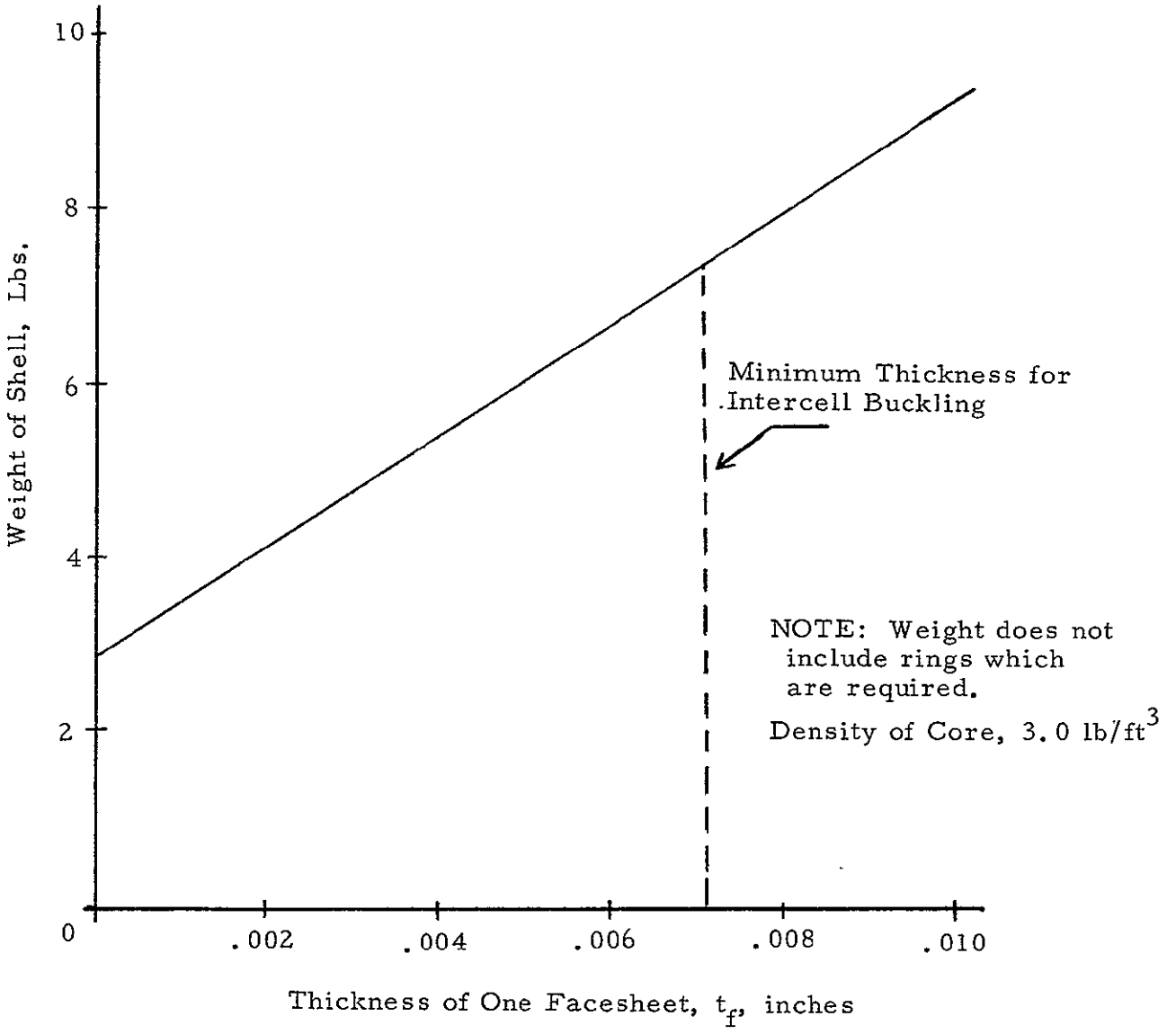

FIGURE 5-28

WEIGHT OF CONICAL HONEYCOMB SHELL
AS A FUNCTION OF FACESHEET THICKNESS

The distortion of the truss structure results from partial shadowing of the structure during a critical sun orientation. Temperature distributions as determined in thermal analysis section of this report were used as input data for the distortion analysis.

Results are obtained for a parameteric study which includes material of truss tubes, graphite/epoxy and aluminum; thermal surface coating, white paint, aluminum paint and polished aluminum; and attachment of interferometer, cantilevered support, fixed rigid member., and fixed non-rigid member. The minimum pointing errors occur for the fixed non-rigid member support of the interferometer horns to the truss support. For the non-rigid fixed support the maximum pointing error calculated using the graphite/expoxy material for the truss tubes is 0.018 degrees, and is independent of type of surface finish. However, the pointing accuracy of the aluminum structure does depend on the type of thermal finish. The only acceptable finish is polished aluminum, which results in a maximum pointing error of 0.041 degrees.

5.3.7.1 Computer Model

A modification of the truss computer model shown in Figure 5-21 is used for the truss distortion analysis. The model is an assemblage of either graphite/epoxy or aluminum frame members. The assumed Young's modulus and thermal coefficient of expansion for graphite epoxy are 24×10^6 psi and 1×10^{-6} inches/inch/$^{\circ}$F, respectively, and for aluminum 10×10^6 psi and 13×10^{-6} inches/inch/$^{\circ}$F respectively.

The reflectors are rigidly attached to the structure at joint 7, 8, 9 and 10 and the intereferometer horns are located at joints 19, 20, 21 and 22. The interferometer receiver is considered located at joint 6 and rigidly attached to the truss structure. Three types of support of the interferometer horns were considered.

1) The interferometer horns cantilevered from the receiver and not connected to the truss supports at joints 19, 20, 21 and 22.

2) The interferometer horns fixed at joints 19, 20, 21 and 22 to the truss structure and connected to the receiver (joint 6) by rigid members.

3) The interfereomter horns fixed at joints 19, 20, 21 and 22 to the truss structure but connected to the interferometer receiver (joint 6) by non-rigid members.

For the latter case the support members (functional coaxial cable) extending from the interferometer horns to the receiver are assumed very flexible and were not included in the model.

A box beam is used to support each interferometer horn from the receiver. The box beams may be cantilevered from the receiver or cantilevered and supported by the main structure at the end which supports the horn; the method of support depended on the case to be analyzed. The size of the box beam is determined assuming a cantilevered condition. It is sized for stiffness criteria assuming a frequency of 50 cps.

5.3.7.2 Distortion Analysis

From the temperature distribution analysis for a critical sun orientation, temperatures of each member of the stiffness model were obtained as a function of member material and surface finish (refer to Thermal Analysis Section). An existing frame analysis computer program (SAMIS) is used to derive the stiffness matrix for the support structure, calculate fixed and actions for each member using the member temperatures and coefficient of thermal expansion, superimposes all actions, and calculates corresponding deflections, rotations, and internal loads. The structure is assumed undistorted at 70°F.

Representative results of the parameteric analysis are presented in Figure 5-29. The results presented in this figure depict the linear displacement in the Y-Z plane. of joints 7, 8, 9 and 10 for the reflectors and joints 19, 20, 21 and 22 for the interferometer horns. It should be noted that the depicted diflections are an order of magnitude greater for the aluminum tubes than for the graphite/epoxy material. Also the minimum displacement of the interferometer relative to the reflectors occurs for the graphite/epoxy material and for fixed non-rigid support members between the interferometer horns and the receiver.

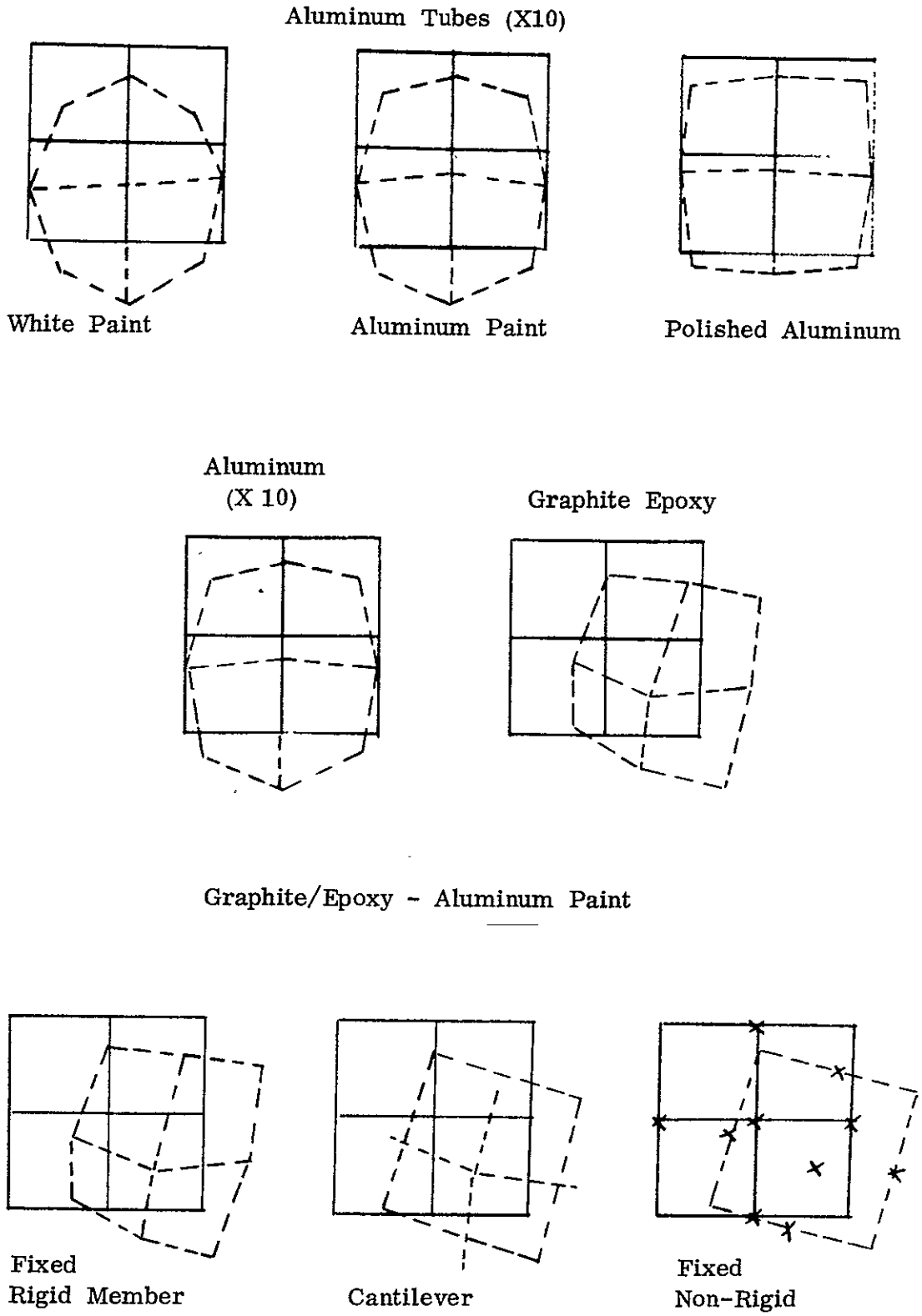

FIGURE 5-29

REFLECTOR AND INTERFEROMETER DEFLECTION STUDIES

The angular rotation of the reflector support joints relative to the interferometer are summarized in Tables 5-12 for the case of fixed support and non-rigid members

The angle α is the pointing error in the X-Z plane and the angle β is the pointing error in the X-Y plane.

The maximum pointing errors for a graphite epoxy structure are between 0.016 and 0.018 degrees (160 to 180 x 10^{-4} degrees, as presented in Table 5-12) for the three surface finishes considered and well below the allowable budgeted error of 0.050 degrees. However, if an aluminum structure is used, the finish must be polished aluminum which gives a maximum pointing error of 0.041 degrees. White and aluminum paint are not satisfactory and result in pointing errors of 0.099 to 0.066 degrees, respectively.

The parameteric distortion analysis for the truss structure has been made for two materials, three surface finishes, and three attachment and support methods. The distortion analyses assuming 1) the interferometer horns cantilevered from the receiver, 2) the interferometer horns fixed to the truss structure and supported from the receiver with rigid members, and 3) the truss members fabricated from aluminum tubes produce pointing errors that exceed the allowable tolerance. It is recommended that the truss members be fabricated from graphite/epoxy material and that the interferometer horns be rigidly fixed to the truss and connected to the receiver with flexible coaxial cable which will provide minimal stiffness.

5.3.8 Reflector Thermal Distortion Analysis

The distortion of the four antenna reflectors is a consequence of partial solar illumination of reflector surfaces. The temperature distribution as a function of solar illumination is determined in the thermal analysis section of this report.

Temperature distributions for two sun angles are investigated with regards to the distortion of the reflector. The maximum temperature difference across the diameter of the antenna reflector is experienced at a sun angle of $\theta = 0^{\circ}$ (sun's rays parallel to plane of the reflector aperature, Y-Z plane) and the maximum distortion also occurs for this case. The maximum thermal stress in the reflector facesheets is experienced when the temperature gradient is a maximum and this condition occurs at a sun angle of $\theta = -10^{\circ}$.

TABLE 5-12

POINTING ERRORS

Truss Member		Reflector	Error, Degrees	
Material	Surface Finish	Joint #	$\alpha \times 10^4$	β
Graphite/Epoxy	White Paint	7	23	46
		8	73	160
		9	12	18
		10	49	78
Graphite/Epoxy	Aluminum Paint	7	62	27
		8	65	180
		9	21	19
		10	33	70
Graphite/Epoxy	Polished Aluminum	7	11	10
		8	19	180
		9	54	43
		10	16	33
Aluminum	White Paint	7	36	12
		8	96	740
		9	980	620
		10	510	510
Aluminum	Aluminum Paint	7	400	210
		8	200	590
		9	660	200
		10	72	12
Aluminum	Polished Aluminum	7	41	350
		8	24	370
		9	36	53
		10	16	230

5.3.8.1 Reflector Distortion Model and Analysis

A finite element model of a reflector was developed in order to predict the reflector thermal distortion. The model is shown in Figure 5-30 and consists of 201 nodes, 348 facets and 4 beam elements. Similar to the thermal model only one half of a reflector is modeled to predict distortion due to symmetry. This model is used in conjunction with the computer routine entitled "Structural Analysis and Matrix Interpretive System" (SAMIS), to predict thermal distortion of the reflector.

The SAMIS computer routine is based on finite element principles. The program can accommodate both triangular shaped elements of constant thickness and frame/truss elements. A stiffness matrix is formulated for each element, based on energy principles, and summed to form a stiffness matrix for the entire model. A loading matrix is formed which is equivalent to the imposed temperature distribution. Appropriate boundary conditions are imposed, and nodal displacements are calculated using a Chaleski decomposition routine.

5.3.8.2 Reflector Distortion Analysis Results

The results of the reflector and feed horn distortion analysis are summarized in Figure 5-31. Distortions of the reflector are shown in the X-Y and in the X-Z plane. The maximum distortion occurs at the sun lit edge and corresponds to deflection of 0.002 inches. The distortion shown in Figure 5-31 can be compared to a small (0.009°) apparent rigid body rotation of the reflector.

The deflection of the feed horn was calculated for both aluminum and invar supports. For the aluminum support the maximum deflection is 0.018 inches and occurs in both the X and Y direction. For the invar support the deflections of the feed horn is an order of magnitude less and is negligible with respect to degradation of RF performance.

The distortion results presented in Figure 5-31 were for the sun condition that produced the maximum temperature difference across the diameter of the reflector. This case occurs when the solar rays are parallel to the reflector aperature ($\theta = 0$). The effect of other sun positions and shadowing of one reflector by another were also studies. The results of these analyses confirmed that the maximum distortion of the antenna occurs for the ease when the temperature difference is a maximum ($\theta = 0$). Also the maximum stresses, substantially lower than the yield stress or buckling stress of the reflector, occur for the maximum thermal gradient case ($\theta = -10^{\circ}$).

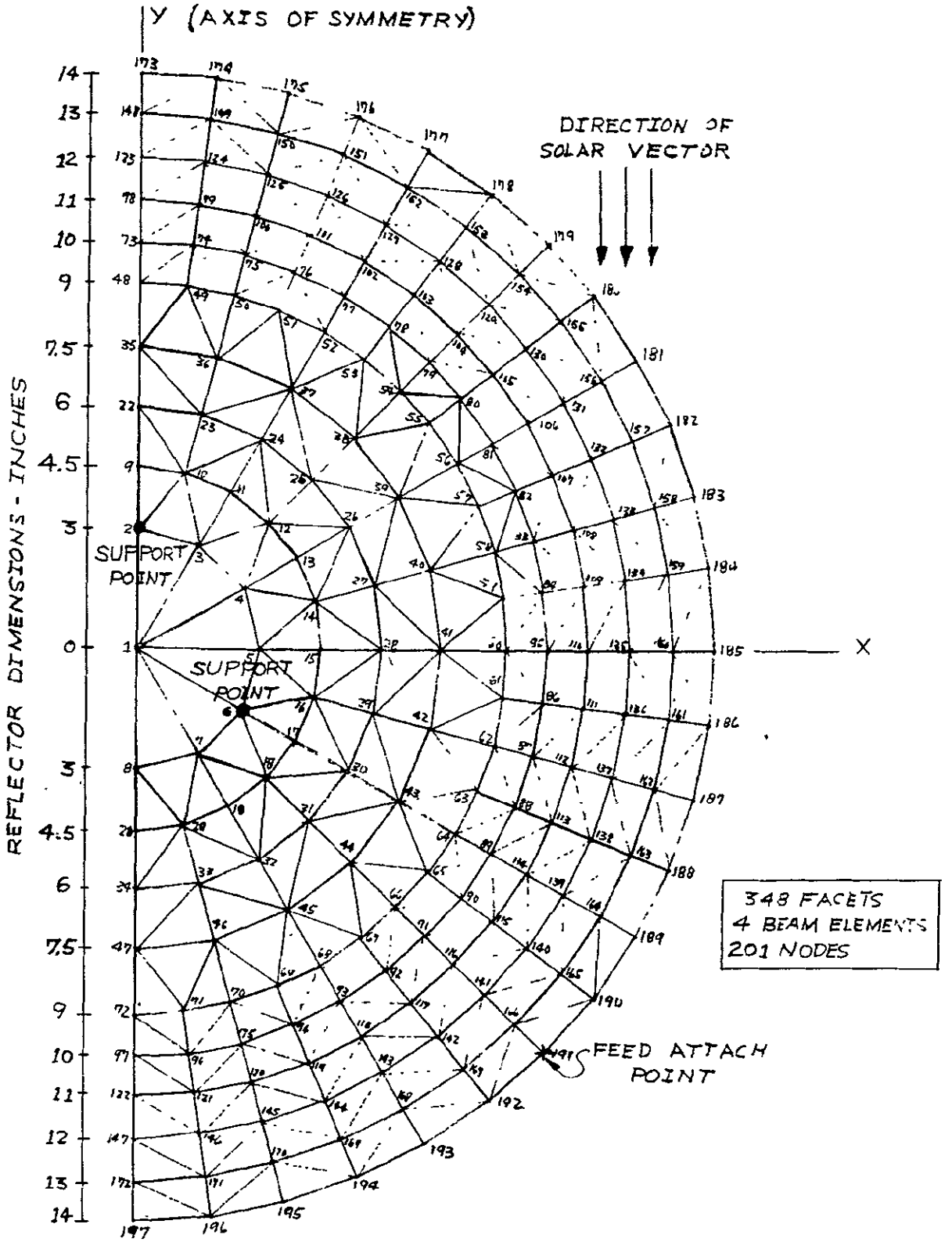

FIGURE 5-30

FINITE ELEMENTS MODEL
NASA LEWIS ANTENNA

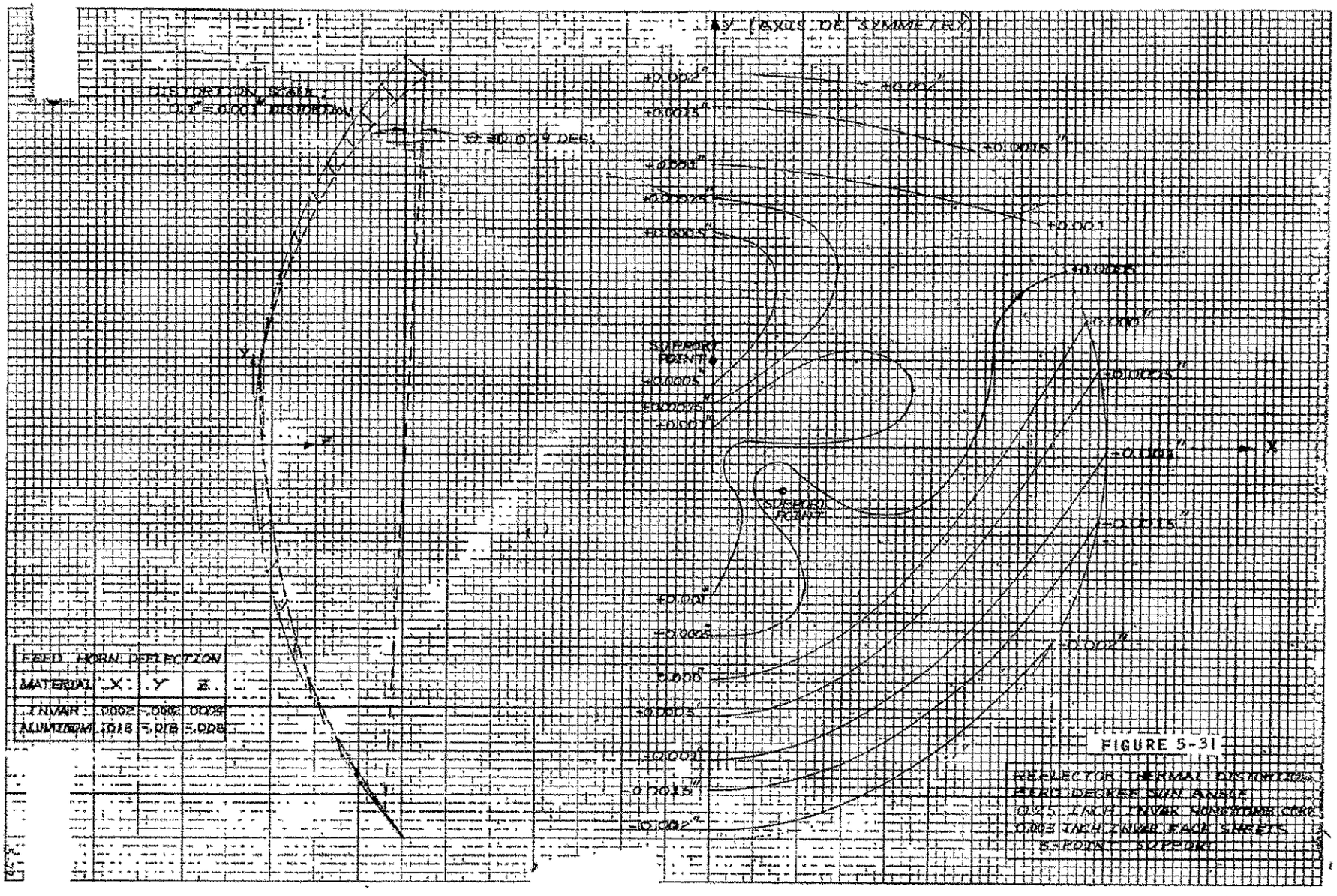

FEED HORN DEFLECTION			
MATERIAL	X	Y	Z
INVAR	.0002	-.0002	.0002
ALUMINUM	.0018	-.0018	-.0018

FIGURE 5-31

REFLECTOR THERMAL DISTORTION
ZERO DEGREE SUN ANGLE
0.25 INCH INVAR HONEYCOMB CORE
0.003 INCH INVAR FACE SHEETS
3-POINT SUPPORT

SECTION VI

ANTENNA CONTROL SUBSYSTEM

6.1 REQUIREMENTS

Two sets of requirements have been considered: a set of baseline requirements, and a set of alternate requirements. The baseline requirements are the following:

a) Point an antenna array at a particular spot on the earth's surface,

b) Rotate 360° per day to permit the spacecraft to track the sun,

c) Change from pointing at one spot on the earth's surface to another within 15 minutes,

d) Operate for a minimum of 5 years,

e) Maintain a pointing accuracy of ± 0.1 degree RSS in the presence of 1) satellite errors of ± 5.0 degrees, 2) satellites rates of 1.0 degree/minute, 3) a 0.5 degree inclination, 4) satellite station longitude errors of ± 0.5 degree, changing at 0.1 degree per day,

f) The accuracy shall be maintained while looking at any point on the surface of the earth within 20 degrees longitude of the satellite sub-point and between 45 degrees north latitude and 10 degrees south latitude.

The alternate requirements considered were the same as those given above, but with two changes made for one set of alternate requirements, and three changes made for the other set. The two changes common to both sets of alternate requirements are:

a) Assume spacecraft attitude is controlled to within $\pm 0.1^{\circ}$,

b) Maximum spacecraft rate is 0.2°/day

One further change in the baseline requirements was considered, which when combined with the two above made up the second set of alternate requirements. This additional change was the elimination of the 360°/day pitch rotation that allowed the spacecraft to track the sun. Thus, instead of pointing the whole spacecraft at the sun, only the solar panels are pointed at the sun while the rest of the spacecraft points at the center of the earth to within ± 0.1 degree.

In addition to the imposed requirements there are what can be called derived requirements. The derived requirements in this case include the total angular excursion required of the antenna control system and the maximum gimbal rate that is required. These are governed by the desired coverage on the earth, the time in which it is to be changed, spacecraft attitude, and spacecraft attitude rates. Table I summarizes these derived requirements.

Another derived requirement is the requirement for a yaw gimbal. At first it was not obvious that a yaw gimbal would be required, but several computer runs were made to determine the effect a 5° yaw error had on the geographic location of the antenna beam. The following cases were studied for antenna pattern "a" of Figure 6-1:

(1) 0°E, 0°N, 0° Yaw

(2) 0°E, 0°N, -5° Yaw

(3) 0°E, 45°N, 0° Yaw

(4) 0°E, 45°N, -5° Yaw

(5) 20°W, 45°N, $+5^{\circ}$ Yaw

(6) 20° W, 45°N, 0° Yaw

(7) 20°W, 45°N, -5° Yaw

TABLE 6-1 - DEVISED REQUIREMENTS

		Baseline Requirements	Alternate Requirements #1	Alternate Requirements #2
Total Angular	Roll	$+11.86^{\circ}$, -6.61°	$+6.96^{\circ}$, -1.71°	$+6.96^{\circ}$, -1.71°
Excursion Req'd	Yaw	$+5^{\circ}$, -5°	+0.0 , - 0.0	+0.0 , - 0.0
	Pitch	Continuous (360°)	Continuous (360°)	$+3.65^{\circ}$, -3.65°
Maximum Gimbal	Roll	±1.23 deg/min	±0.55 deg/min	±0.55 deg/min
Rate Required	Yaw	±1.0 deg/min	±0.0 deg/min	±0.0 deg/min
	Pitch	±1.13 deg/min	± .46 deg/min*	±0.46 deg/min

*Excluding nominal pitch rate.

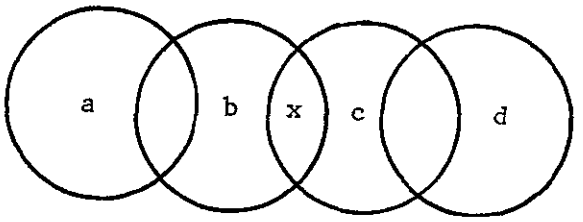

Figure 6-1 Sketch of Antenna Patterns

The patterns were "cut off" at their intersection with the 5° elevation cone. That is, Earth-pattern intersections where the vehicle's elevation would be less than 5° as seen from a ground station were excluded.

The plot (see Figure 6-2) shows the yaw effect qualitatively and indicates the necessity of having a yaw gimbal to remove as much of the effect as possible. For the alternate set of requirements, the effect is negligible and therefore the need for a yaw gimbal is eliminated.

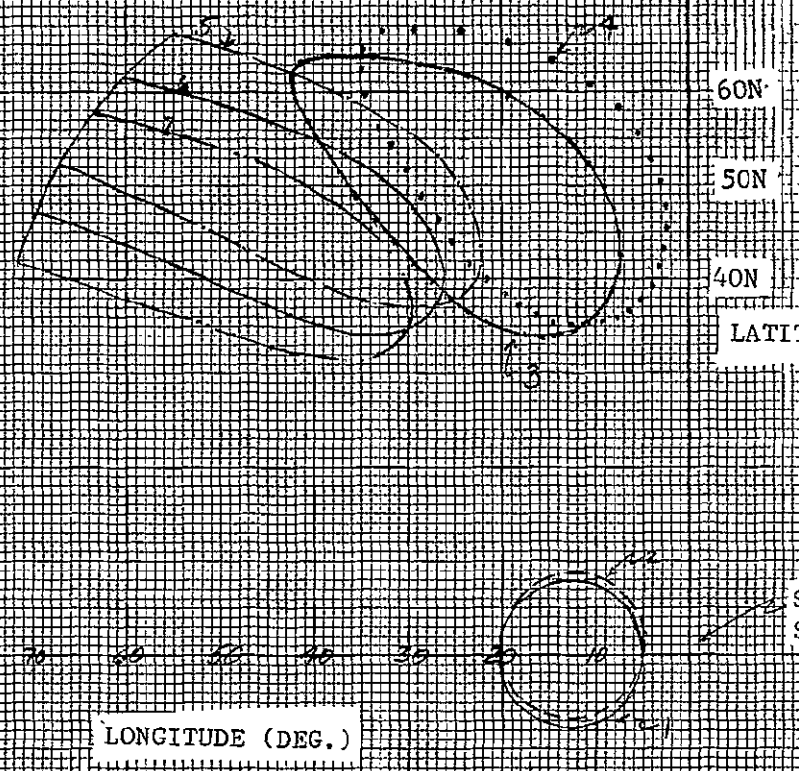

Figure 6-2 Antenna Coverage Effects of a Five Degree Yaw Error

6.2 CONTROL TECHNIQUES

In general, two methods of antenna control are possible for a spacecraft: (1) ground control via a command link, or (2) automatic on-board control. A given control system can use either of these or a combination of both, depending on mission and/or spacecraft requirements. Each technique has its own set of advantages and disadvantages, some of which are discussed below.

6.2.1 Ground Commanded Antenna Control

In the ground commanded antenna control system the interferometer data are fed to the ground terminal via telemetry. At the ground terminal a computer uses the interferometer data to calculate the orientation of the antenna array. The measured antenna orientation is then compared with the desired orientation and the changes required in each of the three gimbal angles is computed. These required gimbal angle changes required in each of the three gimbal angles is computed. These required gimbal angle changes are then sent via command link to the spacecraft where they are used to actuate the gimbal drives. The gimbal drives reorient the antenna, providing a new set of interferometer angles, which are sent to the ground as before. If additional control is required the computer recalculates the gimbal angle changes, and sends them to the spacecraft. This cycle continues all the time that control is required, and represents the biggest disadvantage of this technique.

For the primary requirements, where spacecraft rates are 1 degree/minute and attitude is only maintained to ± 5 degrees, the ground commanded control technique requires a telemetry and commmand link all of the time and the ground based computer is always required at least on a time-shared basis. Further, the lag due to transmission time ($\sim$0.2 second), and computation time on the ground increases the loop stability probelm. Offsetting these disadvantages are a simpler satellite and the ability to change the computation algorithm if desired. Figure 3 summarizes the advantages and disadvantages.

For the alternate requirements this control technique becomes more attractive because the much lower spacecraft rates and higher pinting accuracy allow the gimbal angles to go unchanged for periods as long as several hours, thus eliminating all of the disadvantages.

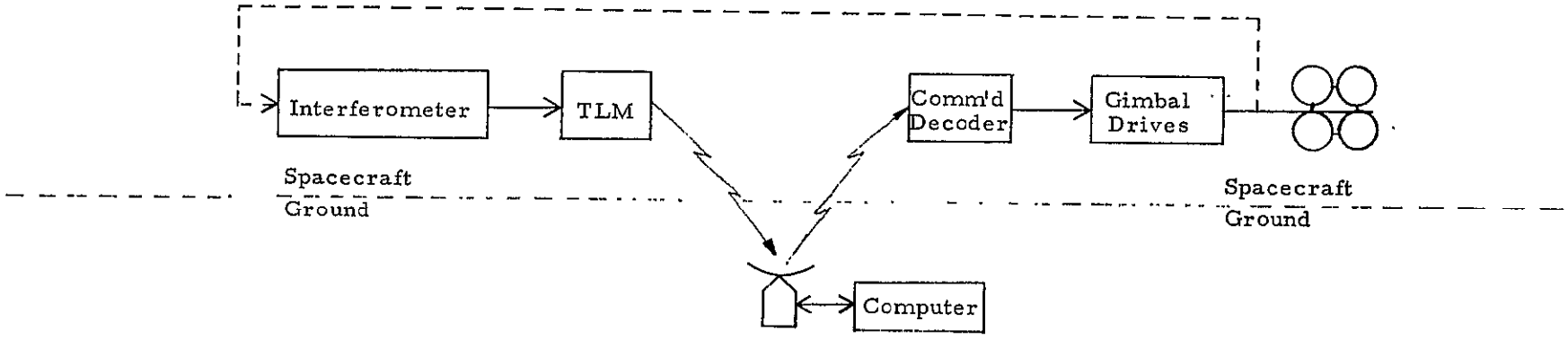

ADVANTAGES:

1. Satellite is simpler.
2. Changes in computations are easy to do, by merely changing program in ground computer.

DISADVANTAGES:

1. Uses command and TLM link all the time.
2. Ground computer is tied up and always required.
3. Time lag between actuation and measurement increases stability problem.

Figure 6-3 Ground Commanded Control Technique

6.2.2 On-Board Antenna Control

The on-board antenna control technique uses the angles measured by the interferometer in an on-board computer. The computer has stored in it a set of desired interferometer angles which are used in conjunction with the measured angles to compute the required changes in the gimbal angles. The required gimbal changes are used to drive the gimbals and hence the antennas. The change in antenna orientation is measured by the interferometer, thus closing the loop. Because it is desired to point the antenna at different spots on the earth's surface the desired interferometer angles will change. Also, the location of the interferometer beacon may be moved from time to time, again requiring a new set of interferometer angles. It is therefore necessary to be able to change the desired angles that are stored in the on-board computer. This is accomplished via the command link.

The system recommended for this application is a combination of the ground commanded and the on-board control techniques, as shown in Figure 6-4. A command override has been provided to ensure control if the computer becomes inoperative. The telemetry readout of the interferometer angles, computer state, and gimbal drive response is optional.

The main disadvantages of this technique are the complexity added to the spacecraft by the on-board computer, and the inflexibility in the solution algorithm. However, the self-contained feature relieves the requirement for telemetry and command channels on a full-time basis, and eliminates the continuous requirement for computation equipment on the ground. Also, there is less time lag in the control loop. easing the stability problem.

For the alternate requirements the command override allows a failure of both the computer and the interferometer, if ground power levels can be used to determine beam position. This is a result of the accurate spacecraft attitude control. The ground commanded technique also has this capability for the alternate requirements.

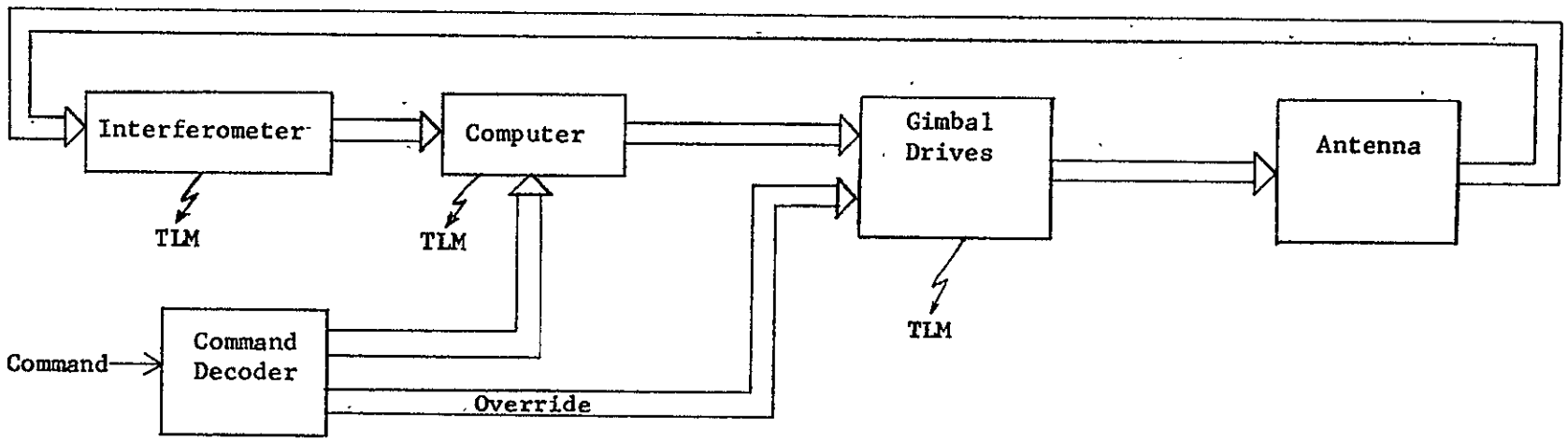

ADVANTAGES:

1. Self contained, relieving requirement for continuous command channel.
2. Less time lag in the loop than for the loop closed through the ground.

DISADVANTAGES:

1. The on-board computer adds complexity to the satellite.

Figure 6-4 On-Board Control Technique

Another derived requirement is placed on the location of the interferometer beacons on the ground. To obtain 3-axis information from the interferometer it is necessary to have two beacon stations separated by some minimum distance. This minimum distance is a function of the accuracy desired and is treated more fully in the error analysis section.

6.3 COMPUTATION REQUIREMENTS

The computation requirements can be divided into two categories: (1) ground computation, and (2) spacecraft computations. The ground computations depend to some extent on whether the control is by ground command or an automatic on-board system. The spacecraft computations are heavily dependent on the type of control being used.

6.3.1 Ground Computations

The purpose of the ground computations is to define the desired interferometer angles, and in the case of the ground commanded system to use the desired interferometer angles with the actual interferometer angles to define the required changes in the gimbal angles. For the on-board control system only the desired angles are computed on the ground, the generation of gimbal angle changes being done on the spacecraft.

Defining the desired interferometer angles requires a knowledge of the position of the interferometer beacons in antenna coordinates. This means that the transformation between the earth frame (in which the interferometer beacon locations are known) and the antenna frame must be known for any point to which the beam pattern must be centered on the earth's surface.

If $\overline{p}$ is the position vector of the center of the beam pattern, (see Figure 6-5), in earth coordinates it can be expressed as:

$$\overline{p} = r_e \sin \zeta_p \overline{E}_1 + r_e \cos \zeta_p \sin \lambda_p \overline{E}_2 - r_e \cos \zeta_p \cos \lambda_p \overline{E}_3$$

$\overline{S_i}$ = Vector from earth's center to $i^{\underline{th}}$ interferometer beacon
$\overline{p}$ = Vector from earth's center to desired location of center of beam pattern
ξ = Lattitude of beacon or pattern center
λ = Longitude of beacon or pattern center referenced to the satellite subpoint

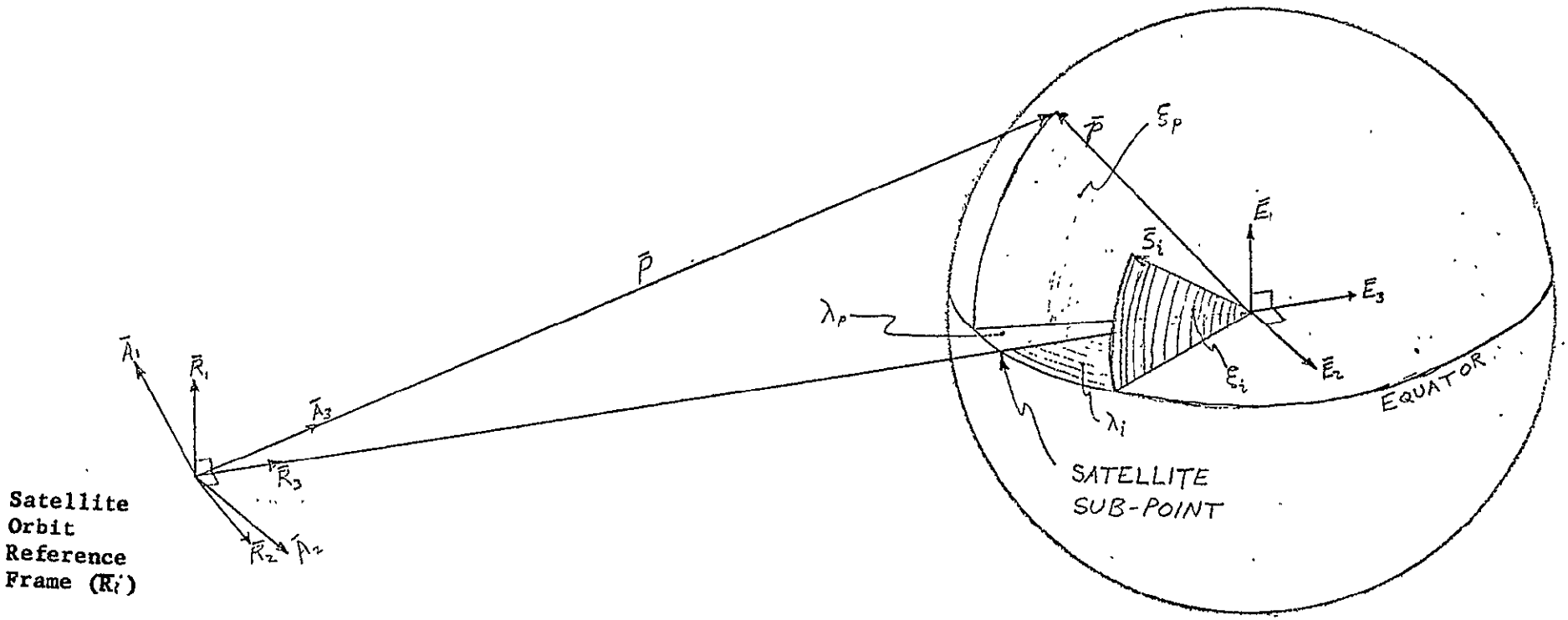

FIGURE 6-5. SYMBOL DEFINITION

and in the satellite orbit reference frame as: (ignoring orbit inclination and station drift.)

$$\overline{P} = r^e \sin \zeta_p \overline{R}_1 + r_e \cos \zeta_p \sin \lambda_p \overline{R}_2 + (r_s - r_e \cos \zeta_p \cos \lambda_p) \overline{R}_3$$

The transformation between the $\overline{R}$ frame and the $\overline{A}$ can be expressed in terms of three Euler angles representing successive rotations about the 1, 2, and 3 axes and denoted herein by γ_1, γ_2, γ_3. Only the first two rotations, i.e., γ_1 and γ_2 are necessary to point the interferometer boresight ($\overline{A}_3$) at the point p. The third rotation, γ_3, is necessary to ensure that the three or four antenna pattern centers maintain a roughly constant latitude.

In orbital coordinates the vector to the location of the desired pattern center is given by $\overline{P}$. After two rotations, γ_1 and γ_2, it is desired to have $\overline{P}$ coincide with the interferometer boresight $\overline{R}_3''$. Thus it is desired that

$$F \overline{R}_3'' = \overline{P}$$

where

$$\overline{R}_3'' = \sin \gamma_2 \overline{R}_1 - \sin \gamma_1 \cos \gamma_2 \overline{R}_2 + \cos \gamma_1 \cos \gamma_2 \overline{R}_3$$

Solving for γ_1 and γ_2 from the above gives:

$$\tan \gamma_1 = \frac{-r_e \cos \zeta_p \sin \lambda_p}{r_s - r_e \cos \zeta_p \cos \lambda_p}$$

$$\tan \gamma_2 = \frac{- \sin \zeta_1 \sin \lambda_p}{\sin \zeta_p \cos \lambda_p}$$

The third Euler angle, γ_3, is found by defining a constant latitude tangent to the earth's surface at the desired pattern center location, and ensuring

that this vector is in the plane defined by three of the beam centers. Doing this defines the third angle to be:

$$\tan \gamma_3 = \frac{\sin (\lambda_p + \gamma_1)}{\cos (\lambda_p - \gamma_1)(\sin \gamma_2 - \cos \gamma_1 \cot \gamma_2)}$$

With the transformation between the orbital reference frame and the desired antenna frame known it is possible to write down the expressions for the desired interferometer angles. If the position vector to the i-th interferometer beacon is defined by its relative longitude λ_i and latitude ζ_i, then in orbital coordinates it is expressed by:

$$\bar{r}_i = r_e \sin \zeta_i \bar{R}_1 + r_e \cos \zeta_i \sin \lambda_i \bar{R}_2 + (r_s - r_e \cos \zeta_i \cos \lambda_i) \bar{R}_3$$

Performing the dot product between the above and the desired axis of the horizontal interometer arm gives the cosine of the desired angle between that arm and the i-th station:

$$\cos \alpha_i = - \frac{r_e}{|\bar{r}_i|} \sin \zeta_i \cos \gamma_2 \sin \gamma_3 + \frac{r_e}{|\bar{r}_i|} \cos \zeta_i \sin \lambda_i (\cos \gamma_1 \cos \gamma_3 - \sin \gamma_1 \sin \gamma_2 \sin \gamma_3)$$

$$+ \frac{(r_s - r_e \cos \zeta_i \cos \lambda_i)}{|\bar{r}_i|} (\sin \gamma_1 \cos \gamma_3 - \cos \gamma_1 \sin \gamma_2 \sin \gamma_3)$$

And likewise for the vertical interferometer arm:

$$\cos \beta_i = \frac{r_e}{|\bar{r}_i|} \sin \zeta_i \cos \gamma_2 \cos \gamma_3 + \frac{r_e}{|\bar{r}_i|} \cos \zeta_i \sin \lambda_i (\cos \gamma_1 \sin \gamma_3 + \sin \gamma_1 \sin \gamma_2 \cos \gamma_3)$$

$$+ \frac{(r_s - r_e \cos \zeta_1 \cos \lambda_i)}{|\bar{r}_i|} (\sin \gamma_1 \sin \gamma_3 - \cos \gamma_1 \sin \gamma_2 \cos \gamma_3)$$

For an orientation system that is contained on the spacecraft and has the loop closed on board, these calculations represent the only capability required on the ground at the command center. As can be seen, all of the calculations use subroutines generally available even to a desk-top computer, and hence present no problem in implementation. Figure 6-6 schematically summarizes the ground computations.

If the effects of inclination and station drift are included, two more rotations are necessary to define the transformation between earth coordinates (in which the beacon locations are known) and the desired antenna orientation. The two additional rotations make the algebraic expressions very long and messy looking, but the same calculations are performed, i.e., sin, cos, arctan. Also rotation subroutines are available, or can be easily generated that eliminate the need for doing all of the messy algebra required to obtain a closed form expression on paper.

If the antenna orientation is controlled entirely from the ground, then additional computation on the ground is necessary to generate the required gimbal angle changes from the actual vs desired interferometer angles. To obtain three axis information it is necessary to have two interferometer beacons on the ground. Let the vectors to the two beacons from the spacecraft be $\overline{\Gamma}_1$ and $\overline{\Gamma}_2$. Define a reference axis system $|\overline{A}|$ such that $\overline{A}_3$ is the axis along which it is desired to point the pattern center. Then $\overline{\Gamma}_1$ and $\overline{\Gamma}_2$ may be defined by:

$$\overline{\Gamma}_1 = \rho_1 \overline{A}_1 + \rho_2 \overline{A}_2 + \rho_3 \overline{A}_3$$

$$\overline{\Gamma}_2 = \Gamma_1 \overline{A}_1 = \Gamma_2 \overline{A}_2 + \Gamma_3 \overline{A}_3$$

The desired interferomter angle can then be expressed as:

$$\cos \alpha_{1D} = \frac{\rho_2}{|\overline{\Gamma}_1|} \qquad \cos \beta_{1D} = \frac{\rho_1}{|\overline{\Gamma}_1|}$$

$$\cos \alpha_{2D} = \frac{2}{|\overline{\Gamma}_2|} \qquad \cos \beta_{2D} = \frac{1}{|\overline{\Gamma}_2|}$$

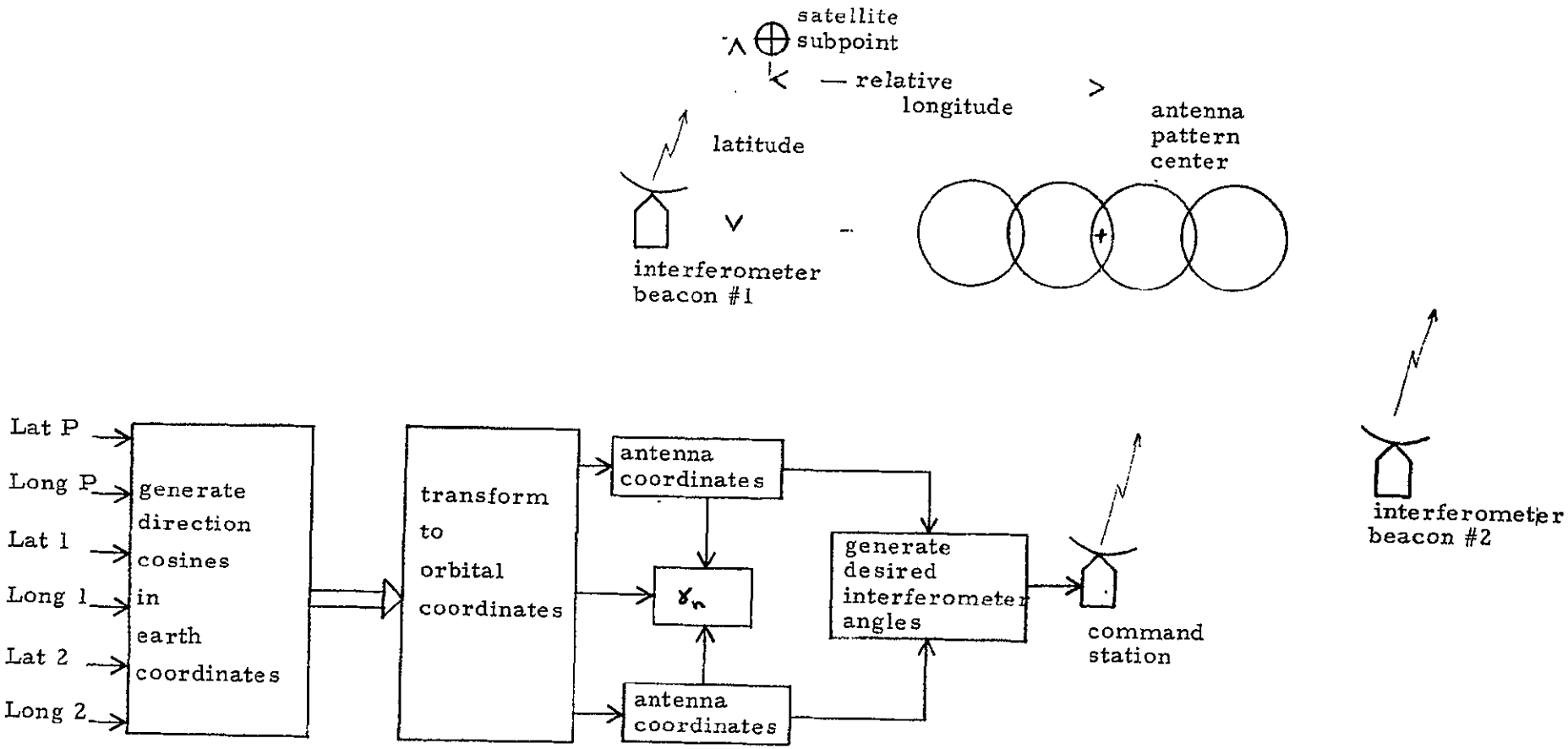

Figure 6-6 Ground Computation Requirements

Now it is necessary to introduce the antenna coordinate axis system $[\bar{a}]$ where $\bar{a}_3$ is along the interferometer boresight axis, and a spacecraft frame $[\bar{b}]$. The spacecraft frame $[\bar{b}]$ is defined to coincide with $[\bar{a}]$ when all gimbal angles are zero. Thus $[\bar{b}]$ and $[\bar{a}]$ are related by three transformations corresponding to the roll gimbal angle Φ_A, pitch gimbal angle θ_A, and yaw gimbal angle ψ_A:

$$[\bar{b}] = [-\theta_A][-\psi_A][-\Phi_A][\bar{a}]$$

Now define nominal gimbal angles Φ_n, θ_n, ψ_n such that the antenna pointing error is zero when the actual gimbal angles Φ_A, θ_A, ψ_A equal the nominal gimbal angle. Thus, the gimbal angle error is given by:

$$\delta\Phi = \Phi_A - \Phi_n$$

$$\delta\theta = \theta_A - \theta_n$$

$$\delta\psi = \psi_A - \psi_n$$

Also, it is known that the desired antenna frame $[\bar{A}]$ is related to $[\bar{b}]$ by:

$$[\bar{A}] = [\Phi_n][\psi_n][\theta_n][\bar{b}]$$

Also:

$$[\bar{A}] = [\Phi_A - \delta\Phi][\psi_A - \delta\psi][\theta_A - \delta\theta][\bar{b}]$$

where the frame $[\bar{A}]$ has been expressed in terms of the gimbal angle transformations and their errors, and the frame $[\bar{b}]$. By substitution, the relationship between the desired antenna frame $[\bar{A}]$ and actual antenna frame $[\bar{a}]$ can be expressed in terms of the following set of successive transformations:

$$[\bar{A}] = [\Phi_A - \delta\Phi][\psi_A - \delta\psi][\theta_A - \delta\theta][-\theta_A][-\psi_A][-\Phi_A][\bar{a}]$$

or more compactly:

$$[\bar{A}] = [K][\bar{a}]$$

where:

$$[K] = [\Phi_A - \delta\Phi][\psi_A - \delta\psi][-\delta\theta][-\psi_A][-\Phi_A]$$

Now it can be shown that:

$$\cos \alpha_{1A} = \frac{\bar{a}_2 \cdot \bar{r}_1}{|\bar{r}_1|} = \frac{1}{|\bar{r}_1|}[\rho_1 K_{12} + \rho_2 K_{22} + \rho_3 K_{32}]$$

$$\cos \alpha_{2A} = \frac{\bar{a}_2 \cdot \bar{r}_2}{|\bar{r}_2|} = \frac{1}{|\bar{r}_2|}[\sigma_1 K_{12} + \sigma_2 K_{22} + \sigma_3 K_{32}]$$

$$\cos \beta_{1A} = \frac{\bar{a}_1 \cdot \bar{r}_1}{|\bar{r}_1|} = \frac{1}{|\bar{r}_1|}[\rho_1 K_{11} + \rho_2 K_{21} + \rho_3 K_{31}]$$

$$\cos \beta_{2A} = \frac{\bar{a}_1 \cdot \bar{r}_2}{|\bar{r}_2|} = \frac{1}{|\bar{r}_2|}[\sigma_1 K_{11} + \sigma_2 K_{21} + \sigma_3 K_{31}]$$

Assuming small angles and linearizing, it can be shown that:

$$K_{11} \doteq K_{22} \doteq 1$$

$$K_{12} \doteq -K_{21} \doteq -\delta\psi$$

$$K_{32} \doteq \delta\theta$$

$$K_{31} = -\delta\Phi$$

so that:

$$\cos \alpha_{1A} \doteq \frac{-\rho_1}{|\bar{r}_1|} \delta\psi + \frac{\rho_2}{|\bar{r}_1|} + \frac{\rho_3}{|\bar{r}_1|} \delta\theta$$

$$\cos \alpha_{2A} \doteq \frac{-\sigma_1}{|\bar{r}_2|} \delta\psi + \frac{\sigma_2}{|\bar{r}_2|} + \frac{\sigma_3}{|\bar{r}_2|} \delta\theta$$

$$\cos \beta_{1A} = \frac{\rho_1}{|\bar{r}_1|} + \frac{\rho_2}{|\bar{r}_1|} \delta\psi - \frac{\rho_3}{|\bar{r}_1|} \delta\Phi$$

$$\cos \beta_{2A} = \frac{\sigma_1}{|\bar{r}_2|} + \frac{\sigma_2}{|\bar{r}_2|} \delta\psi - \frac{\sigma_3}{|r_2|} \delta\Phi$$

But since $\frac{\rho_2}{|\bar{r}_1|} = \cos \alpha_{1D}$, etc., these can be rewritten:

$$\cos \alpha_{1D} - \cos \alpha_{1A} = \cos \beta_{1D} \delta\psi - \delta\theta \cos \lambda_1$$

$$\cos \alpha_{2D} - \cos \alpha_{2A} = \cos \beta_{2D} \delta\psi - \delta\theta \cos \lambda_2$$

$$\cos \beta_{1D} - \cos \beta_{1A} = -\delta\psi \cos \alpha_{1D} + \delta\Phi \cos \lambda_1$$

$$\cos \beta_{2D} - \cos \beta_{2A} = -\delta\psi \cos \alpha_{2D} + \delta\Phi \cos \lambda_2$$

where λ_i is defined as:

$$\lambda_1 = \cos^{-1}\left[\frac{\bar{r}_1 \cdot \bar{A}_3}{|\bar{r}_1|}\right]$$

$$\lambda_2 = \cos^{-1}\left[\frac{\bar{r}_2 \cdot \bar{A}_3}{|\bar{r}_2|}\right]$$

There are 4 equations and only 3 unknowns, so any three of the equations may be solved for $\delta\Phi$, $\delta\theta$, and $\delta\psi$ in terms of α_i and β_i. If the data from the horizontal interferometer arm is used twice (i.e., angles to both beacons are used) then the three equations are:

$$\delta\psi \cos \beta_{1D} - \delta\theta \cos \lambda_1 = \cos \alpha_{1D} - \cos \alpha_{1A}$$

$$\delta\psi \cos \beta_{2D} - \delta\theta \cos \lambda_2 = \cos \alpha_{2D} - \cos \alpha_{2A}$$

$$-\delta\psi \cos \alpha_{1D} + \delta\Phi \cos \lambda_1 = \cos \beta_{1D} - \cos \beta_{1A}$$

Solving for $\delta\Phi$, $\delta\theta$, and $\delta\psi$ gives:

$$\delta\psi = \frac{\cos \lambda_1[\cos \alpha_{2A} - \cos \alpha_{2D}] - \cos \lambda_2[\cos \alpha_{1A} - \cos \alpha_{1D}]}{\cos \beta_{1D} \cos \lambda_2 - \cos \beta_{2D} \cos \lambda_1}$$

$$\delta\Phi = \frac{\cos \beta_{1D} - \cos \beta_{1A}}{\cos \lambda_1} + \delta\psi \frac{\cos \alpha_{1D}}{\cos \lambda_1}$$

$$\delta\theta = \frac{\cos \alpha_{2A} - \cos \alpha_{2D}}{\cos \lambda_2} + \delta\psi \frac{\cos \beta_{2D}}{\cos \lambda_2}$$

The angles given are the angles that the gimbals are in error and are the numbers to be sent to the spacecraft for a ground controlled technique. Computation of these numbers is easily implemented (given the appropriate constants) on a modern computer.

6.3.2 Spacecraft Computations

For the ground controlled technique no calculation of any kind is required on the spacecraft. A command decoder would be necessary to sort out the required changes in each channel and drive the appropriate gimbal drive logic.

For an automatic system the equations of the previous section would need to be solved by an on-board computer. For the pitch and roll gimbals the generation of a drive signal is quite easy once one has a solution for $\delta\psi$. To solve for $\delta\psi$ the computer must be supplied with the following constants via the command link:

$$\cos\lambda_1 \qquad \cos\alpha_{1D} \qquad \cos\beta_{1D}$$

$$\cos\lambda_2 \qquad \cos\alpha_{2D} \qquad \cos\beta_{2D}$$

With these six numbers supplied to the computer from the ground and two interferomter measurements from on-board, the computer can continuously generate the required error signals for all three gimbals.

Regarding the ease of constructing a computer with the above capability it should be pointed out that the only operations involved are addition, subtraction, multiplication, and division, operations very common even to desk top computers. The generation of $\cos\alpha_{iA}$ and $\cos\beta_{iA}$ is done automatically by the interferometer and supplied to the computer.

To summarize the computation requirements, for a ground controlled system, all of the calculations of the previous section must be performed on the ground. For an on-board controlled system the last set of equations in the previous section must be solved on board.

6.4 HARDWARE IMPLEMENTATION

In the implementation of the antenna control system several trade-offs had to be performed. Two of these trade-offs were the choice of open loop versus closed loop control, and stepper motor versus brushless dc motor. To perform the trade-offs it was necessary to know as many of the characteristics of each option as possible.

6.4.1 Open Loop Systems

Open loop drive systems (i.e., systems closed through ground stations) have the advantage of simplicity and high reliability of on-board equipment (see Figure 6-7). An integral part of such a system would be a stepper motor which would, on command from the ground station, be rotated a desired number of steps to re-orient the antenna to the desired position. A ground computer would be required to calculate the number of steps to be taken and the direction of rotation. In addition, commands for the pulse width of the pulses for each step, possibly the pulse repetition rate and whether to stop with motor power on (a particular winding) or power off, must be sent. The variability in pulse width and pulse repetition rate is included in order to alleviate possible step-skipping problems which may occur in operations particularly under environmental extremes.

An open loop system has the disadvantage that it places considerable burden on the ground station computer and operational procedures especially during non-normal behavior. Also, the slew rate would be restricted by the duration of each step transient and may become unduly slow under environmental extremes. Another disadvantage is that for satellite attitude drift rates of 1-2 deg/min, large errors in antenna attitude could accumulate before corrections could be made (access to command link is usually restricted to once every few seconds or minutes during which time the errors can accumulate to intolerably large levels). Thus, although the open loop system has the advantages of simplicity and reliability, it is not recommended for the reasons stated above.

6.4.2 Closed Loop Systems

Two possible closed loop systems with stepper motors are shown in Figures 6-8 and 6-9. The closed loop system of Figure 6-8 employs the same philosophy of the open loop system (i.e., stabilize the transients of each step before the next step is taken) except that most of the computation is done on board. The pulse control system is used to increase the pulse width and decrease the pulse repetition rate in the event that the step and sign change detector

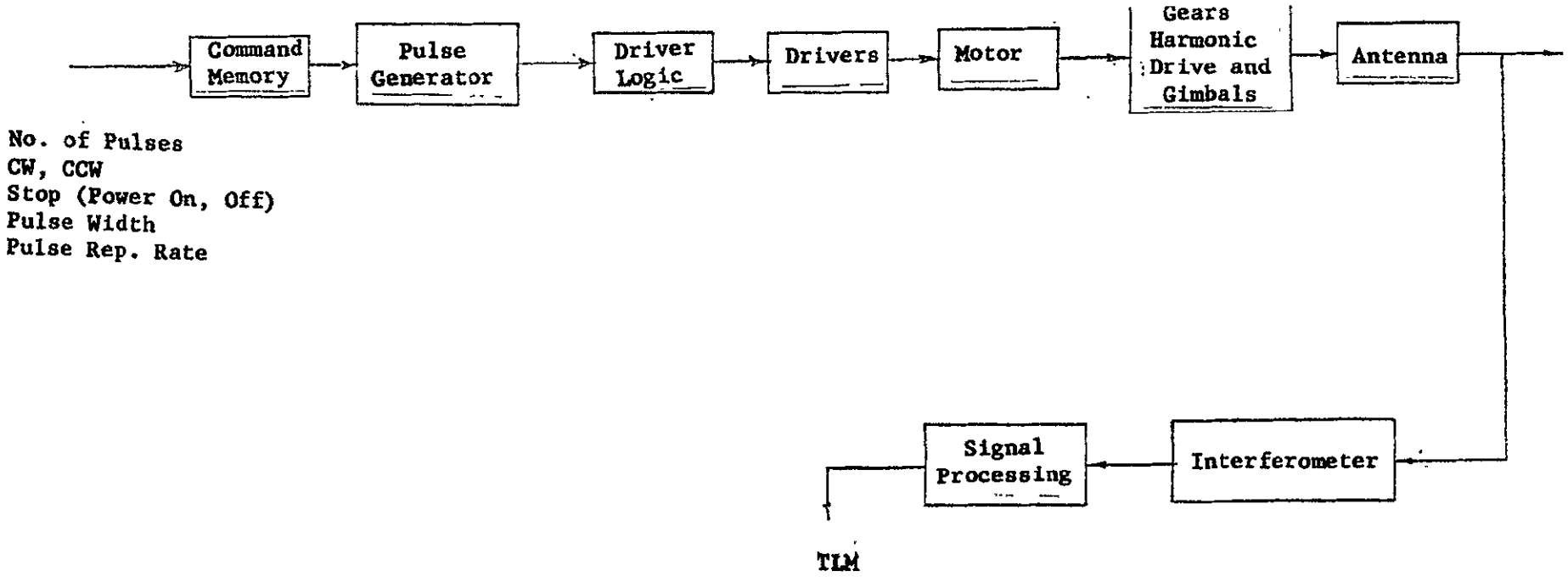

Figure 6-7. Open Loop Stepper Motor Drive System

indicates a non-normal operation (i.e., steps not taken or antenna position exceeds desired position). The primary disadvantage of this system is that the antenna slew rate may become unduly slow under environmental extremes. When friction levels decrease, the transients become longer leading to step-skipping problems when stepped too soon. In order to prevent step-skipping problems, the pulse applied to each motor winding is made longer and the pulse repetition rate is made lower. This system is feasible but may result in very low slew rates. Figure 6-9 shows one of the more promising closed loop systems. It consists of an inner loop which includes the translator and the step detector. This inner loop prevents step-skipping and permits very high slew rates. Step-skipping is prevented by permitting a succeeding step to be taken only after a step change has been detected. The high slew rate is obtained by supplying pulses for the next step change at the initial detection of a step change, i.e., at the first "zero" crossing of a step transient. The outer loop (containing the switching logic) stabilizes the system by supplying the proper CW, CCW or stop commands as a function of the position error and velocity.

Another of the closed loop systems uses a brushless dc motor in the control loop shown in Figure 10. The incremental encoder and encoder electronics provide to the computer the relative rate information necessary for damping and loop stabilization. The interferometer provides antenna angle information to the computer. The computer then generates a digital motor drive signal using data from the encoder, interferometer, and stored command decoder information. The digital motor drive signal is fed to the D/A converter through a command override selection switch where, by ground command, control can be changed from the automatic system to direct ground control. The analog motor drive signal coming from the D/A converter is fed to a modulator that modulates a carrier capable of being transmitted across the rotary transformer.

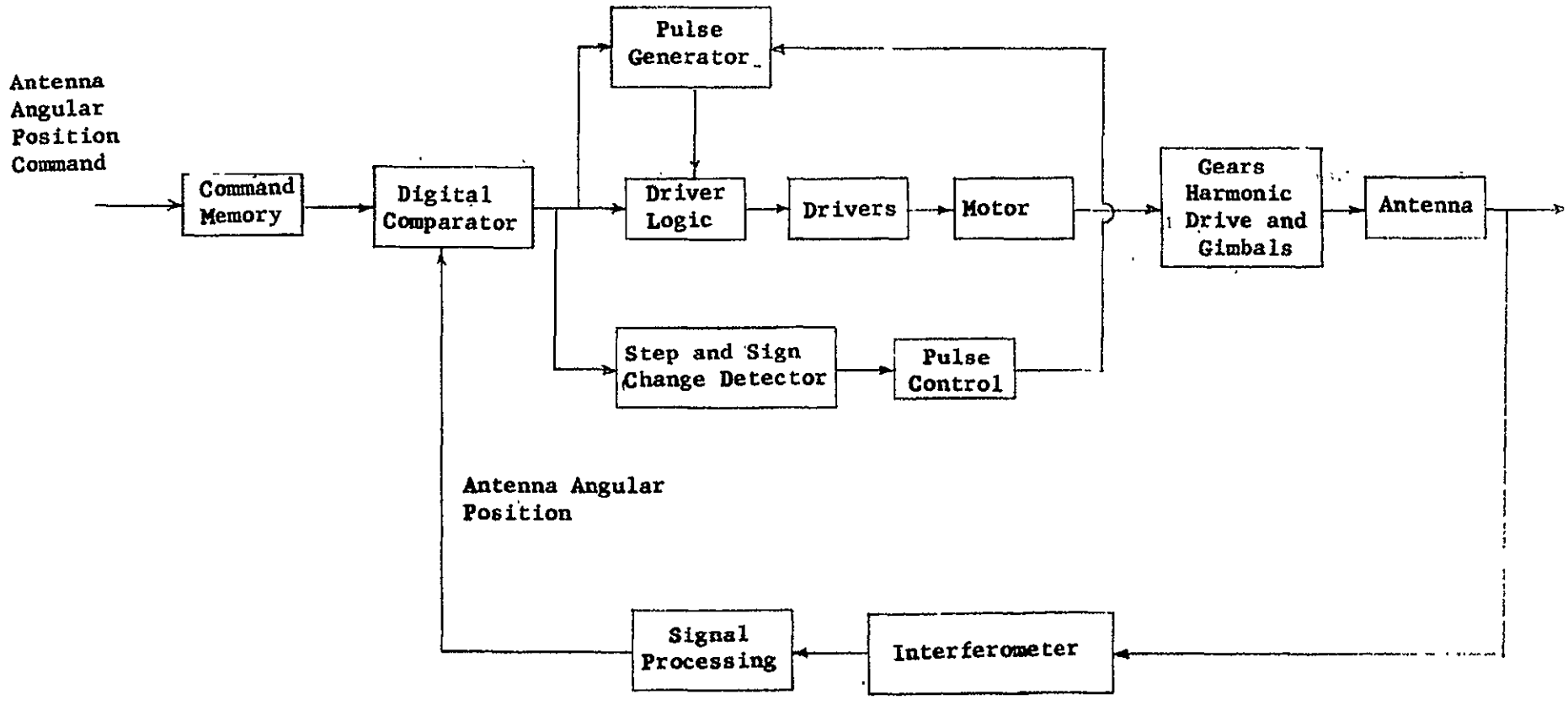

FIGURE 6-8 'CLOSED LOOP STEPPER MOTOR DRIVE

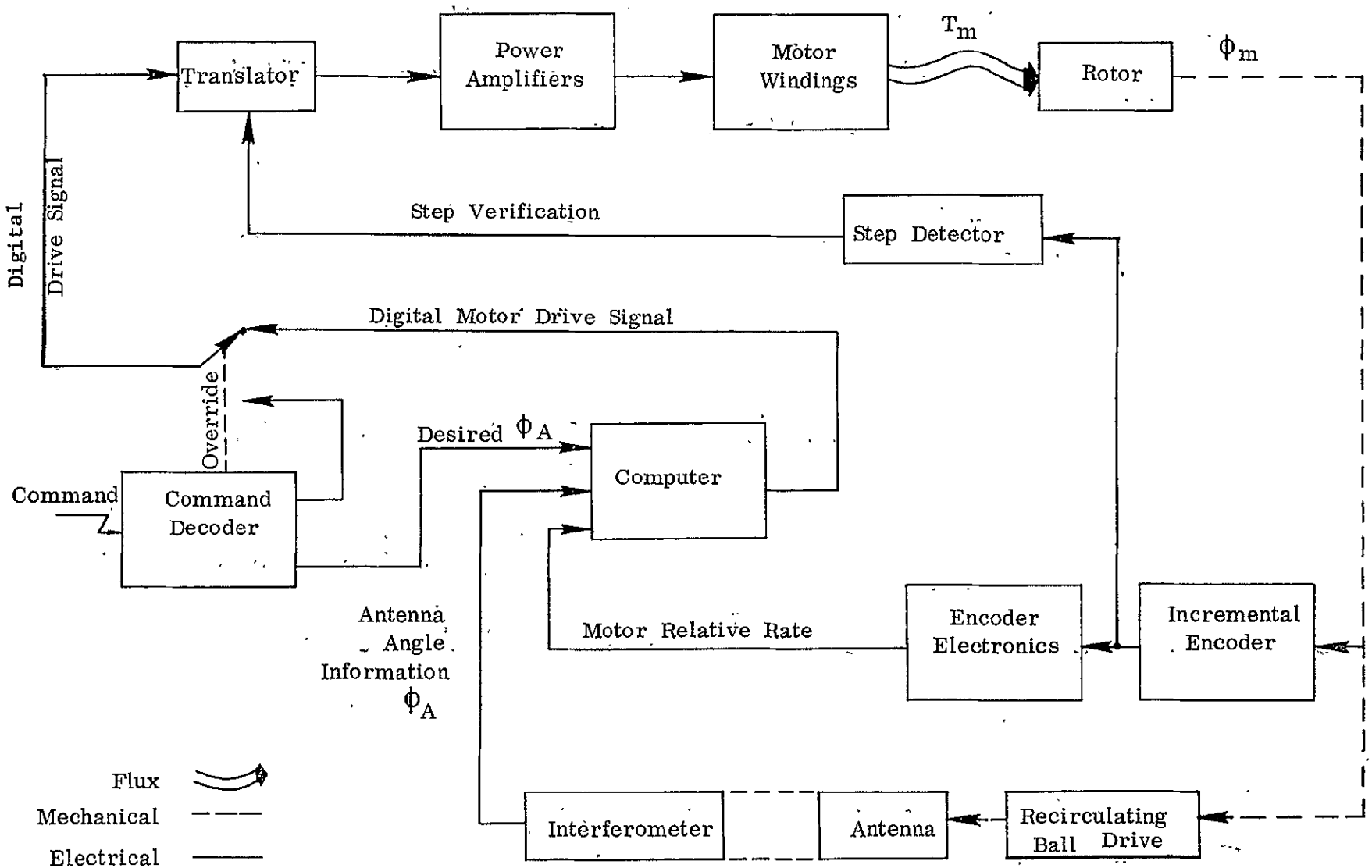

Figure 6-9. Stepper Motor Control Loop

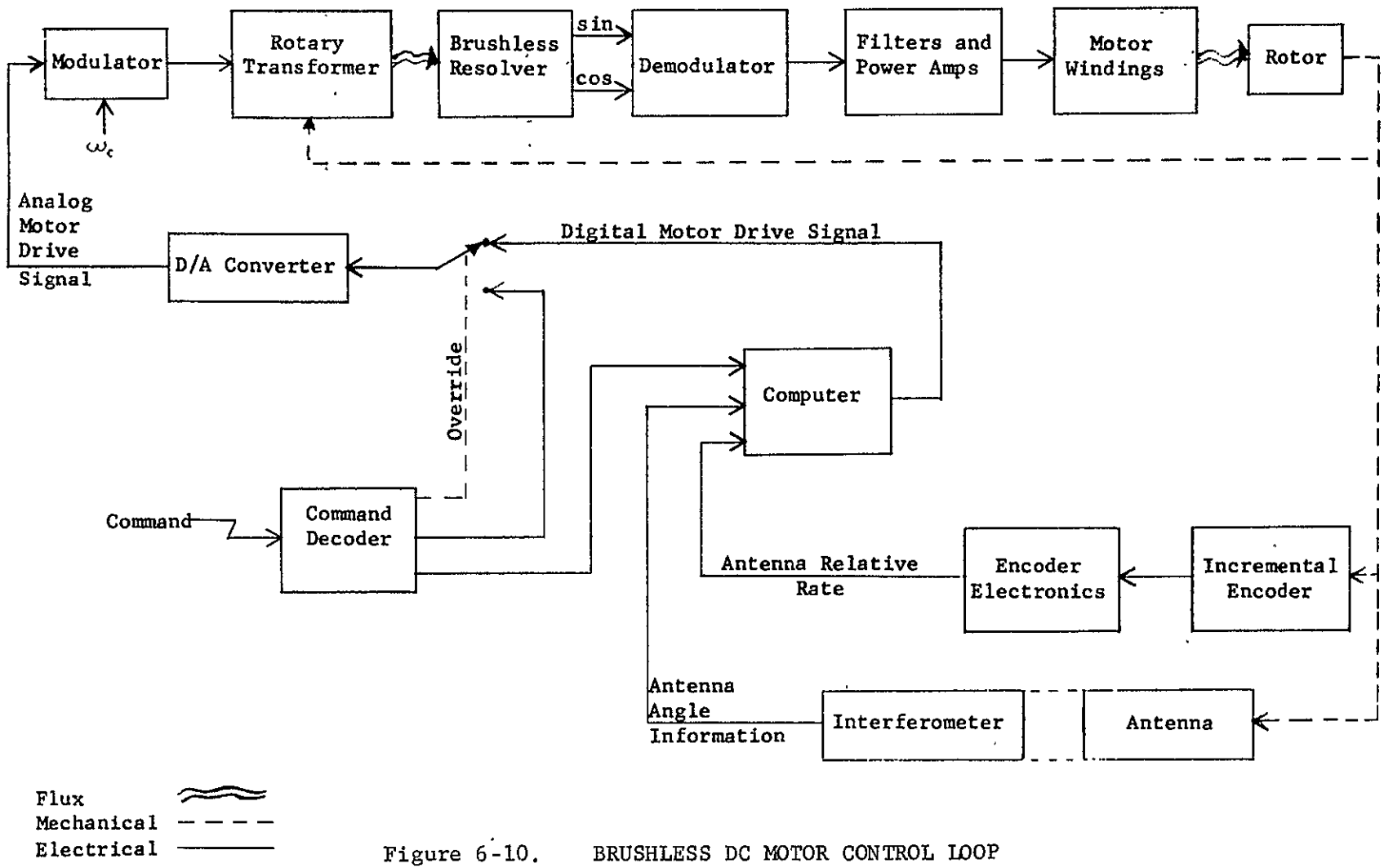

Figure 6-10. BRUSHLESS DC MOTOR CONTROL LOOP

The DC brushless torque motor employs a rotary transformer type resolver which, when properly aligned, acts to commutate the synchronous permanent magnet motor. This is accomplished by the use of an integrally mounted motor, resolver and rotary transformer. The resolver and rotary transformer are actually combined into a single unit. The resolver has an input winding which is excited at 1000 Hz and two output windings which have an output proportional to the input at the input carrier frequency modulated with a trigonometric function of the angular position of the rotor. The rotor is a variable reluctance element having shorted windings, whose turns and winding distribution are controlled to obtain an optimum modulation wave shape on the output winding and a desired phase relationship between the two windings. Schematically, the resolver is shown in Figure 6-11. The figure also shows the relationship between input and output signals where ϕ is an electrical phase shift between the carrier frequency input and output and θ is the angular position of the rotor. The motor, whose rotor is on the same shaft as the resolver rotor, is a permanent magnet two-phase synchronous motor having 8 pole pairs.

The magnet is of Alnico 9 which has the highest energy product of the common magnet materials and has a coercive force of 1600 oersteds, thus exhibiting extremely good stability which assures minimum degradation during satellite life. The motor is energized from the demodulated resolver outputs as shown in Figure 6-12.

The direction of rotation and peak torque per unit power is controlled by the relative positions of the resolver stator and motor stator. This position is mechanically fixed such that the stator rotating field in the motor always leads the rotor rotating field by $\pi/2$ electrical radians.

The output from the resolver is demodulated and power amplified to drive the corresponding motor sine and cosine windings.

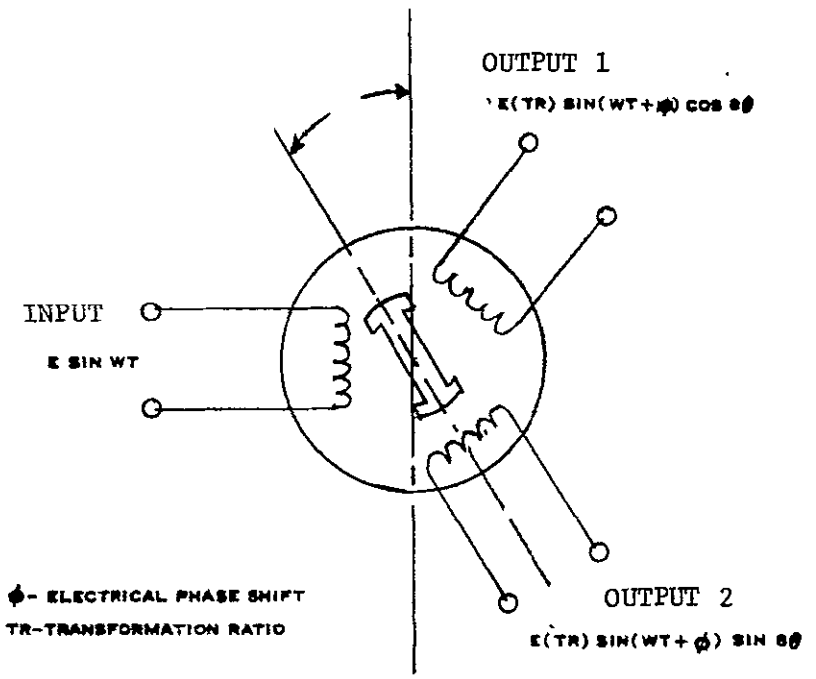

Figure 6-11 Resolver Diagram

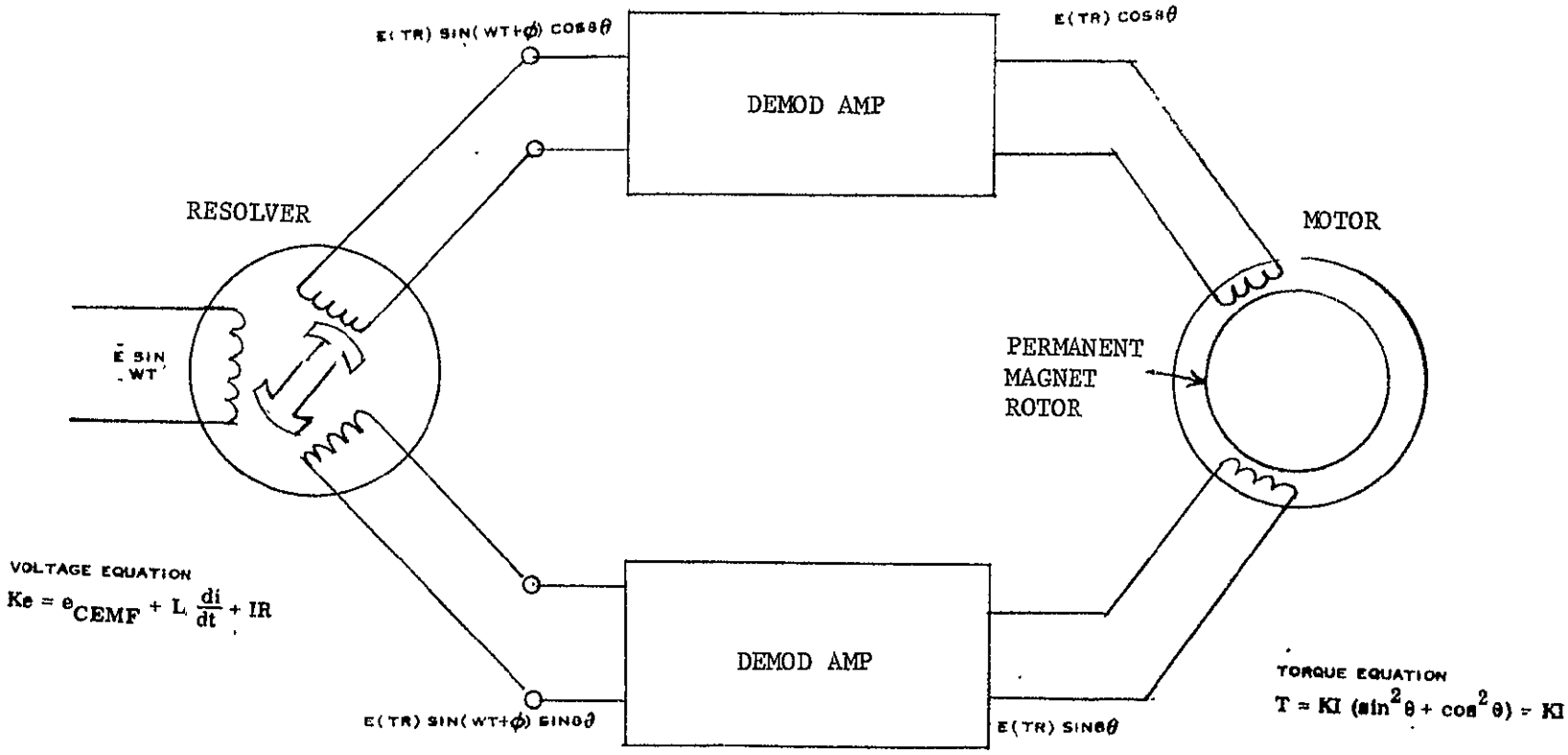

Figure 6-12 Motor-Resolver Block Diagram

6.4.3 Stepper Motor/DC Motor Trade-Off Analysis

In the comparison of the two types of motors it became obvious fairly early that the stepper motor would not be suitable for the pitch gimbal, but was acceptable for the roll and yaw gimbals. The reason the stepper motor is not suitable for pitch is as follows. In this application the required increment in antenna orientation (0.05°) is much smaller than practical step sizes for stepper motors, meaning that a large gear ratio is required. At the same time the high overall accuracy required eliminates those designs having more than $.02^{\circ}$ of backlash. Usually, anti-backlash gear trains have been avoided in space applications requiring long life because of the higher friction levels inherent in their design. The harmonic drive can provide a high gear ratio with virtually no backlash but it is necessary to mount it with its output/input shaft on the axis of desired rotation. For the roll and yaw gimbals this presents no problem, but for the pitch gimbal the R-F rotary joint also has to be on the axis of rotation. Since the two objects obviously cannot occupy the same space, the harmonic drive unit would have to be offset, with a gear coupling to transfer the drive torque to the rotary joint housing. But the purpose of the harmonic drive was to avoid gears and their backlash, so nothing has been gained that couldn't be accomplished with a direct drive DC motor.

The harmonic drive could be used on the roll and yaw gimbals if separate gimbals were being used, and the system was in fact originally designed that way. However, with the use of the spherical bearing and recirculating ball drive, the required 375:1 gear ratio can be easily obtained using a $22\ 1/2^{\circ}$ stepper motor.

For the stepper motor control loop the computations can all be done digitally, since the stepper motor is inherently adaptable to digital control logic. On the other hand, for the brushless DC motor control loop a digital-to-analog converter is necessary at some spot in the loop, as the interferometer output is digital and the motor requires an analog drive signal.

The stepper motor control is less affected by noise than the DC motor control. If noise exists in the DC motor control loop, as it must, this will appear at the motor shaft in varying degrees of attenuation or amplification depending on the noise frequency and the antenna natural frequency. The stepper motor does not respond to control loop noise until the noise level reaches an amplitude sufficient to cause steps to occur. The stepper motor does have another problem: an offset from the nominal step location will exist that is a function of the slope of the detent torque and the coulomb friction on the shaft.

Static friction (stiction) has been shown to cause low amplitude stability problems in some cases in analog control loops. The stepper motor would be unaffected by stiction unless the stiction exceeds the torque capability of the motor.

The translator required for the stepper motor control loop (to shift the excited poles sequentially around the motor) is a simple logic design consisting of "AND" gates. This contrasts with the requirement for a modulator, brushless resolver, demodulator and rotary transformer for the brushless DC motor.

For the alternate requirements where changing the gimbal angles will be fairly infrequent the stepper motor is particularly attractive because, being of the permanent magnet type, it will hold the last position commanded without application of power to the windings. The only way this would be possible for the brushless DC motor in roll or yaw is if the recirculating ball drive pitch were chosen such that the inertia loads on the antenna were not able to drive the motor, i.e., the torque is only transmitted in one direction, namely from the motor to the antenna.

Table 6-2 summarizes the trade-offs.

TABLE 6-2

MOTOR TRADE STUDY

Brushless DC Motor	Stepper Motor
1. No gears are required between motor and load resulting in neater packaging	1. Needs high gear ratio (375:1)
2. Digital interferometer output makes D/A converter necessary in loop	2. All computations can be performed digitally
3. Noise on error signal will show up at output	3. Unaffected by noise until noise is large enough to cause step
4. Power is required continuously to hold a given orientation, unless worm gear is used	4. In the event of a power failure, the last desired position is automatically held
5. Stiction may present a stability problem	5. Stiction no problem unless it is larger than maximum available motor torque
6. Modulator, brushless resolver, demodulator are required (+ rotary transformer for pitch)	6. Translator consists of "AND" gates
7. Direct drive is feasible on pitch axis	7. Harmonic drive plus gear train required for pitch axis

6.4.4 Stepper Motor Control Simulation

The simulation of the stepper motor control loop was performed to verify the control concepts and to ensure that the motor characteristics chosen were compatible with the approximate antenna inertia load. The parameters assumed in the simulation were:

Step Size:	22 1/2° (at motor)
Gear Ratio:	0.06° (at antenna)
Slew Rate:	375:1
Antenna Inertia:	17 slug-ft.^{2}
Motor Inertia:	1.5×10^{-4} slug-ft.^{2}
Peak Motor Torque:	15 in-oz.
Bearing/Gear Drag (coulomb):	1 in-oz.
Detent Torque:	5 in-oz.
Viscons Drag:	10^{-2} in-oz./rad/sec. (at motor)
	.768 in-oz./rad/sec (at antenna)
Backlash:	zero
Gear Teeth Spring Constant:	1.8×10^3 in-oz./rad
Motor Excitation:	30 volts
Motor Winding Resistance:	300 ohms

Computer runs were made with the slope of the control law set at 3 different values. Figures 6-13 through 6-15 show the antenna and motor response along with the rates and motor torque, for increasing values of 'a', the slope of the control law. No attempt was made to optimize 'a' as optimization criteria were not known. However, when the system is being built and inertias and required response rates defined it would become possible to in some way optimize 'a'.

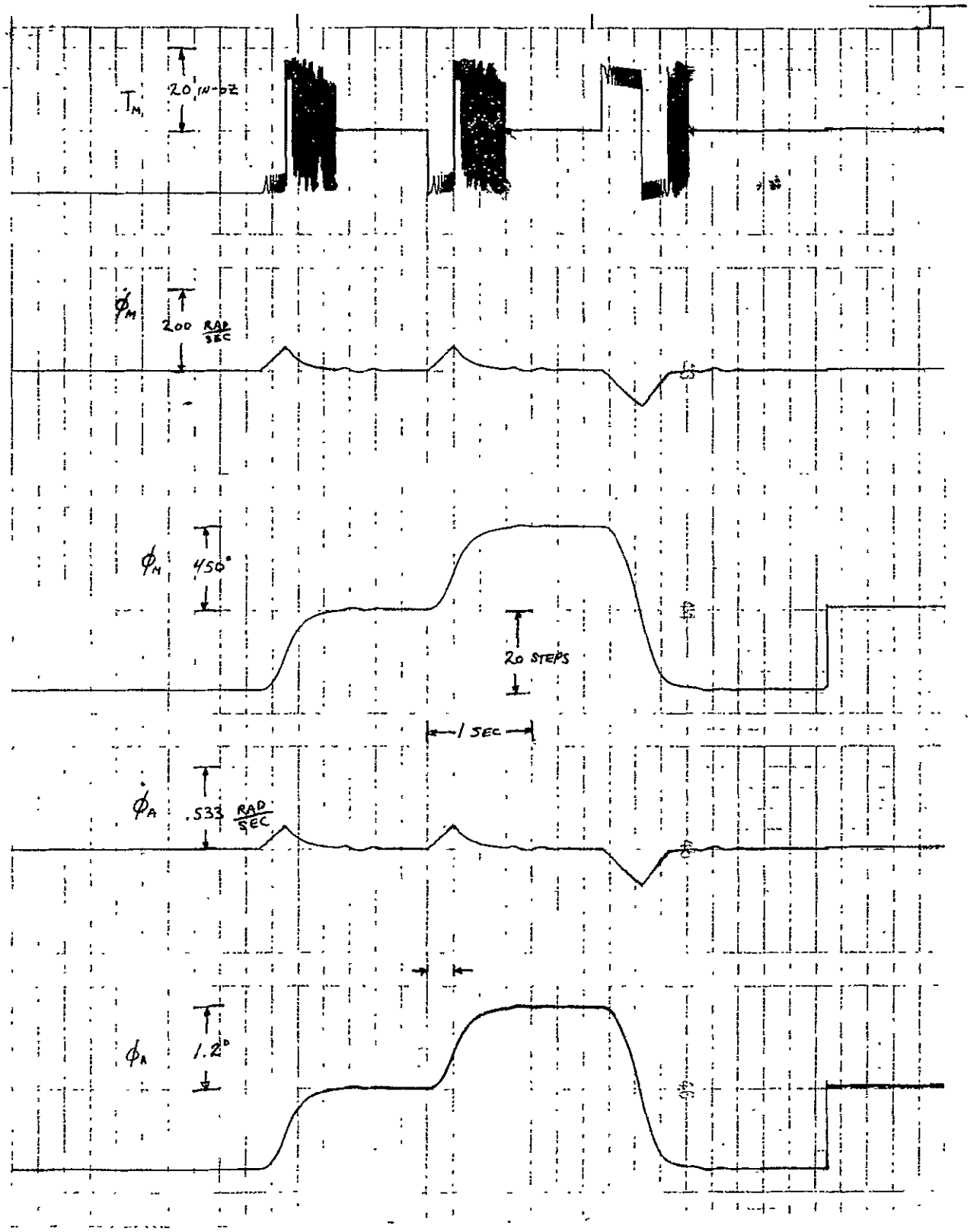

FIGURE 6-13. ANALOG COMPUTER ANTENNA CONTROL RESPONSE

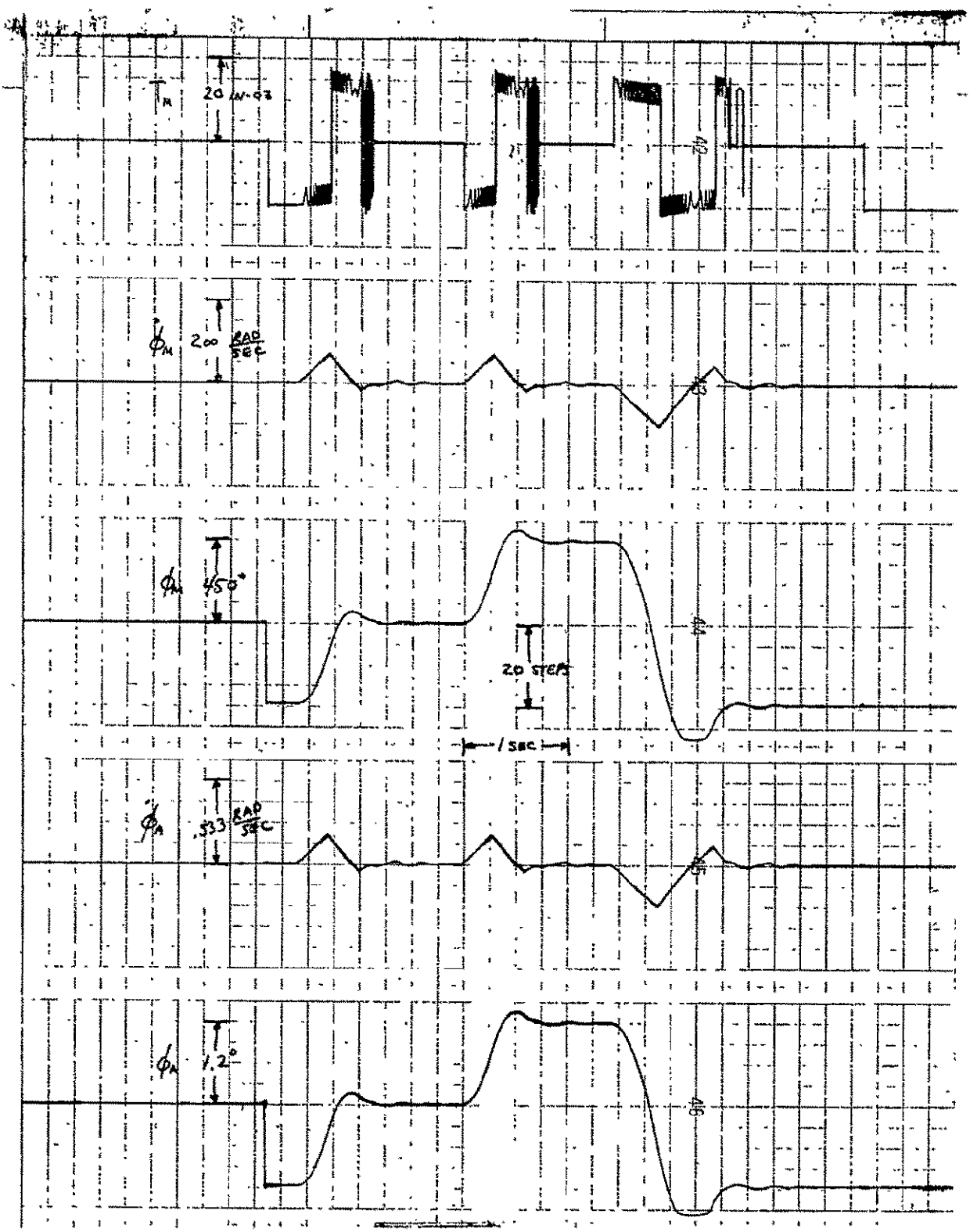

FIGURE 6-14. ANALOG COMPUTER ANTENNA CONTROL RESPONSE

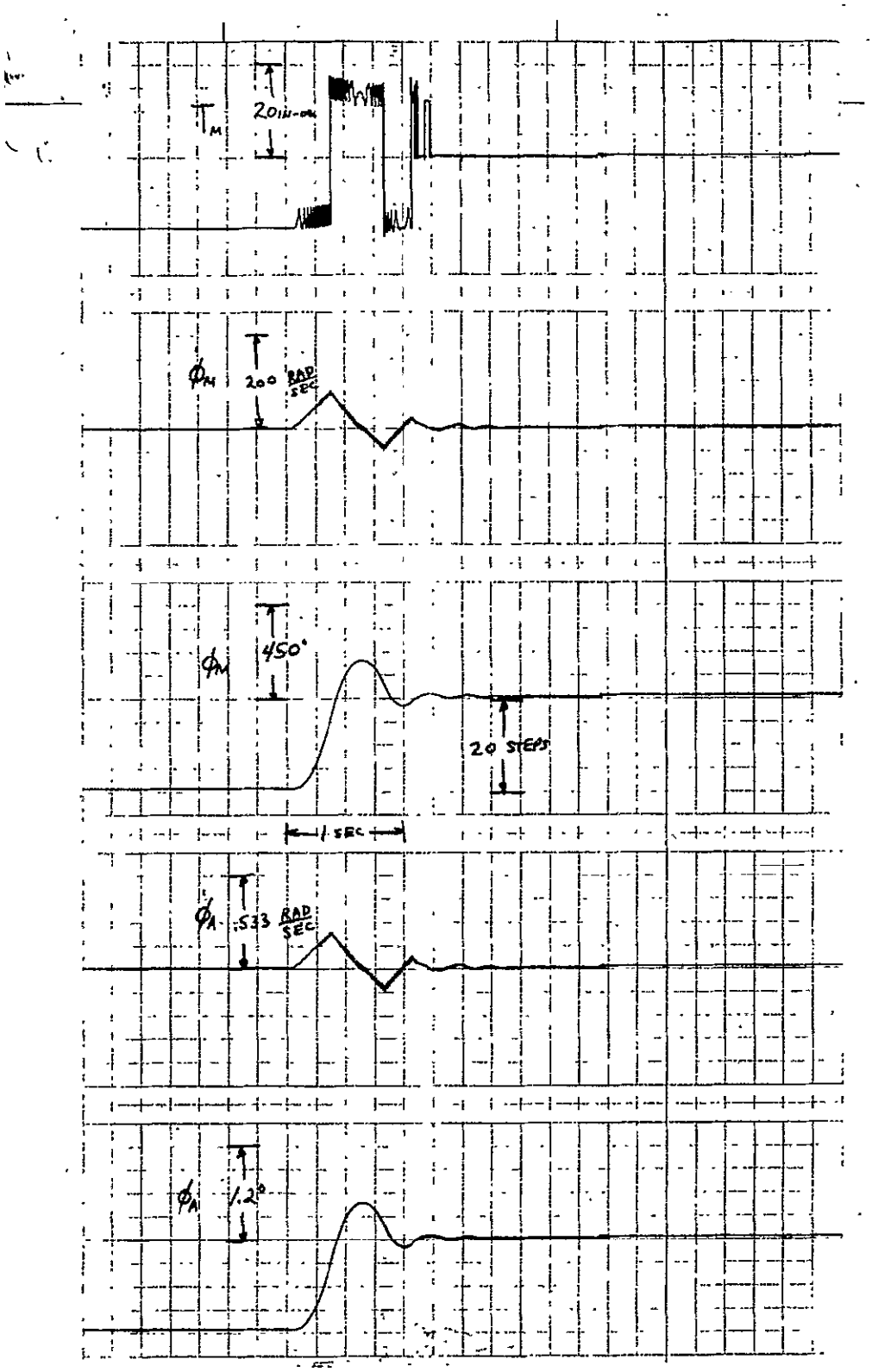

FIGURE 6-15. ANALOG COMPUTER ANTENNA CONTROL RESPONSE

The simulation demonstrates the feasibility of making the required control logic, and also demonstrates the soundness of the approach. There wasn't time to simulate the brushless DC motor control loop, but more previous experience exists with this type of loop so it was felt feasibility was certain.

6.5 ERROR ANALYSES

In a system of this complexity there are many elements, each non-perfect, and hence contributing to the antenna pointing error. Some of these error sources are subject to meaningful analysis and estimation at this stage; others are not. For example the effects of station drift and orbit inclination are fairly readily estimated from preliminary calculations, whereas the amount and frequency spectrum of noise in the DC control loop is more difficult to estimate until a more detailed definition of the amplifiers and logic elements in the loop is available.

6.5.1 Summary of System Errors

Since different errors arise in the different axes, a separate error tabulation for each axis is given below in Table 6-3. The errors represent 35 numbers or worst case, as applicable.

6.5.2 Gear Ratio Selection/Step Resolution

Since a direct drive DC motor is being used on the pitch axis the selection of a gear ratio applies only for the roll and yaw axes. In all of the following a permanent magnet stepper motor is assumed with a 22 1/2° step size. The measurement accuracy of the interferometer was assumed to be $\pm$ 0.02° of which $\pm$ 0.015° was caused by receiver noise and other sources of rapid variation.

TABLE 6-3

SYSTEM ERROR SOURCES

Pitch Axis (Brushless DC Motor Drive)

Alignment of Interferometer to Antenna Structure	$\pm.018$
Thermal Deflection in Horn	$\pm0.06^{\circ}$
Interferometer Measuring Accuracy (20 Hz)	$\pm.02$
Computer Quantizing Errors (10 bit)	±0.02
Station Drift	±0.02
D/A Conversion	±0.01
Yaw Gimbal Error	±0.05
RSS Total	$\pm.088$

Roll Axis (Stepper Motor)

Alignment of Interferometer to Antenna Structure	$\pm0.05^{\circ}$
Thermal Deflection in Horn	$\pm0.06^{\circ}$
Step Resolution	±0.03
Interferometer Measuring Accuracy	$\pm.02$
Linear Actuator Backlash	±0.01
Computer Quantizing Errors	±0.02
Inclination (0.5°)	±0.03
Yaw Gimbal Error ($\pm1^{\circ}$)	±0.05
RSS Total	±0.095

Yaw Axis (Stepper Motor)

Interferometer Measuring Accuracy	±0.95
Step Resolution	±0.03
Linear Actuator Backlash	±0.01
Computer Quantizing Errors	±0.02
RSS Total	$\pm0.95^{\circ}$

The selection of a gear ratio is based on the desire to keep the motor from responding to the high frequency noise, i.e., "hunting" about the nominal position when the nominal position remains fixed. Thus, it is desired to have the step size at the antenna at least twice as large as the jitter in the interferometer signal. For a jitter of $\pm 0.015^{\circ}$ the step size should be about $\pm 0.03^{\circ}$, or since a step can only be taken in one direction, a total size of 0.06° per step has been selected. This is the step size at the antenna. The required gear ratio is the ratio of the motor step size to the antenna step size or 375:1. This gear ratio applies to the roll axis where the roll measurement sensitivity to interferometer errors is about 1:1. For the yaw axis though, the sensitivity is not 1:1 but is determined from the equations of paragraph 6.3.

The yaw gimbal error is determined from two interferometer measurements and the equation:

$$\delta\psi = \frac{\cos\lambda_1[\cos\beta_{2A} - \cos\beta_{2D}] - \cos\lambda_2\,[\cos\beta_{1A} - \cos\beta_{1D}]}{\cos\lambda_1\cos\alpha_{2D} - \cos\lambda_2\cos\alpha_{1D}}$$

$$\frac{2(\delta\psi)}{2\beta_{2A}} \doteq \frac{\cos\lambda_1}{\cos\lambda_1\cos\alpha_{2D} - \cos\lambda_2\cos\alpha_{1D}} \qquad (\text{for } \beta_{2A} \approx 90^{\circ})$$

Suppose that the interferometer boresight is pointed at one of the interferometer beacons, i.e.,

$$\lambda_1 = 0 \qquad \text{and} \qquad \alpha_{1D} = 90^{\circ}$$

Then:

$$\frac{2(\delta\psi)}{2\beta_{2A}} \doteq \frac{1}{\cos\alpha_{2D}}$$

Now, if the second interferometer beacon is located at roughly the same latitude and about 20° longitude away from the first beacon then $\alpha_{2D} \approx 86.5^{\circ}$ and the sensitivity is:

$$\frac{2(\delta\psi)}{2\beta_{2A}} \doteq 16.4$$

Thus, an interferometer jitter of ± 0.015° corresponds to about a ± 0.25° jitter in yaw uncertainty. A yaw step size of 1° is out of the question so it is necessary to have the computer provide some filtering of the yaw gimbal drive signal. The amount of filtering necessary to reduce the jitter by 10:1 would depend on the jitter bandwidth, etc., and could be defined more accurately when the interferometer receiver design is finalized. A 375:1 gear ratio is still planned for the yaw axis if this creates too much of a design problem it can be lowered considerably.

6.5.3 Yaw Measurement Accuracy

The yaw measurement accuracy is a function of two things: beacon separation and interferometer errors in phase measurement.

The equations relating the angles measured by the interferometer to the attitude angles are:

$$(R_o - R_1^{(i)}) \cos\varphi \sin\theta + R_2^{(i)}(\cos\Psi \cos\theta - \sin\Psi \sin\varphi \sin\theta)$$

$$+ R_3^{(i)}(\cos\Psi \sin\varphi \sin\theta + \sin\Psi \cos\theta) = |\rho_i| \left[n_i + \frac{\alpha_{iA}}{2\pi}\right] \frac{\lambda}{d}$$

$$- (R_o - R_1^{(i)}) \sin\varphi - R_2^{(i)} \sin\Psi \cos\varphi + R_3^{(i)} \cos\Psi \cos\varphi =$$

$$|\rho_i| \left[m_i + \frac{\beta_{iA}}{2\pi}\right] \frac{\lambda}{d}$$

where:

R_o	=	radius of satellite from center of earth
$R_1^{(i)}$	=	component of i-th ground station location along line between satellite and earth center
$R_2^{(i)}$	=	component of i-th ground station location along nominal velocity vector
$R_3^{(i)}$	=	component of i-th ground station location along polar axis
φ	=	roll angle of antenna platform
θ	=	pitch angle of antenna platform
Ψ	=	yaw angle of antenna platform
α_{iA}	=	angle measured by interferometer nominally in orbit plane
β_{iA}	=	angle measured by interferometer nominally out of orbit plane
$\lvert\rho_i\rvert$	=	distance from satellite to i-th ground station
λ	=	wavelength received by interferometer
d	=	separation between interferometer receiving antennas
n,m	=	interferometer ambiguities in sensing α_{iA}, β_{iA}

The above equations were linearized for the small angle case. Assuming a priori knowledge of n,m exists, and that signals from two ground stations are available, there exists a unique solution for the angles θ, φ, Ψ when given α_{1A}, α_{2A}, β_{1A}, β_{2A}. Because two stations yield four equations, one equation is redundant, and one can therefore choose which three equations to use. However, the selection is not entirely arbitrary, but is influenced by ground station location. With one ground station at 15°N latitude from the satellite sub-point, the location of a ground station on a constant longitude line represents a singularity for one set of equations, and an almost constant latitude line at $\sim 15^{o}$N latitude represents a singularity for the other set. Thus, if the second ground station is at $\sim 15^{o}$N latitude or 0° longitude (with respect to the satellite sub-point) one is constrained as to which interferometer arm may be used to supply the third equation.

In the presence of perfect interferometer data a perfect knowledge of θ, φ, Ψ can be obtained by using the appropriate three equations. However, the interferometer data will at best give phase information accurate to $\pm 2^{\circ}$ and will more likely be around 3°. With noisy interferometer data and a required accuracy on θ, φ, Ψ, there will exist a region near the first ground station, where the second ground station may not be placed. The size of this region was calculated for a 3° error in phase measurement and an accuracy requirement of $\pm$ .05 degree for θ, φ, and 0.95 degree for Ψ. **Fig. 6-16** shows the minimum separation between station one and two to meet the above accuracy requirements.

The solution for the angles in linearized form is:

$$\theta = a_1\beta_{iA} + a_2\beta_{2A} + b_1m_1 + b_2m_2$$

$$\varphi = c_1\alpha_{1A} + c_2n_1 + c_3$$

$$\Psi = d_1\beta_{1A} + d_2\beta_{2A} + d_3m_1 + d_4m_2$$

where:

$$a_1 = \frac{R_3^{(2)} \, |\rho_1| \, \lambda}{2\pi d[R_3^{(2)}(R_o - R_1^{(1)}) - R_3^{(1)}(R_0 - R_1^{(2)})]}$$

$$a_2 = \frac{R_3^{(1)} \, |\rho_2| \, \lambda}{2\pi d[R_3^{(2)}(R_o - R_1^{(1)}) - R_3^{(1)}(R_o - R_1^{(2)})]}$$

$$b_1 = 2\pi \, a_1$$

$$b_2 = 2\pi \, a_2$$

$$c_1 = \frac{-|\rho_1|\ \lambda}{2\pi d(R_o - R_1^{(1)})}$$

$$c_2 = 2\pi\ c_1$$

$$c_3 = \frac{R_3^{(1)}}{R_o - R_1^{(1)}}$$

$$d_1 = \frac{|\rho_1|\ \lambda}{2\pi d\left[R_3^{(1)} - R_3^{(2)}\ \frac{(R_o - R_1^{(1)})}{(R_o - R_1^{(2)})}\right]}$$

$$d_2 = \frac{|\rho_2|\ \lambda}{2\pi d\left[R_3^{(2)} - R_3^{(1)}\ \frac{(R_o - R_1^{(2)})}{(R_o - R_1^{(1)})}\right]}$$

$$d_3 = 2\pi\ d_1$$

$$d_4 = 2\pi\ d_2$$

With this set of equations it is possible to locate the second ground station anywhere in the region of coverage except near 15°N latitude and subject to the constraints of Figure 6-16.

More detailed analysis of the interferometer receiver indicates that the 35 phase error (per measurement) will be on the order of 4.8°, so to obtain a 0.95° yaw measurement accuracy the shaded area of Figure 6-16. must be increased in size, or the data must be averaged over more than one phase measurement.

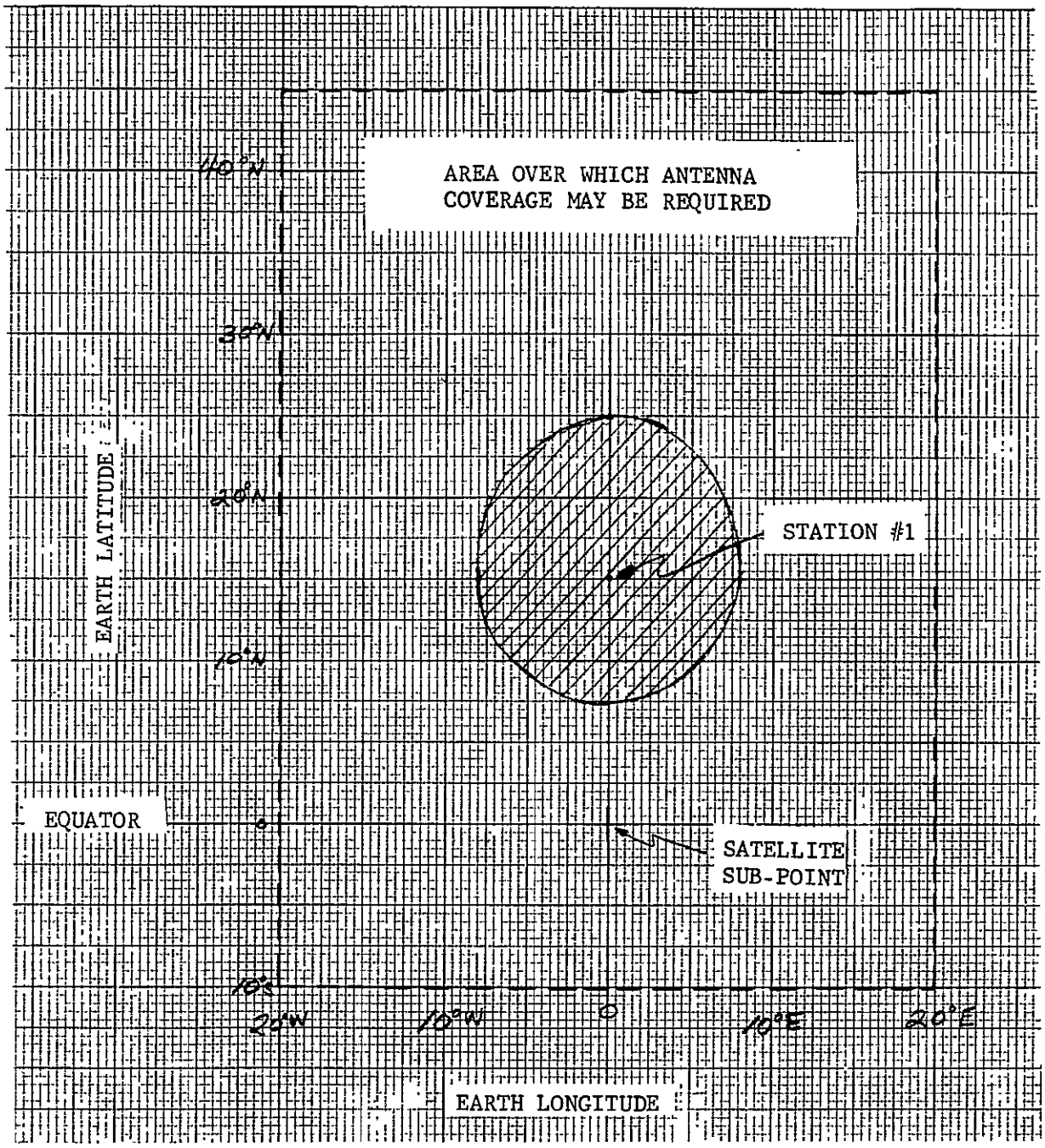

Figure 6-16. EXCLUDED AREA FOR LOCATION OF SECOND GROUND STATION (SHADED AREA)

6.5.4 Effects of Yaw Gimbal Error in Pitch and Roll

As can be seen from the equations of paragraph 6.3, the sensitivities of the roll and pitch gimbal errors are given by:

$$\frac{2(\delta\Phi)}{2(\delta\Psi)} = \frac{\cos \alpha_{1D}}{\cos \lambda_1}$$

$$\frac{2(\delta\theta)}{2(\delta\Psi)} = \frac{\cos \beta_{2D}}{\cos \lambda_2}$$

From a casual inspection of the geometry it can be seen that:

$$-10 < \lambda_2 < 10$$

and:

$$87^\circ < \alpha_{1D} < 93^\circ$$

$$87^\circ < \beta_{2D} < 93^\circ$$

$$\cos \alpha_{1D} \leq .0525$$

$$\cos \beta_{2D} \leq .0525$$

Therefore, if $\delta\Psi$ is $\pm 0.95^\circ$ the uncertainty in the other gimbal angles is:

$$\Delta(\delta\Phi) \leq \pm .05^\circ$$

$$\Delta(\delta\theta) \leq \pm .05^\circ$$

6.5.5 Computer Quantization

In trying to estimate computer quantization errors it will be assumed that the maximum angle to accomodate is 10° and that the computer works with a 10 bit word size. This gives an uncertainty of:

$$\epsilon = \frac{10}{1024} \doteq .01^{\circ}$$

per calculation. Assuming 4 calculations per gimbal angle and that the ϵ's add in an RSS fashion gives a total error due to computer quantization of $\pm\ 0.02^{\circ}$ per channel.

6.5.6 Inclination and Station Drift Errors

The effect of inclination and station drift is to change the desired interferometer angles if the antenna is to remain pointed at a fixed spot on the earth's surface.

Fig. 6-17 shows the geometry, exaggerated for analysis. The north-south situation is chosen because greater latitude differences can occur than longitude differences. It is desired to know the maximum difference that can occur in γ_{11} and γ_{12} as the satellite moves from ρ_1 to ρ_2 due to an orbit inclination of 0.5°. The angles γ_{11} and γ_{12} represent the complement of the angles measured by the vertical interferometer arm.

$$L = 2\ r_e \sin 15^{\circ}$$

$$\theta_1 \doteq 120^{\circ} + \tan^{-1}\left[\frac{r_e \sin 15^{\circ} - r_s \sin 1/2^{\circ}}{r_s - r_e}\right] = 122.033^{\circ}$$

$$\theta_2' \doteq 120^{\circ} + \tan^{-1}\left[\frac{r_e \sin 15^{\circ} + r_s \sin 1/2^{\circ}}{r_s - r_e}\right] = 123.217^{\circ}$$

Thus:

$$\tan \gamma_{11} \doteq \frac{L \cos (\theta_1 - 90)}{r_s - r_e} = \frac{2\ r_e \sin 15^\circ \cos (32.03^\circ)}{5.65\ r_e} = .077670$$

$$\tan \gamma_{12} = \frac{L \cos (\theta_2 - 90)}{r_s - r_e} = \frac{2\ r_e \sin 15^\circ \cos (33.217^\circ)}{5.65\ r_e} = .07665$$

$$\gamma_{11} = 4^\circ\ 26.48'$$

$$\gamma_{12} = 4^\circ\ 23.0'$$

$$\gamma_{11} - \gamma_{12} = 3.48' = 0.058^\circ$$

Therefore, the worst case north-south pointing error would be about ± 0.03 degree.

For the east-west pointing error it is only necessary to observe that the maximum required east-west deviation of the pattern center is about 2/3 of the north-south range in pattern locations, and in addition, θ_1 and θ_2 are much closer to 90° making the sensitivity $\cos (\theta_i - 90)$ much smaller. Also, the effect could be taken out on a daily basis so that not all of the 0.5 degree station error need be included. For these reasons it has been estimated that no difficulty would be encountered in keeping the east-west error from this source below ± 0.01 degree.

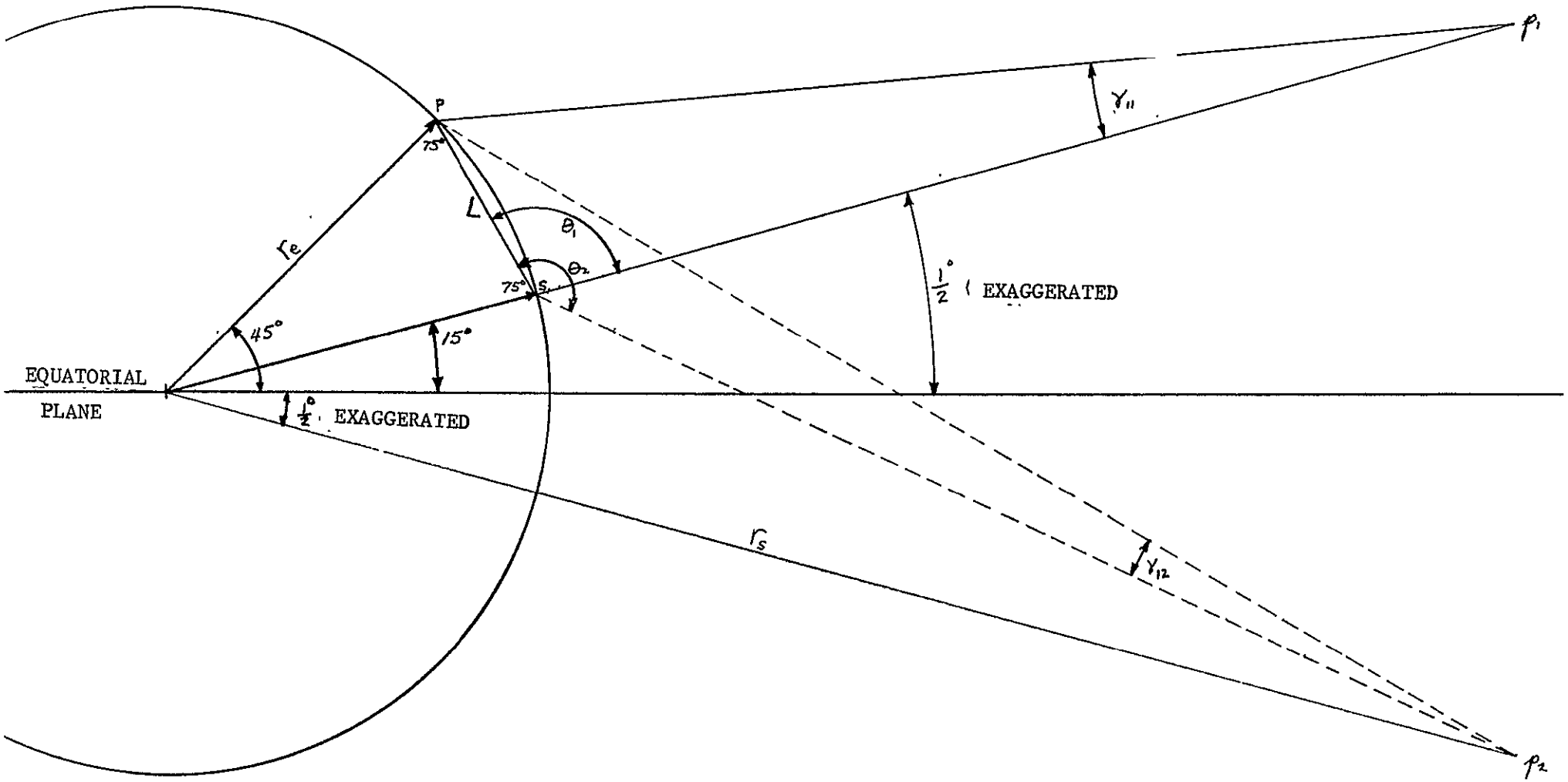

FIGURE 6-17 GEOMETRY & NOTATION

6.6 Alternate Requirements

The effects of the alternate requirements on the antenna pointing control system have been mentioned briefly, but all of the effects have not been summarized yet. The effects of two major changes in antenna pointing requirements have been evaluated. One of the changes is to control the spacecraft attitude to within ± 0.1 degree about all three axes, with a maximum rate of 0.2 degree per day. The other change is to require the 360° rotation per day of the solar array rather than the antenna system.

Tightening the accuracy requirements on the spacecraft attitude to ± 0.1 degree eliminates the practical need for a yaw gimbal, which has been verified in the changed requirements. Thus, instead of 3 gimbals being required, at most 2 will be necessary. The two required gimbals are pitch and roll, with the pitch channel requiring continuous rotation of 360° per day. The choice of a stepper motor drive is natural for this (roll gimbal) application, since the only time the system will need to operate is when the beam direction is changed (for zero inclination and eccentricity). The stepper motor will hold its position until commanded to change. If inclination control isn't used, then the antenna pointing control system will have to remove its effects. This will require changing the stepper motor position more frequently than indicated for the maximum rate of 0.2 degree per day. However, the updating interval for the desired antenna pointing angles is still probably long enough to eliminate the need for an on-board computer. Since this is relatively infrequent it is possible to do all of the necessary computation on the ground, without requiring a telemetry and command channel full time.

The preceding has assumed that the antenna control system pointing reference is different than the spacecraft attitude control system reference. If the spacecraft attitude control system uses the interferometer as its reference, two changes to the foregoing are necessary. First, the pitch-roll gimbals will require angle encoders (14 bit), so that the relative angles between the antenna system and spacecraft are

available. Second, to avoid the need for continuous updating of the desired relative pitch gimbal angle from the ground, some type of clock drive would be desirable on the satellite to perform the updating automatically. Figure 6-18 is a schematic of an automatic updating system that could be used. It is assumed that the clock could be made accurately enough so that the phase update would be required at most every 1/2 to 1 day (1 part in 10^4 is long term stability requirement on oscillator).

For the change eliminating the 360° per day rotation requirement on the antenna control system it is to be assumed that the attitude accuracy is maintained to within $\pm 0.1^\circ$ and that no yaw gimbal is necessary, as before. Again, two choices are available for the attitude control reference: the interferometer, or a separate reference system. Another interesting possibility presents itself when no continuous rotation in pitch is required: that of having only a roll gimbal and pitching the whole spacecraft through the angle that would have been performed by the pitch gimbal. This would mean a slight additional tracking motion would be required of the solar array, which shouldn't cause any problem.

If a separate reference is used for the spacecraft attitude control system then the required computations for control can be done either on the ground or in the spacecraft. Doing the computations on the ground would simplify the electronics required on the spacecraft.

Using the interferometer as a spacecraft attitude reference would require gimbal angle encoders, just as before. However, the clock updating circuit is not required. To determine whether or not the control computations could be done on the ground would require an analysis of the attitude control system and the expected rates. The level of confidence in the predicted rates would also have to be evaluated since the accuracy and stability of the attitude control is a functional of the required vs. available bandwidth in the control computation loop. That is, the processing of data on the ground can be looked at as a very low bandwidth

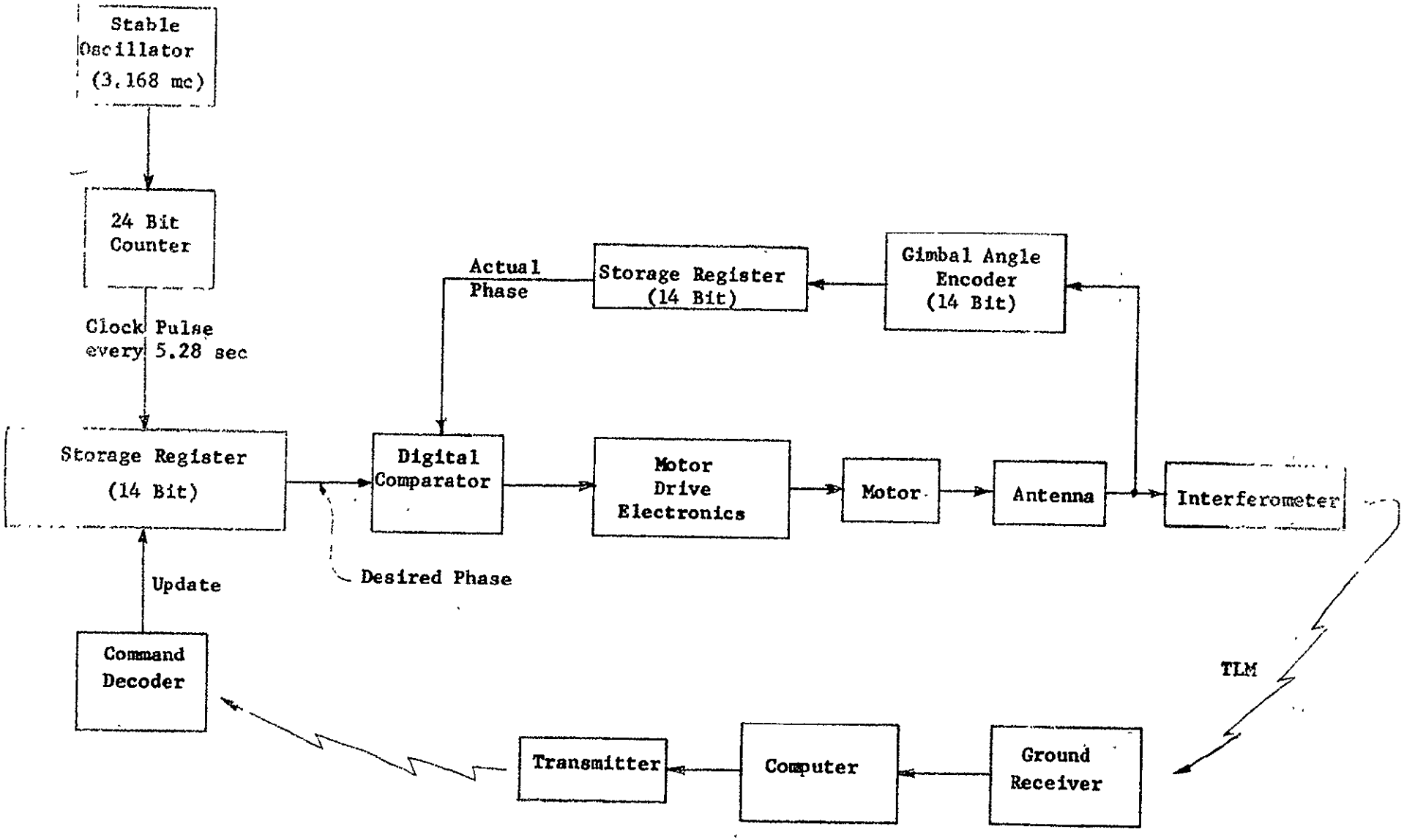

Figure 6-18 Automatic Update System for Use with Ground-Based-Computer-Concept

portion of the system, and if greater bandwidth is required for stability, or accuracy in overcoming the expected torque environment, then the computations will have to be done on the spacecraft to avoid the lag inherent in the ground computation scheme.

Tables 6-4 and 6-5 summarize the effects of the alternate requirements.

TABLE 6-4

EFFECT OF ALTERNATE REQUIREMENTS

ALTERNATE REQUIREMENTS

a) SPACECRAFT ATTITUDE CONTROLLED TO ± 0.1 DEGREES

b) MAXIMUM SPACECRAFT RATE 0.2°/DAY

EFFECT:

- YAW GIMBAL ELIMINATED
- ON-BOARD COMPUTER ELIMINATED
- ROLL GIMBAL GROUND CONTROLLED
- PITCH GIMBAL ON-BOARD CONTROLLED

  or

  WITH CLOCK DRIVE UPDATED BY GROUND COMMAND
- ONLY ONE BEACON STATION REQUIRED
- SOLAR PANEL INTERFERENCE WITH ANTENNA BEAM ELIMINATED

TABLE 6-5

EFFECT OF ALTERNATE REQUIREMENTS

ALTERNATE REQUIREMENT

- SPACECRAFT ATTITUDE CONTROLLED TO $\pm 0.1^{\circ}$ NORTH
- MAXIMUM SPACECRAFT RATE 0.2°/DAY
- ELIMINATION OF 360°/DAY ROTATION IN PITCH (SPACECRAFT EARTH POINTING, SOLAR ARRAY ARTICULATED)

EFFECT

- YAW GIMBAL ELIMINATED EARTH
- ROLL AND PITCH GIMBAL LIMITED MOTION
- ON-BOARD COMPUTER ELIMINATED
- ROLL AND PITCH GIMBAL GROUND CONTROLLED
- RF ROTARY JOINT ELIMINATED
- ANTENNA SUPPORT STRUCTURE REDUCED HEIGHT
- RF LOSSES REDUCED BY 0.4 db